Analysis of Slab-on-Grade Floors Subject to Slab-Mounted Jib Cranes

by

Kington Chu

A thesis
presented to the University of Waterloo
in fulfilment of the
thesis requirement for the degree of
Master of Applied Science
in
Civil Engineering

Waterloo, Ontario, Canada, 2022

Author's Declaration

I hereby declare that I am the sole author of this thesis. This is a true copy of the thesis, including any required final revisions, as accepted by my examiners.

I understand that my thesis may be made electronically available to the public.

Abstract

Free-standing, foundationless jib cranes mounted directly on unreinforced slab-on-grade floors are a common necessity in industrial settings for material handling purposes. Ensuring that existing slabs can support a jib crane is critical, as industrial floors are subject to stringent serviceability requirements. Sudden slab failure can result in dropped loads and the loss of life. The installation of such cranes is typically based on rules of thumb, and no design standards or guidelines currently exist. Slabs-on-grade are typically designed for vertical compressive forces stemming from vehicle wheel loads or storage rack posts; however, a slab-mounted crane transfers both compressive forces and an overturning moment to the slab. In this study, a parametric analysis was conducted by simulating finite element models to investigate the behaviour of unreinforced slab-on-grade floors under foundationless, freestanding crane loads. Statistical methods were used to develop a non-linear model capable of predicting the capacity of such slabs. In particular, for the range of practical values considered in the study, it was found that the slab thickness, concrete strength, and baseplate size were critical parameters greatly affecting the capacity of such slabs. This research provides more confidence and safety when checking the installation and operation of such cranes on plain slabs-on-grade.

Acknowledgements

I would like to thank my supervisor, Dr. Eugene Kim, for his guidance and support over the course of my master's degree. I would like to additionally thank the nonprofit national research organization, Mitacs, for funding the initial portion of this project. I would like to thank Akram Ibrahim and Gary Johnston from Engineered Lifting Systems for first bringing forward the lack of clarity regarding the capacity of slabs supporting foundationless cranes, and for their hospitality in welcoming me to the office even during the pandemic of 2021.

I would also like to give thanks to my friends and classmates who provided valuable insight on the various problems encountered along the way: Suri Zhu, Henny Duong, Dar Mehta, and Ryan Wong.

I would finally like to thank my friends and family for their support.

Table of Contents

List of Figures

List of Tables

1.0 Introduction

1.1 Research Needs

In an industrial warehouse setting, floors are typically thin, jointed plain concrete slabs-on-grade minimally reinforced specifically for temperature and shrinkage control and are supported laterally by adjacent slabs or doweled connections and vertically by the soil it rests on. Cranes (i.e., overhead, gantry, bridge, jib, amongst others) are a common necessity in these settings as they are used for material handling purposes to aid workers in the mobility of loads often beyond the capability of human strength. In particular, foundationless jib cranes are cranes without any supplementary poured concrete foundations and are instead mounted directly to the slab via post-installed anchor bolts. Foundationless cranes of this nature boast flexibility in terms of the time and cost required for installation or future relocation, making it a very attractive option for warehouse owners. However, foundationless, slab-mounted cranes force the slab they are mounted on to bear all of the self-weight and load of the crane in conjunction with the overturning moment produced by the eccentric loading of the crane's arm. This combination can produce large bending stresses that a thin, unreinforced slab may not be able to resist. The typical industry practice for installing jib cranes involves adopting an upper bound of 8-kip-ft (approximately 10.8 kNm) for the maximum allowable overturning moment that a slab can support. The origins and validity of this rule-of-thumb are unfortunately unclear, and its practical applications are questionable at best as established crane manufacturers (Gorbel, 2012; Spanco, 2018) regularly install foundationless jib-cranes with load capacities licensed up to 16-kip-ft (approximately 21.6 kNm) based on their minimum requirements: a minimum concrete strength of 3000 psi, subgrade bearing capacity of 2500 psf, and a slab thickness of 6". However, in practice, foundationless cranes are often mounted to pre-existing slabs-on-grade that may have unclear dimensions and material properties; it is reasonable to assume that the actual thickness of the slab varies between 4" – 8". A typical foundationless, slab-mounted jib crane is depicted in Figure 1.1:

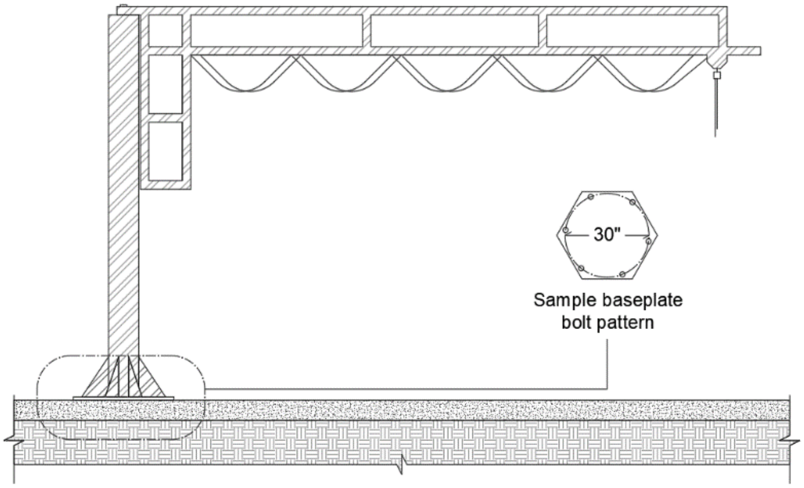

Figure 1.1: Typical side view of a foundationless, freestanding jib crane

Contemporary methods for designing slabs-on-grade are closely linked to the design of airport and highway pavements and are largely based on the Winkler spring model following the prevailing efforts of Harald Westergaard, who, throughout much of the early 20th century, provided rigorous theoretical solutions for the maximum deflections and critical bending stresses of infinite and semi-infinitely spanning slab-on-grade pavements subject to various vertical concentrated loadings (Westergaard, 1926). While Westergaard's solutions were specifically presented for the design of highway, railroad, and airport runway pavements, his analyses and solutions have been ubiquitously adopted for general applications of slabs-on-grade. His work has largely stood the test of time and has been the subject matter of rigorous analysis and discussion over the past century (Ioannides, 1989), and now serves as the basis for the three conventional design methodologies accepted by the American Concrete Institute: 1) the Portland Cement Association (PCA) method, 2) the Wire Reinforcement Institute (WRI) method, and 3) the Corps of Engineers (COE) method (McKinney et al., 2006). Notably, all three methods do not address the effects of any vertically applied uplifting forces acting on the slab. A Winkler soil model by definition provides artificial tensile stiffness to a slab, and as a result, is unsuitable for use when considering a slab-on-grade subject to an overturning moment. A need therefore arises to develop guidelines for this type of structural problem. This study aims to address these overturning moments by substituting an equivalent elastic soil model without any tensile support and establishing generalized equations used to predict the maximum moment capacities for slab-on-grade problems of this nature.

1.2 Objectives

The overarching aim of this research is to investigate the performance of industrial slab-on-grade floors of various dimensions (length and thickness) and material properties (concrete and subgrade strength) mounted by cranes of various sizes (load capacity and load distribution). The scope of this study is limited to freestanding, foundationless jib cranes with a maximum capacity of 1-ton mounted to slab-on-grade floors minimally reinforced for crack control. Most design checks (i.e., allowable deflection, soil bearing, anchor-associated failure, one-way and two-way shear, and concrete) can be easily performed by existing guidelines. As the serviceability limit states govern over the ultimate limit states for warehouse floor applications, this study will only investigate the first cracking of the concrete caused by tensile stresses.

The following objectives in this study have been outlined below:

- Determine a relationship between the Winkler spring model and an elastic half-space model that removes the artificial tensile stiffness by relating the modulus of subgrade reaction to an equivalent modulus of elasticity.
- Develop a simplified finite element (FE) model in Abaqus representing the typical slab-soil system seen in industrial settings. The initial finite element model will be verified against existing analytical solutions for simple problems and previous finite element studies of the same form (Hu and Hartley, 1994; Silva et al., 2001; etc.).

- Conduct a parametric study on various slab-soil dimensions and material properties by automating the mass simulation of calibrated FE models through Python and Matlab.
- Conduct a non-linear, multivariate statistical regression on the data obtained from the parametric study to develop a mathematical model that can be used to adequately predict the moment capacity of any slab-soil system with dimensions and material properties within the range of considered values.

1.3 Thesis Organization

This thesis is divided into 5 chapters. The information presented in each chapter has been summarized below:

- Chapter 1 provides a brief overview on the research topic and provides insight on the motivations, goals, and objectives.
- Chapter 2 provides a comprehensive literature review involving the contemporary methods for slabs-on-grade design presented by the American Concrete Institute, historical methods for idealizing soil mediums, and any existing analytical and numerical solutions for the problem of a slab-on-grade.
- Chapter 3 provides the formulation of the FE model used in this study. In particular, the selection of the model parameters (slab length, slab thickness, specific concrete compressive strength, subgrade strength, baseplate radius, and vertical compressive force) and the upper and lower bounds for each variable are discussed. The model definition and verification and validation results are also provided.
- Chapter 4 presents the numerical results associated with the data collection and analysis of the parametric study. The influence of each model parameter and the performance of the slab-on-grade with respects to changes in any parameter is discussed, and the non-linear multivariable regression model is validated. The final general equation is also presented.
- Chapter 5 summarizes the findings in this study and provides recommendations for areas of future work.

2.0 Literature Review

2.1 Design of Slabs-on-Grade

In general, the contemporary design methods of slabs-on-grade in North America (including the Canadian Concrete Handbook, CSA A23) are largely detailed by three methods presented by American Concrete Institute (ACI 360R-06) and the United States Air Force Manual (TM-5-809):

1. the Portland Cement Association (PCA) method,
2. the Wire Reinforcement Institute (WRI) method, and
3. the Corps of Engineers (COE) method.

All three methods are based on analyses largely attributed to Westergaard's work on infinitely spanning slabs resting on Winkler-type foundations (citing works from 1923, 1925, and 1926) and subject to wheel loads idealized as concentrated loads distributed over a small circular or elliptical area. An important assumption that all three methods make (which conveniently allows for the use of a Winkler foundation) is that a slab-on-grade remains in full, continuous contact with the ground throughout the duration of its deformation (McKinney et al., 2006). This assumption produces artificial tensile stiffness between the slab and the soil but is largely negligible for the vast majority of slab-on-grade design applications involving vehicle wheel loads (forklifts and other vehicles), concentrated, strip, and line loads produced by various warehouse equipment (i.e., storage posts and racks), and distributed loads (produced by pallets, etc.) in which the critical deflections and bending stresses are overwhelmingly in the vertical, downwards direction and found on the bottom surface of the slab.

The following sections will briefly summarize each of the design guidelines listed above.

2.1.1 PCA Design Method

PCA offers design guidelines to establish the thickness of a slab-on-grade limited to the case of a slab-on-grade loaded near the center and away from its edges. The design charts and tables provided by PCA are limited to considering single- or double axle- vehicular wheel loads, concentrated loads, and uniform loads and assumes that the critical tensile stresses develop on the bottom surface of the slab centrally under the load.

The PCA design method has been loosely summarized below by considering the case of a slab-on-grade subject to a central single-axle wheel load. It is assumed that the concrete material properties, subgrade material properties, and loading conditions are all known and predetermined.

The factor of safety must first be established. Typical values are recommended as varying between 1.7 – 2 but may otherwise be left to the judgement of the engineer (Packard, 1996).

The working stress of concrete may then be determined:

$$WS = \frac{MR}{SF} \tag{2.1}$$

in which *WS* is the concrete working stress, *MR* is the modulus of rupture of concrete, and *SF* is the factory of safety.

The slab stress per 1000 lb (4448 N) of load is then determined:

$$SS = \frac{WS}{load,\ kips} \tag{2.2}$$

in which *SS* is the slab stress per 1000 lbs. The design chart in Figure 2.1 is then used to determine the required slab thickness based on *SS,* wheel spacing, effective contact area, and subgrade strength.

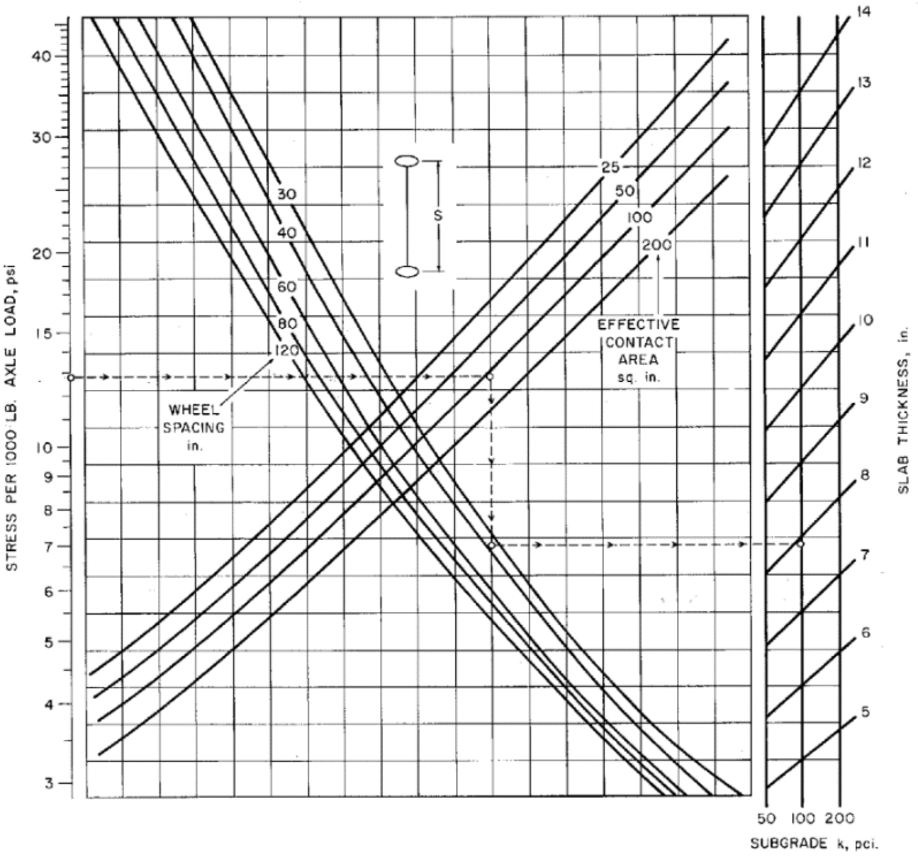

Figure 2.1: PCA design chart – design slab thickness determined by wheel spacing, effective contact area, and subgrade strength (McKinney et al., 2006)

A horizontal line is first drawn towards the right from the known axle load stress until it intersects with the curve associated with the effective contact area. A vertical line from this intersection is drawn downwards until it intersects with the curve associated with the wheel spacing. Finally, a horizontal line is then drawn towards the right from this intersection until it intersects with the curve associated with the slab thickness and subgrade strength.

After determining the initial concrete slab thickness, Figure 2.2 can be used to check if the actual contact area is sufficient; else, the procedure should be restarted but using the new effective contact area:

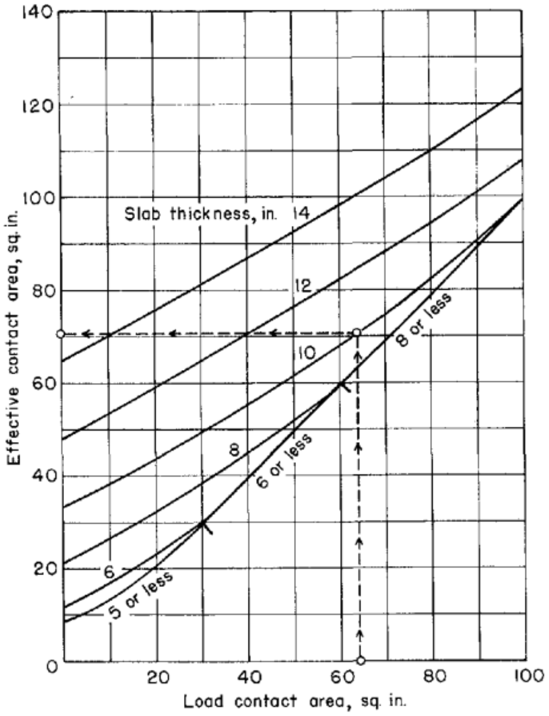

Figure 2.2: PCA design chart – effective load contact area based on slab thickness (McKinney et al., 2006)

A vertical line is first drawn upwards starting from the known load contact area until it intersects with the curve associated with the determined initial slab thickness. A horizontal line can then be drawn to the left to determine the effective contact area.

This design procedure may be followed for any of the loading cases considered and is nearly identical. For a comprehensive, detailed guide on the PCA design method, the reader is suggested to examine 'Design of Slabs-on-Ground' (McKinney et al., 2006) and 'Slab Thickness Design for Industrial Concrete Floors on Grade' (Packard, 1996).

2.1.2 WRI Design Method

Like the PCA method, WRI offers design guidelines limited to the case of a slab-on-grade subject to a central load away from any edges. The design charts provided by WRI are limited to single-axle vehicular wheel loads, though concentrated loads may be considered by determining an equivalent or representative wheel load. In the case of a wheel load, it is assumed that the critical stresses develop on the bottom surface of the slab. WRI also provides design charts for the case of uniformly distributed loads on either or both sides of an aisle (i.e., the pedestrian floorspace between two storage racks). In the case of this uniform loading pattern, it is assumed that the critical stresses develop on the top surface of the slab (McKinney et al., 2006).

The WRI design method has been loosely summarized below by considering the case of a slab-on-grade subject to a central single-axle wheel load. It is assumed that the concrete material properties, subgrade material properties, and loading conditions are all known and predetermined.

An initial trial thickness, *H*, is arbitrarily assigned. The design chart in Figure 2.3 is used to determine to relative stiffness parameter between the slab and the subgrade, *D/k*:

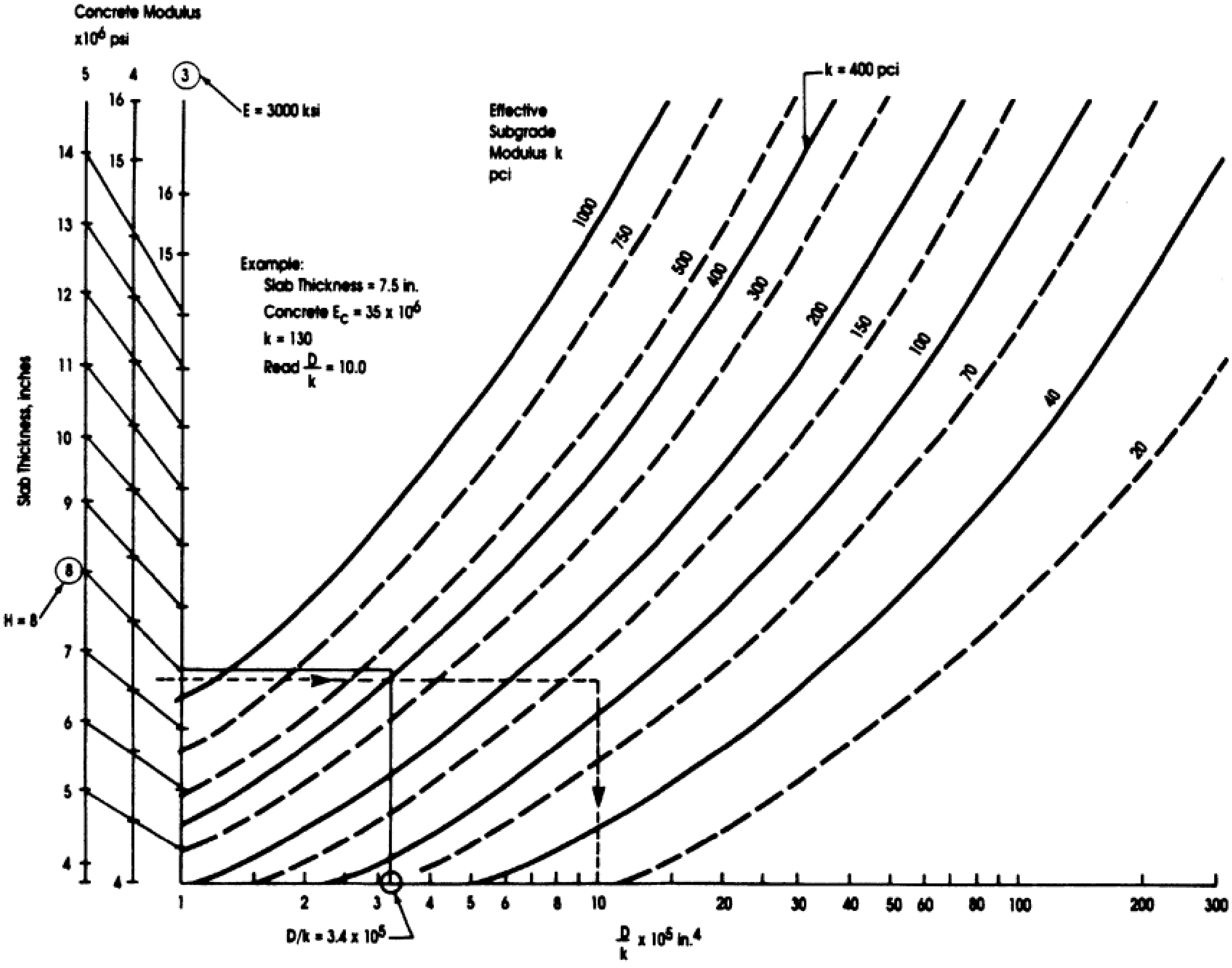

Figure 2.3: WRI design chart – relative stiffness parameter determined by the subgrade strength and trial slab thickness (McKinney et al., 2006)

A horizontal line is drawn from the intersection of the trial slab thickness and modulus of elasticity of concrete towards the right until it intersects with the curve associated with the known subgrade strength. From there, a vertical line can be drawn downwards to find the relative stiffness parameter.

Next, the diameter of the equivalent contact area based on the actual wheel contact area should be determined:

$$d_{equiv.} = \sqrt{\frac{4(\pi r^2)}{\pi}} \tag{2.3}$$

in which r is the radius of the actual wheel contact area. The diameter of the equivalent contact area, wheel spacing, and the relative stiffness parameter obtained from Figure 2.3 may then be used in Figure 2.4 to determine the basic moment induced by the wheel and the additional moment induced by a wheel spaced further out:

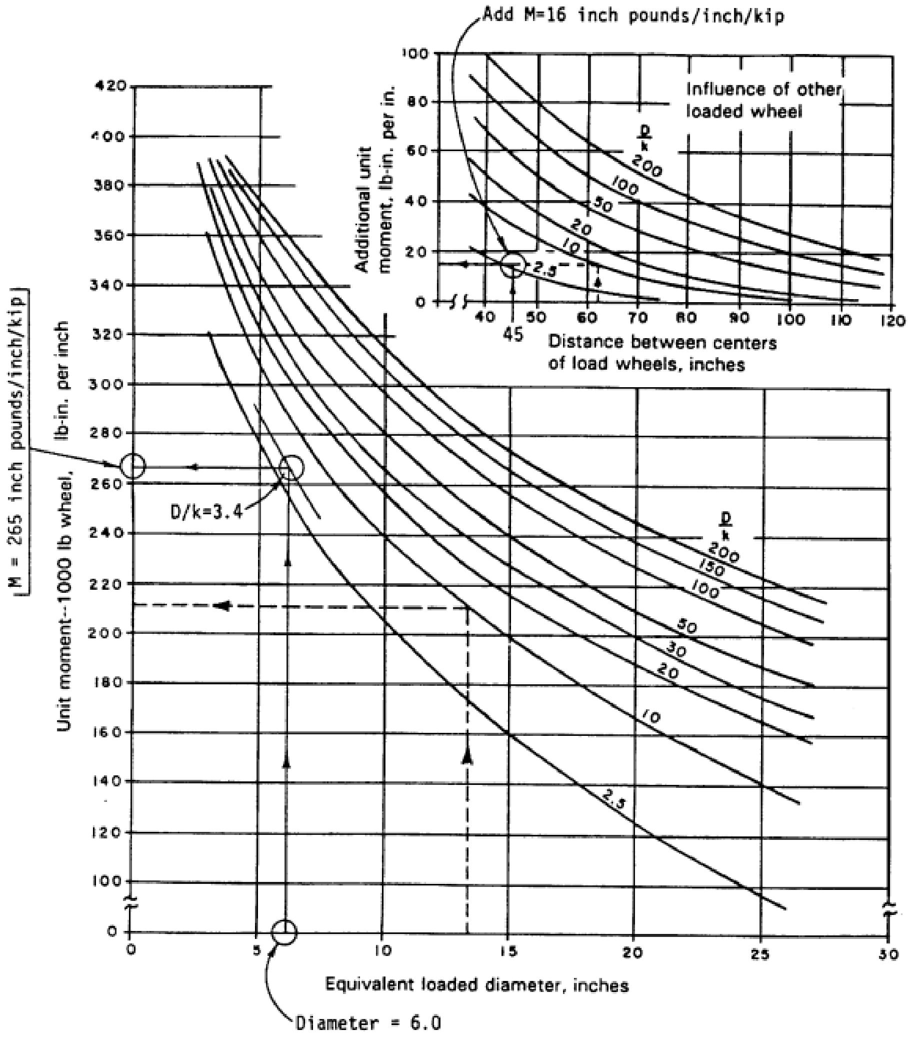

Figure 2.4: WRI design chart – basic moment and additional moment determined by the diameter of the equivalent contact area and wheel spacing, respectively (McKinney et al., 2006)

A line is first drawn vertically upwards from the known equivalent loaded diameter until it intersects with the known relative stiffness. A horizontal line can then be drawn to the left to find the unit moment.

Finally, using the calculated moment and the allowable tensile stress, Figure 2.5 may be used to determine the required slab thickness.

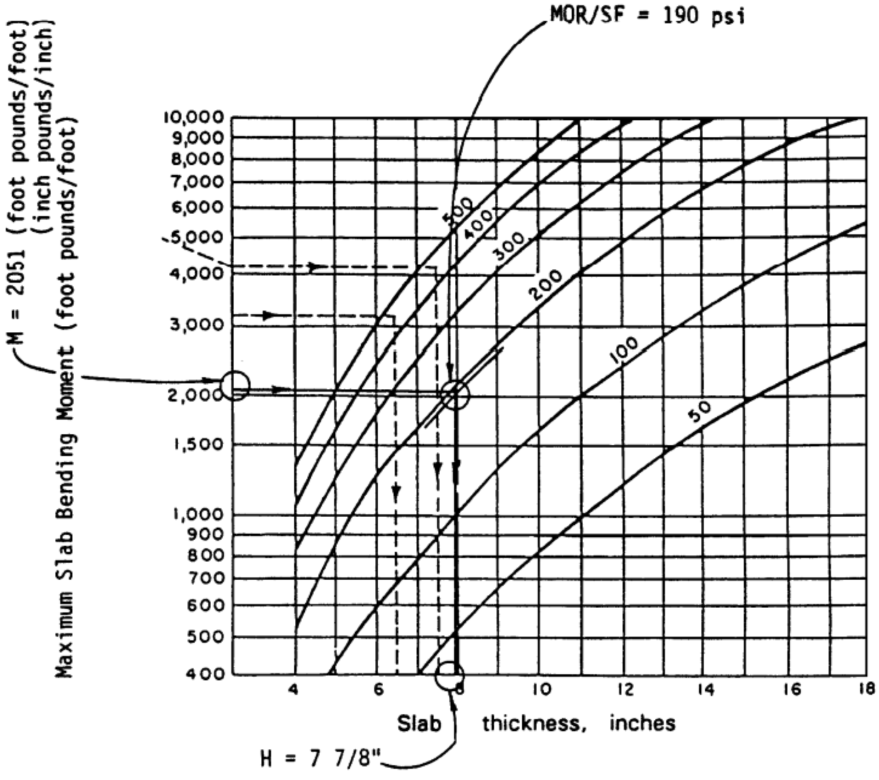

Figure 2.5: WRI design chart – design slab thickness determined by the maximum moment and allowable tensile stress (McKinney, et al., 2002)

A line is first drawn horizontally towards the right from the known combined slab bending moment until it intersects with the known allowable tensile stress. A line can then be drawn vertically to determine the slab thickness.

If the required thickness differs substantially from the initially assumed thickness, the design procedure should be restarted with the determined thickness as the new initial trial thickness (McKinney, 2002).

For a comprehensive, detailed guide on the WRI design method, the reader is suggested to examine ‘Design of Slabs-on-Ground’ (McKinney et al., 2006) and ‘Design of Slab-on-Ground Foundations’ (Snowden, 1981).

2.1.3 COE Design Method

While the PCA and WRI methods are used for the case of interior loading, the COE design method is intended for slabs-on-grade loaded directly at an edge or a joint and aims to limit the tensile stresses at the bottom of said joint. COE provides design charts limited solely to single- and double-axle vehicular wheel loads and do not consider concentrated, uniform, or strip loads. In particular, the determination of size and load of considered wheels are dependent on the classification of a vehicle design index. Therefore, an exact slab thickness required for a particular wheel load cannot be determined, and instead, a general slab thickness may be obtained for each class of wheel loads.

The COE design method has been loosely summarized by considering the case of a slab-on-grade subject to a single-axle wheel load applied at an edge. It is assumed that the concrete material properties, subgrade material properties, and loading conditions are all known and predetermined.

First, a given wheel loading must be classified based on a nominal capacity determined by Figure 2.6:

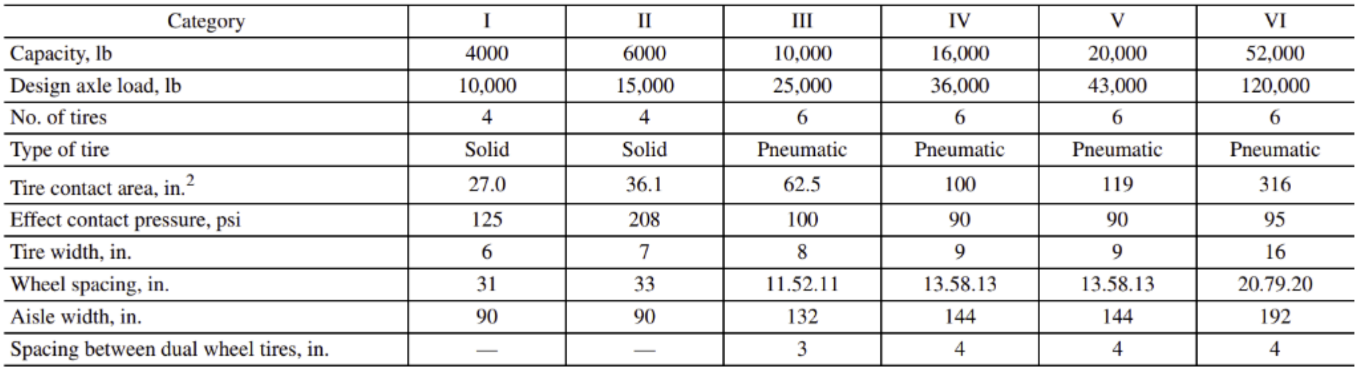

Category	I	II	III	IV	V	VI
Capacity, lb	4000	6000	10,000	16,000	20,000	52,000
Design axle load, lb	10,000	15,000	25,000	36,000	43,000	120,000
No. of tires	4	4	6	6	6	6
Type of tire	Solid	Solid	Pneumatic	Pneumatic	Pneumatic	Pneumatic
Tire contact area, in.^{2}	27.0	36.1	62.5	100	119	316
Effect contact pressure, psi	125	208	100	90	90	95
Tire width, in.	6	7	8	9	9	16
Wheel spacing, in.	31	33	11.52.11	13.58.13	13.58.13	20.79.20
Aisle width, in.	90	90	132	144	144	192
Spacing between dual wheel tires, in.	—	—	3	4	4	4

Figure 2.6: COE design chart – vehicle design index (McKinney et al., 2006)

The design index category controls the various loading conditions applicable to the slab. Once this is established, the Figure 2.7 may be used to determine the required thickness:

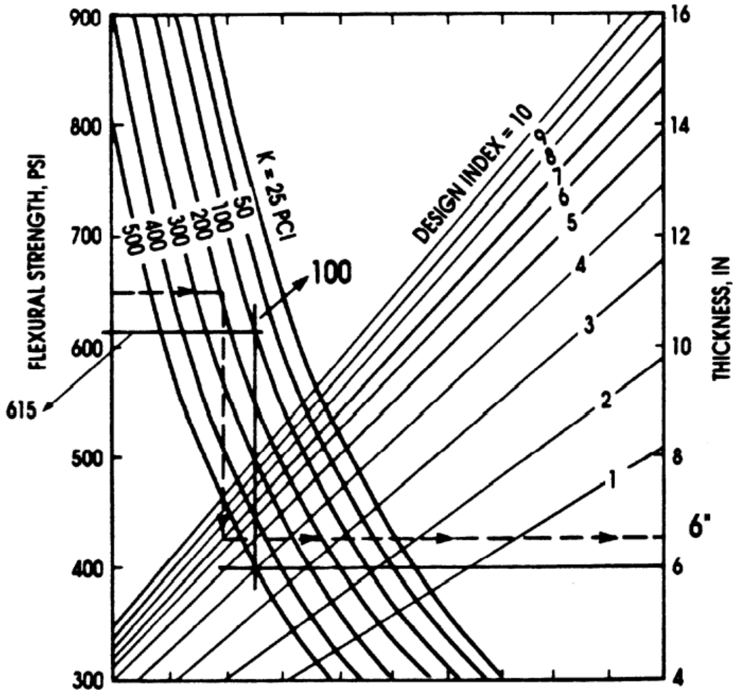

Figure 2.7: COE design chart – required slab thickness determined by design index, subgrade strength, and flexural strength, (McKinney et al., 2006)

A line is first drawn horizontally to the right from the known flexural strength until it intersects with the known subgrade strength. A line is then drawn vertically downwards until it intersects with the known design index. Lastly, a line is then drawn horizontally to the right to find the required thickness.

For a comprehensive, detailed guide on the COE design method, the reader is suggested to examine ‘Design of Slabs-on-Ground’ (McKinney et al., 2006).

2.2 Idealized Linear Elastic Soil Models

One of the differences that the design of slabs-on-grade have over conventional slab design (i.e., typical one-way or two-way spanning slabs supported by beams, columns, or walls) is that slabs-on-grade are continuously supported on its bottom face by the subgrade over which it rests on. Therefore, the behaviour of the slab is dependent on the behaviour of the subgrade, which is difficult to accurately characterize. The characterization of a subgrade’s behavior under loading requires a complete stress-strain relationship of the soil; however, this proves highly challenging as soil can be best described as a nonlinear, irreversible, time-dependent, and anisotropic and inhomogeneous material (Ioannides, 1984; U.S. Army, 1987; Lukanen, 2005; amongst others). Moreover, the behaviour of soil differs when tested in-situ versus in the lab, and its various material properties can be influenced by a variety of external factors, including the soil depth, moisture content, loaded region, and temperature (Bowles, 2001; McKinney et al., 2006; AASHTO SCDOT, 2019; amongst others). In lieu of a comprehensive geotechnical investigation, researchers and engineers have historically modelled soil mediums using one of two simplified approaches.

One such idealization is the Winkler spring model, which represents the soil medium as an infinitely spanning array of linear elastic and independently acting springs. The model can be characterized by a single spring constant called the modulus of subgrade reaction, k, with units of pressure per length (e.g., kPa/mm, psi/in). By definition, the springs act independently with respect to one another, and as a result, any particular spring (or any specific point in the soil medium) deflects solely due to an externally applied pressure acting on that spring (Winkler, 1867; McKinney et al., 2006).

The other common idealization is the Boussinesq elastic half-space, which represents the soil medium as an infinitely spanning, linear elastic, isotropic and homogeneous elastic block. The model therefore can be accurately characterized by a modulus of elasticity, E, and Poisson’s ratio, u. In the half-space model, the soil acts like any typical elastic body, and as a result accounts for the effects of continuity (i.e., a point in the body will deform to some degree if a pressure is applied to another point in the body) (Boussinesq, 1885; Ioannides, 1984).

Historically, the Boussinesq half-space has been considered to be mathematically complex and shared one of the main problems of the Winkler spring model of having only a single characterizing parameter (E and k, respectively, with u being negligible in most cases) (Selvadurai, 1979; Ioannides, 1984; Bowles, 2001). The actual behaviour of in-situ soil is generally expected to lie somewhere between the Winkler model and the Boussinesq model, as shown in Figure 2.8:

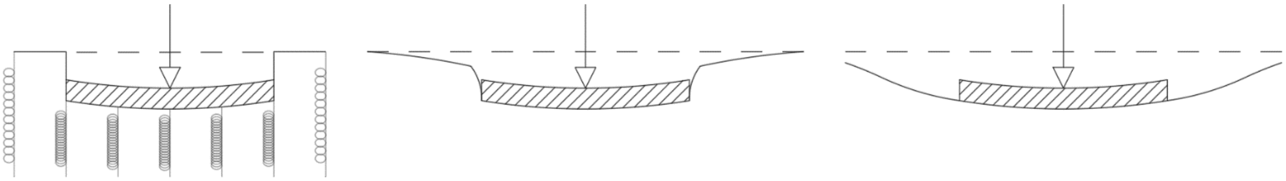
(a) (b) (c)

Figure 2.8: Soil behaviour of a (a) Winkler spring model, (b) realistic, in-situ soil, (c) Boussinesq elastic half-space

The Winkler model from Figure 2.8 (a) has no deflection outside of the loaded region. Conversely, the Boussinesq model from Figure 2.8 (c) yields deflection everywhere, including outside of the loaded region. Realistic, in-situ soil, as shown in Figure 2.8 (b), is expected to have limited, rapidly decreasing deflection outside of the loaded region.

2.2.1 Winkler Spring Model

Proposed by Emil Winkler (1835 – 1888), the Winkler spring model idealizes the subgrade as an infinitely spanning array of tightly spaced and independently acting linear elastic springs. Each spring is assumed to have a linear pressure-deflection relationship (Winkler, 1867; McKinney et al., 2002), and can therefore be described with the following equation:

$$p = kw \tag{2.4}$$

where p is the vertical contact pressure acting as some point on the surface of the soil, w is the vertical deflection in the soil below that point, and k is a proportionality factor characterizing the subgrade material known as the modulus of subgrade reaction. The modulus of subgrade reaction is expressed as a load intensity per unit length of displacement and is the sole characterizing parameter of the Winkler model. Figure 2.9 shows the behaviour of a Winkler soil subject to an arbitrary load:

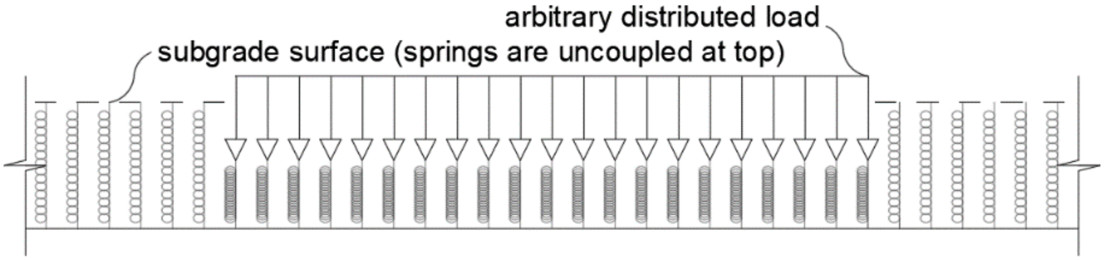

Figure 2.9: Winkler soil subject to arbitrary distributed load

Because each spring acts independently of one another, shear discontinuity between individual springs is present (Ioannides, 1987). This means that any point in the soil will only deform due a pressure applied at that specific point; this introduces a discontinuity of deflections and stresses at the edges of the loaded regions, and as a result, the deflections in the soil caused by a pressure do not spread in the transverse direction. The simplicity of the Winkler model means that its use is easily extended to contact problems. For instance, consider the case of a beam resting on a Winkler elastic foundation. Traditional Euler-Bernoulli beam theory describes the behaviour of an elastic beam as:

$$EI\frac{d^4\Delta}{dx^4} = w \tag{2.5}$$

in which EI is the flexural rigidity of the beam and w is the applied load. When supported by independently acting springs, the differential equation describing the behaviour of the elastic beam then becomes:

$$EI\frac{d^4\Delta}{dx^4} + k\Delta = w \tag{2.6}$$

in which k is the modulus of subgrade reaction and the other variables are as previously defined.

The displacement response for any particular loading combination has an analytical solution determined by considering the boundary conditions of the beam but is not presented here in this study for conciseness. The closed form deflection is well-documented in readings by Hetenyi (1946), Selvadurai (1979), amongst others.

The determination of an appropriate value for the modulus of subgrade reaction also proves to be a challenge and is one of the main limitations of the Winkler model (Straughan, 1990; Vallabhan et al., 1991). Firstly, the definition of the modulus of subgrade reaction means it assumes that the soil has a linear relationship between pressure and deflection. However, realistic, in-situ soil does not behave as such, and in general, the relationship can be expected to be nonlinear (McKinney et al., 2006; Lukanen, 2005). Because the actual relationship is highly nonlinear, two values of idealized subgrade moduli may be very different. This idea is shown in Figure 2.10:

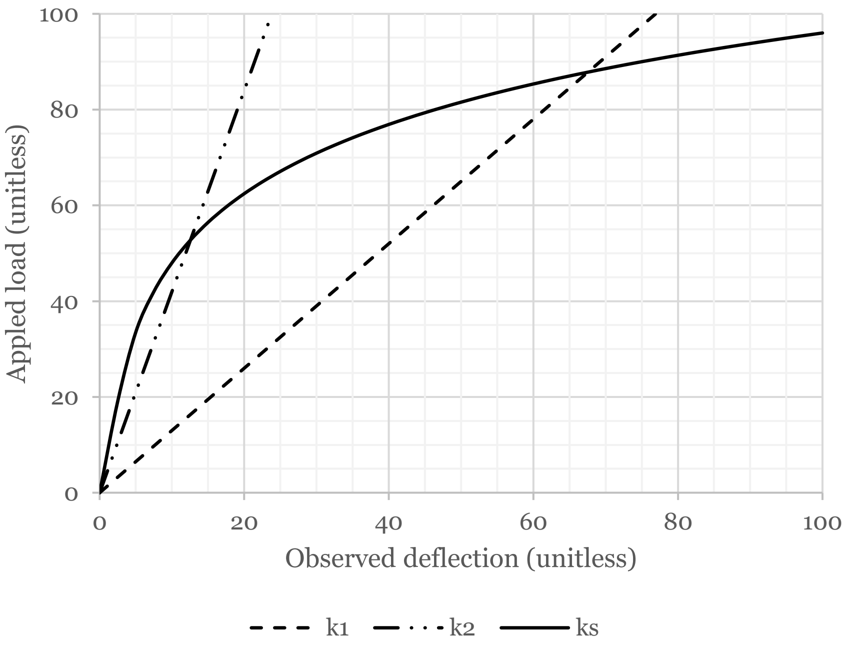

Figure 2.10: Applied bearing load versus observed deflection, from McKinney et al. (2006)

Here, the solid black line, k_s, represents the relationship between the soil deflection and applied load of a theoretical field test. The dotted black line, k_1, represents an idealized linear relationship for the modulus of subgrade reaction when a linear function is simply fitted equally to the measured data. The double dotted black line, k_2, represents an idealized linear relationship when the function is weighted more heavily towards the initial portion of the curve for smaller applied loads. It can be seen that the two linear idealizations present two drastically different slopes for the modulus of subgrade reaction.

It is important to highlight that the modulus of subgrade reaction is a fictious property of soil and that the value is variable dependent on the testing mechanism, such as the size of load, shape of load, depth considered, consolidation of soil, repeated testing versus non-repeated testing, and the other properties of soil, such as the moisture content or temperature, amongst others (Selvadurai, 1979; Lukanen; 2002, FHWA, 2006; amongst others). As a result, even the empirical measured relationship between the deflection of soil and externally applied load will change with changes to any of the variables listed (Selvadurai, 1979; Dalogulu and Vallabhan, 2000; Lukanen, 2005; McKinney et al., 2006). General tests conducted to establish a representative modulus of subgrade reaction include the plate loading test, pressure meter test, consolidation test, and triaxial test, amongst others (Westergaard, 1923; Terzaghi, 1955; Recordon, 1957; Weissman and White, 1961; Teng, 1962; Nielson, 1963, 1969; Bowles, 2001).

Several researchers have developed empirical relationships for the modulus of subgrade reaction based on soil properties or soil type. Biot (1937) presented an empirical equation for the modulus of subgrade reaction by calibrating the maximum bending moments in a beam resting on a Winkler foundation to that of a beam resting on an elastic half-space (Biot 1937, Daloglu et al. 2000, Selvadurai 1979), and as a result is dependent on both the elastic properties of the soil medium and the beam:

$$k = \frac{0.95E_s}{(1-v_s{}^2)}\left[\frac{B^4E_s}{(1-v_s{}^2)EI}\right]^{0.108} \tag{2.7}$$

in which B is the width of the beam, *EI* is the flexural rigidity of the beam, v_s is Poisson's ratio of the soil, and E_s is the modulus of elasticity of the soil. Notably, Biot assumed that the modulus of subgrade reaction is determined for a beam, and therefore, his equation is largely incompatible when considering slabs or beams with very large widths.

Terzaghi (1955) concluded that the modulus of subgrade reaction was dependent on the width of a footing or a plate, so long as the applied load was half the ultimate bearing stress of the soil and the footing or plate could be assumed as rigid (Terzaghi, 1955; Selvadurai, 1979). He presented the following equation for a rectangular plate of any width *B*:

$$k = k_1\left[\frac{B+0.305}{2B}\right]^2 \tag{2.8}$$

in which k_1 is the modulus of subgrade reaction determined through an empirical test using a plate with a width of 0.305 m (Terzaghi, 1955). Teng (1955) later expanded on Terzaghi's work and concluded that the modulus of subgrade reaction was additionally dependent on the depth at which testing was conducted at (as the confining stress is assumed to increase with increases in depth), modifying Terzaghi's equation to:

$$k = k_1\left[\frac{B+0.305}{2B}\right]^2\left[1+2\frac{D}{B}\right] \leq 2k_1\left[\frac{B+0.305}{2B}\right]^2 \tag{2.9}$$

in which the variables are the same as before and *D* is the depth at testing. Teng (1955) and Terzaghi's (1955) equations are, of course, limited by the requirement of empirical load testing data to determine k_1, but are more suitable for general applications of plates and slabs.

Lenczner (1962) developed an equation relating the modulus of subgrade reaction to both the modulus of elasticity of the soil, the soil depth, and the width of the footing or plate:

$$k = \frac{2E_s}{b\log\left(1+\frac{2H}{b}\right)} \tag{2.10}$$

in which *b* is the width of the footing or plate, *H* is the depth of the soil, and E_s is the modulus of elasticity of the soil.

Many other researchers have developed similar equations to the ones presented in this section. In general, equations developed by research are dependent on the elastic properties of the soil (i.e., the modulus of elasticity and/or Poisson's ratio) and dimensions of the structure resting on the soil. Occasionally, some researchers introduced the effects of depth. Table 2.1 provides an overview on the efforts of many such researchers:

Table 2.1: Summary of empirical equations determining the modulus of subgrade reaction

Researcher	Equation	Intended Use	Equation
Biot (1937)	$k = \frac{0.95E_s}{(1-v_s{}^2)}\left[\frac{B^4E_s}{(1-v_s{}^2)EI}\right]^{0.108}$	Beams	(2.7)
Galin (1943)	$k = \frac{\pi E_s}{2b(1-v_s{}^2)\log\left(\frac{l}{b}\right)}$	Beams	(2.8)
Terzaghi (1955)	$k = k_1\left[\frac{B+0.305}{2B}\right]^2$	Plates	(2.11)
Vesic (1961)	$k = \frac{0.65E_s}{(1-v_s{}^2)}\sqrt[12]{\frac{B^4E_s}{EI}}$	Beams	(2.12)
Teng (1962)	$k = k_1\left[\frac{B+0.305}{2B}\right]^2\left[1+2\frac{D}{B}\right]$	Plates	(2.7)
Lenczner (1962)	$k = \frac{2E_s}{b\log\left(1+\frac{2H}{b}\right)}$	Plates	(2.10)
Meyerhof (1965)	$k = \frac{E_s}{B(1-v_s{}^2)}$	Plates	(2.13)
Vlasov and Leontiev (1966)	$k = \frac{E_s}{H(1+v_s)(1-2v_s)}$	N/A	(2.14)
Reti (1967)	$k = \frac{2.15}{h}\sqrt[3]{\frac{E_s{}^4}{E_b}}$	Beam	(2.15)
Horvath (1983)	$k = \frac{E_s}{H}$	N/A	(2.16)
Bowles (2001)	$k = \frac{E_s}{B(1-v_s{}^2)(mI_sI_f)}$	Plates	(2.17)

Figures 2.11 to 2.14 provide a visual comparison of the modulus of subgrade reactions obtained from the equations presented in Table 2.1. Figures 2.11 and 2.12 present relationships between the modulus of subgrade reaction and the modulus of elasticity for various equations. Figures 2.13 and 2.14 present relationships between the modulus of subgrade reaction and the width of the beam or plate.

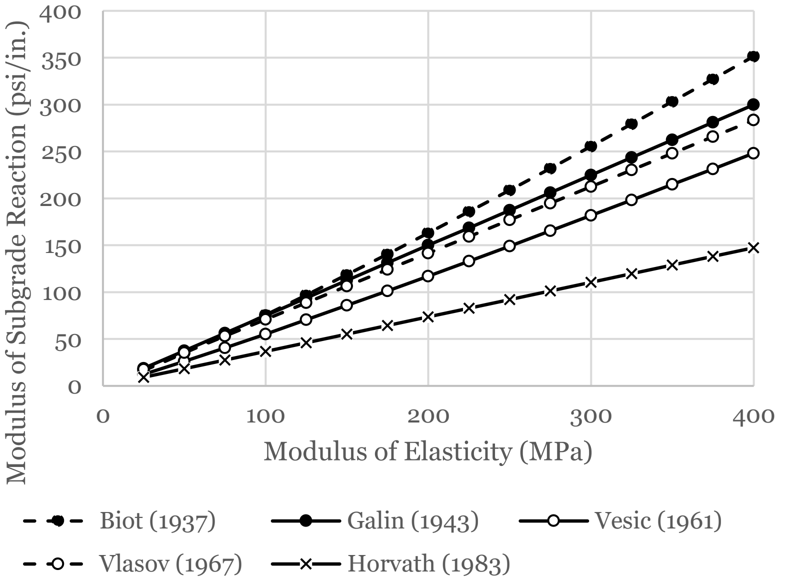

Figure 2.11: Empirical equations of the modulus of subgrade reaction with the modulus of elasticity of soil as the dependent variable for beams; v_b = 0.2, v_s = 0.3, E_b = 26,000 MPa, h = 150 mm, L = 6,000 mm, and H = 10,000 mm

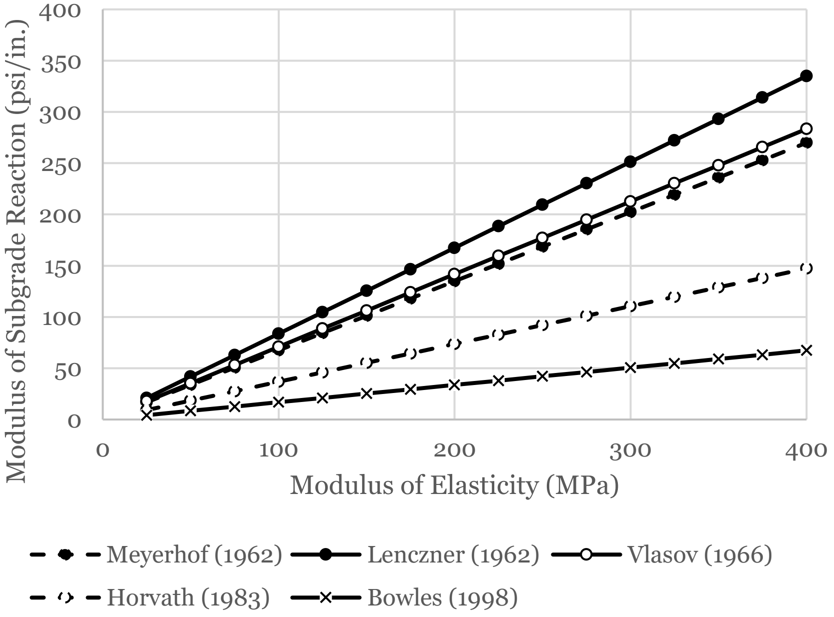

Figure 2.12: Empirical equations of the modulus of subgrade reaction with the modulus of elasticity of soil as the dependent variable for plates; v_b = 0.2, v_s = 0.3, E_b = 26,000 MPa, h = 150 mm, L = 6,000 mm, and H = 10,000 mm

Figure 2.11 and 2.12 provides comparisons of modulus of subgrade reaction versus the modulus of elasticity of the soil for various equations intended for the usage of beams or plates. It is clear that there is a large variance in the modulus of subgrade reaction especially when considering higher values of the modulus of elasticity (and consequently, for high-value subgrade reaction moduli). In particular, it can be noted that all of the equations seen here adopt a linear relationship between the modulus of subgrade reaction and modulus of elasticity.

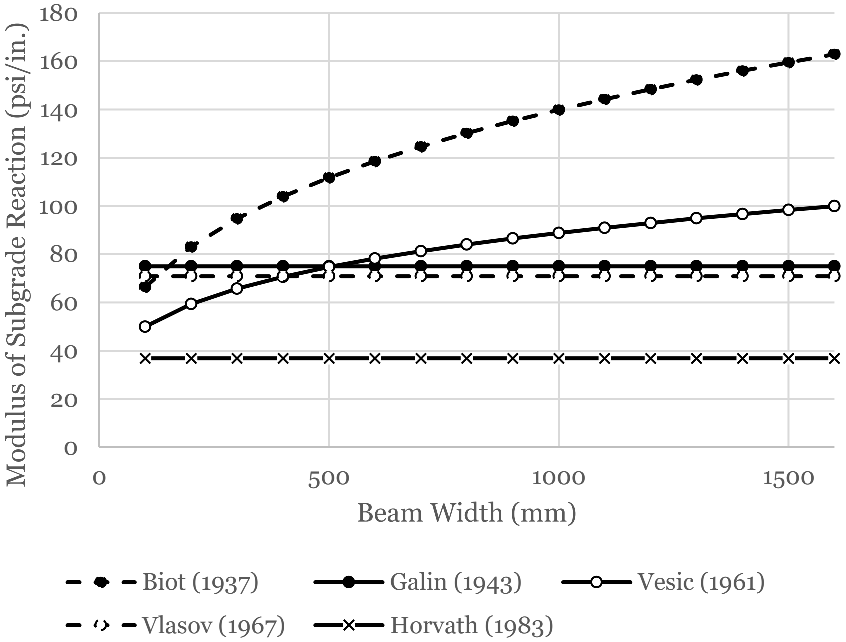

Figure 2.13: Empirical equations of the modulus of subgrade reaction with the depth of soil as the dependent variable for beams; v_b = 0.2, v_s = 0.3, E_b = 26,000 MPa, h = 150 mm, H = 10,000 mm, and E_s = 100 MPa

Figure 2.13 provides a comparison of the modulus of subgrade reaction versus the beam width for various equations. Immediately, it can be noted that Galin (1943), Horvath (1983), and Vlasov (1967) do not consider the effects of the beam width on the modulus of subgrade reaction. It can be seen that the modulus of subgrade reaction increases with increases to the beam width.

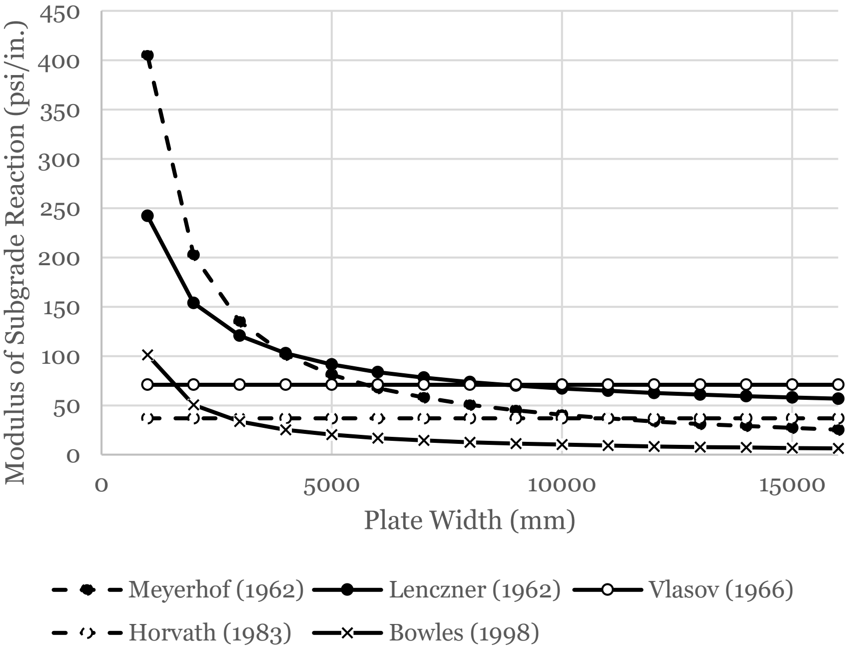

Figure 2.14: Empirical equations of the modulus of subgrade reaction with the depth of soil as the dependent variable for plates; v_b = 0.2, v_s = 0.3, E_b = 26,000 MPa, h = 150 mm, H = 10,000 mm, and E_s = 100 MPa

Figure 2.14 provides a comparison of the modulus of subgrade reaction versus the plate width for various equations. Immediately, it can be noted that Vlasov (1966) and Horvath (1983) do not consider the effects of the plate width on the modulus of subgrade reaction. Contrastingly to the case of the beam, increasing the plate width rapidly decreases the modulus of subgrade reaction.

Researchers have also attempted to link a range of modulus of subgrade reaction values to the type or classification of a particular soil (i.e., silts, sands, clays, etc.).

Terzaghi (1955) provides a suggested range of modulus of subgrade reaction values for clayey soils based on the relative density of soil particles, consistency, and approximate moisture content:

Table 2.2: Typical values off modulus of subgrade reaction (N/m^3 ×10^{-3}) (Terzaghi, 1955; Selvadurai, 1979)

Granular soils			
	Relative density		
	Loose	Medium	Dense
Dry or moist sand	6.25 – 18.7	18.7 – 93.6	93.6 – 312.0
Submerged sand	7.8	25.0	97.0
Over consolidated clays			
	Consistency		
	Stiff	Very stiff	Hard
Unconsolidated clays	96 – 192	192 – 384	384
Consolidated clays	1.5	1.5 – 7.8	

Terzaghi's (1955) suggested ranges were based off of experimental plate loading tests with plates of width 0.305 m (Selvadurai, 1987). It is clear that the range of proposed values are only useful in providing a general estimation of the modulus of subgrade reaction values for a particular soil type. For instance, a dense, dry sand has a suggested range of 93,000 to 312,000 kN/m^3, with no further recommendations for selecting within this range.

Gurbuz and Avci (2018) provides a summary from various researchers (from Terzaghi, 1955; Zeevaert, 1983; Baldouf, 1988; Dorken and Dehne, 1995; Ersoy, 1995; Bowles, 2001; Das et al., 2007; and Uzuner, 2011) and categories the range of modulus of subgrade reaction values based on type (gravels, sands, clays), density, and moisture content and have been obtained by various plate load tests:

Table 2.3: Typical values of modulus of subgrade reaction ($N/m^3 \times 10^{-3}$), compiled from various researchers (Gurbuz and Avci, 2018)

Soil Type	Range of *k*
Loose sand	4.8 – 20
Medium to dense sand	9.6 – 100
Dense sand	50 – 320.1
Clayey medium-dense sand	32 – 80
Silty medium-dense sand	24 – 48
Dry loose sand	8 – 25
Dry medium sand	25 – 125
Dry dense sand	125 – 375
Moist loose sand	10 – 15
Moist medium-dense sand	35 – 40
Moist dense sand	130 – 150
Sandy gravel	200 – 250
Dense sandy gravel	100 – 150
Soft clay	5 – 10
Plastic clay	5 – 10
Stiff clay	15
Very stiff clay	> 96
Rock	> 2000

Like Terzaghi's (1955) recommendations, the summary compiled by Gurbuz and Avci (2018) showcases a large range of modulus of subgrade reaction values for each type of soil. When considering the case of a dry, dense sand, Gurbuz and Avci (2018) suggests a range of values between 125,000 – 375,000 kN/m^3.

McKinney et al. (2006) provides a summary for approximating the modulus of subgrade reaction against a particular soil type based on an ASTM, AASHTO, or FAA soil classification system in the form of a logarithmic chart:

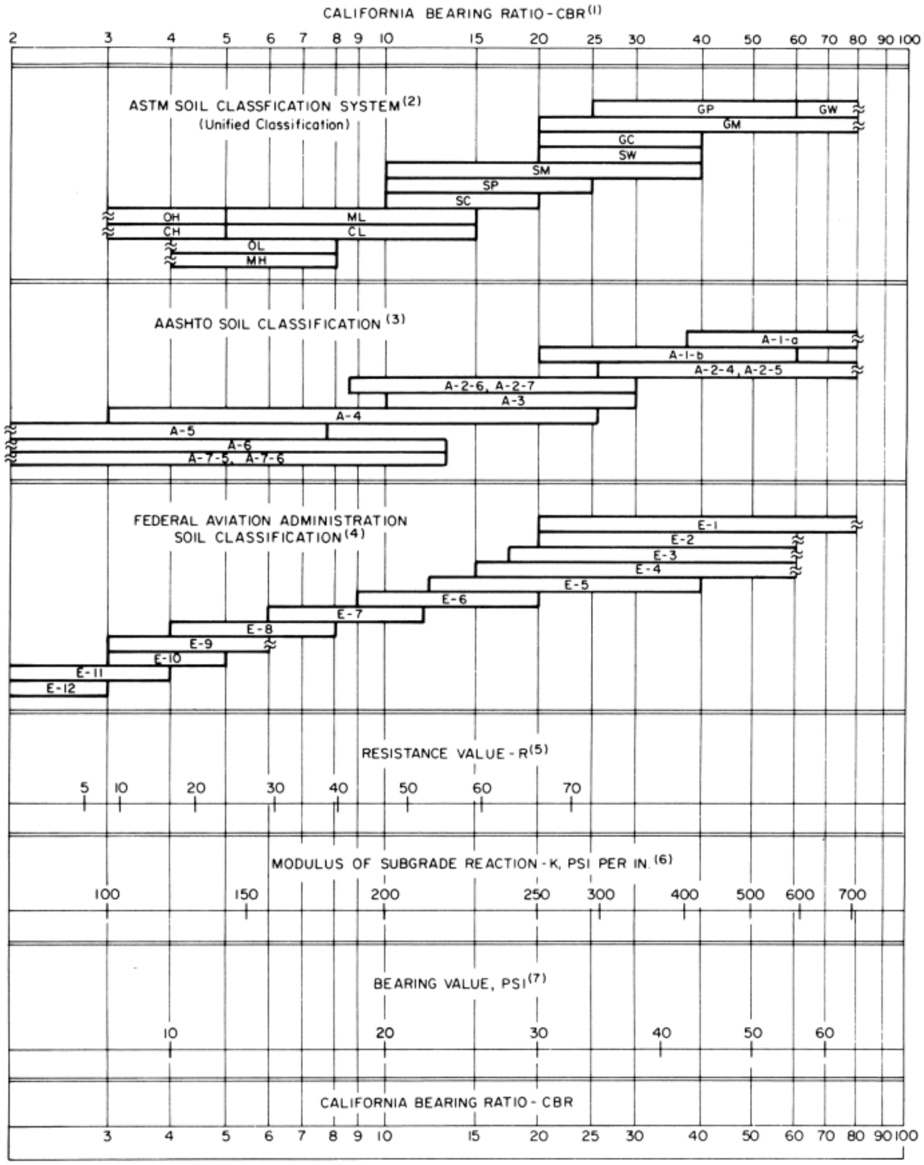

Figure 2.15: Approximate interrelationships of soil classifications and bearing values (McKinney et al., 2006)

The equivalent modulus of subgrade reaction for each type of soil classification is based on the California bearing ratio for each soil type. In the case of a sandy soil, the ACI guidelines suggest a value between 200 – 400 psi/in. (approximately 56,000 – 125,000 kN/m^3).

It is clear from this section that the value of the modulus of subgrade reaction for any particular soil type or configuration of soil is a controversial and contested parameter. Researchers (Galin, 1943; Terzaghi, 1955; etc.) have come up with several equations of various forms dependent on various variables (size of plate, depth of subgrade, modulus of elasticity, etc.) to establish a representative, linear modulus of subgrade reaction, yet for a particular soil configuration, may produce a large disparity between determined values, as shown previously in Figures 2.11 through 2.14. Researchers (Terzaghi, 1955; McKinney et al., 2006; etc.) have likewise recommended ranges of values for the modulus of subgrade reaction based on the classification or type (i.e., sands versus clays) of soil. These ranges tend to be very large for any particular soil type, and the upper bound of any soil type may be up to three times the lower bound, as evidenced in Tables 2.2, 2.3, and Figure 2.15. While in general this makes sense – as a given soil type may vary greatly with respects to density, stiffness, moisture content (i.e., plasticity), etc. – this is simply a testament to how variable the modulus of subgrade reaction is and reiterates that a particular soil medium or configuration of soil does not have a single modulus of subgrade reaction value that perfectly captures its behaviour. Recall that the modulus of subgrade reaction itself is simply a linear representation or idealization of the actual nonlinear behaviour of the soil and is largely affected by the type and method of testing completed.

Despite the difficulty in obtaining a representative value for the modulus of subgrade reaction, it is widely accepted for practical applications that an approximate value of k provides reasonable confidence in the behaviour of a slab-soil system, as changes in k result in minor changes in the critical stresses (Westergaard, 1926; Ioannides, 1987, Lukanen, 2005). The impacts of k on a slab-soil system will be investigated and discussed further on in this study. Westergaard (1926) in particular suggests that increases to the modulus of subgrade reaction of up to four times only causes minor changes in the important stresses of the slab, and therefore, an approximate value of the modulus of subgrade reaction should be sufficient in due regards to critical stresses. This is specifically in regard to the maximum principal stresses under a loaded region; here, the minor changes mentioned by Westergaard may be differences of up to 20%. Contrastingly, the deflection of a slab resting on a Winkler soil is greatly affected by changes to the modulus of subgrade reaction (Lukanen, 2005, McKinney at al., 2006).

With such a variety of methods and recommendations for the modulus of subgrade reaction, it becomes instructive to discuss some of the typical values of the modulus of subgrade reaction often used in literature and in practical design applications. Westergaard (1926), whose work is considered the pioneering analysis for slabs-on-grade design, considers a range of modulus of subgrade reactions between 50 to 200 psi/in. to be fairly typical. Contemporary slab-on-grade design methods summarized in Section 2.1 also considers practical values for the modulus of subgrade reaction. In particular, the PCA design methodology considers values between 50 to 200 psi/in. (like Westergaard) to be typical, while the WRI design method and COE design method considers values between 20 to 1000 and 25 to 500 psi/in. to be typical, respectively (Packard, 1966; McKinney et al., 2006; Ioannides et al., 2006).

In foundation and footing design, the bearing value of the soil is often provided or required by code or design and analysis guidelines – see Canadian Handbook Annex D (Adebar et al., 2017). For practical applications, these values often fall between 2000 to 3000 psf (Council of American Building Officials, 1995); similarly, the minimum bearing strength of soil required by contemporary crane manufacturers is 2500 – 3000 psf (Gorbel, 2012; Spanco, 2018). Using the log-table provided by McKinney et al. (2006), an equivalent range of modulus of subgrade reaction values can be determined to be approximately 150 to 200 psi/in.

2.2.2 Boussinesq Elastic Half-Space

Named after the French physicist Joseph Boussinesq (1842 – 1929), the Boussinesq elastic half-space idealizes the subgrade as an infinitely spanning, linear elastic, isotropic, and homogenous solid body (Ioannides, 1984). Its name (Boussinesq half-space) is often used in the literature to describe a solid elastic body (i.e., terms such as “elastic solid”, “elastic continuum”, “elastic body”, etc.) and in this text will simply be shortened to “elastic half-space”.

The soil is represented by a continuous body, and unlike the Winkler spring model, will consider the effects of shear throughout the soil. An elastic half-space loaded by an arbitrarily defined distributed force deflects under the loaded region as well as away from the loaded region; the response at any point within the soil is influenced by any applied loading directly above the point and, to some extent, the applied loading at neighbouring points. This is depicted in Figure 2.16:

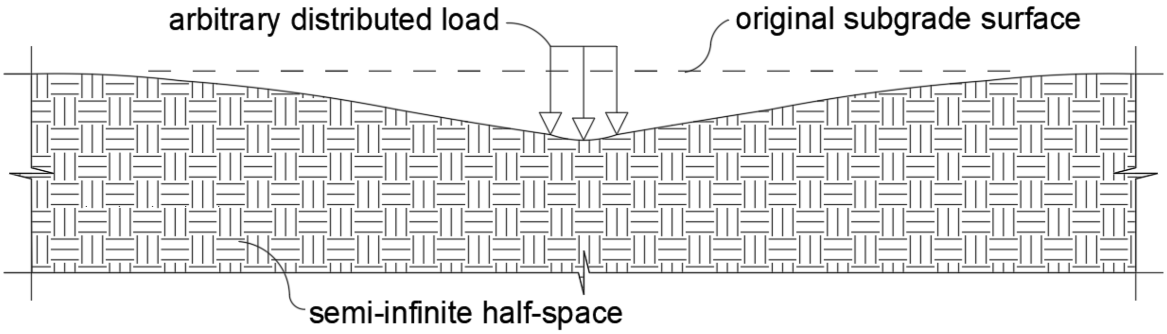

Figure 2.16: Boussinesq half-space subject to an arbitrary distributed load

Boussinesq (1885) in particular provides the following equation to determine the deflection at a point in the soil due to a concentrated force acting at the top of the soil:

$$w(r,z) = \frac{Q}{4\pi G_s\sqrt{r^2+z^2}}\left[2(1-v_s)+\frac{z^2}{r^2+z^2}\right] \tag{2.18}$$

where Q is the concentrated force, z is the vertical depth, and r is the horizontal distance (Selvadurai, 1979).

The elastic half-space model is considered to be a more realistic interpretation of typical in-situ soils, as soils often possess cohesion, and therefore should be expected to transmit forces transversely. A load applied at a particular point on the surface of the soil should then cause a degree of deflection elsewhere on that body. Notably, some experimental studies have shown the deflection elsewhere in in-situ soil tend to be of less significance than of those predicted by the Boussinesq half-space (Ioannides, 1984). However, due to the continuous nature of the elastic body and the use of traditional three-dimensional continuum mechanics, significant mathematical complexities often develop when considering contact problems involving the half-space (Ioannides, 1984; Lukanen, 2005), and the analytical solutions these problems are often unobtainable in a simple closed form (Selvadurai, 1979). This can be illustrated by considering the case of a beam resting on an elastic half-space. While the elastic behaviour of the beam itself is given by equation 2.5 presented in Section 2.2.1, the response of the beam resting on a half-space is given by:

$$EI\frac{d^4\Delta}{dx^4}+\bar{q}(x)=w \tag{2.19}$$

in which $\bar{q}$(x) is the average contact stress of the beam.

Selvadurai (1979) provides a relationship between the deflection and the average contact stress:

$$w(x)=\frac{(1-v_s)}{2\pi^2 G_s}\int_{-l/2}^{l/2}\int_{-b/2}^{b/2}\frac{\bar{q}(\xi)dyd\xi}{\sqrt{(\frac{b^2}{4}-y^2)((x-\xi)^2-y^2)}} \tag{2.20}$$

in which G_s is the shear modulus of the soil.

Solving this equation, and by extension the general response of the beam in equation 2.19, typically involves complicated mathematical approximations, and therefore is typically avoided in lieu of the simpler Winkler model (Selvadurai, 1979; Ioannides, 1984, Lukanen, 2005).

The elastic half-space also requires determining its elastic parameters. However, the two parameters that define an elastic body, its elastic modulus, E, and Poisson's ratio, u, are largely up for debate when considering a soil medium. While the modulus of elasticity is in fact a natural, intrinsic property of any elastic body and may be empirically determined via laboratory experiments, the variable nature of soil properties (i.e., the confining stress, void ratio, level of consolidation, moisture content, etc.) means that a single elastic modulus is likely incapable of characterizing a large body of soil with a high degree of confidence. As a result, it can be expected that the moduli of elasticity determined through laboratory or field testing for several samples of soils of same soil medium are likely to be different (Bowles, 2001; Selvadurai, 1979). Therefore, the elastic half-space model simply provides an idealized linear representation (through the modulus of elasticity) of a non-linear system and relies on the assumption that the particular soil medium is homogeneous and isotropic.

Historically, the modulus of elasticity for a given soil medium is determined by empirical equations related to field testing data obtained from unconfined, triaxial, or oedometric compression tests (Selvadurai, 1979), or by assigning a range of elastic moduli to a particular type of soil or soil classification system (i.e., UCSC, AASHTO, FAA).

Selvadurai (1979) offers an empirical equation based on oedometer readings:

$$E_s=E_{oed}\frac{(1+v_s)(1-2v_s)}{(1-v_s)} \tag{2.21}$$

in which E_{eod} is the oedometric stiffness modulus determined through an oedometer compression test and υ_s is the Poisson's ratio of the soil. In particular, equation 2.21 is appropriate only for unsaturated soils, or for saturated soils with a Poisson's ratio of < 0.5.

Bowles (2001) offers empirical equations based on field testing data of standard penetration (SPT) and cone penetration tests (CPT):

Table 2.4: Modulus of elasticity (kPa) of soil determined via SPT and CPT, from Bowles (2001)

Soil Type	SPT	CPT
Sand (normally consolidated)	$E = 500(N + 15)$	$E = 8000\sqrt{q_c}$
Sand (saturated)	$E = 250(N + 15)$	$E = Fq_c$, Where F = 3.5 or 7 based on a void ratio of 1.0 or 0.6, respectively.
Sand (over consolidated)	$E = (2600 \ to \ 2900)N$	
Gravelly sand	$E = 1200(N + 6)$	
Clayey sand	$E = 320(N + 15)$	$E = (3 \ to \ 6)q_c$
Silts, sandy silt, or clayey silt	$E = 300(N + 6)$	$E = (1 \ to \ 2)q_c$
Soft clay or clayey silt		$E = (3 \ to \ 8)q_c$

In Table 2.4, q_c represents the cone penetration resistance and is a measure of the CPT. N refers to the blow count and is a measure of the SPT. Bowles recommends SPTs and CPTs over other laboratory-based testing methods (such as unconfined compression tests and triaxial tests) as they tend to be less prone to sample disturbance. Other empirical equations correlated to test data may be found in readings by Bowles (2001), Kulhawy et al. (1990), and others, and have been omitted in this study for conciseness.

Notably, empirical equations offered by researchers for the modulus of elasticity is much more focused on the correlations to test data (whether it be field testing or laboratory testing) compared to the modulus of subgrade reaction, which is dependent on the size of testing done and various other soil parameters (such as the depth).

In lieu of empirical test data, Bowles (2001) presents a range of typical values for sands, silts, and clays dependent on the stress history, water content, density, and age of deposit:

Table 2.5: Typical values for the modulus of elasticity of soil, from Bowles (2001)

Soil	Modulus of Elasiticty (MPa)
Clay	
Very soft	2 – 15
Soft	5 – 25
Medium	15 – 50
Hard	50 – 100
Sandy	25 – 250
Glacial till	
Loose	10 – 150
Dense	150 – 720
Very dense	500 – 1440
Loess	15 – 60
Sand	
Silty	5 – 20
Loose	10 – 25
Dense	50 – 81
Sand and gravel	
Loose	50 – 150
Dense	100 – 200
Shale	150 – 5000
Silt	2 – 20

Table 2.5 is the result of summarizing the moduli of elasticity obtained from various empirical field tests for various soil types. In particular, Bowles notes that the range of values for any particular soil type are, in general, too large to consider using an averaged value. For instance, the range of moduli of elasticity for very dense glacial till ranges between 500 – 1440 MPa. Using an average value of 970 MPa would be misrepresentative when considering the applications of design.

The American AASHTO LRFD specifications (2019) provides values for the modulus of elasticity of soil based on the density and type of soil. The range of moduli of elasticity were obtained from various laboratory testing methods (i.e., unconfined, confined, undrained, drained, etc.) methods for various soil types. Values have been converted to metric (MPa) for clarity.

Table 2.6: Typical values for the modulus of elasticity of soil, from AASHTO (2019)

Soil	Modulus of Elasticity (MPa)
Clay	
Soft, sensitive	2.4 – 14.4
Medium stiff to stiff	14.4 – 48
Very stiff	48 – 96
Silt	2 – 19.1
Fine sand	
Loose	7.6 – 11.5
Medium-dense	11.5 – 19.1
Dense	19.1 – 29
Sand	
Loose	9.6 – 29
Medium-dense	29 – 48
Dense	48 – 76.6
Gravel	
Loose	28 – 76.6
Medium-dense	76.6 – 96
Dense	96 – 190

In general, the range of values presented by the AASHTO (2019) is in good agreement with the values suggested by Bowles (2001).

From this section, it can largely be seen that the modulus of elasticity for a particular type of soil may have a broad range of values. In particular, because the modulus of elasticity is affected by a variety of factors, including the moisture content, consolidation ratio, degree of confinement, level of soil disturbance, etc., determining the actual modulus of elasticity for a given soil is difficult and requires in-situ testing. For the purposes of design, engineers tend to use personal judgement when establishing a representative modulus of elasticity (Bowles, 2001; AASHTO, 2019).

2.2.3 Multi-Parameter Soil Models

The Winkler spring model and Boussinesq half-space can be considered to be the two simplest linear elastic idealizations of soil mediums. The behaviour of both models can be characterized by a single parameter (either the modulus of subgrade reaction or the modulus of elasticity, respectively). The major difference separating the Winkler model from the elastic half-space model is the discontinuity present in the Winkler model that ultimately causes it to appear more unrealistic than its half-space counterpart. Various researchers have proposed alternative formulations for the idealization of soil mediums to retain the simplicity of the Winkler model while attempting to provide continuity between springs. These models are typically coined multi-parameter continuum models and often combine elements of the Winkler spring model with elastic continuum elements. While these models will not be rigorously discussed in this study, a brief overview of the more well-known models have been included for completeness.

Filonenko-Borodich (1945) attempted to improve on the Winkler spring model by coupling the top of the Winkler springs with a stretched elastic membrane laterally held in tension. Filonenko-Borodich's model can be described by equation 2.22 and reduces to the Winkler model when the tensile force is set to 0:

$$p = kw - T\nabla^2 w \tag{2.22}$$

in which T is a laterally acting tensile force on the elastic membrane, p is the pressure acting at a point, w is the deflection at that point, and ∇ is the Laplace operator (Selvadurai, 1979).

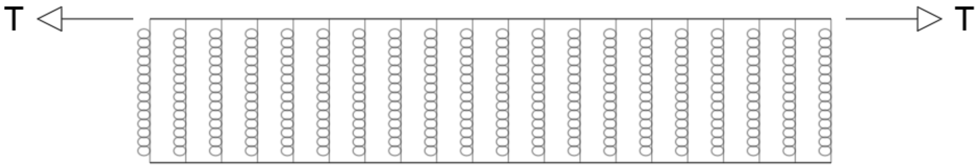

Figure 2.17: Two-parameter model presented by Filonenko-Borodich (1945) with an additional elastic membrane under tension

Pasternak (1954) attempted to address the lack of shear continuity within a Winkler spring model by introducing a shear layer attached to the top of the Winkler springs. In this case, the shear layer acts only in shear (i.e., if the shear parameter is set to 0, Pasternak's model reduces to the Winkler model). Pasternak's model was presented as follows:

$$p = kw - GH\nabla^2 w \tag{2.23}$$

in which G is the shear modulus of the shear layer, H is the thickness of the shear layer, and the other variables as previously defined (Selvadurai, 1979).

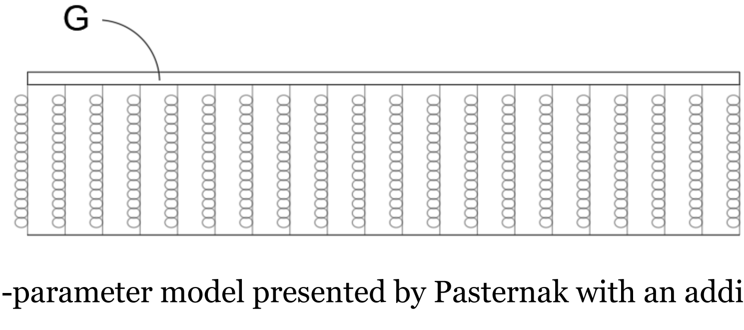

Figure 2.18: Two-parameter model presented by Pasternak with an additional shear layer

Many more such modified- or adjusted-Winkler models exist, such as other 2-parameter models developed by Straughn (1990), Vallabhan et al. (1991), Tanahashi (2007), or 3-parameters developed by Kerr (1964), Vlasov and Leontiev (1966), but are not summarized in this text and are listed only for completeness.

2.3 Analysis of Plates on Linear Elastic Soils

Historically, the analysis of structural elements (beams, footings, foundations, slabs, etc.) resting on soil mediums have been conducted through an idealization of the soil medium (through a Winkler subgrade or a solid continuum) and the structural element (Bernoulli-Euler beam theory, classical thin plate theory, or thick plate theory) (Selvadurai, 1979).

This section discusses analytical solutions that have been developed for a plate loaded with a concentrated load at its center resting atop an elastic foundation. These analytical solutions were used to validate the finite element models developed in this study.

2.3.1 Plates on Winkler Soils

Hertz (1884) first presented a solution for an infinite plate subject to a concentrated load resting on a deformable fluid (Stradler, 1971; Selvadurai, 1979). He found that the deflection profile, *w(r)*, could be described in the form of an infinite series:

$$w(r) = \frac{Pa^2}{2\pi\gamma}\left[\frac{(ra)^2}{4}\ln(ra) - \frac{(ra)^6}{2304}\left(\ln(ra) - \frac{5}{6}\right) + \cdots + \frac{\pi}{4}\left(1 - \frac{(ra)^4}{64} + \frac{(ra)^8}{147456} - \cdots\right) + \cdots\right] \tag{2.24}$$

in which *w(r)* is the deflection at a point *r* away from the loaded point, *P* is the concentrated force, γ is the unit weight of the fluid, and a is a length parameter given by:

$$a = \sqrt[4]{\frac{12(1 - v_b{}^2)\gamma}{E_b h^3}} \tag{2.25}$$

in which v_b is the Poisson's ratio of the plate, E_b is the modulus of elasticity of the plate, and h is the thickness of the plate. Owing to the fact that the behaviour of a dense fluid is very similar to that of a Winkler spring model (Selvadurai, 1979), a clean substitution can be made between the unit weight of the fluid, γ, and the modulus of subgrade reaction of a theoretical soil, k.

The maximum deflection under the load obtained by Hertz is:

$$w(0) = \frac{a^2 P}{8\gamma} \tag{2.26}$$

Wyman (1950) arrived at nearly the same solution as Hertz (1884) by using superposition for loads of an infinite plate subject to a concentrated load resting on a deformable fluid (again with unit weight). He presents a succinct form of Hertz' solution in the form of Kelvin's function of order zero:

$$w(r) = -\frac{Pl^2}{2\pi D} kei(r/l) \tag{2.27}$$

in which *w(r)* is the deflection at a point *r* away from the loaded point, *P* is the concentrated force, *D* is the flexural rigidity of the plate, *kei* is the imaginary Kelvin function of order zero, and *l* is a length parameter given by:

$$l = \sqrt[4]{\frac{D}{\gamma}} \tag{2.28}$$

in which the variables are as previously defined. Notably, this length parameter is identical to the length parameter given by Hertz (1884), but simply inverted.

The imaginary Kelvin function of order zero (the imaginary portion of the modified Bessel function of the second kind), kei_o, can be expressed as the infinite summation series:

$$kei(x) = -\ln\left(\frac{x}{2}\right) bei(x) - \frac{\pi}{4} ber(x) + \sum_{k=0}^{\infty} (-1)^k \frac{\psi(2k+2)}{[(2k+1)!]^2} \left(\frac{x^2}{4}\right)^{2k+1} \tag{2.29}$$

in which $bei_o(x)$ and $ber_o(x)$ are the imaginary and real parts of the fifth order Bessel function of the first kind, respectively, and ψ is the digamma function.

The Digamma function, ψ, can be defined as the logarithmic derivative of the Gamma function:

$$\psi(x) = \frac{d}{dx} \ln(\Gamma(x)) \cong \ln(x) - \frac{1}{2x} \tag{2.30}$$

The imaginary and real parts of the fifth order Bessel function of the first kind, *bei(x)* and *ber(x)*, respectively, can be expressed as an infinite summation series:

$$bei(x) = \sum_{k=0}^{\infty} (-1)^k \frac{1}{[(2k+1)!]^2} \left(\frac{x}{2}\right)^{4k+2} \tag{2.31}$$

$$ber(x) = 1 + \sum_{k=1}^{\infty} (-1)^k \frac{1}{[(2k)!]^2} \left(\frac{x}{2}\right)^{4k} \tag{2.32}$$

in which the variables are as previously defined.

While *kei(x)*, *bei(x)*, and *ber(x)* are infinite series, taking an arbitrary value *k'* as the upper limit of the infinite series expansion may result in dubious results, especially when considering large arguments of *(x)*. As a result, it becomes worth investigating the relationship between the output, the input argument *(x)*, and the value of the upper limit taken, *k'*. In order for the succeeding term in the infinite summation series to yield a sufficiently negligible (i.e.; converging) value, an expression can be obtained as follows (using *ber(x)* as an example):

$$(-1)^{k'} \frac{1}{[(2k'+2))!]^2} \left(\frac{x}{2}\right)^{4k'+4} \leq 10^{-n} \tag{2.33}$$

in which *k'* is the upper limit considered in the infinite summation series and n is an arbitrary value that will yield a sufficiently negligible value, and yielding the following expression:

$$k' \geq \frac{x}{4} e^{1+y} - \frac{5}{4} \tag{2.34}$$

in which y is expressed as follows:

$$y = \frac{1}{ex} \ln\left(\frac{10^n}{256\pi} x^7\right) \tag{2.35}$$

As the input argument *(x)* increases in magnitude, the upper limit, *k'*, also increases. Therefore, for small arguments of *(x)* (i.e.; $x < 15$), only a small upper limit is required.

Notably, the imaginary portion of Kelvin's function is a rapidly converging oscillatory function. As a result, it is expected that plates resting on a Winkler spring model will produce a limited amount of vertical deflection specifically away from the loaded region.

The maximum deflection under the load obtained by Wyman is:

$$w(0) = \frac{P}{8\gamma l^2} \tag{2.36}$$

In particular, Wyman's equation reduces to the exact same form as Hertz' (1884) equation; both equations for the maximum deflection under the concentrated load reduce to:

$$w(0) = \frac{P}{8\sqrt{\gamma D}} \tag{2.37}$$

Using Hertz and Wyman's equations, the deflection profile for an infinite plate subject to a concentrated load resting on a Winkler soil may be produced:

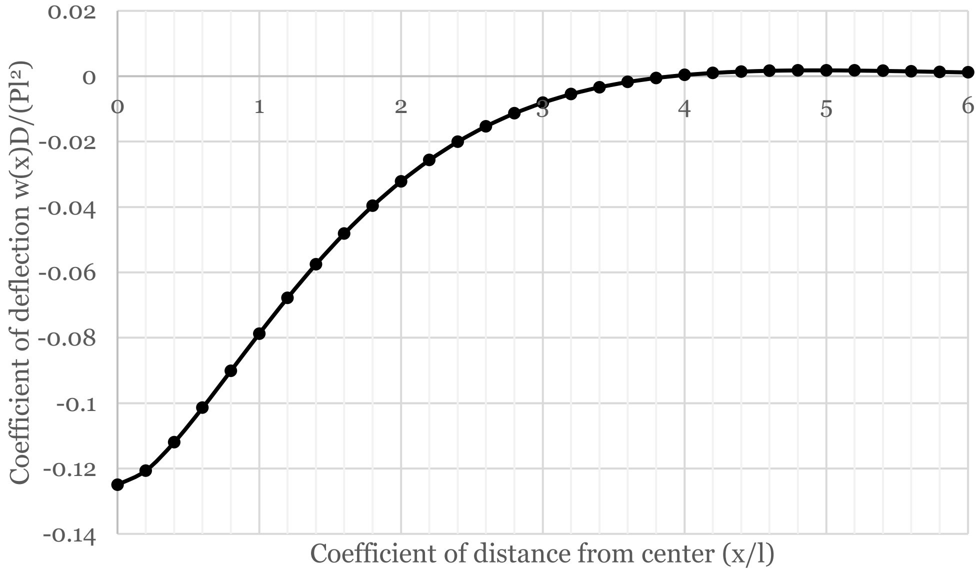

Figure 2.19: Deflection profile for an infinite plate resting on a Winkler medium subject to a concentrated load, produced by Hertz's (1884) and Wyman's (1950) equations

Here, Figure 2.19 compares the dimensionless coefficient of deflection to the coefficient of distance from the center. Both Hertz's (1884) and Wyman's (1950) equations are effectively identical.

Reissner (1955) expanded on the application of loads and presented a solution for an infinite plate subject to a circular load resting on a Winkler soil. He presented the deflection profile in the form of Bessel and Kelvin functions:

$$w(r) = \begin{cases} \frac{p_0 c}{kl}\left[ber'\left(\frac{a}{l}\right)ker\left(\frac{r}{l}\right) - bei'\left(\frac{a}{l}\right)kei\left(\frac{r}{l}\right)\right] \text{ if } a \leq r \\ \frac{p_0}{k} + \frac{p_0 c}{kl}\left[ker'\left(\frac{a}{l}\right)ber\left(\frac{r}{l}\right) - kei'\left(\frac{a}{l}\right)bei\left(\frac{r}{l}\right)\right] \text{ if } a \geq r \end{cases} \tag{2.38}$$

in which *w(r)* is the deflection at a point *r* away from the loaded point, p_o is the stress intensity, *a* is the radius of the loaded region, *l* is the length parameter presented by Wyman (1950), *k* is the modulus of subgrade reaction, and *ker, kei, ber,* and *bei* are the real and imaginary Kelvin functions of the zeroth order.

The Kelvin functions *kei* (imaginary portion of the modified Bessel function of the second kind), *ber* and *bei* (real and imaginary portion of the Bessel function of the first kind) have been defined in the previous section. The Kelvin function *ker* (real portion of the modified Bessel function of the second kind) can be expressed as the following infinite summation series:

$$ker(x) = -\ln\left(\frac{x}{2}\right)ber(x) + \frac{\pi}{4}bei(x) + \sum_{k=0}^{\infty}(-1)^k \frac{\psi(2k+1)}{[(2k)!]^2}\left(\frac{x^2}{4}\right)^{2k} \tag{2.39}$$

in which ψ is the Digamma function defined in the previous section.

The derivatives of the Kelvin functions can be expressed as follows:

$$ker'(x) = \frac{1}{\sqrt{2}}[ker_1(x) + kei_1(x)] \tag{2.40}$$

$$kei'(x) = -\frac{1}{\sqrt{2}}[ker_1(x) - kei_1(x)] \tag{2.41}$$

$$ber'(x) = \sqrt{ber_1^2(x) + bei_1^2(x)}\cos\left(\tan^{-1}\left(\frac{bei_1(x)}{ber_1(x)}\right) - \frac{\pi}{4}\right) \tag{2.42}$$

$$bei'(x) = \sqrt{ber_1^2(x) + bei_1^2(x)}\sin\left(\tan^{-1}\left(\frac{bei_1(x)}{ber_1(x)}\right) - \frac{\pi}{4}\right) \tag{2.43}$$

in which ker_1, kei_1, ber_1, and bei_1 are the Kelvin functions of the first order.

The real and imaginary Kelvin functions of the nth order, ker_n, kei_n, ber_n, and bei_n, can be expressed as the following infinite summation series:

$$\begin{aligned} ker_n(x) = {} & -\ln\left(\frac{x}{2}\right)ber_n(x) + \frac{\pi}{4}bei_n(x) \\ & + \frac{1}{2}\left(\frac{x}{2}\right)^{-n}\sum_{k=0}^{n-1}\cos\left(\left(\frac{3n}{4} + \frac{k}{2}\right)\pi\right)\frac{(n-k-1)!}{k!}\left(\frac{x^2}{4}\right)^k \\ & + \frac{1}{2}\left(\frac{x}{2}\right)^{n}\sum_{k=0}^{\infty}\cos\left(\left(\frac{3n}{4} + \frac{k}{2}\right)\pi\right)\frac{\psi(k+1) + \psi(n+k+1)}{k!\,(n+k)!}\left(\frac{x^2}{4}\right)^{2k} \end{aligned} \tag{2.44}$$

$$\begin{aligned} kei_n(x) = {} & -\ln\left(\frac{x}{2}\right)bei_n(x) - \frac{\pi}{4}ber_n(x) \\ & - \frac{1}{2}\left(\frac{x}{2}\right)^{-n}\sum_{k=0}^{n-1}\sin\left(\left(\frac{3n}{4} + \frac{k}{2}\right)\pi\right)\frac{(n-k-1)!}{k!}\left(\frac{x^2}{4}\right)^k \\ & + \frac{1}{2}\left(\frac{x}{2}\right)^{n}\sum_{k=0}^{\infty}\sin\left(\left(\frac{3n}{4} + \frac{k}{2}\right)\pi\right)\frac{\psi(k+1) + \psi(n+k+1)}{k!\,(n+k)!}\left(\frac{x^2}{4}\right)^{2k} \end{aligned} \tag{2.45}$$

$$ber_n(x) = \left(\frac{x}{2}\right)^n\sum_{k=0}^{\infty}\frac{\cos\left(\left(\frac{3n}{4} + \frac{k}{2}\right)\pi\right)}{k!\,\Gamma(n+k+1)}\left(\frac{x^2}{4}\right)^k \tag{2.46}$$

$$bei_n(x) = \left(\frac{x}{2}\right)^n\sum_{k=0}^{\infty}\frac{\sin\left(\left(\frac{3n}{4} + \frac{k}{2}\right)\pi\right)}{k!\,\Gamma(n+k+1)}\left(\frac{x^2}{4}\right)^k \tag{2.47}$$

in which Γ is the Gamma function.

The Gamma function, Γ, can be expressed as the following:

$$\Gamma(\mathrm{x}) = \int_0^{\infty} t^{x-1}e^{-t}dt \tag{2.48}$$

in which *e* is Euler's number.

The maximum deflection under the load at *r* = 0 reduces to the following:

$$w(0) = \frac{p_0}{k}\left(1 + \frac{c}{l}ker'\left(\frac{a}{l}\right)\right) \tag{2.49}$$

in which all variables are as previously defined.

For various radii of loaded regions, Reissner's equations provide the following deflection profiles:

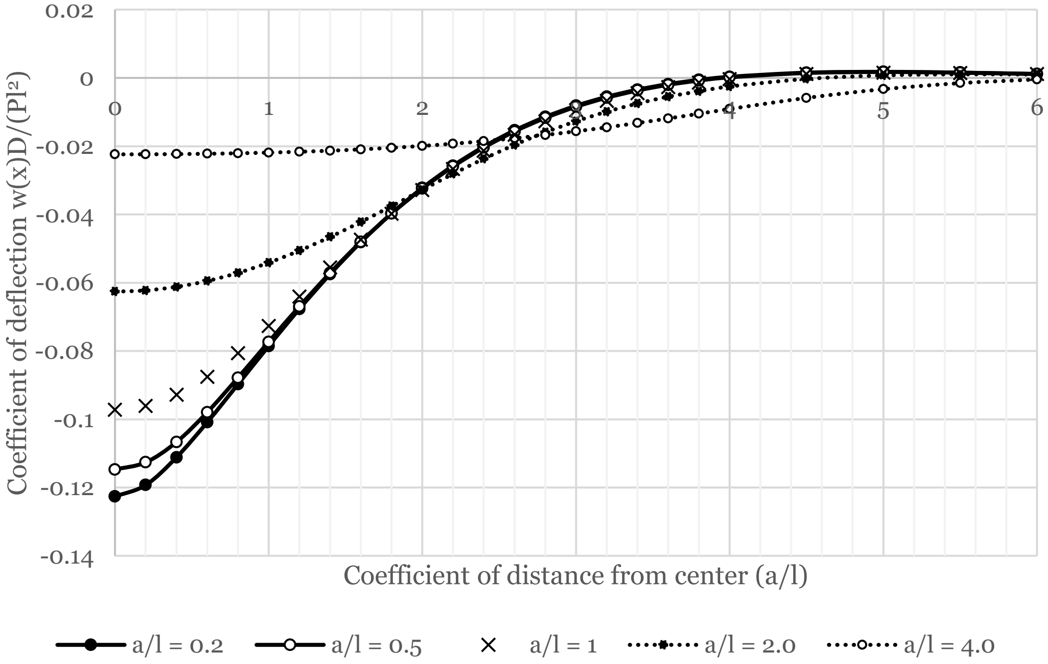

Figure 2.20: Deflection profiles for an infinite plate resting on a Winkler medium subject to a load distributed over various radii, produced by Reissner's (1955) equations

Here, Figure 2.20 compares the dimensionless coefficient of deflection to the coefficient of distance from the center for various areas over which the load is distributed over, notated as having a radius of *a/l*. Notably, Ressiner's equation for a load distributed over a small area (in which *a/l* ≤ 0.2) produces a deflection profile effectively identical to that of Hertz's (1884) and Wyman's (1950) equation for a concentrated load. In particular, it can be seen that the area over which the load is distributed over predominantly affects the maximum deflection under the load.

Westergaard (1926) introduced analytical solutions for the deflection profiles and the critical stresses for a slab-on-grade subject to a concentrated load resting on a Winkler soil. While his work was predominantly written for highway pavements and airport runways, his work later became the basis for contemporary slab-on-grade design (McKinney et al., 2006). Although Westergaard did not provide his derived closed-form analytical solutions, he did provide deflection profiles in the slab graphically as a function of the load, *P,* the modulus of subgrade reaction, *k*, and a length parameter *l* that he terms the radius of relative stiffness.

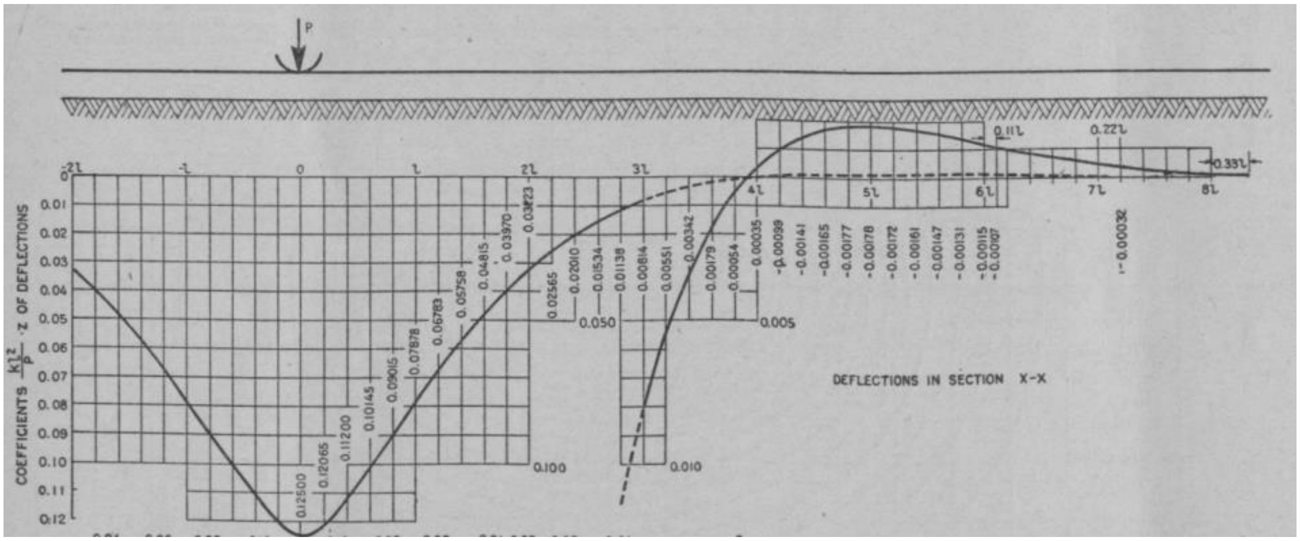

Figure 2.21: Deflection profile for an infinite plate resting on a Winkler medium subject to a concentrated load (Westergarad, 1926)

Figure 2.21 compares the dimensionless coefficient of deflection to the coefficient of distance from the center. It can be seen that the maximum deflection under the load is in agreement with the results obtained by Hertz (1884), Wyman (1950), and Reissner (1955).

Westergaard denotes the length parameter, l, as the radius of relative stiffness, or proportionality factor between the stiffness of the slab to the stiffness of the denoted by equation 2.50 (Westergaard, 1926):

$$l = \sqrt[4]{\frac{Eh^3}{12(1-\mu^2)k}} \tag{2.50}$$

where E is the elastic modulus of the concrete slab, u is Poisson's ratio of concrete, h is the thickness of the slab, and k is the modulus of subgrade reaction. Notably, this length parameter falls in line with those presented by Hertz (1884), Wyman (1950), and Reissner (1955). Additionally, the deflection profile presented in Figure 2.21 is effectively identical to those produced from Hertz's, Wyman's, and Reissner's concentrated load equations.

Westergaard's solutions are distinguished through the use of the 'ordinary theory' and 'special theory'. The ordinary theory of elasticity for beams is simply Euler-Bernoulli beam bending theory (Westergaard, 1926). In terms of slabs (plate theory), the ordinary theory is effectively classical plate theory, or Kirchhoff-Love plate theory following the assumptions that plane and perpendicular sections to the neutral mid-surface remain plane and perpendicular in bending.

Westergaard's 'special theory' involves abandoning the plane cross-section theory and instead considers the deformations due to vertical stresses (Westergaard, 1926). The 'special theory' is used specifically when the area over which a concentrated load is distributed is very small and when the local effects around the load are of concern. Westergaard suggests that the critical stress under such a load can be found using the 'ordinary theory' if an equivalent radius expressed in terms of the actual radius and thickness of the slab are used. He notes that as the area over which the concentrated load is distributed increases, the difference in calculated critical stress between the 'ordinary' and 'special theory' converges towards unity. In particular, this is effectively correcting for the effects of a highly concentrated load by using thick plate theory over the conventional ordinary thin plate theory (Westergaard, 1926; Selvadurai, 1979). Concepts of establishing an equivalent area over which a highly concentrated load acts based on thick plate theory are well-defined by Roark (1938), Holl (1938), Selvadurai (1979), Packard (1996), and McKinney et al. (2006) specifically for highly concentrated loadings. Figure 2.22 shows this relationship:

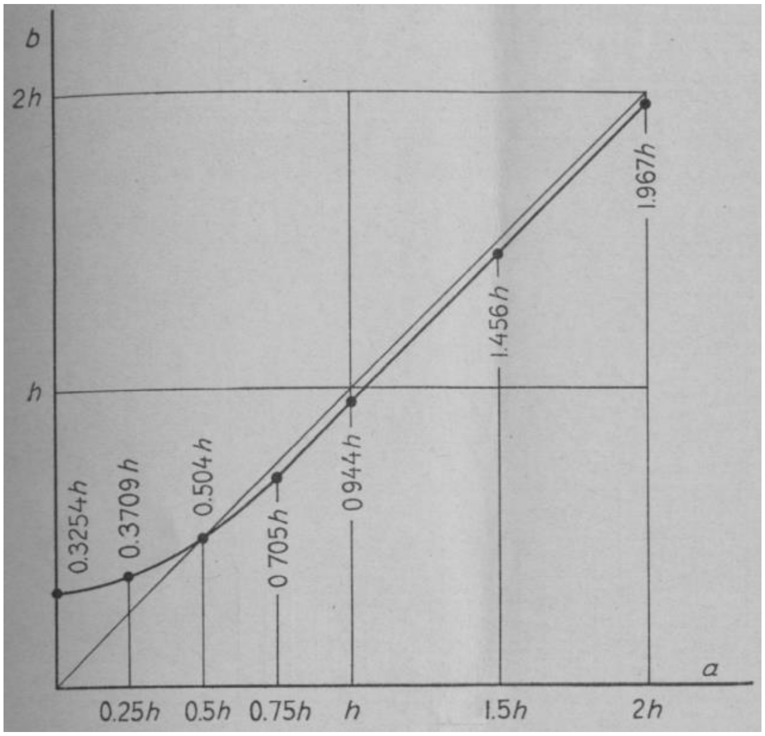

Figure 2.22: Equivalent radius versus the actual radius of contact for a highly concentrated loading condition, (Westergaard, 1926)

Westergaard (1926) suggests that the equivalent radius, b, need only replace the actual radius, a, of a highly concentrated load when the actual radius is less than approximately 1.5 times the thickness of the slab.

While Westergaard does not provide a stress profile like he did with deflections, he does provide equations solving for the critical stress under a concentrated load. For the 'ordinary theory', he provides the following equation:

$$\sigma_i = \frac{3(1+v)P}{2\pi h^2}\left[\ln\left(\frac{l}{a}\right) + 0.6159\right] \tag{2.51}$$

in which v is the Poisson's ratio of the slab, P is the concentrated load, h is the slab's thickness, l is the radius of relative stiffness, and a is the radius of the loaded area.

If the loaded area is sufficiently small as defined by $a < 1.724h$, then the 'special theory' should be considered by substituting the radius a with the equivalent radius:

$$b = \sqrt{1.6a^2 + h^2} - 0.675h \tag{2.52}$$

One particular point of interest is that Westergaard considers that an approximate value of the modulus of subgrade reaction to be sufficient for the determination of the critical stresses in a slab (Westergaard, 1926). In particular, Westergaard states that an increase in the modulus of subgrade reaction from 50 psi/in. to 200 psi/in. (i.e., a 300% increase) caused the maximum stress to decrease by roughly 15 – 20% based on the considered thickness of slab (between 6 – 12") and radius over which the load was distributed (0 – 8"). Figure 2.23 shows the change in stress as a function of the modulus of subgrade reaction:

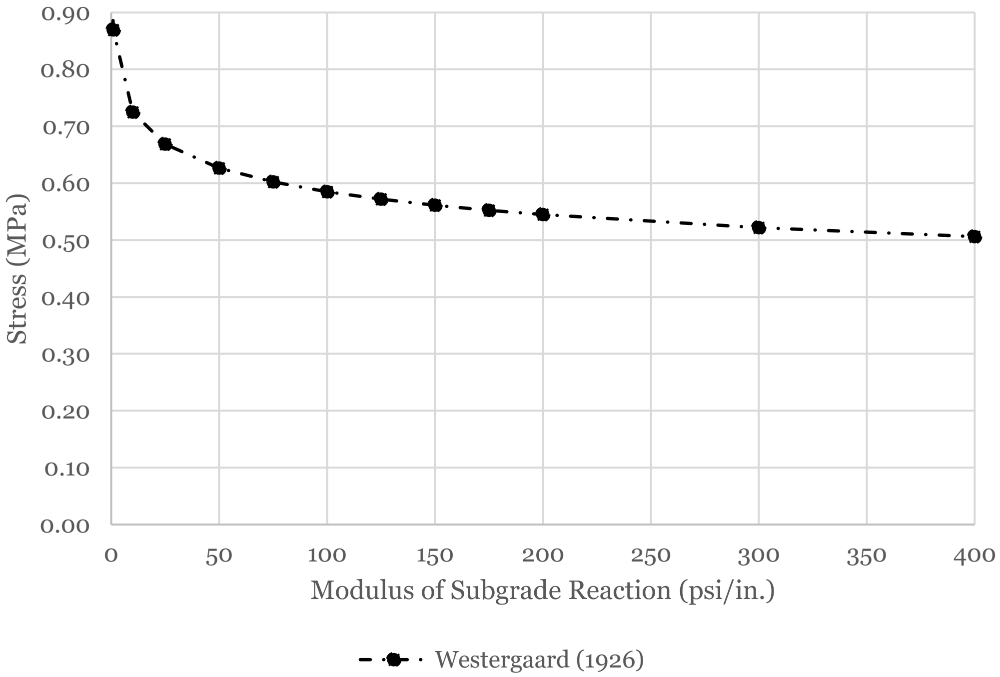

Figure 2.23: Effect of the modulus of subgrade reaction on the maximum stress for an infinite plate resting on a Winkler medium subject to a concentrated load, produced by Westergaard's (1926) equations; h = 150 mm, E_b = 26,000 MPa, P = 10 kN, a = 150 mm

It can be seen from Figure 2.23 that the critical stress decreases depreciatingly with respects to subsequent increases in the modulus of subgrade reaction. In this particular example, increasing the modulus of subgrade reaction from 50 psi/in. to 200 psi/in. (like in Westergaard's statement) results in a decrease of about 12% of the critical stress. As a percentage, a 50% increase in the modulus of subgrade reaction results in approximately 5% decrease in the critical stress. For typical values of the modulus of subgrade reaction, Westergaard's assumption of a representative modulus of subgrade reaction value is reasonable. Notably, Westergaard does not make any mention to the effect of the modulus of subgrade reaction on the deflections of the slab (mostly because the controlling factor in most slab-on-grade design are dominated by the critical stresses and not deflections). However, it should be noted that the deflections are more sensitive to changes to the modulus of subgrade reaction, and is shown in the Figure 2.24:

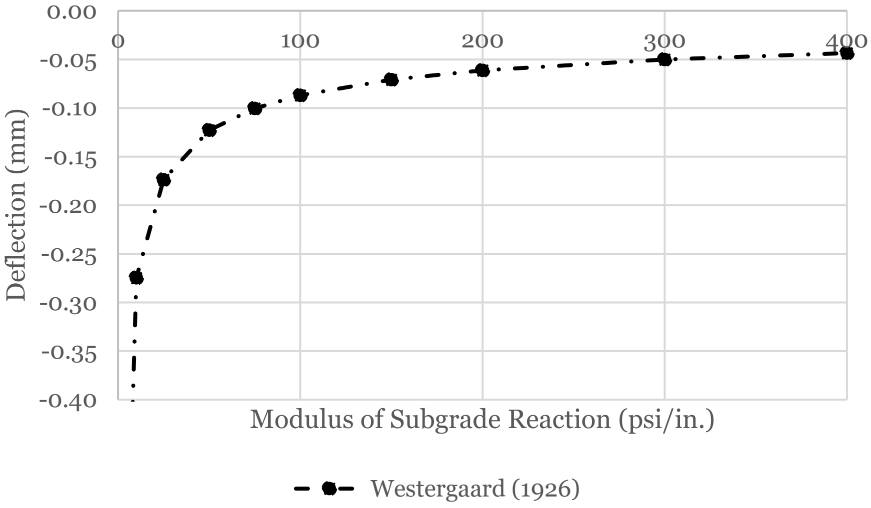

Figure 2.24: Effect of the modulus of subgrade reaction on the maximum deflection for an infinite plate resting on a Winkler medium subject to a concentrated load, produced by Westergaard's (1926) equations; h = 150 mm, E_b = 26,000 MPa, P = 10 kN, a = 150 mm

As a percentage, a 50% increase in the modulus of subgrade reaction results in approximately 20% decrease in the maximum deflection. As a result, it can be seen that more care should be taken when approximating a modulus of subgrade reaction when the deflections are of major concern.

Of note for both the stresses and the deflection are the magnitude of values used for the modulus of subgrade reaction. In particular, modulus of subgrade values less than approximately 100 psi/in. are very sensitive, and small changes result in larger changes in the critical stresses and deflections.

Westergaard (1943) introduced much of the derivations involved with establishing his 1926 equations for stresses. He introduced a correction for if the loaded area was larger than a typically assumed highly concentrated loading condition (Westergaard, 1943). So long as the concentrated load remains concentrated and distributed over a circular area with radius no greater than the radius of relative stiffness, Westergaard provides the following equation for the critical stress:

$$\sigma_i = \frac{3(1+\mu)P}{2\pi h^2}\left[\ln\left(\frac{l}{a}\right) + 0.6159 + \frac{\pi}{32}\left(\frac{a}{l}\right)^2\right] \tag{2.53}$$

in which v is the Poisson's ratio of the slab, P is the concentrated load, h is the slab's thickness, l is the radius of relative stiffness, and a is the radius of the loaded area.

Notably, the additional correction factor can actually be used regardless of if one would consider a loaded area to be too large to be rated as small, so long as the radius remains less than the radius of relative stiffness. This is true because the correction factor trends towards zero as the radius over which a load is distributed decreases. As long as the actual radius is less than one-fourth of the radius of relative stiffness, Westergaard suggests ignoring this correction factor for practical applications (Westergaard, 1943).

Westergaard (1948) introduced modifications to his equations if the considered concentrated load was not distributed over a circle but instead an ellipse (Westergaard, 1948). This was done in an attempt to provide a more realistic distribution of force when considering loads produced by wheels. This time, Westergaard's critical stress equations provided values up until the edge of the loaded region. The equations are provided:

$$z = \frac{P}{8kl^2}\left[1 - \frac{a^2 + b^2 + 4x^2 + 4y^2}{16\pi l^2}\ln\left(\frac{Eh^3}{k\left(\frac{a+b}{2}\right)^4}\right) - \frac{a^2 + 4ab + b^2}{16\pi l^2} + \frac{(a-b)(x^2-y^2)}{2\pi l^2(a+b)}\right] \tag{2.54}$$

$$\left.\begin{matrix}\sigma_x \\ \sigma_y\end{matrix}\right\} = \frac{3(1+\mu)P}{8\pi h^2}\left[\ln\left(\frac{Eh^3}{k\left(\frac{a+b}{2}\right)^4}\right) \mp 2\frac{a-b}{a+b}\right] \tag{2.55}$$

in which *a* and *b* are the short and long lengths of the ellipse, *x* and *y* are the considered distances in the short and long directions, respectively, and all other variables are defined as before.

Strangely, while one would assume that considering an ellipse with equal radii in both directions would produce the same results as his 1926 equations, this is not entirely true (but for most practical applications is not of great concern). Reducing both of the above equations when taking $a = b$ yields the following simplified equations for maximum deflection and stress under the load at $x = y = 0$:

$$z = \frac{P}{8kl^2}\left[1 - \frac{a^2}{8\pi l^2}\left(\ln\left(\frac{Eh^3}{ka^4}\right) + 3\right)\right] \tag{2.36}$$

$$\sigma_i = \frac{3(1+\mu)P}{2\pi h^2}\left[\ln\left(\frac{l}{a}\right) - \frac{1}{4}\ln(12(1-\mu^2))\right] \tag{2.57}$$

It is worth mentioning that Westergaard's original 1926 equations for deflections do not consider the loaded region over which the concentrated load is distributed, and it is assumed that any load provided must be sufficiently concentrated (hence the introduction of his corrective term in 1943). Comparing curve deflections between Reissner (1955) and Westergaard indicates that this area should roughly be a/l ≤ 0.2 to be considered a concentrated load.

Ioannides et al. (1985) published a reexamination of Westergaard's solutions and succinctly summarizes all, if any, of the changes to the empirical equations. Ioannides et al. provides what they consider to be the updated equations for the maximum load of an infinite slab on a Winkler medium subjected to a concentrated load:

$$z = \frac{P}{8kl^2}\left[1 + \frac{1}{2\pi}\left[\ln\left(\frac{a}{2l}\right) + \gamma - 1.25\right]\left(\frac{a}{l}\right)^2\right] \tag{2.58}$$

$$\sigma_i = \frac{3(1+\mu)P}{2\pi h^2}\left[\ln\left(\frac{2l}{a}\right) + 0.5 - \gamma\right] + \frac{3(1+\mu)P}{64h^2}\left[\left(\frac{a}{l}\right)^2\right] \tag{2.59}$$

Like Westergaard's 1948 equation, Ioannides et al. (1985) provided a deflection that is influenced by the loaded area.

The latter term in the critical stress equation is additional stress used to account for the effects of the loaded area (Ioannides et al., 1985) and refers to the correction factor introduced by Westergaard in 1948, and when factored into the main equation yields the same term. Ioannides et al. (1985) replaces the original constant of 0.6159 with a function expressed in terms of Euler's constant and instead now yields a constant of 0.61593… which is sufficiently accurate. Notably, when Poisson's ratio is taken at 0.15 (as Westergaard does in his original 1926 paper), the natural log function returns -0.615537… which, for all intents and purposes, is sufficiently close to the constant of 0.6159 he originally uses. So long as the Poisson's ratio of concrete considered remains in the generally accepted range (0.1 to 0.2), Ioannides et al.'s (1985) updated equations produce identical maximum deflections and critical stresses as Westergaard's 1948 and 1943 equations, respectively, for all practical applications.

A comparison of the critical values (maximum deflections and stresses under a concentrated load) between various researchers has been presented in Figures 2.26 through 2.27. In general, the equations presented in this section can be loosely described as follows: equations for deflections that consider a highly concentrated loading, such as those from Hertz (1884), Wyman (1950), and Westergaard (1926), equations for deflections that are influenced by the area of the loaded region, such as those from Reissner (1955), Westergaard (1948), and Ioannides et al. (1985), and equations for maximum stress, such as those from Westergaard (1926), Westergaard (1943), Westergaard (1948), and Ioannides et al. (1985).

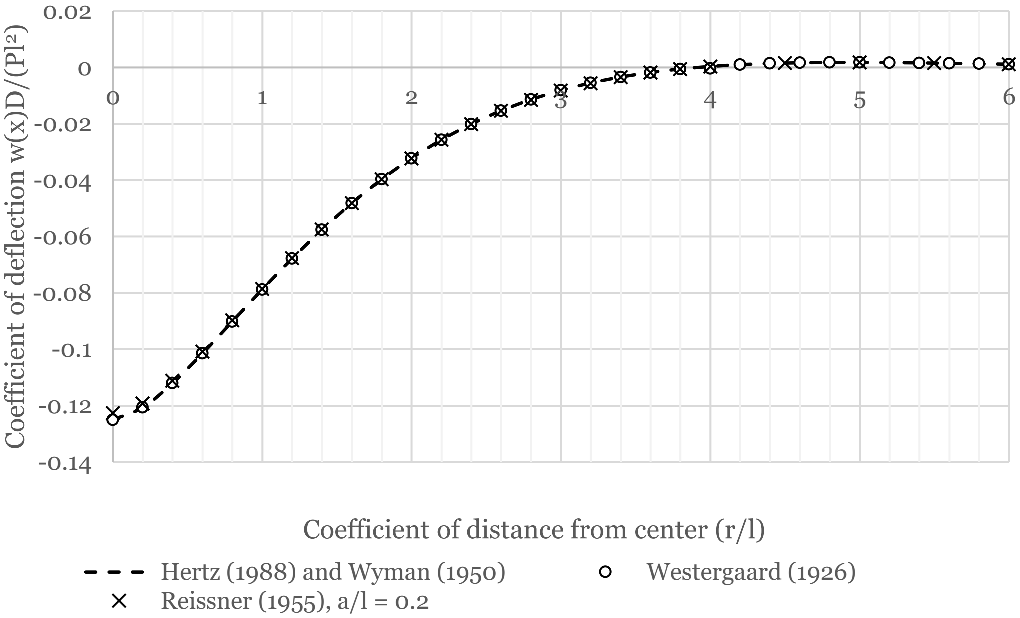

Figure 2.26: Comparison of deflection profiles for an infinite plate resting on a Winkler medium subject to a concentrated load

Clearly, the results obtained by Hertz, Wyman, Westergaard, and Reissner are effectively identical when considering a highly concentrated load. Notably, Reissner's equations predict very slightly less deflection directly under the loaded region, which suggests that the ratio of the loaded region to the radius of relative stiffness should be slightly less than 0.2 to be considered as a concentrated load. For practical applications, this makes no meaningful difference.

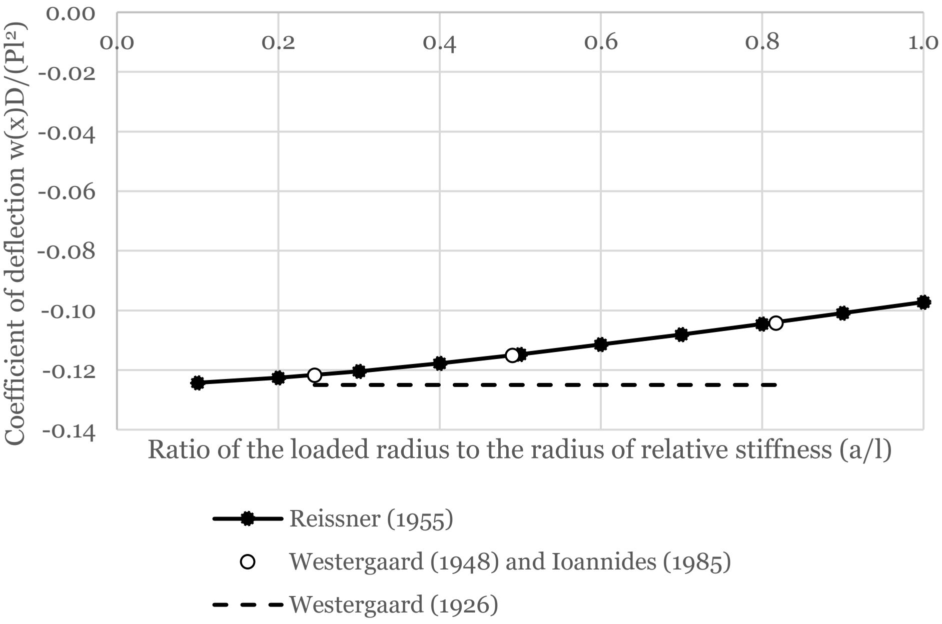

Figure 2.27: Comparison of the maximum deflection for an infinite plate resting on a Winkler medium subject to a concentrated load distributed over a variable area

From Figure 2.27, it becomes clear that the area over which the load is distributed over plays an important role in determining the maximum deflection. When one does not consider these effects (such as Westergaard's 1926 equations), then it should be ensured that the radius over which the load is distributed is relatively small (i.e., the ratio of the loaded region to the radius of relative stiffness should be slightly less than 0.2).

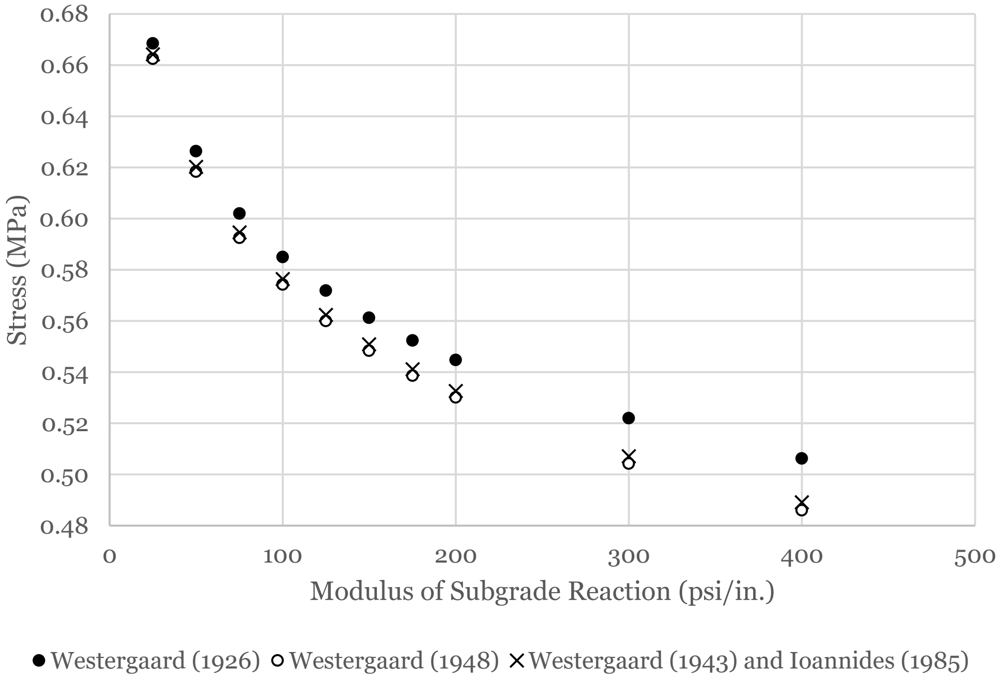

Figure 2.28: Comparison of the maximum stress for an infinite plate resting on a Winkler medium subject to a concentrated load distributed over a variable area (note that the y-axis begins at 0.48 MPa for clarity); h = 150 mm, E_b = 26,000 MPa, P = 10 kN, a = 150 mm)

It can be seen that Westergaard's (1926) original equations overpredicts the maximum stress for all values of the modulus of subgrade reaction, and this is more apparent with larger values of k.

2.3.2 Plates on Elastic Half-Space Soils

The problem of a plate subject to a concentrated load resting on an elastic half-space is well-known to be governed by the indefinite Fourier-Bessel integro-differential equation and was first provided by Biot (1935):

$$w(r) = \frac{Pa^2}{2\pi D}\int_0^\infty \frac{\xi J_0(\xi \frac{r}{a})}{\xi^4 + \Delta} d\xi \qquad (2.60)$$

in which delta is a random parameter and a is a length parameter (akin to Westergaard's radius of relative stiffness). The length parameter, a, can be expressed as follows:

$$a = \sqrt[3]{\frac{D(1 - v_s)}{G_s}} \tag{2.61}$$

Hogg (1938) presented an approximate solution for an infinite plate subject to a concentrated resting on an isotropic elastic block. He found that the deflection profile, *w(r)*, could be represented as an infinite summation series:

$$w(r) = \frac{Pa^2}{2\pi D} \sum_{m=0}^{\infty} (-1)^m \left[\frac{\left(\frac{b}{2}\right)^{6m+2} \left(\ln\left(\frac{b}{2}\right) - \Phi(3m + 2) \right)}{[(3m + 1)!]^2} + \frac{2\pi}{\sqrt[2]{27}} \frac{\left(\frac{b}{2}\right)^{6m}}{[(3m)!]^2} \right. \\ \left. - \frac{2\pi}{\sqrt[2]{27}} \frac{\left(\frac{b}{2}\right)^{6m+4}}{[(3m + 2)!]^2} + \frac{\pi}{2} \frac{\left(\frac{b}{2}\right)^{6m+5}}{[\Gamma(3m + 3.5)]^2} \right] \tag{2.62}$$

in which $b = r/a$, Γ is the Gamma function expressed in equation 2.48, and Φ is a finite summation series.

Hogg's self-defined function, Φ, can be expressed as follows:

$$\Phi(\mathrm{r} + 1) = -C_E + \sum_{n=1}^{r} \frac{1}{n} \tag{2.63}$$

in which C_E is Euler's constant (0.577 ...).

The maximum deflection directly under the load at *r = 0* reduces to the following:

$$w(0) = 0.1925 \frac{Pa^2}{D} \tag{2.64}$$

Hogg also presents the contact stress at the loaded region:

$$q(0) = \frac{\sqrt{3}}{9} \frac{P}{a^2} \tag{2.65}$$

Figure 2.29: Deflection profiles for an infinite plate resting on an elastic half-space subject to a concentrated load, produced by Hogg's (1938) equations

Notably, Hogg's approximated predictions are useful only when considering points within or nearby the loaded region (r/a ≤ 2), as the predicted deflections deteriorate rapidly beyond this point (Selvadurai, 1979). This can be seen from Figure 2.29; beyond r/a > 3, Hogg's approximation begins to predict uplift deflections.

Gorbunov-Posadov (1940, 1959) and Gorbunov-Posadov and Serebrjanyi (1961) presented graphical results from his application of a double power series method (Selvadurai, 1979). In particular, Gorbunov-Posadov assumed that a plate could be assumed to be rigid if the relative stiffness parameter, K_g, which was a measure of the stiffness between the plate and the subgrade, satisfied the following inequality:

$$K_g = \frac{12\pi(1 - v_b{}^2)}{(1 - v_s{}^2)}\left(\frac{E_s}{E_b}\right)\left(\frac{l}{h}\right)^2\left(\frac{b}{h}\right) \leq \frac{8}{\sqrt{\frac{l}{b}}} \tag{2.66}$$

in which v_b and v_s are the Poisson's ratio for the plate and the soil, respectively, E_s and E_b are the modulus of elasticity for the soil and the plate, respectively, h is the plate thickness, and l and b are the lateral dimensions of the plate.

For a typical plate and soil, Gorbunov-Posadov provides the following deflection profile:

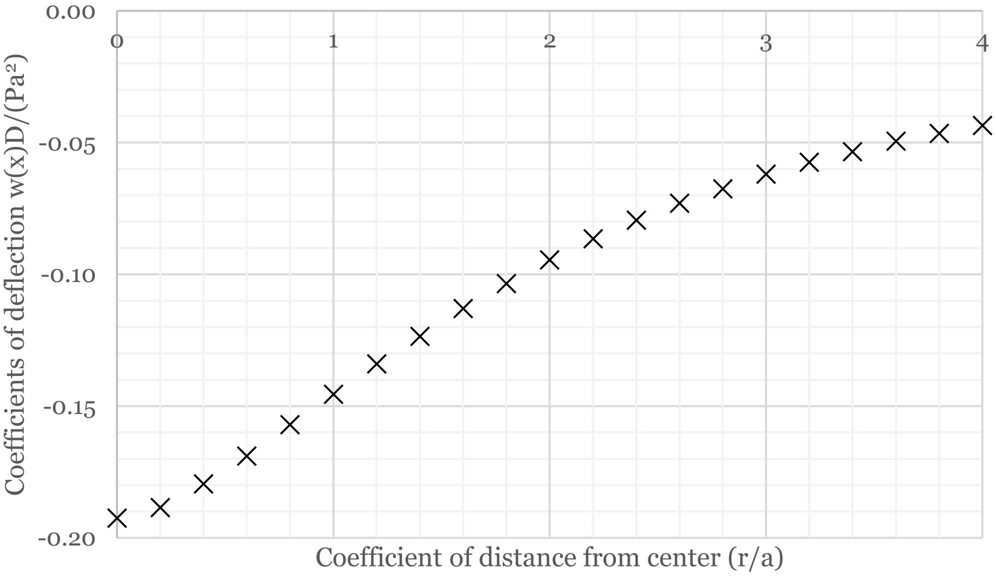

Figure 2.31: Deflection profile for an infinite plate resting on an elastic half-space subject to a concentrated load, produced by tables provided by Gorbunov-Posadov (1959) and Selvadurai (1979)

Unlike Hogg's (1938) approximation, Gorbunov-Posadov predicts continued downwards deflection away from the loaded region even beyond r/a > 2.

Cheung and Zienkiewicz (1965) presented the distribution of contact stresses using numerical methods of finite differences for plates subject to concentrated or uniform loading:

$$q(x) = \bar{q}\frac{P_0}{L^2} \tag{2.67}$$

in which L is the length of the finite plate, P_o is the concentrated load, and $\bar{q}$ is a dimensionless coefficient determined using Figure 2.32:

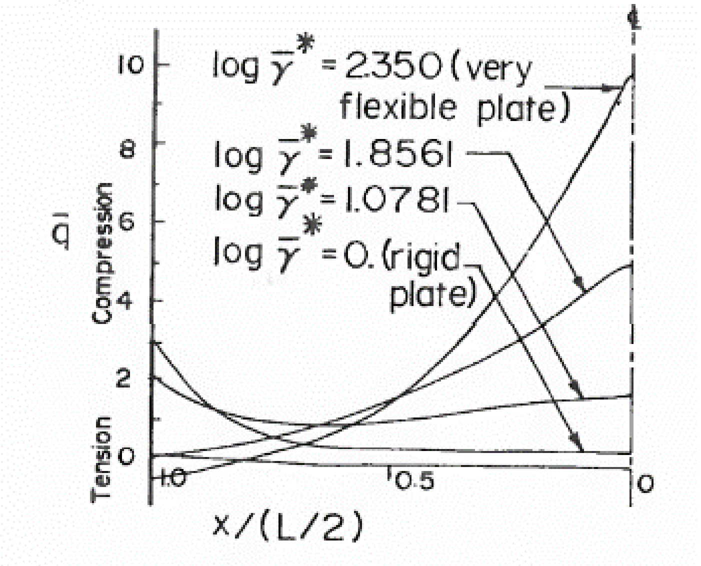

Figure 2.32: Contact stress profiles for a plate resting on an elastic half-space subject to a concentrated load (Cheung and Zienkiewicz, 1965; Selvadurai, 1979)

Here, $\bar{\gamma}^*$ is a relative stiffness parameter between the plate and the subgrade, determined as:

$$\bar{\gamma}^* = 180\pi \frac{E_s}{E_b}\left(\frac{a_0}{h}\right)^3 \tag{2.68}$$

in which a_o is one-sixth of the length of the plate.

When the plate is very stiff (i.e., almost rigid), Cheung and Zienkiewicz (1965) predict almost no contact stress except near the edges. Conversely when the plate is very flexible, they predict significant contact stress directly under the loaded region at the center of the plate.

Selvadurai (1979) presented, using a Gauss-Legendre quadrature approximation, a more accurate approximation of Biot's (1935) indefinite integral. He presents the following solution for the deflection profile:

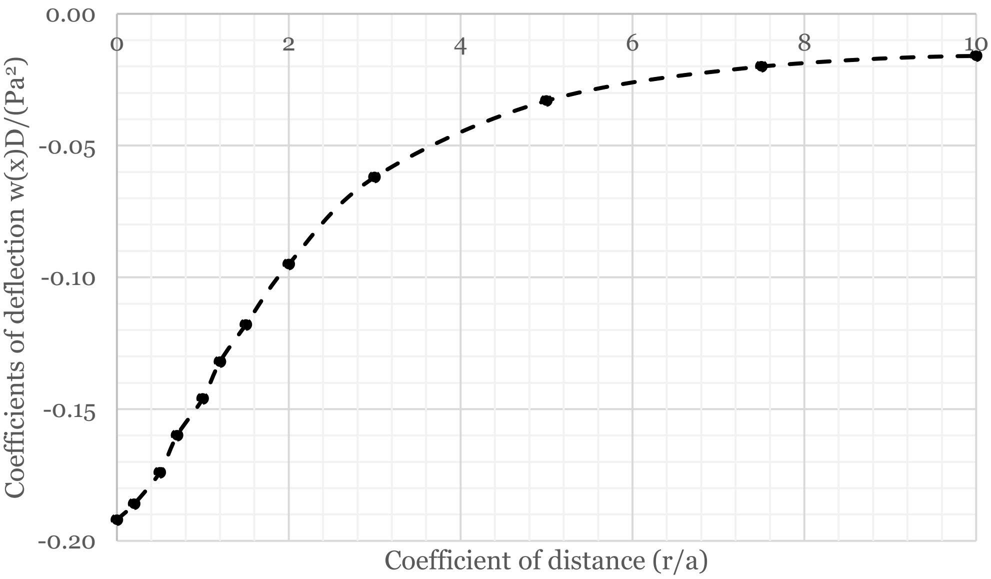

Figure 2.32: Deflection profiles for an infinite plate on an elastic foundation subject to a concentrated load, produced by Selvadurai's (1979) numerical approximations

Unlike Hogg's (1938) approximation, Selvadurai predicts continued downwards deflection away from the loaded region even beyond r/a > 2.

Hu and Hartley (1994) and later Silva et al. (2001) explored the use of finite element methods to numerically compute the deflections and contact stresses of a plate subject to concentrated or uniform loading on an elastic half-space. They presented the deflection profiles and contact stress profiles as follows:

$$w(r) = \bar{w}\frac{0.913(1 - v_s{}^2)P_0}{2aE_s} \tag{2.69}$$

$$q(r) = \frac{P_0\bar{q}}{4a^2} \tag{2.70}$$

in which a is the length of half the finite plate, P_o is the concentrated load, E_s is the modulus of elasticity of the soil, v_s is the Poisson's ratio of the soil, and $\bar{w}$ is a dimensionless deflection coefficient and $\bar{q}$ is a dimensionless contact stress coefficient determined by Figure 2.33:

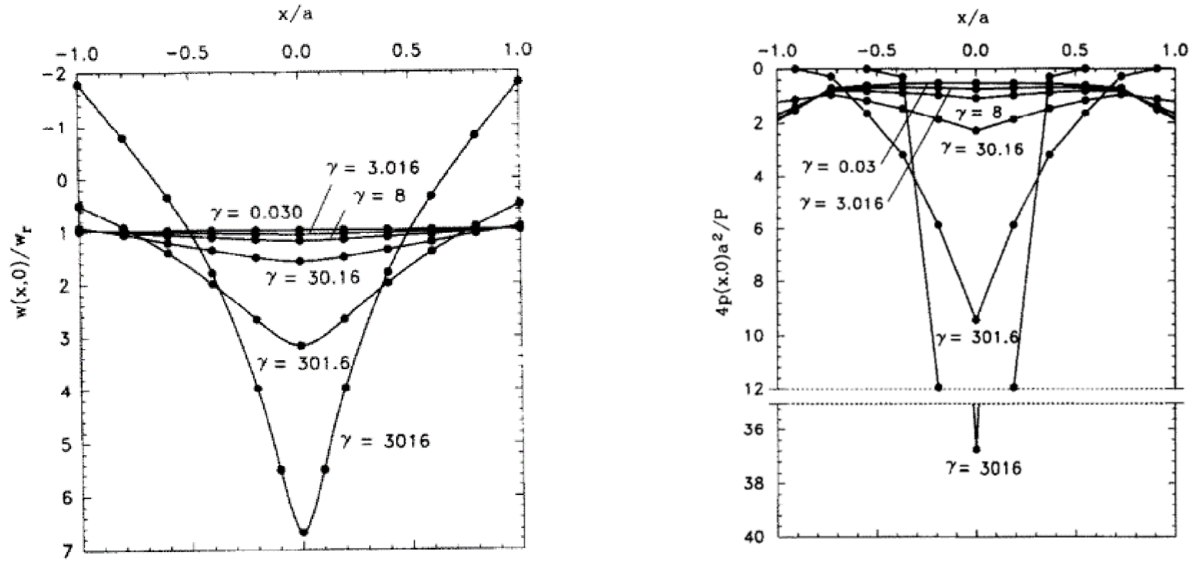

(a) (b)

Figure 2.33: (a) Deflection profile and (b) Stress profiles for a finite plate on an elastic half-space subject to a concentrated load for various relative stiffnesses (Hu and Hartley, 1994)

Here, γ is a relative stiffness parameter between the plate and the subgrade, determined as:

$$\gamma = \frac{\pi E_s a^3}{D(1 - v_s{}^2)} \tag{2.71}$$

in which *D* is the flexural rigidity of the plate and the other variables are as previously defined.

When the relative stiffness is very low ($\gamma < 8$), the plate can be considered as rigid. A rigid plate is expected to deflect uniformly (as the plate itself no longer deflects), and in agreement with the results presented by Cheung and Zienkiewicz (1965), exhibits larger contact stresses near the edges of the plate.

A comparison of the deflection profiles and contact stress profiles established for the case of a plate resting on an elastic half-space subject to a concentrated load as determined by various researchers using various methods (numerical approximation, finite element methods, power series methods, etc.) is provided in Figures 2.34 and 2.35:

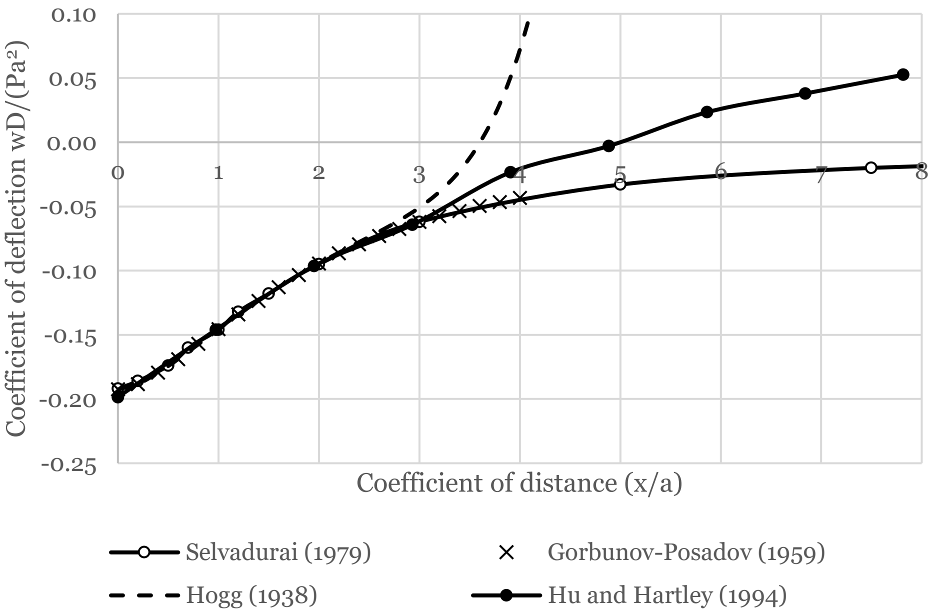

Figure 2.34: Comparison of the deflection profiles for a plate resting on an elastic half-space subject to a concentrated load; (h = 165 mm, E_b = 34,000 MPa, E_s = 100 MPa, P = 10 kN, $L = B$ = 10,000 mm, γ = 3016)

In Figure 2.34, *a* is the length parameter presented by Biot (1935) and associated with a ratio of stiffness between the subgrade and an infinite plate. It particular, it should be noted that Hogg's (1938), Gorbunov-Posadov's (1959), and Selvadurai's (1979) deflection profiles are based on a plate of infinite length, while Hu and Hartley's (1994) are based on a plate of finite length, hence the disparity in deflection created by uplift at the end of Hu and Hartley's curve. Additionally, as stated previously, Hogg's (1938) equations are reasonable only when considering areas near the loaded region (i.e., for x/a < 2). It can be seen from Gorbunov-Posadov (1959) and Selvadurai (1979) that an infinite plate is expected to deflect continuoulsy along its centerline length when subject to a concentrated load, even far away from the loaded region. In fact, the deflection only reaches a negligible value (i.e., a deflection that is less than 1% of the maximum deflection) at 100*a*.

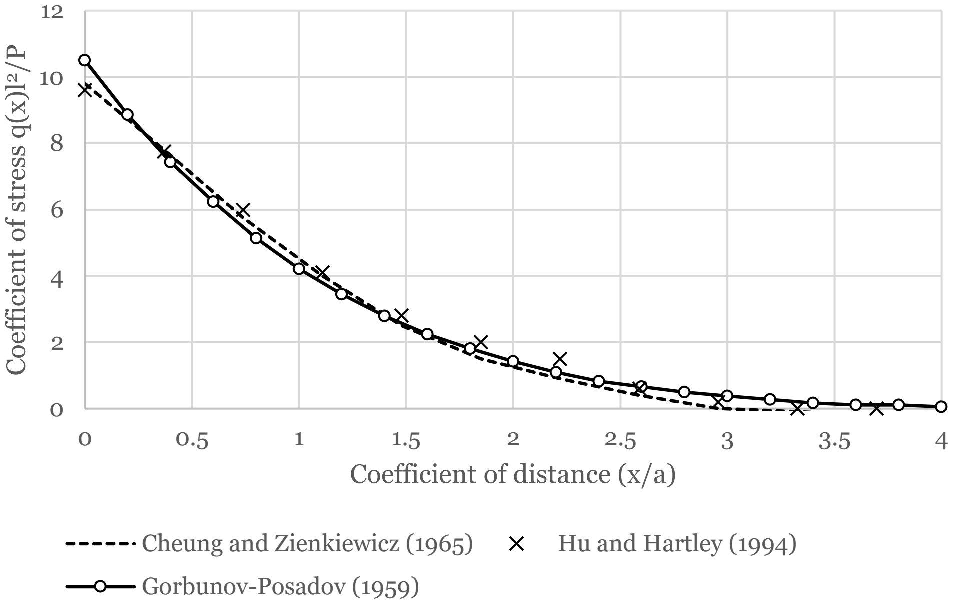

Figure 2.35: Comparison of the contact stress profiles for plates resting on an elastic half-space subject to a concentrated load; h = 250 mm, E_b = 40,000 MPa, E_s = 200 MPa, P = 10 kN, $L = B$ = 6,000 mm, γ = 301, $\bar{\gamma}^*$ = 2.35

In Figure 2.35, *a* is the length parameter presented by Biot (1935) and associated with a ratio of stiffness between the subgrade and an infinite plate. It particular, it should be noted that Gorbunov-Posadov's (1959) contact stress profiles are based on a plate of infinite length, while Cheung and Zienkiewicz's (1965) and Hu and Hartley's (1994) are based on a plate of finite length. In general, all three researcher's equations were in good agreement. In particular, Gorbunov-Posadov (1959) predicted slightly more stress directly under the load, but in general this does not have a significant impact on practical applications.

2.3.3 Relationship Between Characterizing Parameters

At this point it is instructive to compare the deflections and stresses determined between a plate resting on a Winkler spring model against that of a plate resting on an isotropic half-space.

While clearly the two models are sufficiently dissimilar that a perfect correlation between deflection profiles and stresses (and by extension, their independent system characterizing parameters k and E_s) does not exist, a representative relationship between the modulus of subgrade reaction and the elastic constants of a half-space can still be formed by either considering one of the several empirically determined equations for the modulus of subgrade reaction or by calibrating the analytical solutions for the critical values in the plate.

This section will present the latter method by calibrating the various analytical solutions associated with a plate resting on a Winkler spring model to that of a plate resting on an isotropic elastic half-space. Here, it should again be noted that a change in the modulus of subgrade reaction has significantly greater effects on the deflections of a plate compared to the maximum stresses (see

Figures 2.23 and 2.24). Therefore, it is more important to calibrate the analytical solutions for deflections (as the critical stresses will only be minorly affected).

By equating the maximum deflection directly under the loaded region of a plate resting on a Winkler model (i.e., obtained from Westergaard (1926), Hertz (1884), Wyman (1950), Reissner (1955), etc.) to that of a plate resting on an elastic half-space (i.e., obtained from Hogg (1938), Gorbunov-Posadov (1959), etc.), the following relationship may be produced:

$$k = \frac{2500}{5929} \frac{DG^{4/3}}{(D(1-v_s))^{4/3}} \tag{2.72}$$

in which k is the modulus of subgrade reaction, D is the flexural rigidity of the plate, G is the shear modulus of the soil, and v_s is the Poisson's ratio of the soil. By considering the flexural rigidity of the plate as a constant, direct relationships between k and E_s can be determined:

$$k = E^{4/3} \frac{1}{D^{1/3}} \frac{2500}{5929} \frac{1}{2\sqrt[3]{2}} \frac{1}{(1-{v_s}^2)^{4/3}} \tag{2.73}$$

$$E_s = 2k^{3/4} D^{1/4} \frac{5929}{250\sqrt{154}} (1-{v_s}^2) \tag{2.74}$$

This relationship has been plotted in Figure 2.36:

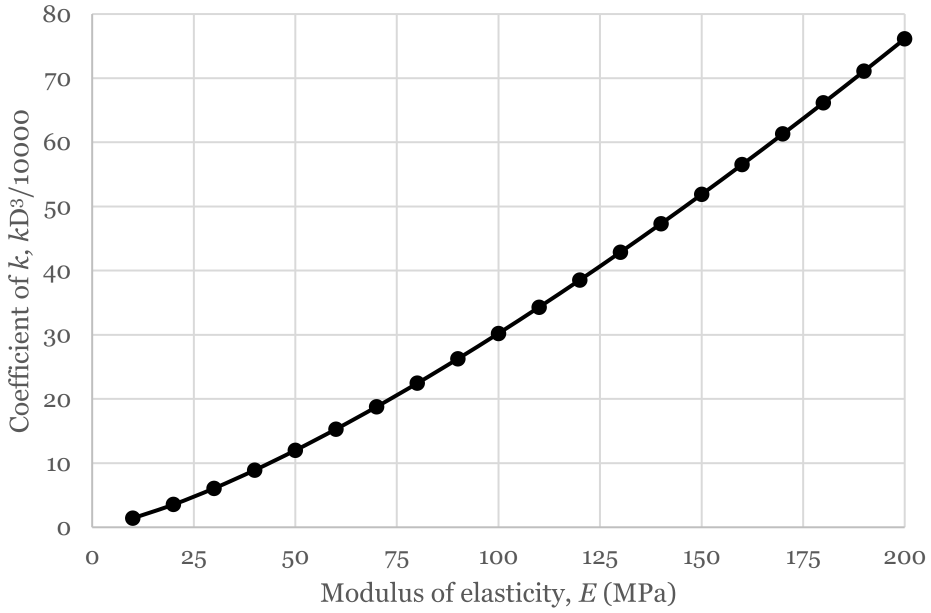

Figure 2.36: Modulus of elasticity versus the coefficient of the modulus of subgrade reaction when calibrated for maximum deflection

It can be seen that the relationship between the modulus of elasticity and modulus of subgrade reaction is nonlinear when the flexural rigidity of the plate is taken as a constant value.

For practical applications, consider the following cases of arbitrarily assigned values plotted in Figure 2.37:

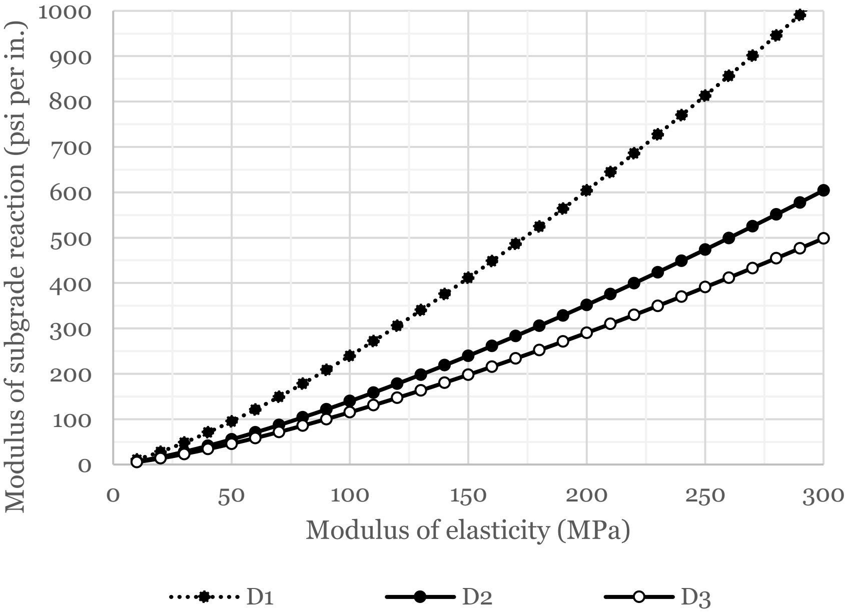

Figure 2.37: Modulus of elasticity versus modulus of subgrade reaction when calibrated for maximum deflection for various values of flexural rigidity, D; D_1 = 2,000 kNm, D_2 = 10,000 kNm, D_3 = 18,000 kNm

Again, it is noted that the modulus of elasticity shares a nonlinear relationship with the modulus of subgrade reaction. Figure 2.37 also showcases the effects of the flexural rigidity of the plate. In particular, it can be seen that linear increases in the flexural rigidity (through any combination of thickness and elastic modulus) yields depreciatingly decreasing results between the modulus of elasticity and modulus of subgrade reaction.

As the purpose of this relationship is to determine an equivalent modulus of elasticity, it is useful to now note the effects of the modulus of subgrade reaction, slab depth, and slab strength on the equivalent modulus of elasticity in the above calibrated relationships. Immediately, it is expected that the equivalent elastic modulus is most sensitive to the assigned modulus of subgrade reaction and depth of slab compared to the compressive strength of concrete (simply by considering the mathematical form presented in equation 2.73 and 2.74).

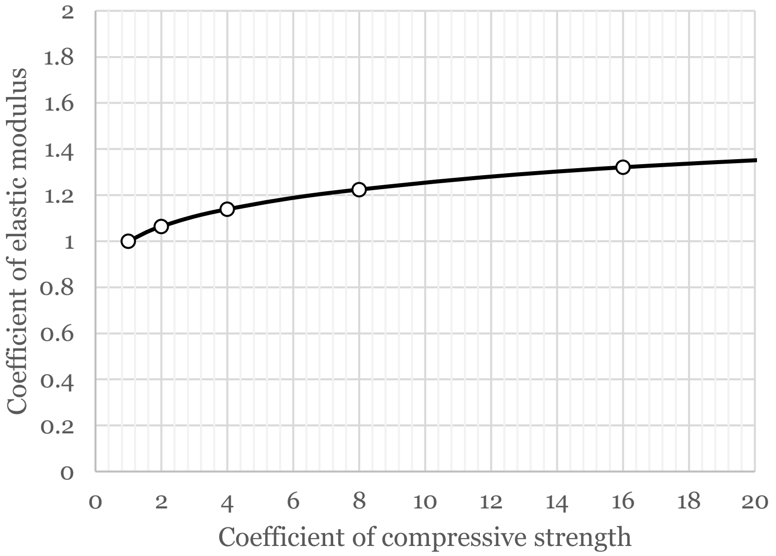

Figure 2.38: Effect of compressive strength on the equivalent modulus of elasticity

Here, with respects to any value of *k* and *h*, doubling the compressive strength increases the equivalent elastic modulus by 5 – 10% (i.e., diminishing increases of *E* with respects to *f'c*).

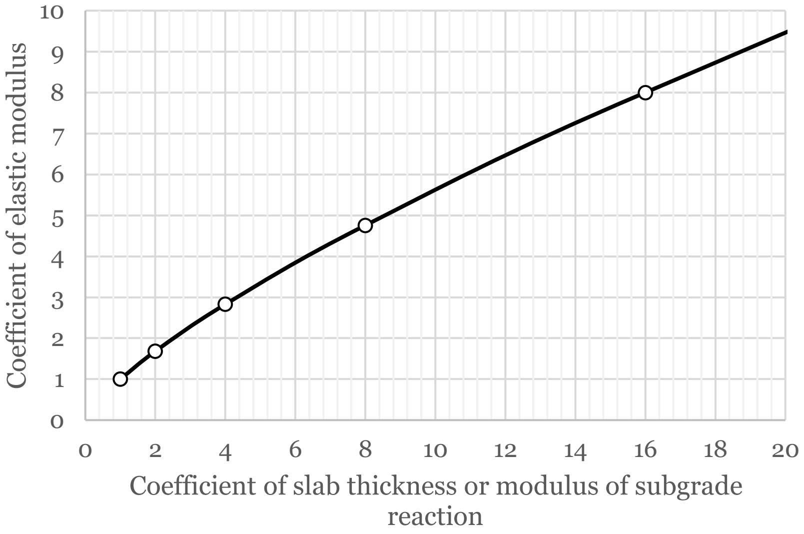

Figure 2.39: Effect of the slab depth or modulus of subgrade reaction on the equivalent modulus of elasticity

Here, with respects to any value of *f'c*, doubling *k* or *h* (while holding the other static) increases the equivalent elastic modulus by 68% (constant increase with respects to *k* or *h*). Therefore, it is clear that changes in the modulus of subgrade reaction or slab depth have an equally impactful effect on the equivalent modulus of elasticity, while changes to the compressive strength are, by and large, negligible.

Figure 2.40 shows the deflection profiles for a plate subject to a concentrated load resting on a Winkler soil and elastic half-space when calibrated for maximum deflection:

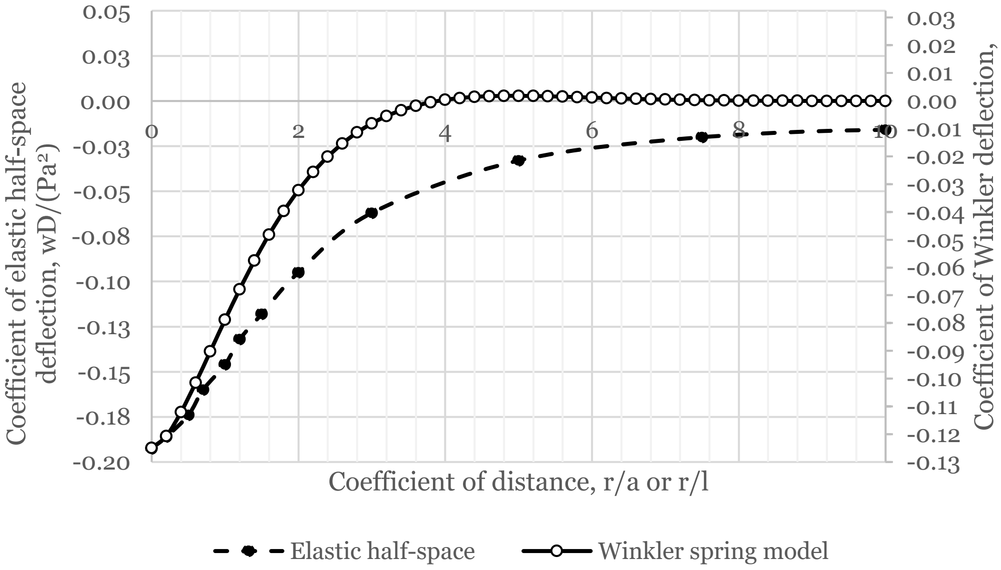

Figure 2.40: Comparison of deflection profiles between an infinite plate resting on a Winkler medium or elastic half-space and subject to a concentrated load when calibrated for the maximum deflection

Figure 2.40 shows that the plate resting on the elastic half-space will deflect more away from the loaded region when compared to the plate resting on the Winkler soil. In particular, it can also be seen that the plate resting on the Winkler soil also experiences a very brief moment of uplift. In actuality, due to the mathematical nature of the equation for the response of a plate resting on a Winkler soil, the plate is expected to oscillate between deflecting upwards and downwards away from the loaded region (Selvadurai, 1979). For practical applications, this is largely negligible. It is important to note that the x-axis provided in Figure 2.40 is shared between the two deflection profiles and is read as the ratio of considered distance, r, to the respective length parameter, a, or l, of the elastic half-space and Winkler model (i.e., the x-axis is composed of normalized, dimensionless values). Consider a case with arbitrarily assigned values; the equivalent deflection profiles are provided in Figure 2.41:

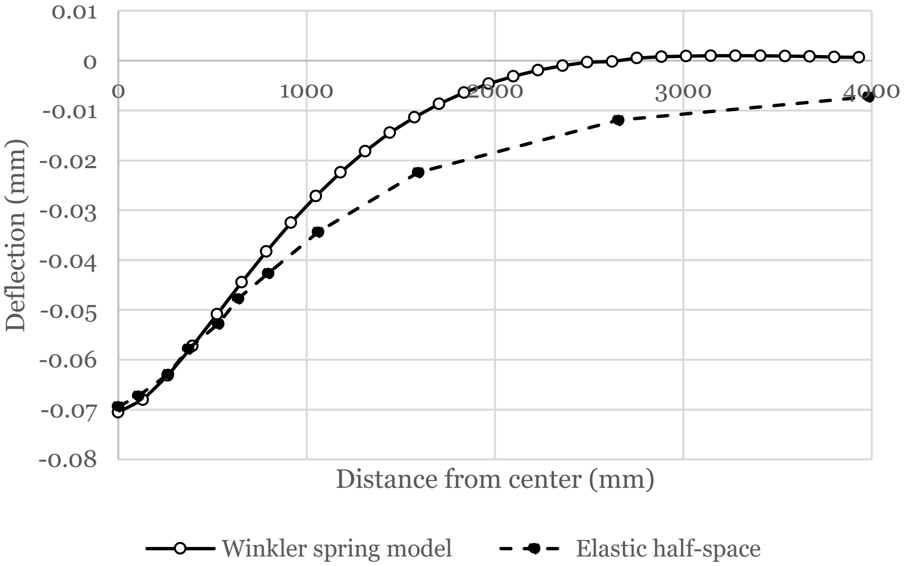

Figure 2.41: Comparison of deflection profiles between an infinite plate resting on a Winkler medium or elastic half-space and subject to a concentrated load when calibrated for the maximum deflection; note that the length parameters, l and a, are 635 and 531 mm, respectively; P = 10 kN, k = 150 psi/in., h = 150 mm, E_b = 26,625 MPa, $E_{s,equiv.}$ ≈ 100 MPa

Again, it can still be noted that the plate resting in a Winkler medium deflects significantly less when considering points away from the loaded region when compared against the plate resting on an elastic half-space. Unlike in Figure 2.40, the x-axis in Figure 2.41 has been depicted in terms of length. It can be seen that the disparity in deflection away from the loaded region is not as large as compared to Figure 2.40.

2.4 Summary of Background

The contemporary design of slabs-on-grade are provided by the American Concrete Institute and summarizes methods produced by the Portland Cement Association, Wire Reinforcement Institute, and the Corps of Engineers (McKinney et al., 2006). Each method requires the loading conditions and slab and soil material properties in order to establish the design slab thickness through various design charts and design tables. All three design methods are largely based on the analysis provided by H. Westergaard for infinitely spanning slabs resting on Winkler-type soils and subject to various concentrated loads. As a result of the simplification of the soil as a Winkler spring foundation, the slab is assumed to have continuous contact with the subgrade throughout its deformation. While this is satisfactory for the design of roads and pavement slabs, in which stresses produced by discontinuity between the slab and the soil due to effects such as slab curling are minimized, freestanding, foundationless cranes impose tensile, uplifting forces bearing directly onto the slab-on-grade. The assumption of a Winkler model (and therefore the assumption of continuous contact) for this type of loading condition dramatically overstates the tensile resistance provided to the slab from the subgrade. Notably, modern design methods for slabs-on-grade do not consider any type of uplifting effects, and only considers compressive forces (e.g., concentrated, strip loads, and uniformly distributed loads).

Historically, researchers have simplified the subgrade in structure-soil interaction problems to that of a Winkler spring model or a Boussinesq half-space model. While both models are linear interpretations of an ultimately non-linear medium, the Boussinesq half-space model idealizes the subgrade as an elastic block characterized by the modulus of elasticity, while the Winkler spring model idealizes the subgrade as a series of springs characterized by the modulus of subgrade reaction. The values of either parameter are typically determined via in-situ or laboratory soil testing through methods including cone penetration tests, standard penetration tests, consolidation tests, etc., but have also been approximated based on the soil classification (i.e., from soil classification systems such as the USCS, AASHTO, etc.) of the subgrade medium.

For slabs resting on Winkler soil mediums, Hertz (1884), Wyman (1950), Reissner (1955), and Westergaard (1926, 1943, 1948) produced analytical solutions for the deflections and critical stresses due to a concentrated load. In particular, Hertz and Wyman provided the initial profiles of slab deflection, Reissner investigated the effects of the distributed area of the concentrated loads, and Westergaard produced the critical tensile stresses at the bottom surface under the concentrated load. For slabs resting on a Boussinesq elastic half-space medium, Biot (1935), Hogg (1938), Gorbunov-Posadov (1940, 1959, 1961), Cheung and Zienkiewicz (1965), Selvadurai (1979), and Hu and Hartley (1994) were all responsible for contributing to the development of deflection profiles and contact stress profiles. In particular, Biot and Hogg presented the initial deflection profiles close to the loaded region, Gorbunov-Posadov and Selvadurai expanded the deflection profile to significant distances away from the loaded region, and Cheung and Zienkiewicz and Hu and Hartley provided deflection profiles and stress profiles for finite slabs of systems with various stiffness.

The mains gaps in literature have been identified as follows:

- Modern methods of slab-on-grade design are based on road and pavement design and do not consider any uplifting forces imposed on the slab.
- In these methods, the soil is idealized as a Winkler soil, and a continuous contact is assumed between the slab and the soil. Therefore, the soil overstates the tensile resistance provided to the slab.
- In general, designers familiar with contemporary slab-on-grade design are familiar with the modulus of subgrade reaction of a given soil medium, but not the modulus of elasticity of the same soil medium. Moreover, in practical applications, the modulus of elasticity of soil must be determined through typically unavailable geotechnical investigations of in-situ soil.
- Limited analysis of slabs-on-grade of finite length are available in literature.

In this study, slabs-on-grade supporting combined compressive and overturning moments are investigated. The characterizing parameter of the Winkler model – the modulus of subgrade reaction – is linked to the modulus of elasticity, which is the characterizing parameter of another simplified soil model that accounts for uplifting forces acting on a slab. An extensive parametric study investigates the effects of various slab-soil properties and loading conditions on the moment capacity of a slab-on-grade.

3.0 Representative Model (Finite Element Formulation)

This section discusses the assumptions made and the process taken in modelling a finite element representation of a freestanding jib-crane mounted directly to a partition of unreinforced concrete slab resting atop a soil medium. The finite element model was created in the finite element software Abaqus, a standard commercial software for the application of finite element analysis (MathWorks, 2012). The representative model was broken down into several components, including the soil block, the slab, the baseplate, and the crane structure composed of a mast and stiffeners. Figure 3.1 shows a real, slab-mounted, foundationless jib crane, and Figure 3.2 shows the modelled FE model:

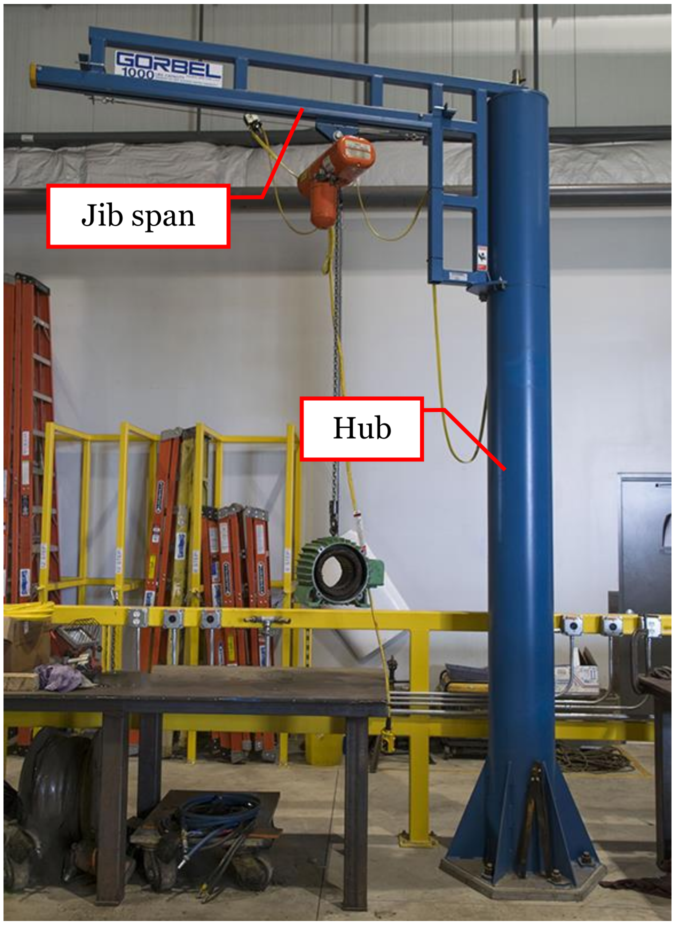

Figure 3.1: Real slab-mounted jib crane (Gorbel, 2012)

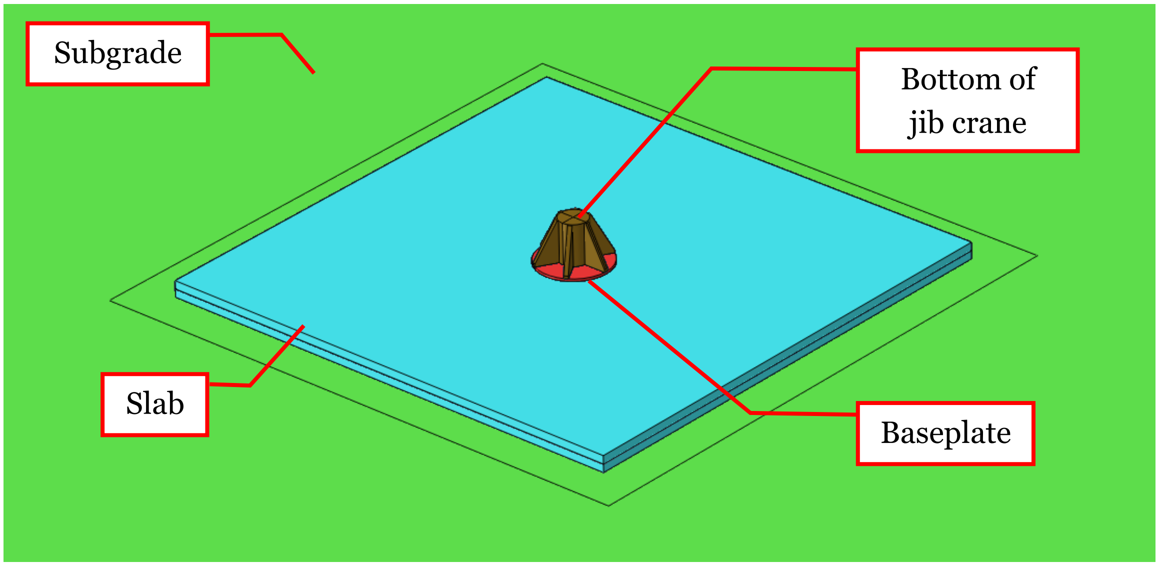

Figure 3.2: Representative finite element model

In Figure 3.2, the soil is modelled as the green block (extents not shown for clarity), the concrete slab is modelled as the blue part, the baseplate is modelled as the red circular part, and the base of the crane is modelled as the brown part.

3.1 Model Parameters

For various compressive loading cases, the methods presented by the American Concrete Institute (PCA, WRI, and COE) consider the compressive loading, area over which the load is distributed, subgrade strength, concrete strength, and slab thickness as prominent variables. In this study, the overturning moment and length of slab will also be included as variables to be considered. In particular, all but the overturning moment will be considered as independent variables while the overturning moment will be considered the dependent output variable to be investigated. The goal will be to establish the nominal moment capacity of any particular slab-soil configuration and material properties.

3.1.1 Overturning Moment

The overturning moment acting on the slab is the dependent output parameter investigated in this study and can be defined as the load carried by the crane multiplied by the lever arm (length of its jib). Typical, freestanding jib cranes have maximum load capacities ranging between 600 – 4500 N, with typical jib lengths ranging between 2400 – 4800 mm. Including the weight of the jib beam, typical overturning moments range between 2 – 25 kNm (Gorbel, 2012; Spanco, 2018). Table 3.1 shows some of the maximum moments licensed for jib cranes by the crane manufacturing company Gorbel:

Table 3.1: Maximum moment associated with jib cranes, from Gorbel (2012)

Load lbs.	Hub ft.	Span ft.	Mf lbs.-ft	Mf kNm
150	8	8	1200	1.63
150	8	10	1500	2.03
150	10	16	2400	3.25
150	12	16	2400	3.25
250	8	8	2000	2.71
250	12	10	2500	3.39
250	8	16	4000	5.42
250	12	14	3500	4.75
250	10	16	4000	5.42
250	12	16	4000	5.42
500	8	8	4000	5.42
500	10	14	7000	9.49
500	10	16	8000	10.85
500	12	16	8000	10.85
1000	8	8	8000	10.85
1000	10	8	8000	10.85
1000	10	14	14000	18.98
1000	12	16	16000	21.69

In Table 3.1, the load refers to the maximum capacity that the jib crane is licensed to carry. The hub refers to the vertical height of the crane, while the span refers to the maximum lateral distance that the load can be from the center of the hub.

3.1.2 Slab Thickness

The minimum slab thickness required by crane manufacturers is 150 mm (Gorbel, 2012; Spanco, 2018). However, the actual thickness of a particular warehouse floor can be considered to be largely unknown due to a variety of factors during construction (e.g., unevenness of the subgrade, uneven concrete pouring, etc.). In this study, a uniform thickness within a range (100 – 200 mm) was considered to capture a wider variety of thickness effects.

3.1.3 Concrete Specified Strength

The minimum specific strength of concrete required by crane manufacturers is 3000 psi (i.e., approximately 20 MPa) (Gorbel, 2012; Spanco, 2018). Typical values of concrete strength have been considered and range between 20 – 60 MPa for minimum strength and high strength concrete, respectively.

3.1.4 Slab Length

In this study, the length of slab refers to the distance between opposing joints of a slab-on-grade. For conservativeness, it is further assumed that slab joints (dowels, partially continuous connections, etc.) provide zero load carrying or load transfer capabilities, and that any particular partition of slab is discontinuous and free at its edges. In particular, a partition of slab is assumed to be able to freely deflect vertically and rotate at its edges. The joint spacing recommended by the American Concrete Institute is based on the thickness of the slab and the compressive strength of concrete, summarized in Figure 3.3:

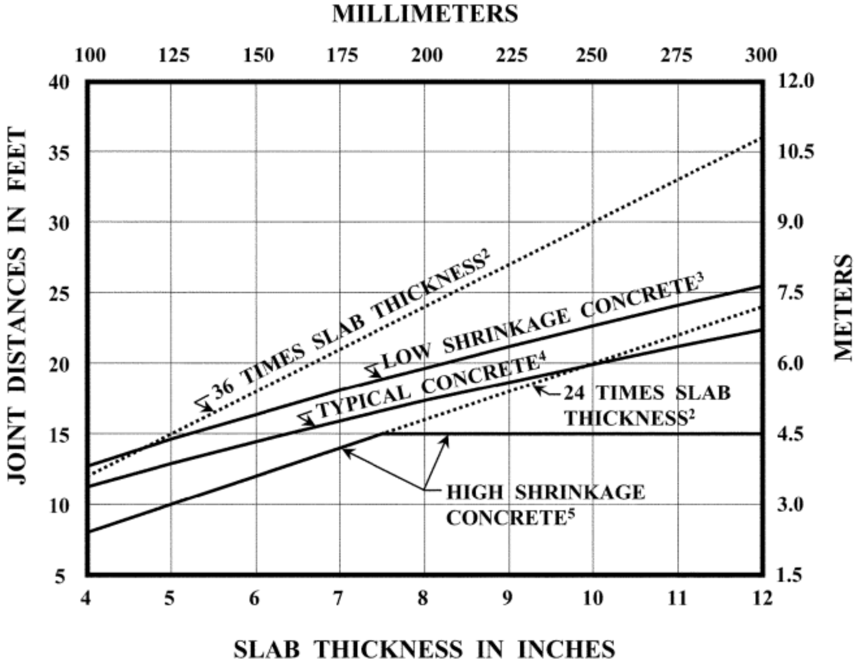

Figure 3.3: Recommended joint spacing based on slab thickness and concrete strength (McKinney et al., 2006)

The crane manufacturer Spanco requires a minimum 120 square-foot area, or an approximate square area with side lengths of 3400 mm on which a crane may be installed upon (Spanco, 2018). The crane manufacturer Gorbel requires that the crane to be installed a minimum of 1200 mm from any wall or joint (Gorbel, 2012). As the range of slab thicknesses previously identified lies between 4" – 8", and the range of concrete compressive strengths may be either low or high strength, the range of slab lengths considered in this study, based on Figure 3.2 and the requirements listed by Gorbel and Spanco, range between 12.5' – 20' (approximately 3700 – 6000 mm).

3.1.5 Soil Capacity

The minimum soil bearing capacity required by crane manufacturers is 2500 psf (Gorbel, 2012; Spanco, 2018), or a modulus of subgrade reaction of approximately 175 psi/in (McKineny et al., 2006). As the strength of the soil is difficult to characterize and approximated at best, a range of subgrade strengths (bearing capacities between 2000 – 3000 psf, or moduli of subgrade reaction between 130 – 230 pci) were considered. The equivalent modulus of subgrade reaction based on the required bearing capacity values were determined via Figure 2.15 provided by the American Concrete Institute.

3.1.6 Vertical Compressive Force

The vertical compressive force can be defined as a combination of the crane's self-weight and the load carried by the jib. Typical, freestanding jib cranes have total compressive loads ranging between 2000 – 11000 N (Gorbel, 2012). Table 3.2 shows some of the maximum compressive force licensed for jib cranes by the crane manufacturing company Gorbel:

Table 3.2: Maximum compressive force associated with jib cranes, from Gorbel (2012)

Load lbs.	Hub ft.	Span ft.	Pf lbs.	Pf kN
150	8	8	540	2.40
150	8	10	561	2.50
150	10	8	577	2.57
150	12	14	780	3.47
150	10	16	784	3.49
150	12	16	829	3.69
250	8	8	711	3.16
250	10	16	956	4.25
250	12	16	1141	5.08
500	8	8	1018	4.53
500	10	8	1063	4.73
500	12	14	1546	6.88
500	10	16	1547	6.88
500	12	16	1809	8.05
1000	8	8	1631	7.26
1000	10	8	1698	7.55
1000	8	10	1702	7.57
1000	8	16	2271	10.10
1000	10	16	2300	10.23
1000	12	14	2350	10.45
1000	12	16	2450	10.90

In Table 3.2, the load refers to the maximum capacity that the jib crane is licensed to carry. The hub refers to the vertical height of the crane, while the span refers to the maximum lateral distance that the load can be from the center of the hub. The total vertical load includes both the maximum capacity of the crane and its self-weight.

3.1.7 Baseplate Dimensions

The size of baseplates and masts are reflective of the maximum capacity and arm length they are licensed to carry. In particular, baseplate dimensions are of importance because they govern the area over which vertical forces are transferred into the slab as a bearing pressure. In this study, it is assumed that the mast of a crane is equivalent to a solid or HSS column, and therefore the crane superstructure can be likened to that of a column-baseplate system. In this manner, it can be assumed that for any particular size of baseplate, the diameter of a circular mast has no significant effect on the load that the concrete bears; while the axial force is distributed from the column end to the column baseplate in direct bearing, the baseplate is assumed to distribute the axial force to the concrete as a uniform bearing pressure (Thornton et al., 2011). Therefore, an assumption can be made that the concrete bearing pressure is affected solely by the size of the baseplate.

In general, crane manufacturers have their own discrete dimensions used for any particular crane specification. In this study, Gorbel's WSJ360 foundationless, freestanding cranes have been investigated (Gorbel, 2012). The baseplates used include a square plate of length 15" (i.e., approximately 375 mm) and various hexagonal plates with vertex-to-vertex diameters ranging from 30 – 36" (i.e., approximately 750 – 900 mm), shown in Figure 3.4:

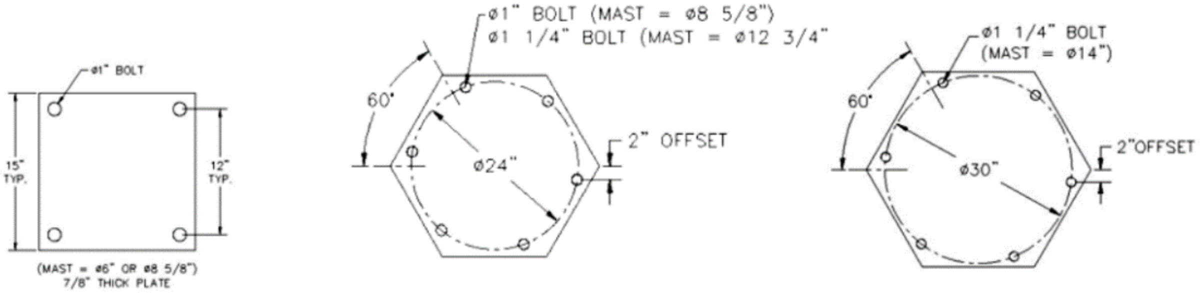

Figure 3.4: Sample of baseplates (Gorbel, 2012)

To simplify and remain consistent, all baseplates in this study were modelled as equivalent circular baseplates with an equivalent area. Equivalent circular baseplate diameters considered in this study ranged between 18 – 36", or approximately 450 – 900 mm, shown in Figure 3.5:

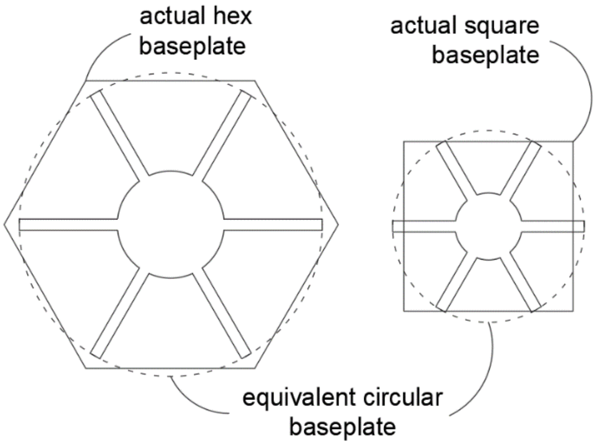

Figure 3.5: Equivalent circular baseplate for hexagonal and square baseplates

For consistency, the diameter of the circular mast used in this study was approximately 35% of the diameter of an equivalent circular baseplate. Six stiffeners were also provided.

3.2 Material Properties

All materials used in the finite element model (concrete, steel, and soil) were assumed to be perfectly linear elastic as the serviceability limit state governs the design of the slab. The stress-strain relationships of steel and soil were not of particular interest as it was assumed that the critical failing mechanism of the system would be the concrete in tensile failure. Failure of the steel anchors and soil are out of the scope of this study, though they can be easily checked by readily available design aids, including A23.3-14 Annex D and Section 9 of the Canadian Concrete Handbook, respectively, for anchorage analysis and soil bearing capacity effects (Adebar et al, 2017). Buckling of the steel baseplate, stiffeners, and mast of the crane were outside of the scope of this study and not expected to occur.

3.2.1 Concrete

The stress-strain relationship of concrete was assumed to be linear-elastic up until the first cracking in either compression or tension and defined by its specific compressive strength. The modulus of elasticity was determined by the compressive strength through the use of clause 8.6.2.2 in the Canadian Concrete Handbook (Adebar et al, 2017):

$$E_c = \left(3300\sqrt{f'_c} + 6900\right)\left(\frac{\gamma_c}{2300}\right)^{1.5} \tag{3.1}$$

in which γ_c is the unit weight of concrete and assumed to be 2400 kg/m^3 and f'_c is the specific compressive strength of concrete.

In this study, compressive failure was assumed to be the least critical failure mode and as a result was not considered.

In tension, failure was assumed to occur whenever the maximum principal stresses observed exceeded the tensile yield stress defined by the concrete's modulus of rupture. The modulus of rupture was determined through clause 8.6.4 in the Canadian Concrete Handbook (Adebar et al, 2017):

$$f_r = 0.6\gamma\sqrt{f'_c} \tag{3.2}$$

where γ is the modification factor for concrete density and assumed to be 1 (Adebar et al, 2017).

This failure mode is based on the maximum principal stress theory of failure and was selected in this study as plain, unreinforced concrete exhibits brittle behaviour in tension, shear stresses developed in the slab were assumed to have negligible impact, and because the concrete was assumed to be isotropic.

The stress-strain relationship for concrete in tension used in this study is shown in Figure 3.6:

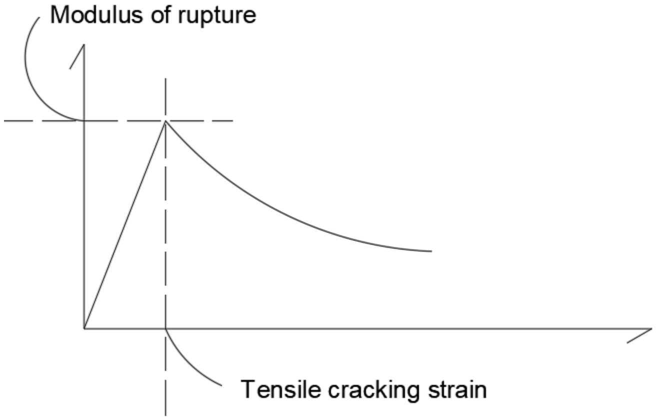

Figure 3.6: Stress-strain curve of concrete in tension

In Abaqus, concrete was defined using a modulus of elasticity (variable, dependent on assigned specific compressive strength) and a typical Poisson's ratio of 0.2 (Adebar et al., 2017).

3.2.2 Steel

In Abaqus, steel was defined using a typical modulus of elasticity of 200,000 MPa and Poisson's ratio of 0.2 (Wong et al., 2015).

3.2.3 Soil

In Abaqus, soil was defined using a modulus of elasticity (variable, dependent on assigned specific modulus of subgrade reaction). It was assumed that a Poisson's ratio of 0.2 was an adequate representative value for most soil types (Selvadurai, 1979).

3.3 Finite Element Model Definition

3.3.1 Pseudo-Infinite Elastic Half-Space Soil

The soil medium was idealized as an isotropic, homogeneous, linear-elastic half-space that spans infinitely in the lateral and downward directions and can be characterized by a modulus of elasticity and Poisson's ratio. The conscious decision to model the subgrade as an elastic half-space over a Winkler spring model is explained in detail in previous sections of this work.

The half-space was modelled using 8-node linear solid hexahedral elements with reduced integration (C3D8R) and enhanced hourglass control. The soil was expected to take on a very simple geometry in the form of a rectangular prism or cube, and therefore, hexahedral (brick) elements were selected over tetrahedral (triangular) elements (which are more appropriate for complex geometries with curves, acute angles, and the like). Linear elements were selected over quadratic elements as the subgrade was deep enough such that a sufficient number of elements could be provided in the thickness (Abaqus recommends a minimum of four elements in the thickness of any body in flexure) (Abaqus, 2012). Additionally, the mesh density of the subgrade primarily impacted the convergence of deflections rather than stresses; the stresses developed in the soil was not part of the scope of this study, and a simply defined subgrade was considered sufficient. While it should be noted that a variety of element types could be feasibly used with the same degree of accuracy (such as linear brick elements with full integration, linear incompatible elements, quadratic elements with full or reduced integration, any of the tetrahedral elements, etc.), the selected element type (C3D8R) was considered the most appropriate fit. As the subgrade is expected to behave as if it spanned infinitely, modelling the subgrade as a cylinder was also considered, but was ultimately found to not have any significant impact on reducing the total number of required elements.

An infinitely spanning subgrade cannot be feasibly or practically modelled; in this case, a subgrade with finite dimensions that behaves as if it were infinitely spanning (i.e., the response of the finite subgrade is in good agreement with the theoretical response of an infinite subgrade) is required. In particular, the modelled finite subgrade must behave infinitely when supporting a slab of any particular size loaded by a concentrated force and its own self-weight. This can be achieved by either making use of Abaqus' solid infinite elements (CIN3D8, amongst others) or by selecting adequate subgrade dimensions and boundary conditions that facilitate convergence of deflections and stresses. The latter method was selected due to simplicity in the modelling and simulation process.

Figures 3.7 and 3.8 show the convergence of the maximum deflection and stress observed in the soil for various subgrade dimensions and boundary conditions.

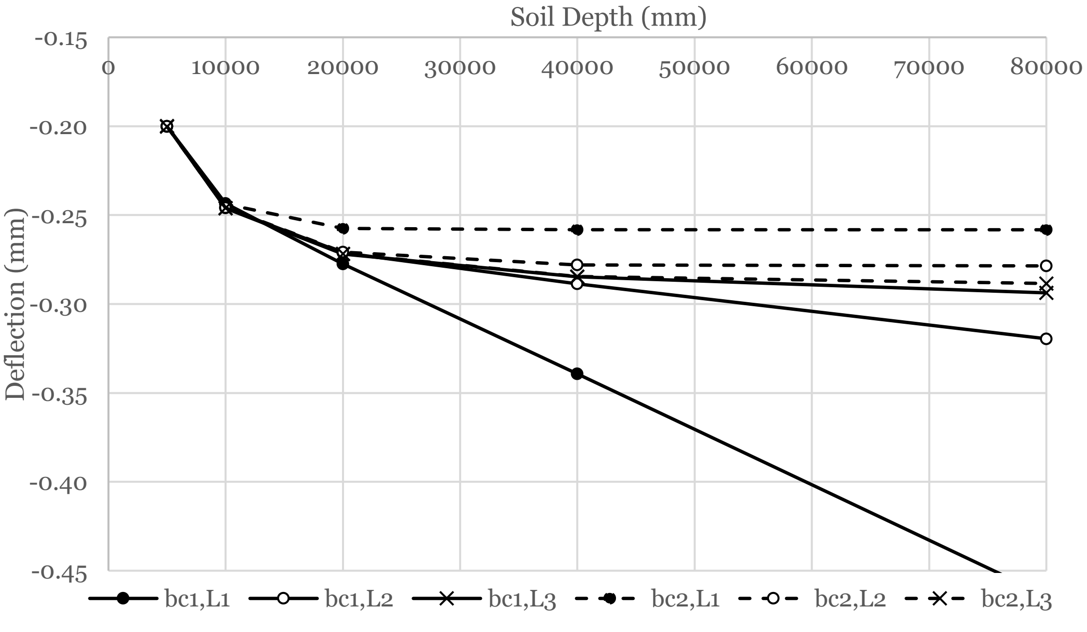

Figure 3.7: Maximum deflection observed in a slab resting on various soil depths, soil lengths (L_1 = 20,000 mm, L_2 = 40,000 mm, L_3 = 80,000 mm), and soil boundary conditions (bc$_1$ and bc$_2$ refers to either free or pinned boundary conditions, respectively prescribed to the subgrade's lateral faces)

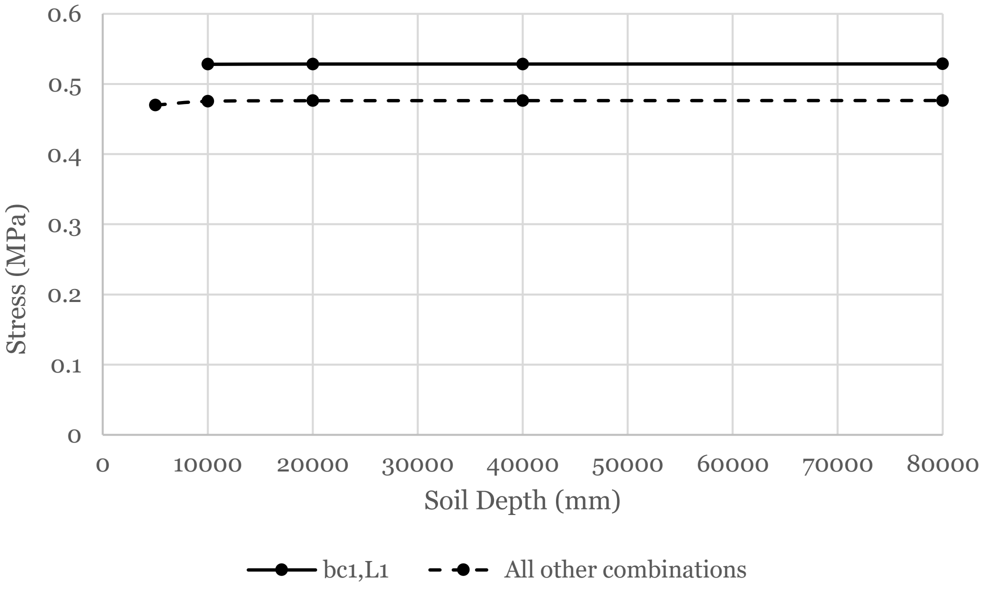

Figure 3.8: Maximum stress observed in a slab resting on various soil depths, soil lengths (L_1 = 20,000 mm), and soil boundary conditions (bc_1 and bc_2 refers to either free or pinned boundary conditions, respectively prescribed to the subgrade's lateral faces)

In these tests, two types of boundary conditions (bc_1 = free, bc_2 = pinned) were considered at the lateral faces of the subgrade. The bottom of the subgrade was always considered pinned. Five different subgrade depths (5 m, 10 m, 20 m, 40 m, and 80 m) and three different subgrade lengths (20 m, 40 m, 80 m) were considered in order to illustrate the effects of convergence. Solid lines represent soils bounded laterally by free conditions while dotted lines represent soil bounded by pinned conditions. Note that the boundary conditions are applied at the face of the soil – in this manner, a pin condition is equivalent to a fixed condition in the sense that rotation has been constrained. This is due to the definition of a three-dimensional solid element in Abaqus (nodes of these elements cannot rotate) (Abaqus, 2012). For clarity, if a pinned end with the ability to rotate is desired, as is the case for a simply supported plate, then the pinned end condition must be applied to an edge or one-dimensional line of nodes rather than a face or two-dimensional set of nodes. It is clear that both a sufficient subgrade depth and subgrade length is required for convergence. In particular, it can be seen that an unbounded subgrade approaches convergence from, and a bounded subgrade with pinned sides approaches convergence from above with respects to subsequent increases in length and depth. It is expected that continuing to increase both the subgrade depth and length to approach an infinite subgrade will yield results somewhere in-between the bounded and unbounded subgrades.

Considering a subgrade with dimensions larger than 40 m begins to create prohibitive computational times. As a result, a laterally pinned subgrade ($u_x = u_y = u_z = 0$) with a length of 40 m and depth of 20 m was considered. The bottom face of the subgrade was also pinned ($u_x = u_y = u_z = 0$). The deflections for a subgrade with these dimensions were within 6% of the 'converged' values for a subgrade with dimensions of 80 m x 80 m x 80 m and was considered adequate for the purposes of this study. Asides from the case of an unbounded subgrade with a length of 20m, the stresses observed in the slab yielded insignificant changes with changes to the subgrade dimensions or lateral boundary conditions.

Figure 3.9 shows the selected dimensions and boundary conditions used to model the soil:

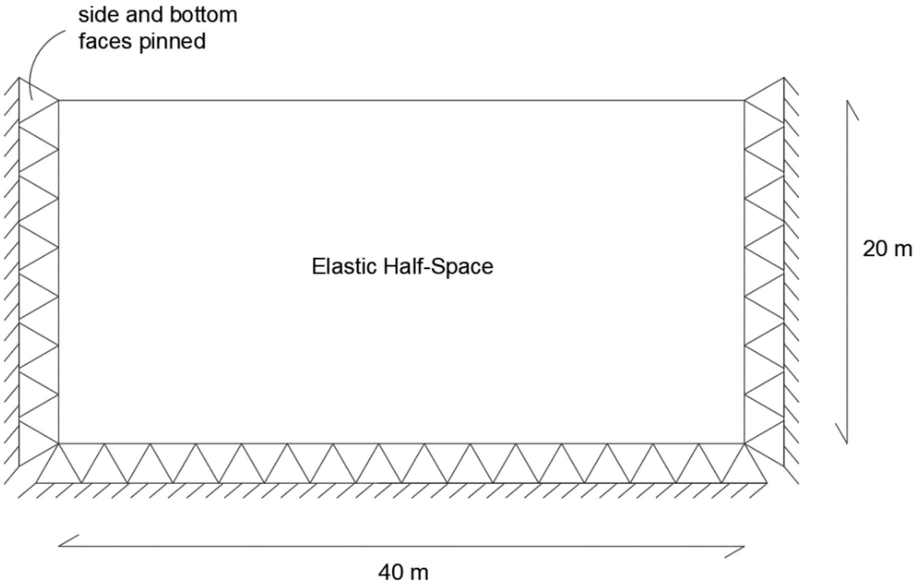

Figure 3.9: Boundary conditions of elastic half-space, 2D side view

Figures 3.10 to 3.12 depict the three-dimensional view, top-down view, and side view of the elastic half-space and meshing pattern used:

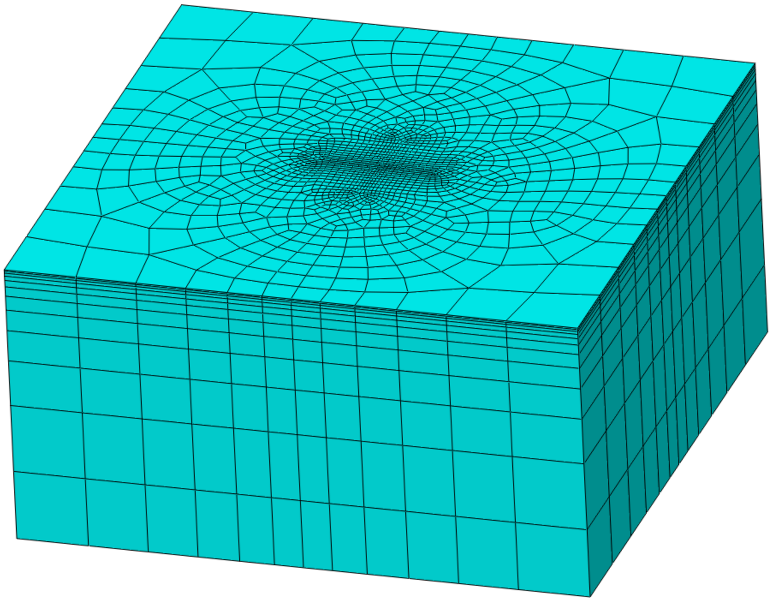

Figure 3.10: Mesh of elastic half-space, 3D view

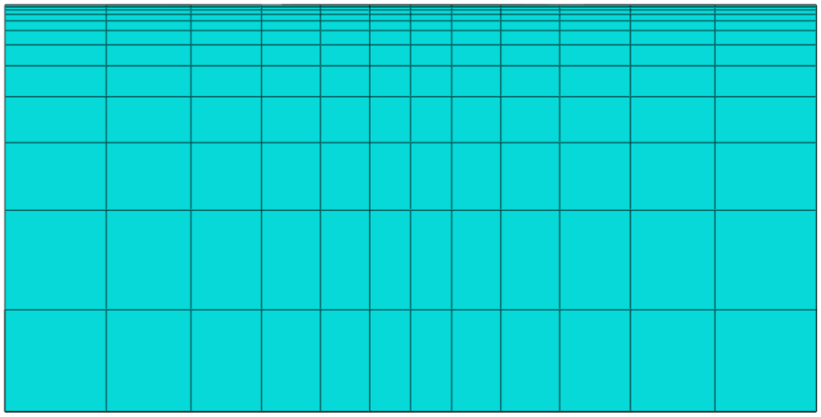

Figure 3.11: Mesh of elastic half-space, 2D side view

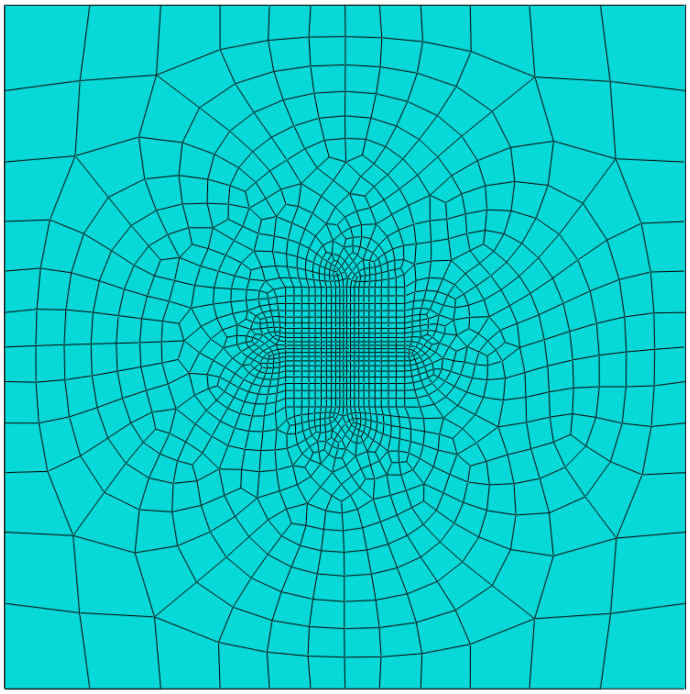

Figure 3.12: Mesh of elastic half-space, 2D top-down view

It can be seen that a highly varied mesh pattern was employed in the subgrade. In general, the meshing philosophy was as follows: 1) use a fine mesh density in areas of concern (i.e., regions of contact between the slab and subgrade and areas in which deflections and stresses were of importance) in order to achieve simulation convergence and accuracy of results, and 2) use a coarse mesh density in areas not of concern in order to reduce the total number of elements and computational time and effort.

In the thickness, element sizes varied linearly from 1000 mm at the bottom to 100 mm at the top surface. A square partition with a side length of 7000 mm (greater than the maximum considered slab length) was created at the center of the subgrade. This area was meshed more densely than other areas because it was an area of concern and an area of contact. Within this partition, the element size varied linearly between 500 at the corners to 200 at the center.

It was assumed that settlement and consolidation of the soil due to its self-weight and the weight of any pre-existing structures had already taken place, and therefore no weight was assigned to the soil.

3.3.2 Two-Way Concrete Slab

The concrete slab is idealized as an isotropic, homogenous, linear-elastic concrete plate that can be characterized by a modulus of elasticity and Poisson's ratio. The slab was modelled using conventional 4-node linear quadrilateral shell elements (S4R) with reduced integration. Shell elements were selected over solid elements (of any type; i.e., linear or quadratic hexahedral or tetrahedral solids) because the considered thicknesses of the slab (ranging between 100 – 200 mm) were significantly smaller than the considered lengths of the slab (ranging between 3800 – 6000 mm) and because shell elements perform significantly better than their solid counterparts in bending-dominated problems such as this one when the effects of shear deformation can be considered negligible.

In bending-dominated problems, three-dimensional linear elements may suffer from hourglassing effects or shear locking, which either causes over- or under-prediction, respectively, of deflections and/or stresses. While these phenomena can be addressed, solutions typically involve increasing the number of solid elements in the thickness (Abaqus recommends a minimum of 4 linear elements in the thickness for bending-dominated problems) or by selecting more complex and computationally heavy elements (such as three-dimensional quadratic elements) (Abaqus, 2012).

Consider the simplified case of a plate fixed on all four sides subject to a concentrated load distributed over a small radius at midspan (8b. in Table 11.4 of Roark's Stress and Strain Handbook). Figure 3.13 and 3.14 shows the maximum deflections and stresses observed in a finite element model of the problem using a varying number of total elements compared the analytical solution provided by Roark (Young and Budynas, 2002).

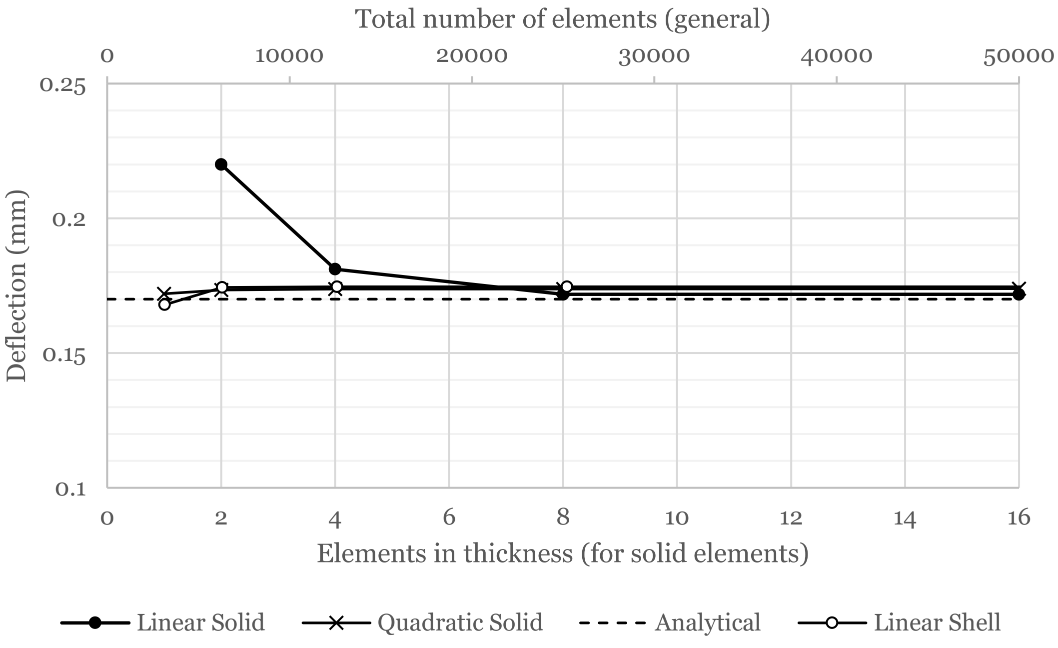

Figure 3.13: Number of elements versus the maximum observed deflection for a clamped plate subject to a concentrated load distributed over a small central circle

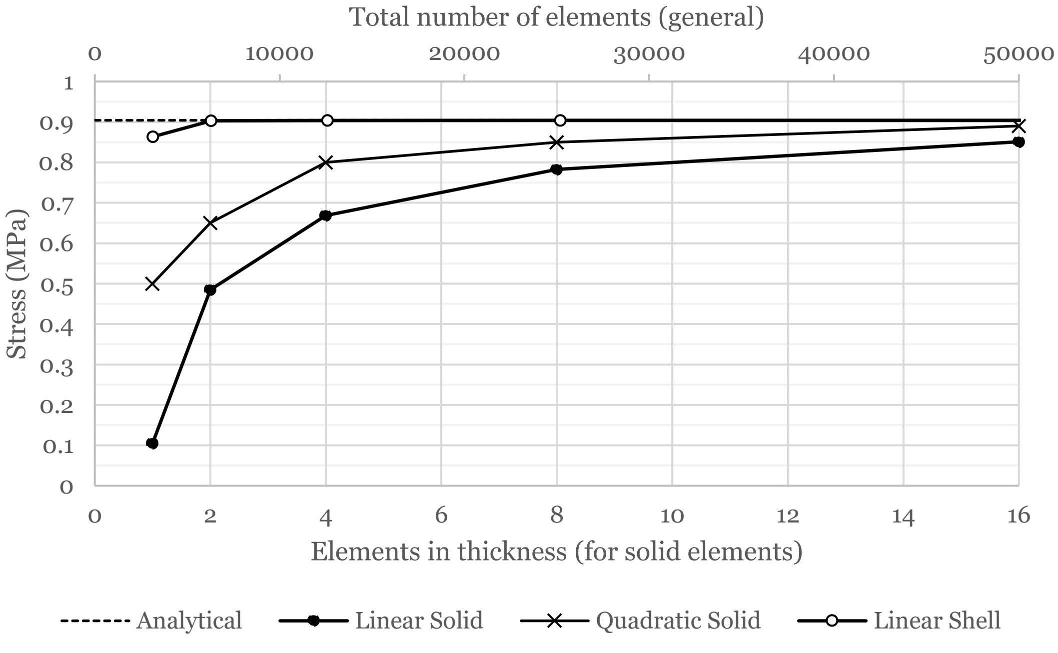

Figure 3.14: Number of elements versus the maximum observed stress for a clamped plate subject to a concentrated load distributed over a small central circle

As expected, there is a minimum number of three-dimensional elements (<15,000) is required to converge to the analytical stresses. An inordinate number of three-dimensional linear (50,416) or quadratic (25,208) elements are required to converge to within 5% of the analytical stresses. Conversely, with the same top-down mesh used as the three-dimensional solids, shell elements readily converge to the analytical solution for both deflections and stresses. Notably, increasing the number of three-dimensional elements to obtain accuracy within 5% becomes prohibitive in regard to computational time. For instance, providing 16 quadratic elements in the thickness resulted in a 30-minute simulation time (for clarity, 8 quadratic elements resulted in several minutes of simulation time). When considering that the example problem tested is very simple (one part, one distributed load, no contact interfaces, basic boundary conditions, etc.), the use of shell elements for the slab when considering the slab-soil system as a whole became attractive.

Additionally, three-dimensional solid elements uniquely suffer from numerical singularity issues (areas of stress concentrations that increase with increasing mesh density) that often arise from the application of highly concentrated loading patterns and from bodies in contact. While typical solutions for singularities involve ignoring them (if possible), it is expected that stress singularities will build up in areas of concern (specifically, at the top surface of the slab in contact with the crane, with singularities induced by tensile forces produced by the embedded anchor bolts). Therefore, to consider stresses in both the top and the bottom of the slab, shell elements were selected.

Figure 3.15 shows a top-down view of the mesh used. Figure 3.16 shows a close-up view of the slab's expected contact interface with the crane.

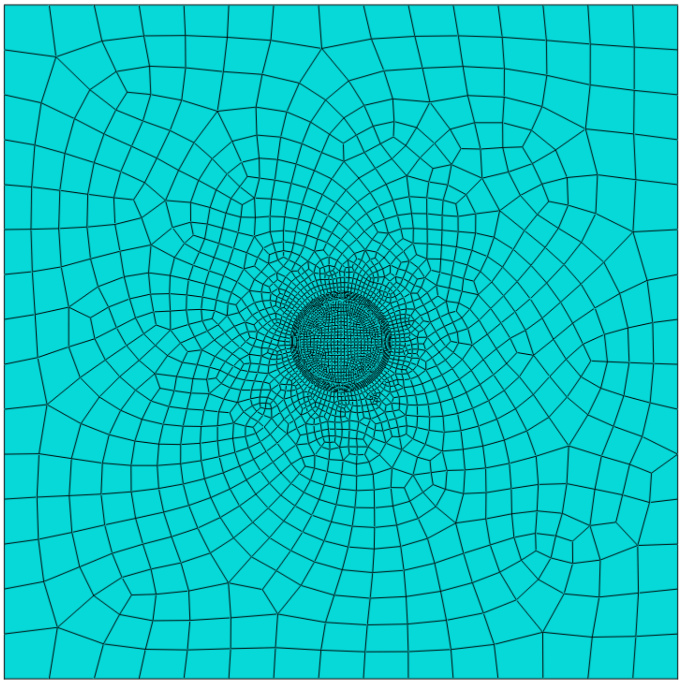

Figure 3.15: Mesh of slab, 2D top-down view

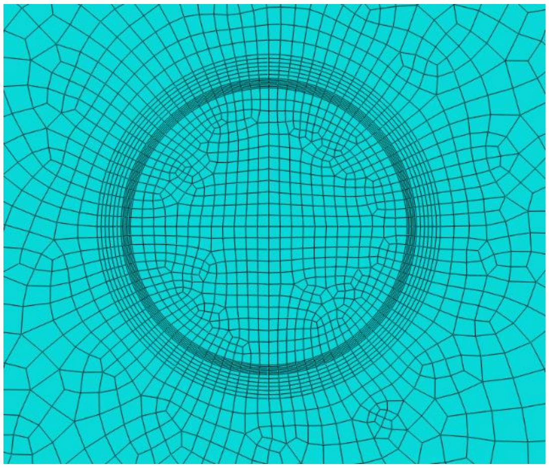

Figure 3.16: Mesh of slab interior partition, 2D top-down view

It can be seen that, like the subgrade, a highly variable mesh pattern was employed akin to the subgrade. Again, a fine mesh density was provided to areas of concern, while a coarser mesh was used in areas not of concern. Element sizes of 400 mm were provided along the sides of the slab. A circular partition with a radius equal to the radius of the modelled baseplate was created in the area of the slab and was used as an area of contact between the slab and the crane. This area was meshed significantly more dense than other areas because it was the most critical (an area of concern and an area of contact). The circular partition itself is composed of three parts: an outer ring, a very dense inner ring, and the interior circle. In general, the outer rings required the densest mesh composition, because it was expected that critical stresses would build up in the circular embedded bolt pattern and the edges of the baseplate. The exterior ring was meshed with elements sized 30 mm x 10 mm, while the inner ring was meshed with elements sized 30 mm x 5 mm. The interior circle was meshed with elements sized 30 mm. This contact interface between the slab and the crane is discussed in further detail in Section 3.3.4.

Any existing joints were assumed to be cracked and provide no additional load transfer or support; therefore, the sides of the slab were assumed to be free (the slab is supported solely by the subgrade). Vertical deflection and all rotations at the edges were unrestrained, but lateral displacement restraints ($u_x = u_y = 0$) were provided at the edges to prevent instability in the event of any lateral sliding effects.

The slab's self-weight is important as it acts as a dominant counterbalance to the induced overturning moment. The self-weight was assumed to be 2400 kg/m^3 and was applied as a distributed body force volumetrically throughout the slab.

Figure 3.17 shows the boundary conditions and loading of the slab:

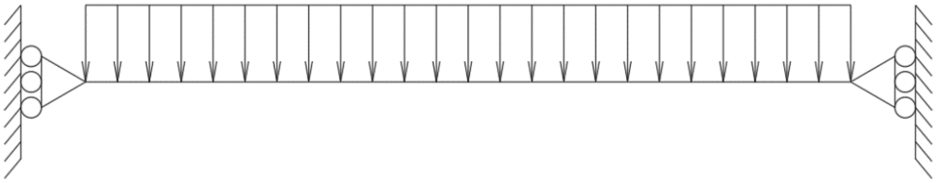

Figure 3.17: Loading and boundary conditions of concrete slab, 2D side view

While the slab diagram in Figure 3.17 appears unstable as its edges are restrained only by vertically-free pinned roller supports, in reality, the slab will also be supported continuoulsy along its bottom face by the subgrade.

3.3.3 Crane Superstructure

The crane, stiffeners, and baseplate have been idealized as isotropic, homogenous, and linear elastic steel solid component that can be adequately characterized by a modulus of elasticity and Poisson's ratio. In particular, it should be noted that only the bottom portion of the crane's mast was modelled, as modelling additional portions of the crane was not necessary and would only increase the required number of elements.

All three components were modelled using three-dimensional 8-node linear solid hexahedral elements with reduced integration (C3D8R) and enhanced hourglass control. The model geometry was not complex enough to warrant the use of tetrahedral elements. Linear elements were selected over quadratic elements as the superstructure was not of particular importance (mesh density is required solely for adequate transfer of forces and for contact), and a sufficient number of linear elements was provided in the thickness of all three components. Again, like the subgrade, a multitude of varying element types could have been used to adequately model the crane superstructure (i.e., such as the use of shell elements for the stiffeners and plate), but the use of linear elements was found to be the simplest when defining contact interactions between each individual component. All components were provided a simple tie constraint between one another. The tie constraint effectively acts as a welded connection.

The modelled mast height was 500 mm. The baseplate diameter was variable. The mast diameter was always taken as roughly 35% of the baseplate diameter. Figures 3.18 and 3.19 showcase the mesh of the mast and baseplate.

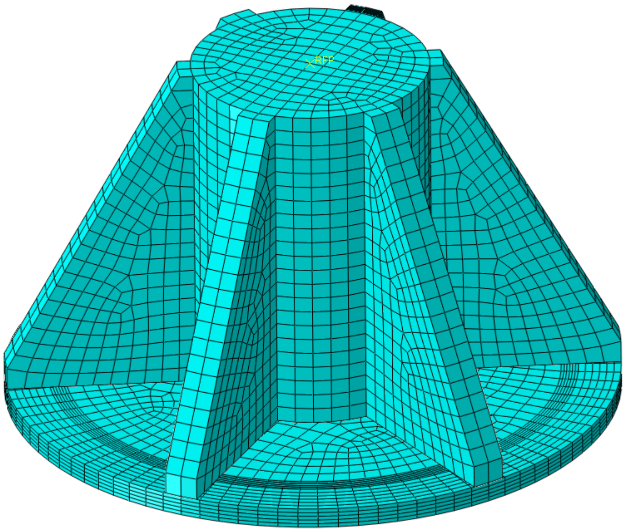

Figure 3.18: Mesh of mast, stiffeners, and baseplate, 3D view

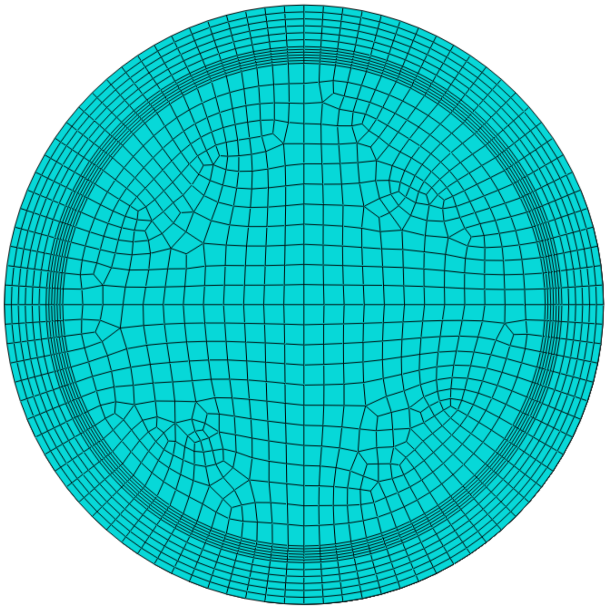

Figure 3.19: Mesh of baseplate, 2D top-down view

A fairly typical mesh pattern was employed for the modelled mast and stiffener. The mast and stiffener were meshed with elements of size 25 mm. The baseplate was meshed using the same pattern as the interior circular partition of the slab. This was done for adequate load transfer and simulation convergence at the contact interface. The exterior ring was meshed with elements sized 30 mm x 10 mm, while the inner ring was meshed with elements sized 30 mm x 5 mm. The interior circle was meshed with elements sized 30 mm.

The crane stability is achieved through a contact interface with the slab discussed later in Section 3.3.4. To prevent lateral slipping, lateral restraints ($u_x = u_y = 0$) were applied on a single edge of the baseplate; in this manner, by applying the restraint to one edge, the baseplate was still free to rotate about the x- and y-axis.

Both the axial load and overturning moment was applied to a reference point (marked “RFP” in Figure 3.20) that coupled the entire top surface of the modelled mast. Figure 3.20 additionally shows another view of the boundary conditions and loading conditions:

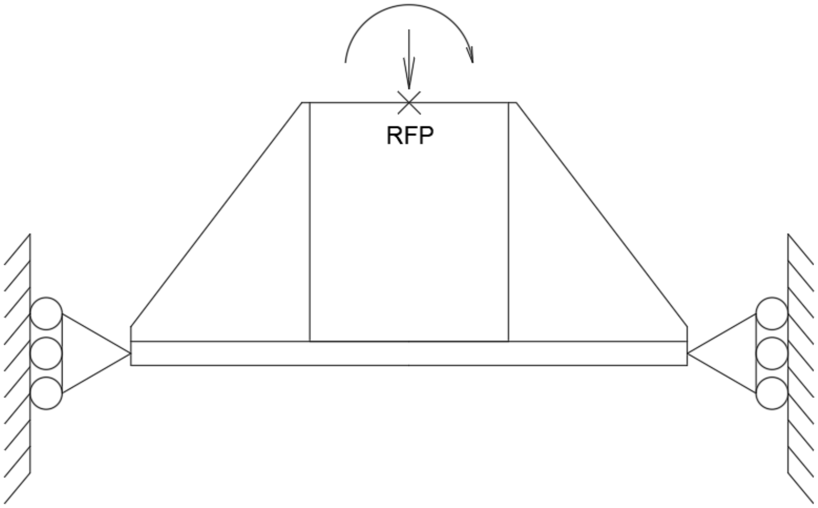

Figure 3.20: Loading and boundary conditions of crane superstructure, 2D side view

3.3.4 Contact Interaction

In Abaqus, contact interactions define how two or more bodies behave when in contact (Abaqus, 2012). Two regions with contact interfaces are identified in this study: one between the slab and the soil, and one between the baseplate and the slab.

3.3.4.1 Slab-Soil Interface

In order to avoid artificial stiffness in tension, a separation-based, hard contact interaction was defined between the slab and the soil that allows the slab to lift up off the soil given large uplifting forces. This contact was defined throughout the entirety of the bottom of the slab and the top portion of the partitioned subgrade.

3.3.4.2 Baseplate-Slab Interface

In reality, a foundationless jib-crane is mounted to a slab-on-grade via post-installed adhesive chemical anchors attached to a baseplate. After installation, the adhesive chemical bonds to both the steel anchor and the concrete it is embedded in, providing a chemical bond and frictional force when loaded in tension. To simplify and avoid modelling detailed bolt-to-concrete connections, the interface between the baseplate and the slab was modelled as a circular ring using a tied connection. The ring has a width equal to that of the diameter of the anchor bolts, and the ring’s center-to-center diameter is equivalent to the center-to-center diameter of the group of anchor bolts. The remaining portions of the contact interface between the baseplate and the slab was defined using a typical hard, separation-allowed interaction. Figure 3.21 shows the partitions used in defining contact:

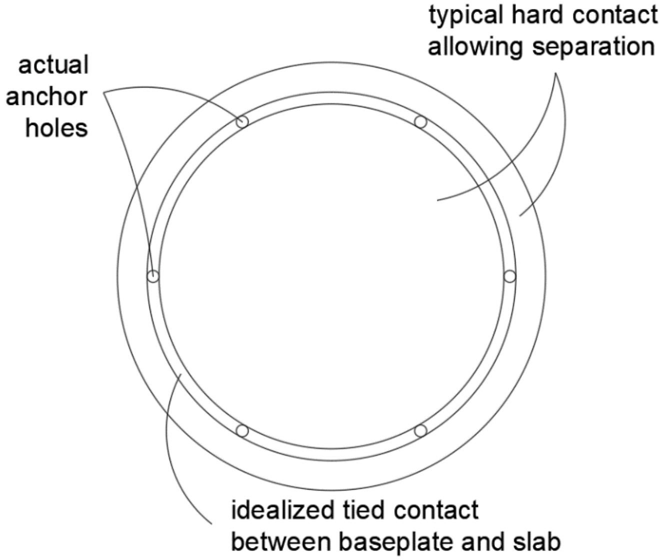

Figure 3.21: Contact partition definition between baseplate and slab

Here, the forces experienced by the anchor bolts are distributed to the partitioned ring. Notably, it is still expected that stress will congregate around the locations of the actual anchor bolts on the ring, as the initial transfer of forces from the crane to the baseplate is through the mast and stiffeners of the crane. For simplicity, it is assumed that the stiffeners are aligned with the locations of the anchor bolts (in reality, the anchor bolts are slightly offset from the stiffeners). Figure 3.22 visualizes this effect:

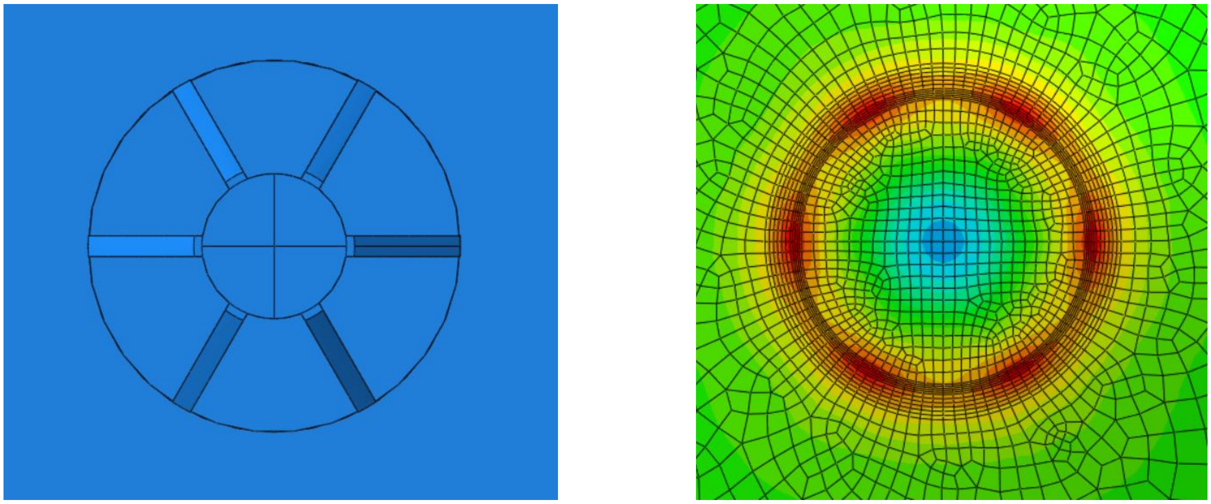

(a) (b)

Figure 3.22: Top-down view of (a) the slab, baseplate, and mast and stiffeners, and (b) maximum principal stress concentrations in contact partition between baseplate and slab

Figure 3.22 (b) was produced by applying a concentrated tensile force at the top of the mast. The baseplate is tied to the slab along the entirety of the partitioned ring, but as some of the force transfer is distributed from the mast to the baseplate through the stiffeners, stress concentrations appear around the locations of the stiffeners on the partitioned ring.

Figures 3.23 and 3.24 show the contact interface and the meshing used at the contact interface.

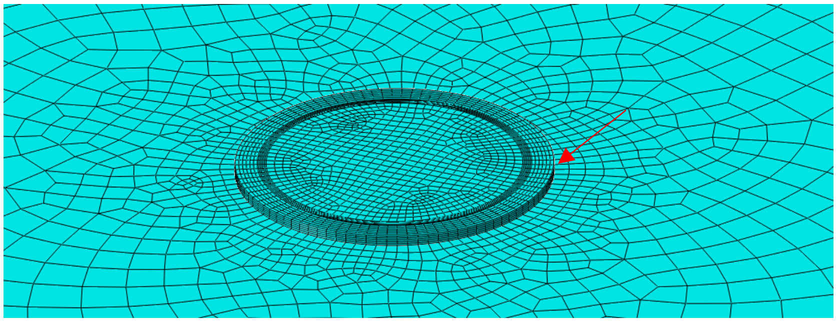

Figure 3.23: Contact interface between baseplate and slab, 3D view; marked by the red arrow

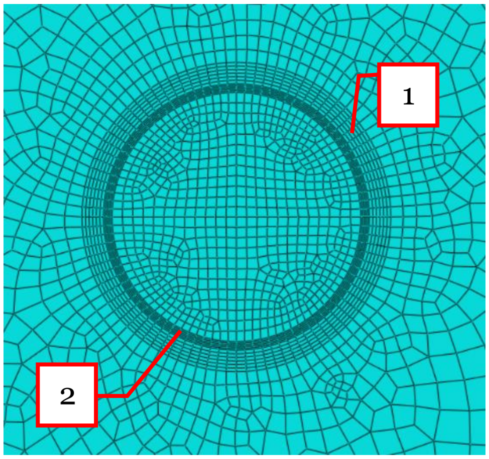

Figure 3.24: Mesh of contact interface between baseplate and slab, 2D top-down view; area marked as (1) is the outer edge of the baseplate; area marked as (2) is the inner circular ring

In particular, the two regions that are meshed finely (notated as (1) and (2) on Figure 3.24) are the outer edge of the baseplate and the circular ring described earlier in this section that ties the baseplate to the slab. The meshing pattern for this circular section is identical on both the slab and the baseplate to ensure adequate transfer and simulation convergence. In the outer ring defining the outer edge of the baseplate, an element size of 30 mm x 10 mm was provided. In the dense inner ring defining the tied connection between the baseplate and the slab, an element size of 30 mm by 5 mm was provided. The interior circle was meshed with an element size of 30 mm.

It was assumed that this idealization adequately represented the transfer of loads from the bolts to the concrete slab; again, for bolt-associated failure checks, the reader is directed to the various readily available design aids and software.

3.4 Verification & Validation

This section discusses the tests completed and methods used to verify and validate the finite element model. For verification, a local mesh refinement study was completed to show convergence of deflections and stresses in the critical regions. For validation, a simplified model consisting of the subgrade supporting a slab subject to a concentrated load distributed over a small, central area is compared against existing analytical and numerical solutions.

3.4.1 Mesh Refinement

Local mesh refinement is required to ensure that a given mesh is sufficiently dense at areas of concern in order to achieve convergence of stresses and deflections. Additionally, mesh refinement is also important for checking for the presence of any stress concentrations. In this finite element model, the mesh areas of concern are as follows:

1. Thickness of the baseplate,
2. Baseplate mesh at contact interface with slab,
3. Slab mesh at contact interface
4. Slab mesh immediately adjacent to contact interface between the baseplate and slab,
5. Subgrade mesh at contact interface with slab, and
6. Thickness of the subgrade.

The model was simulated several times with varying element densities at the areas of concern. Figures 3.25 to 3.27 depict the observed maximum stresses and deflections in the slab based on refinement of mesh densities to the baseplate, slab, and subgrade:

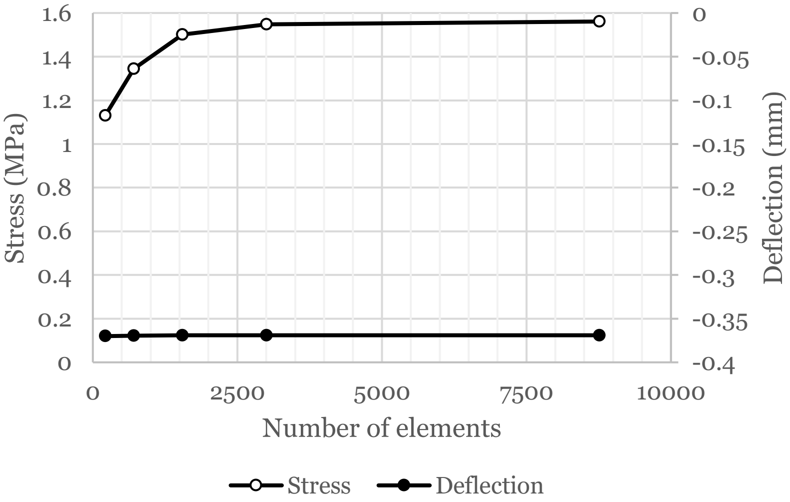

Figure 3.25: Number of elements used in the slab versus the observed maximum stress and deflection in the slab

Figure 3.26 shows that increasing the number of elements in the slab beyond 2500 resulted in negligible change in the critical stresses and deflections.

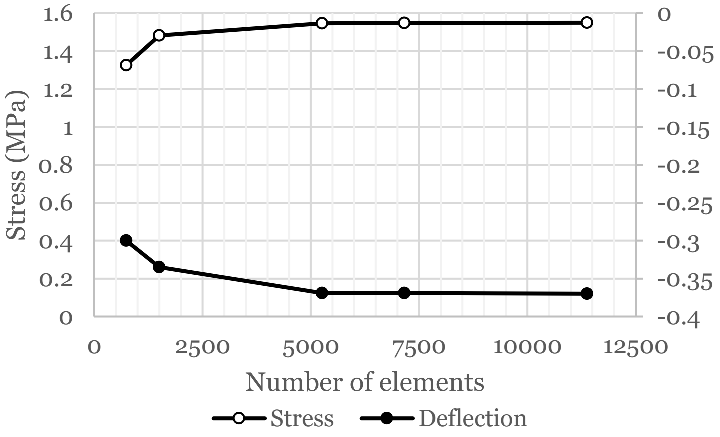

Figure 3.26: Number of elements used in the soil versus the observed (a) maximum stress, and (b) maximum deflection in the slab

Figure 3.27 shows that increasing the number of elements in the subgrade beyond 5000 resulted in negligible change in the critical stresses and deflections.

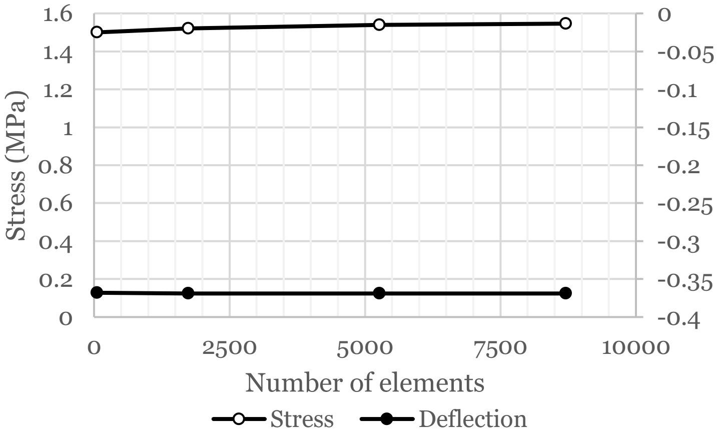

Figure 3.27: Number of elements used in the baseplate versus the observed maximum stress and deflection in the slab

Figure 3.27 shows that any particular number of elements used in the baseplate were appropriate when considering the critical stresses and deflections.

It can be seen that the stresses and deflections in the critical regions converges rapidly with increases to the number of elements in the critical regions. It can be immediately seen that there are no stress singularities present (i.e., stresses do not continuoulsy increase with continued increases in the number of elements in local areas). In particular, it was found that the critical stresses and deflections were most sensitive to the mesh densities provided in the slab and the subgrade. The mesh density of the baseplate was found to not have a particular effect on the critical stresses on the slab (note, however, that this is true only as the areas of concern are in the slab; should the areas of concern be in the baseplate, the baseplate element density should be refined). At each area of concern, a sufficient element density was provided to achieve convergence. Adequacy of convergence was assumed when subsequent doubling of the total number of elements yielded less than 1% change in the stress or deflections observed in these regions.

3.4.2 Comparison to Solutions on a Winkler Model

For validation, a simplified finite element model consisting of the subgrade supporting either a finite- or infinitely spanning slab subject to a concentrated load distributed over a small, central area is compared against Westergaard's (1926) analytical solutions and results obtained by a jointed plain concrete pavement analysis tool, EverFE (Davids et al., 2003).

In particular, a slab of depth 150 mm with lengths of either 6,000 or 16,000 mm were considered. Two lengths were considered in order to examine differences between a 'finite' and a so-called 'infinite' slab. A concentrated load of 10 kN was applied over a square 300 mm x 300 mm area. For the modulus of subgrade reaction was taken as 150 psi/in. and an equivalent elastic modulus of approximately 110 MPa was used in the Abaqus model.

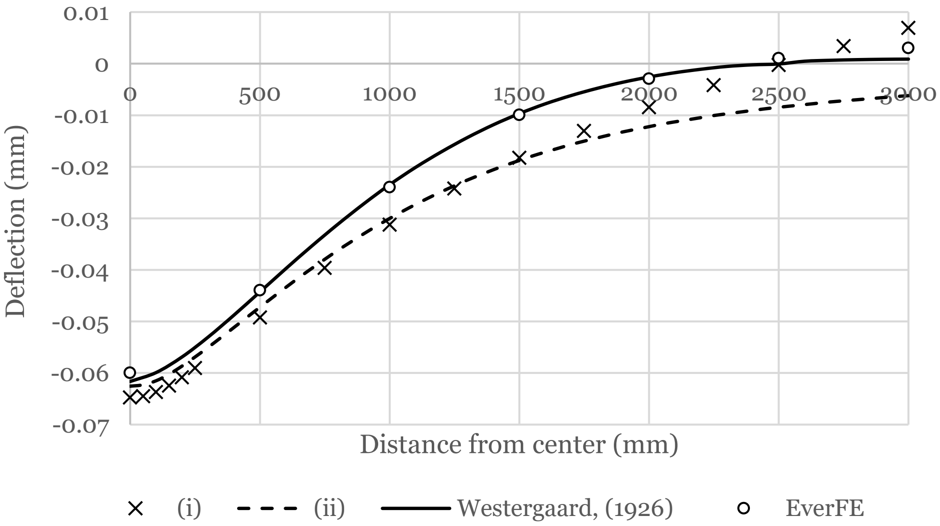

Figure 3.28: Comparison of the deflection profiles for a plate resting on an elastic half-space with an equivalent modulus of elasticity to a concentrated load distributed over a small square area versus the analytical solutions on a Winkler medium; (i): finite plate with L = 6,000 mm, and (ii): pseudo-infinite plate with L = 16,000 mm

In general, Westergaard's (1926) solutions pair well with the solution predicted by EverFE. In particular, EverFE predicts slightly greater uplift away from the loaded region. This is because while Westergaard considers an infinitely spanning slab, EverFE considers a finite slab. Compared to the equivalent elastic half-space models, Westergaard's (1926) solutions yield effectively the same results derived in Section 2.3; the deflections under the load are equivalent, and the half-space models predict more deflection away from the loaded region as a result of shear stress continuity in the soil. The case of the finite plate resting on the elastic half-space predicted slightly more deflection directly under the loaded region, and considerable uplift at the end of the plate. It was found that this uplift was greater than that of the uplift predicted by EverFE; this again was expected as the Winkler springs used in EverFE's solutions continue to provide support even in tension. The results obtained from this comparison were expected.

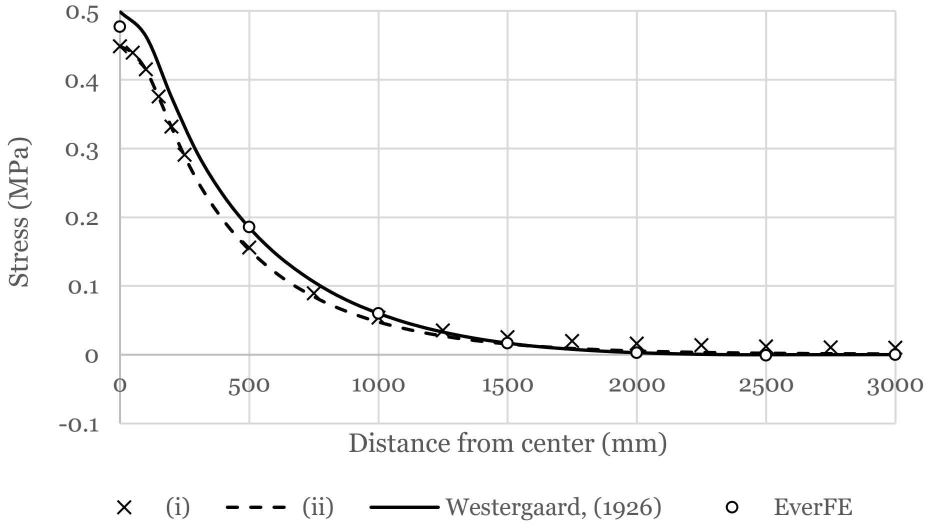

Figure 3.29: Comparison of the stress profiles for a plate resting on an elastic half-space an equivalent modulus of elasticity to a concentrated load distributed over a small square area versus the analytical solutions on a Winkler medium; (i): finite plate with L = 6,000 mm, and (ii): pseudo-infinite plate with L = 16,000 mm

In general, Westergaard's (1926) solutions matched with the solutions predicted by EverFE. EverFE predicted slightly lower stresses directly under the loaded region. Compared to the Abaqus models, the solutions using the Winkler model predicted approximately 15% greater stresses. Negligible difference was observed between the finite and pseudo-infinite plate. Figure 3.30 shows an additional comparison of maximum stresses under the loaded region when considering different values for the modulus off subgrade reaction:

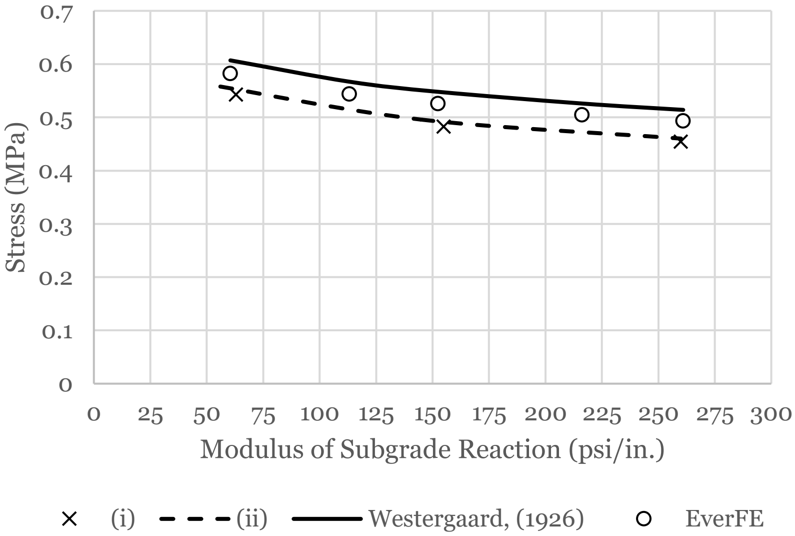

Figure 3.30: Comparison of the maximum stress for a plate resting on an elastic half-space an equivalent modulus of elasticity subject to a concentrated load distributed over a small circular area versus the analytical solutions on a Winkler medium; (i): finite plate with L = 6,000 mm, and (ii): pseudo-infinite plate with L = 16,000 mm

As before, it is evident that Westergaard (1926) predicts the greatest overall stress compared to EverFE and the Abaqus elastic half-space models, and negligible difference between the finite and pseudo-infinite plate was observed. In general, for all values of the modulus of subgrade reaction, the Abaqus elastic half-space models predicted approximately 10-15% less stress than Westergaard's (1926) solutions. Notably, the variation in critical stress for the elastic half-space models match Westergaard's (1926) initial assumptions of the effects of the modulus of subgrade reaction. In the particular slab-system defined in Figure 3.27, increasing the modulus of subgrade reaction from 50 psi/in. to 200 psi/in. resulted in a decrease from ~0.55 MPa to ~0.48 MPa.

3.4.3 Comparison to Analytical Solutions on a Half-Space

For validation, a simplified finite element model consisting of the subgrade supporting either a finite- or infinitely spanning slab subject to a concentrated load distributed over a small, central area is compared against Selvadurai's (1979) and Gorbunov-Posadov's (1959) analytical solutions and Hu and Hartley's (1994) numerical solutions.

For the infinite case, several slab-soil systems of varying dimensional configurations were simulated. This was completed in order to show the effects of more closely emulating infinite slab-soil conditions. A load of 10 kN was distributed over an increasingly smaller circular area, starting with a radius of 150 mm. Figure 3.31 shows the comparison of deflection curves obtained from Abaqus against the analytical solution presented by Selvadurai (1979):

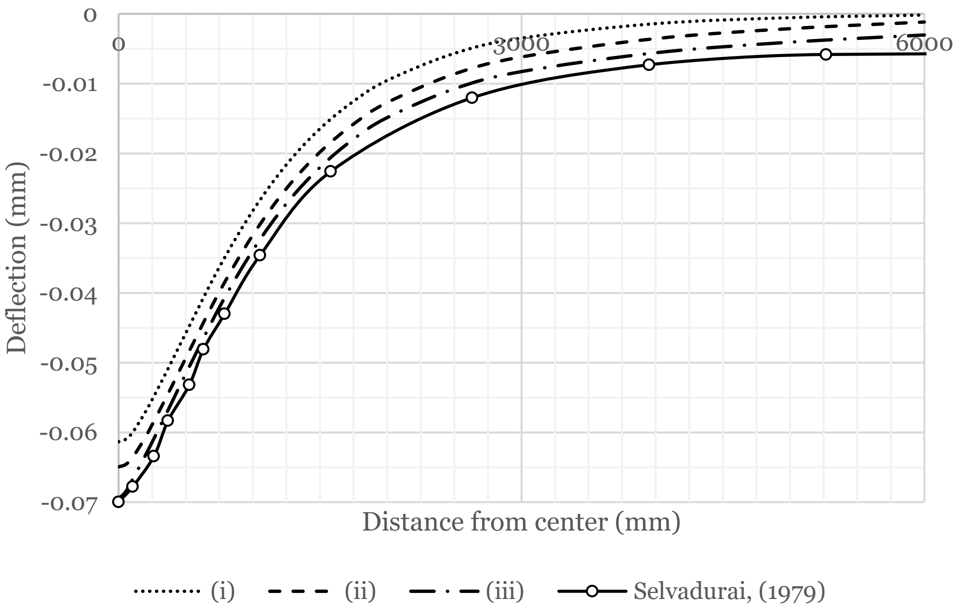

Figure 3.31: Comparison of the deflection profiles for a very long, 'pseudo'-infinite plate resting on an elastic half-space versus the analytical solutions developed by Selvadurai (1979); (i): H = 5,000 mm, L = 12,000 mm, r = 150 mm, (ii): H = 10,000 mm, L = 16,000 mm, r = 150 mm, (iii): H = 40,000 mm, L = 26,000 mm, r = 25 mm

Here, H is the subgrade depth, L is the slab length, and r is the radius over which the load is distributed over. As the slab-soil system trends towards emulating infinite slab and soil conditions (i.e., slab length, subgrade length, and subgrade depth → ∞ and the area over which the concentrated load is distributed over → 0), the deflection curves produced by the system begins to closely match those presented by the analytical solution. Obtaining deflection curves for slab-soil dimensions longer than the ones presented in Figure 3.31 becomes prohibitive in terms of computational effort and have been omitted. As the slab-soil system approaches infinite conditions, it is expected that the observed deflections will meet the analytical solution presented by Selvadurai (1979).

Figure 3.32 shows the contact stresses for the case of a very long plate resting on a deep and wide subgrade:

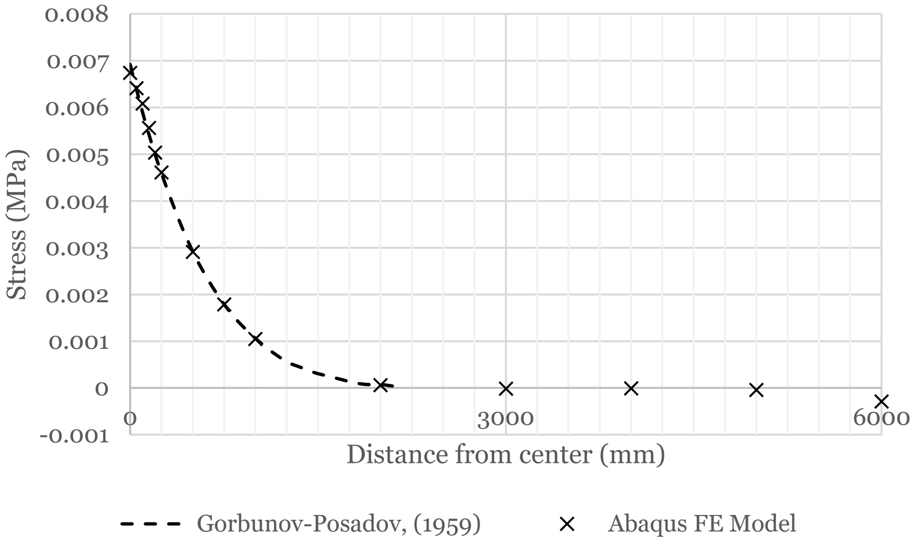

Figure 3.32: Comparison of the contact stress for a very long, 'pseudo'-infinite plate resting on an elastic half-space versus the analytical solutions developed by Gorbunov-Posadov (1959); H = 40,000 mm, L = 26,000 mm, r = 25 mm

It was found that the contact stresses did not vary much with changes to the slab-soil dimensions, so long as the dimensions were of reasonably sufficient length and depth.

For the finite case, dimensions and material properties were taken by matching the relative stiffness parameter outlined by Gorbonuv-Posadov (1959), γ, to the same values used in the numerical study presented by Hu and Hartley (1994). For instance, for γ = 3016, the following values were used: E_s = 260 MPa, E_b = 26000 MPa, h = 150 mm, and L = 6000 mm. It should be noted that this is not the only combination of slab-soil parameters that achieves this relative stiffness value. A concentrated load of 10 kN was distributed over a circular area with a radius of 150 mm. Figures 3.33 and 3.34 present these results:

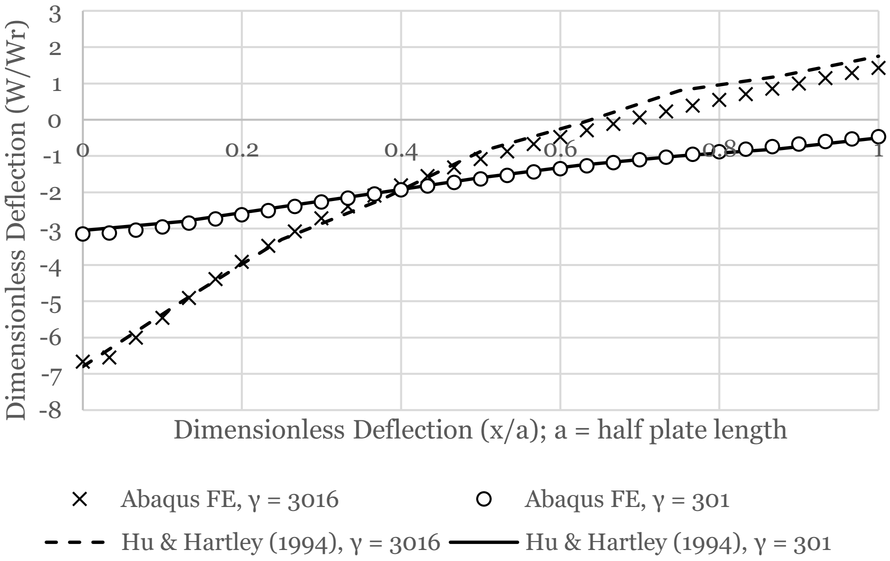

Figure 3.33: Comparison of the deflection profiles for a finite plate resting on an elastic half-space versus the analytical solutions developed by Hu and Hartley (1994)

For various values of the relative stiffness parameter, γ, the Abaqus elastic half-space models showed very good agreement with Hu and Hartley's (1994) numerical results. There are some slight discrepancies that can be seen specifically for slab-soils with higher relative stiffness values, but these can largely be attributed to the visual approximation of the values presented by Hu and Hartley.

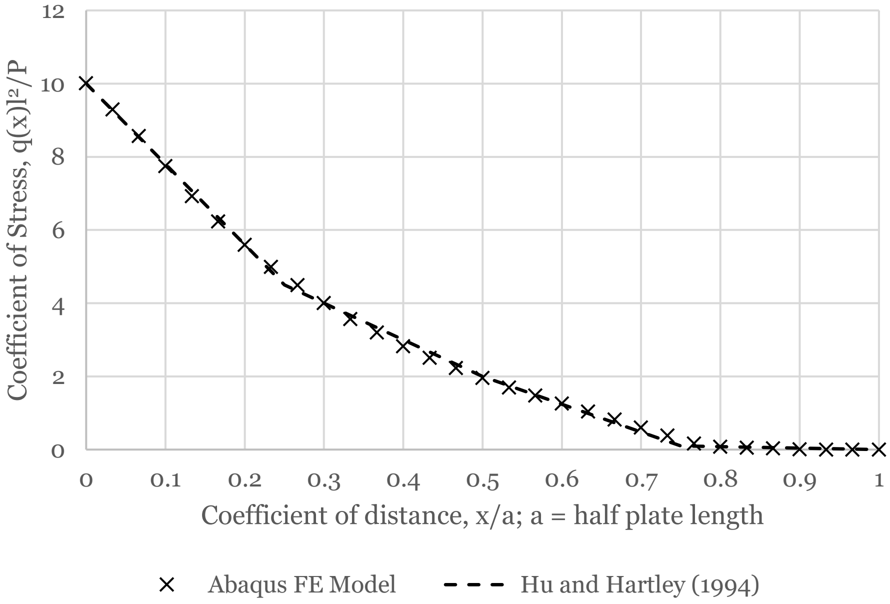

Figure 3.34: Comparison of the contact stress for a finite plate resting on an elastic half-space versus the analytical solutions developed by Hu and Hartley (1994); γ = 301

As before, the finite element model with a finite slab matched very well against the numerical studies presented by Hu and Hartley (1994) and Silva et al. (2001). As before, any discrepancies noted can be attributed to visual approximation of the values presented by the authors.

4.0 Data Collection & Analysis

This section details the methodology and procedure used to collect and analyze the results obtained from the finite element model developed in the previous section.

4.1 Methodology

The procedure for data collection involved a large-scale parametric study requiring the mass simulation of finite element models at varying variable values. Within each parameter's considered range of values, a minimum of 3 data points were taken: the upper bound, lower bound, and a value in-between. It was assumed that 3 data points per variable were sufficient in identifying the mathematical relationship between the parameters and the dependent variable. As contemporary slab-on-grade design methods are thickness design methods (i.e., the required thickness of the slab is the critical dependent variable), it was expected that the slab depth would be a critical parameter, and therefore 5 data points were taken (the upper bound, lower bound, and 3 values in-between).

An Abaqus finite element model can be defined in terms of an input (.inp) file detailing the nodal and element construction, material properties, model interactions, loading properties, and more. As the input file can be read as a plain text (.txt) file, the mass simulation of these FE models involved editing a text file with the predetermined variable values and running the models sequentially. This was completed using a Matlab script. Once finished running, an Abaqus model stores the results (i.e., of deflections, stresses, and other user-desired outputs) in an output database (.odb) file. The database file cannot be read as a typical text file, and as a result, a Python script was required to scrape the maximum principal stresses observed in the slab. In particular, it was important to extract the stresses in both the top and bottom of the slab, as the location of the critical stress (i.e., on top of bottom of the slab) was unknown.

It was expected that a linear change in the applied moment or compressive load would result in a linear increase in the observed maximum principal stress as the concrete was defined as a perfectly linear-elastic material. As a result, every model was simulated twice using two exploratory moments in order to develop a linear relationship between the load and the stress. The actual moment required for cracking of the slab would then be linearly interpolated or extrapolated using the exploratory moments and observed stresses as known values. Figure 4.1 depicts this process:

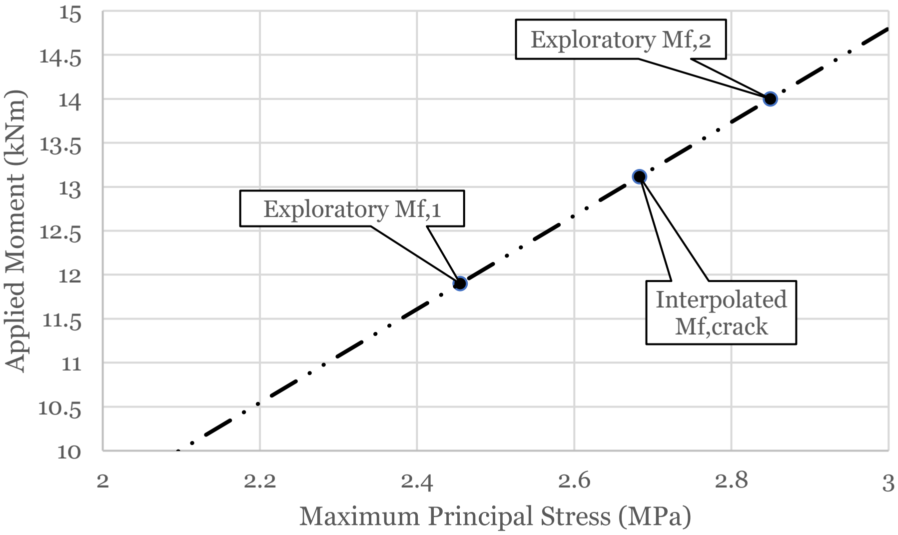

Figure 4.1: Linear interpolation to determine the applied moment required for cracking (the x-axis starts at 2 MPa and the y-axis starts at 10 kNm for clarity); f_r = 2.68 MPa

Here, the particular model is first simulated with an initial exploratory moment of ~12 kNm, with an observed maximum stress of ~2.45 MPa. The model was simulated again with a second exploratory moment of ~14 kNm, yielding an observed maximum stress of ~2.85 MPa. With these four values known alongside the modulus of rupture of the concrete (~2.68 MPa), it becomes trivial to apply linear interpolation and determine that the required cracking moment was ~13.2 kNm. A check can be completed by simulating the model once more at this cracking moment. It was found that the observed maximum stress at the linear interpolated cracking moment was ~2.69 MPa, well within the reasonable bounds of error.

Figures 4.2 to 4.7 shows an example of the model output of a centrally loaded slab visualized in Abaqus. Arbitrary model parameters were assigned.

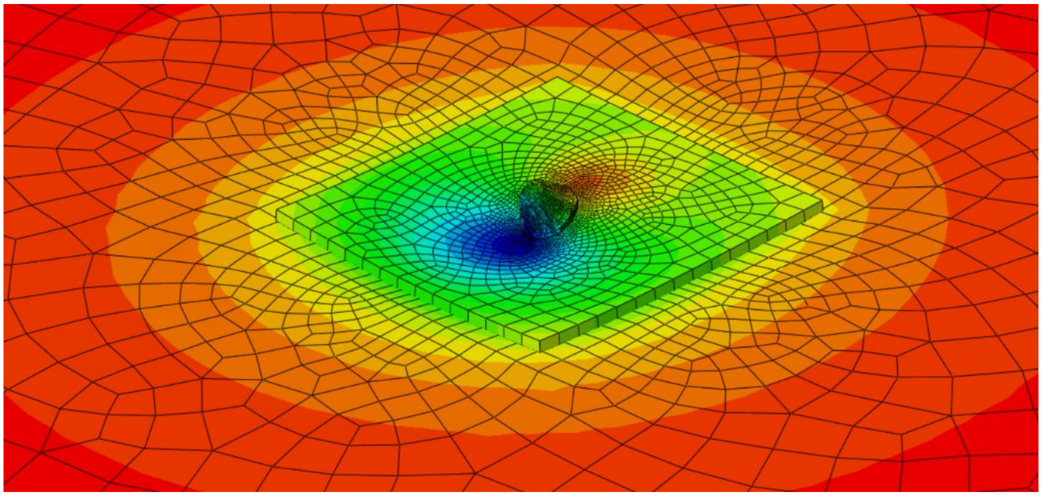

Figure 4.2: Deflection of a centrally loaded slab, 3D view

Figure 4.2 showcases the vertical deflection distribution of a centrally loaded slab. The area marked in blue indicates downwards deflection. The areas marked in red (such as the vast majority of the half space) indicates negligible deflection. A side view of the slab deflection is provided in Figure 4.3:

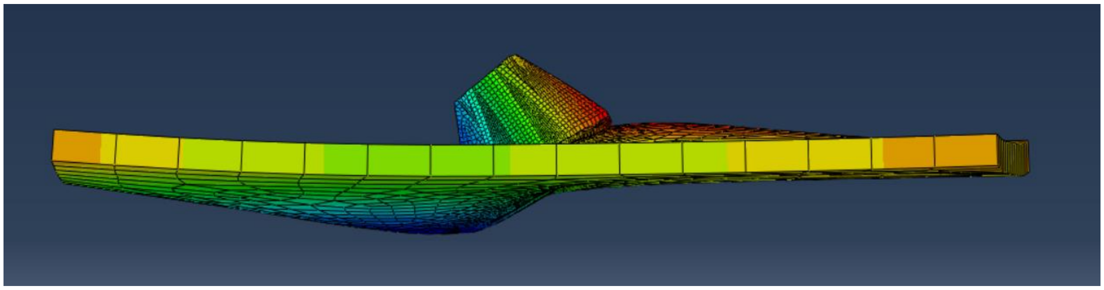

Figure 4.3: Deflection of a centrally loaded slab, 2D side view

Here, the soil has been removed for clarity. While it can be seen that the slab experienced some upwards deflection (area marked in red), this could be considered deflection local to the slab. The actual deflection of the slab when considering the soil was overall downwards.

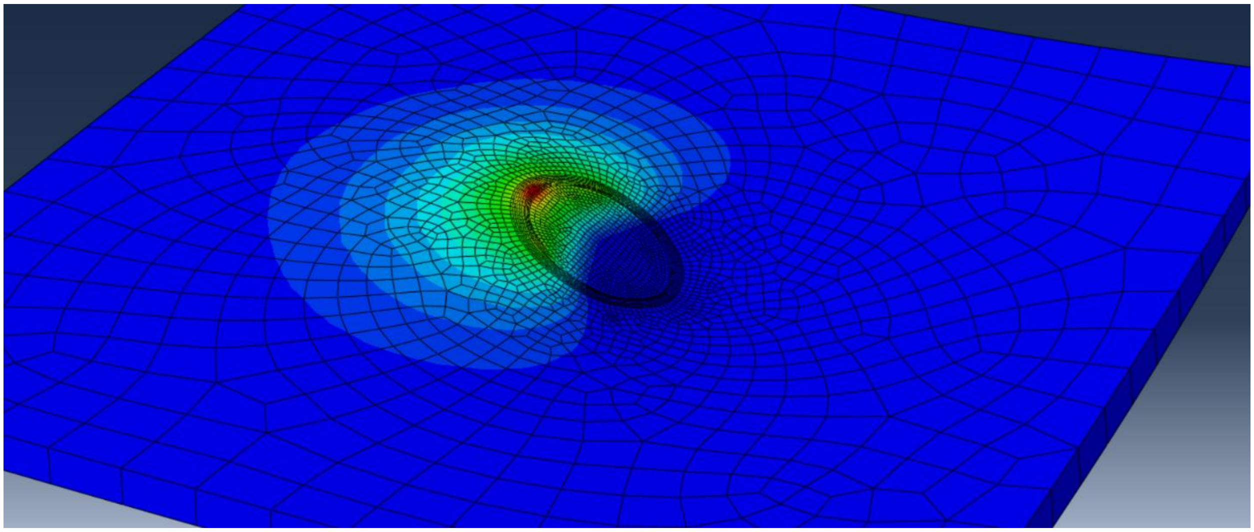

Figure 4.4: Maximum principal stress on top surface of slab, 3D view

In Figure 4.4 the soil, crane, and baseplate have been removed for clarity. The maximum principal stress on the top surface of the slab occurs on the uplifting component of the overturning moment. In particular, the area of maximum stress is found in the inner ring partition (defined in Section 3.3) where the slab is tied to the baseplate. The stress propagates out from this location. In particular, there are two more pockets of stress concentrations on the inner ring. This is shown more clearly in Figure 4.5:

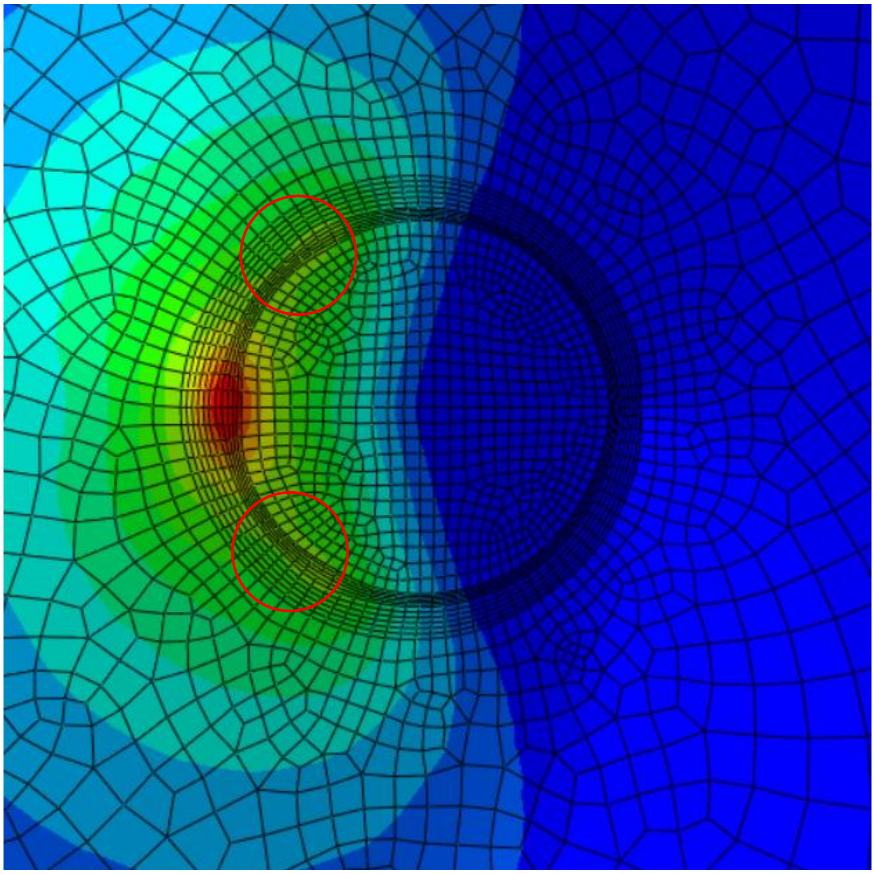

Figure 4.5: Maximum principal stress on top surface of slab, 2D top-down view

The area contoured in red is the maximum principal stress observed in the top surface of the slab as discussed in the previous figure. The two areas marked within the drawn red circles are secondary areas of slightly larger principal stresses (compared to the remainder of the circular ring partition) and exist at the ends of the stiffener flanges, as discussed in Section 3.3.

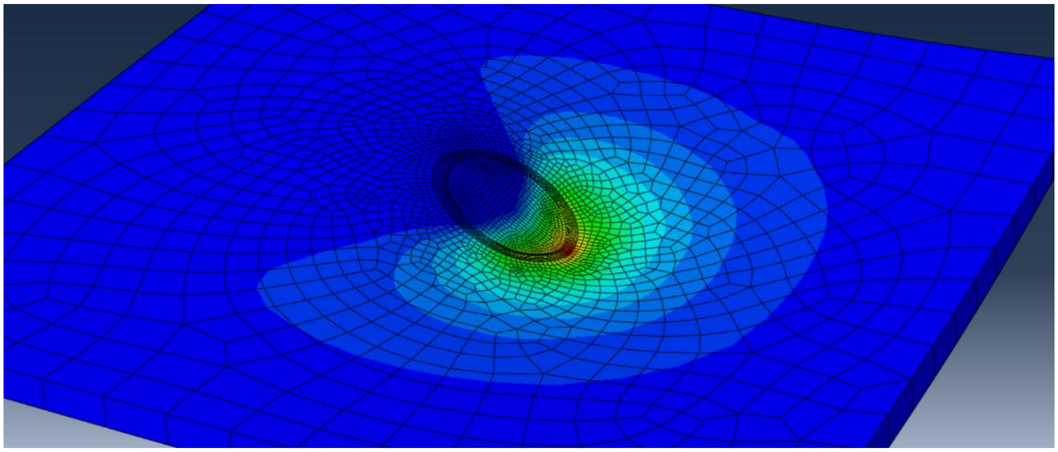

Figure 4.6: Maximum principal stress on bottom surface of slab, 3D view

In Figure 4.6 above, the soil, crane, and baseplate have been removed for clarity. The maximum principal stress on the bottom surface of the slab occurs on the downwards component of the overturning moment at the edge of the baseplate. Figure 4.7 depicts a top-down view of the critical location:

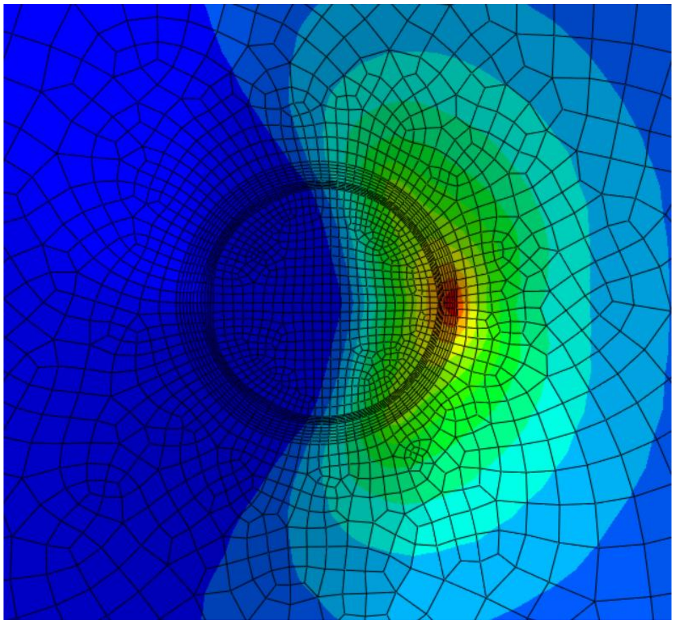

Figure 4.6: Maximum principal stress on bottom surface of slab, 2D top-down view

Here, it is clear that the maximum principal stress on the bottom surface of the slab appears at the location of the edge of the baseplate in contact with the slab.

4.2 Results

The relationships of the critical model parameters and the moment capacity of a slab with a centrally loaded crane obtained from the parametric study have been summarized below. Additionally, the effects of any particular model parameter on the relationship between any other model parameter and the moment capacity of the slab are examined. In general, discussion on the results obtained for loading cases near the edge or corner of the slab have been omitted from this section for conciseness, as it was found that their results were sufficiently similar to that of a slab loaded at its center. Figures for edge and corner loading cases may be found in Appendix A and B, respectively.

It becomes instructive to note that the model parameters considered in this study are not completely independent variables; while the value of each parameter is independent of one another, the relationship (i.e., the rate of change) between a particular parameter and the moment capacity of the slab is affected by changes to other parameters. Figures 4.7 to 4.12 first summarizes the effects of each of the model parameters acting independently. All other independent variables were held at constant values arbitrarily selected to illustrate the effects of the considered variable.

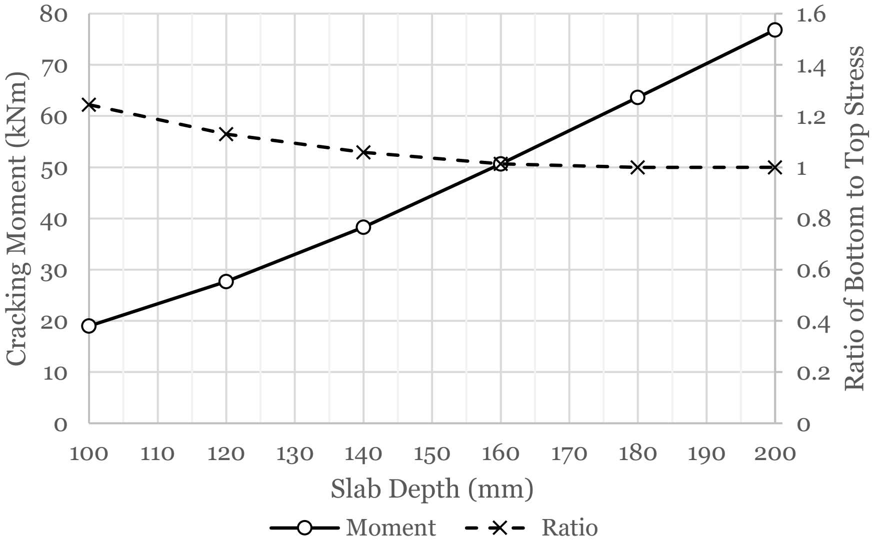

Figure 4.7: Slab depth versus moment capacity of a centrally loaded slab; L = 6,000 mm, r = 450 mm, P = 10 kN, k = 180 psi/in., f'_c = 40 MPa

Here, it can be seen that increasing the slab thickness increases the moment capacity. For this particular configuration of system dimensions and material properties, it can also be noted that increasing the slab thickness decreases the ratio of bottom to top stress. This means that while the slab is thin, the critical portion of the slab is on the bottom surface. As the slab gets thicker, the critical portion of the slab flips to the top surface. Notably, after the critical portion begins to occur on the top surface of the slab, subsequent increases to the slab depth only minimally affects this ratio (i.e., for all intents and purposes, the top and bottom stress are approximately equal.).

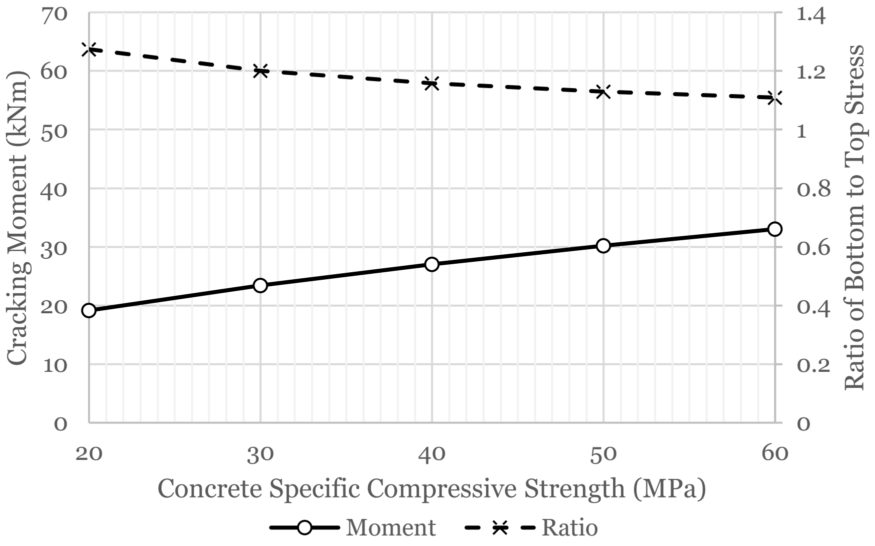

Figure 4.8: Concrete compressive strength versus moment capacity of a centrally loaded slab; L = 6,000 mm, r = 450 mm, P = 10 kN, k = 130 psi/in., h = 120 mm

Here, it can be seen that increasing the concrete compressive strength increases the moment capacity of the slab. For this particular configuration of system dimensions and material properties, it can also be noted that increasing the compressive strength decreases the ratio of bottom to top stress. It can be expected that further increases to the compressive strength may eventually cause the critical portion of the slab to be on the top surface.

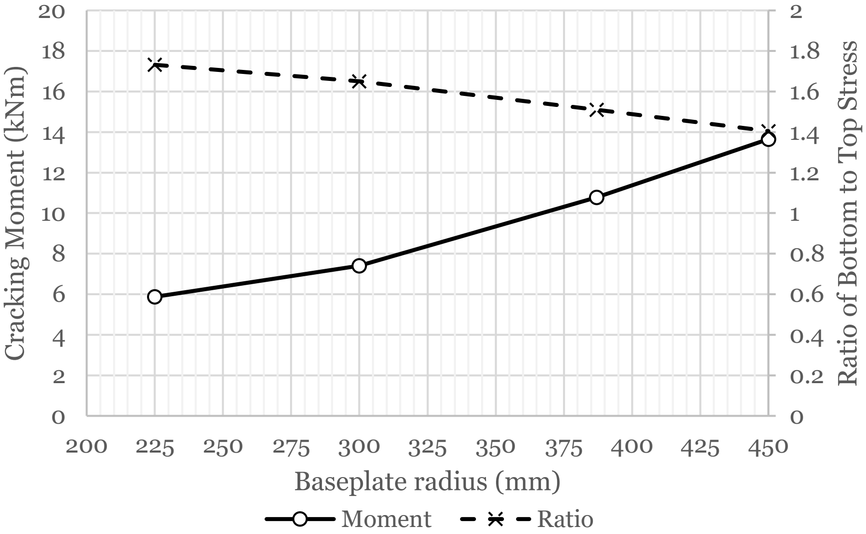

Figure 4.9: Baseplate radius versus moment capacity of a centrally loaded slab; L = 4,500 mm, P = 10 kN, k = 180 psi/in., f'_c = 20 MPa, h = 100 mm

Here, it can be seen that increase the baseplate radius increases the moment capacity of the slab. For this particular configuration of system dimensions and material properties, it can also be noted that increasing the baseplate radius also decreases the ratio of bottom to top stress. This is expected, because the effects of vertical forces are more pronounced when distributed over a smaller area (hence the bottom surface is critical). Therefore, in general, as the area over which the load is distributed increases, the ratio of bottom to top stress will decrease.

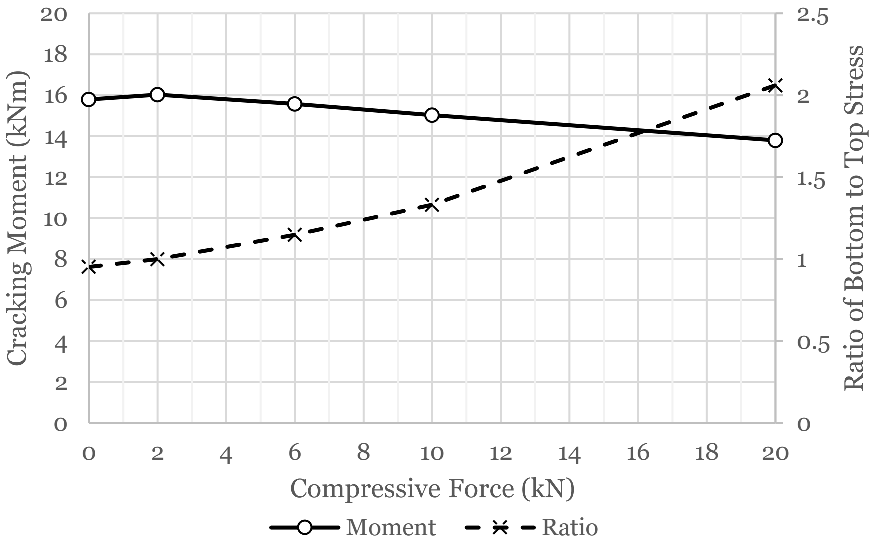

Figure 4.10: Compressive force versus moment capacity of a centrally loaded slab; L = 6,000 mm, r = 387 mm, k = 130 psi/in., f'_c = 40 MPa, h = 100 mm

Here, it can be seen that for this particular configuration of system dimensions and material properties, increasing the compressive force beyond 2 kN decreases the moment capacity of the slab and increases the ratio of bottom to top stress. Contrastingly, reducing the compressive force beyond 2 kN also decreases the moment capacity of the slab and decreases the ratio of bottom to top stress. This maximum at approximately 2 kN is expected; when a large compressive force is exerted on the slab, the critical area will be located on the bottom surface of the slab, and therefore will not require as much moment to produce rupture. So long as the critical area is located on the bottom surface, increasing the compressive force will decrease the moment capacity and vice versa, up until the aforementioned maximum. At the maximum, the stress experienced on the bottom and top surface of the slab reaches unity, and subsequent decreases to the compressive force will cause the top surface to become stress critical. When the top surface of the slab is the critical location, decreasing the compressive force also decreases the moment capacity, as the counterbalancing force to this moment is effectively removed. For clarity, Figure 4.10 above showcases the effects of the compressive force beyond the range of values considered in this study.

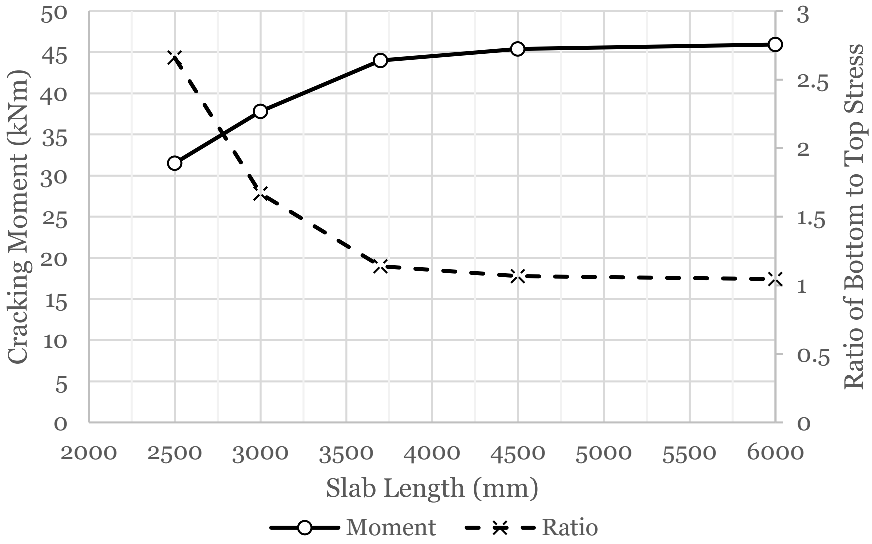

Figure 4.11: Slab length strength versus moment capacity of a centrally loaded slab; r = 450 mm, P = 10 kN, k = 130 psi/in., f'_c = 60 MPa, h = 140 mm

Here, it can be seen that increase the slab length increases the moment capacity of the slab, up to a point. For this particular configuration of system dimensions and material properties, subsequent increases to the slab length increases the moment capacity depreciatingly as the ratio of bottom to top stress approaches unity from above. In this case, this occurs at approximately L = 3700 mm. This is expected as further increases or decreases to the slab length multiplicatively increases or decreases the total volume of the slab, respectively, and consequently affects the amount of self-weight of the slab acting as a counterbalance to the overturning moment. For smaller slabs there is effectively no counterbalancing force, and therefore the overturning moment produces a critical stress on the bottom surface of the slab. For the purposes of this study, the slab length appears to have no real impact on the moment capacity of the slab, as the minimum considered slab length is 3700 mm. For clarity, Figure 4.11 above showcases the effects of the slab length beyond the range of values considered in this study.

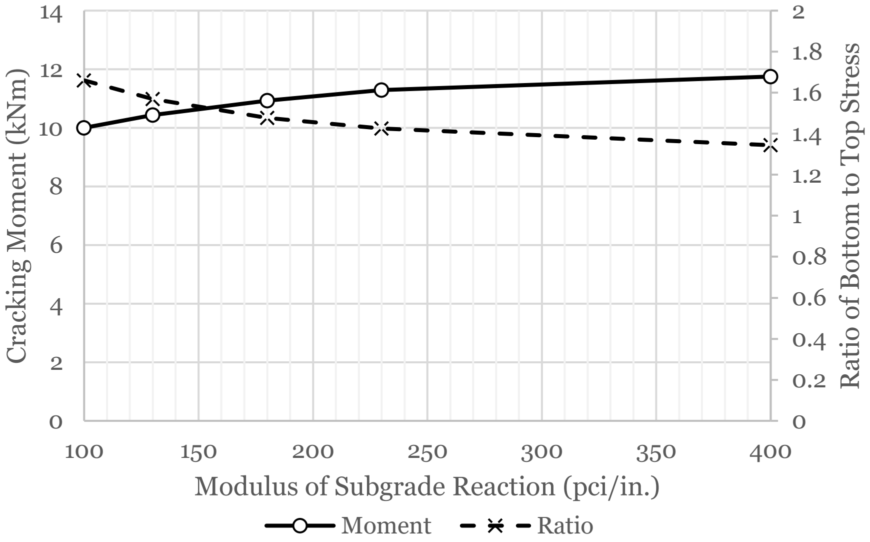

Figure 4.12: Modulus of subgrade reaction versus moment capacity of a centrally loaded slab; *L* = 6,000 mm, *r* = 387 mm, *P* = 10 kN, f'_c = 20 mm, *h* = 100 mm

Here, it can be seen that increasing the modulus of subgrade reaction increases the moment capacity of the slab. Additionally, for this configuration of system dimensions and material properties, increasing the modulus of subgrade reaction decreases the ratio of bottom to top stress. Changes in the modulus of subgrade reaction follows the expectations outlined by Westergaard (1926) and others. As stated before, changes to the modulus of subgrade reaction begins to have increasingly pronounced effects for increasingly small values. Therefore, so long as the modulus of subgrade reaction remains above a particular value, it can be expected that the modulus of subgrade reaction has insignificant effects on the moment capacity, such as in this study where the minimum considered modulus of subgrade reaction value is 130 psi/in. For clarity, Figure 4.12 above showcases the effects of the modulus of subgrade reaction beyond the range of values considered in this study.

It should be noted that parameters not being directly considered (i.e., not in the x-axis) are not held constant if one were to compare Figures 4.7 through 4.12. This is because the constant parameter values were selected in order to produce a significant change in the relationship between the considered parameter and moment capacity and/or ratio of stresses. If the constant parameter values were held constant between figures, then several parameters would appear to have a completely negligible relationship with the moment capacity. Despite carefully selecting the constant parameter values, it is clear that are *f'c*, *d*, and *h* are critical parameters (i.e., changes to the values of these parameters have the greatest impact on the moment capacity of the slab). Conversely, the less critical parameters are *L, P,* and *k*. In general, for the vast majority of cases, changes to these values negligibly impact the moment capacity of the slab. For a few specific cases (such as in the cases for smaller baseplates installed on highly flexible slab-soil systems that realistically should not have cranes installed on them), there is slightly more impact on changes to the values of less critical parameters.

Additionally, critical parameters have a non-negligible effect on the relationship between other critical parameters and the moment capacity, whereas they merely have a translational effect on the relationship between less critical parameters and the moment capacity. Contrastingly, less critical parameters do not affect the relationship on other parameters in any meaningful capacity. The effects of a particular parameter on the relationship of other parameters and the moment capacity have been summarized below.

4.2.1 Effects of *f'c* and *r* on *h* versus the moment capacity

The effects of various combinations of the compressive strength and the baseplate radius on the relationship between the slab depth and the moment capacity are summarized below. In each figure, L = 4,500 mm, P = 10 kN, and k = 180 psi/in.

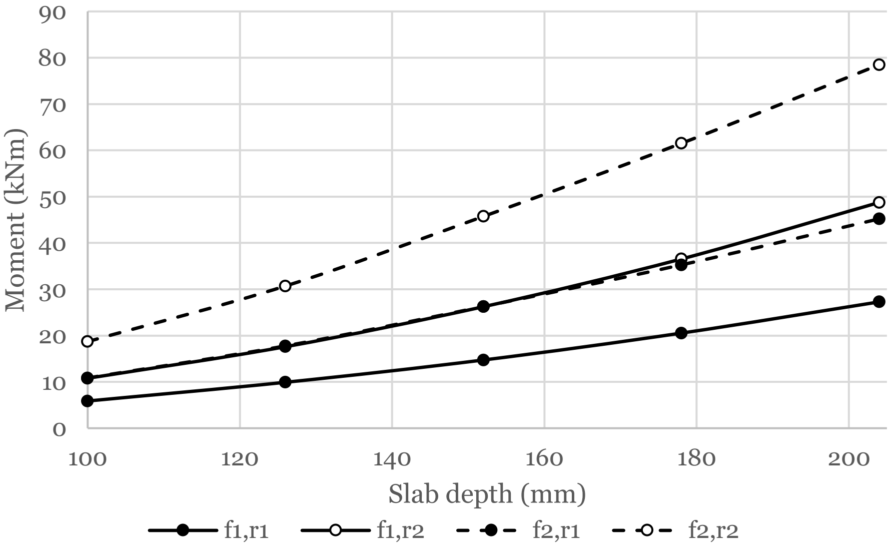

Figure 4.13: Effects of compressive strength and baseplate radius on the slab depth versus the moment capacity for a centrally loaded slab; $f'_{c,1}$ = 20 MPa, $f'_{c,2}$ = 60 MPa, r_1 = 225 mm, r_2 = 387 mm

When considering slabs of low compressive strength (notated by a solid black line), the rate of change between the slab depth and the moment capacity is lower than for slabs of high compressive strength (notated by a dashed black line). In particular, it can be noted that the effect of changing from a slab with a low compressive strength to one with a high compressive strength is more pronounced when considering larger baseplates (notated by white circles) compared to smaller ones (notated by black circles).

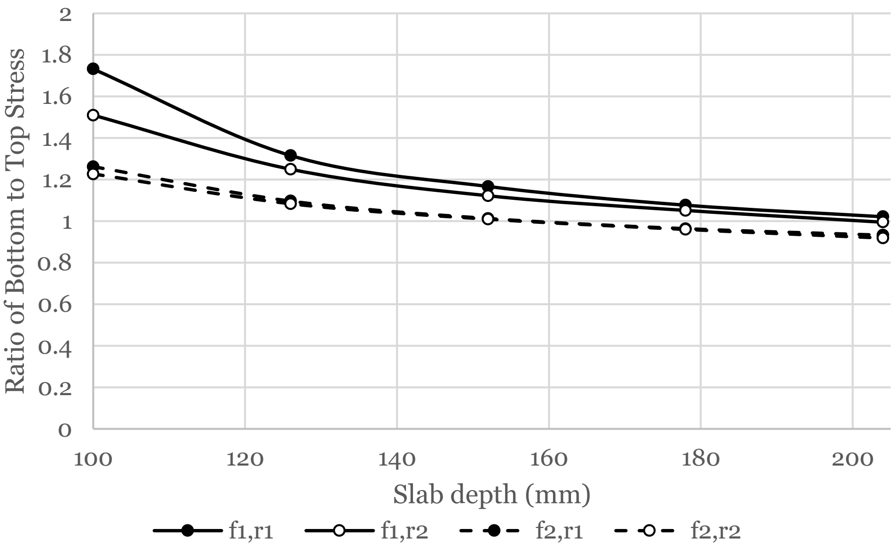

Figure 4.14: Effects of compressive strength and baseplate radius on the slab depth versus the ratio of bottom to top stress for a centrally loaded slab; $f'_{c,1}$ = 20 MPa, $f'_{c,2}$ = 60 MPa, r_1 = 225 mm, r_2 = 387 mm

It can be seen here that there are more pronounced differences between large baseplates (notated by white circles) and smaller baseplates (notated black circles) when considering different compressive strengths. For slabs of low compressive strength (notated by a solid black line), the change in baseplate size noticeably affects the ratio of bottom to top stress, specifically for thin slabs. This effect peters out as the slab thickness increases. For slabs of high compressive strength (notated by a dashed black line), the baseplate size appears to offer no significant change. Therefore, it is expected that the baseplate size affects the slab more when it is flexible (i.e., low compressive strength and thin) than when it is stiff. For all combinations of $f'c$ and r, increasing the slab depth causes the ratio between the bottom and top stress to decrease until the slab becomes stress critical on the top surface.

4.2.2 Effects of h and r on $f'c$ versus the moment capacity

The effects of various combinations of the slab depth and the baseplate radius on the relationship between the compressive strength and the moment capacity are summarized below. In each figure, L = 4,500 mm, P = 10 kN, and k = 180 psi/in.

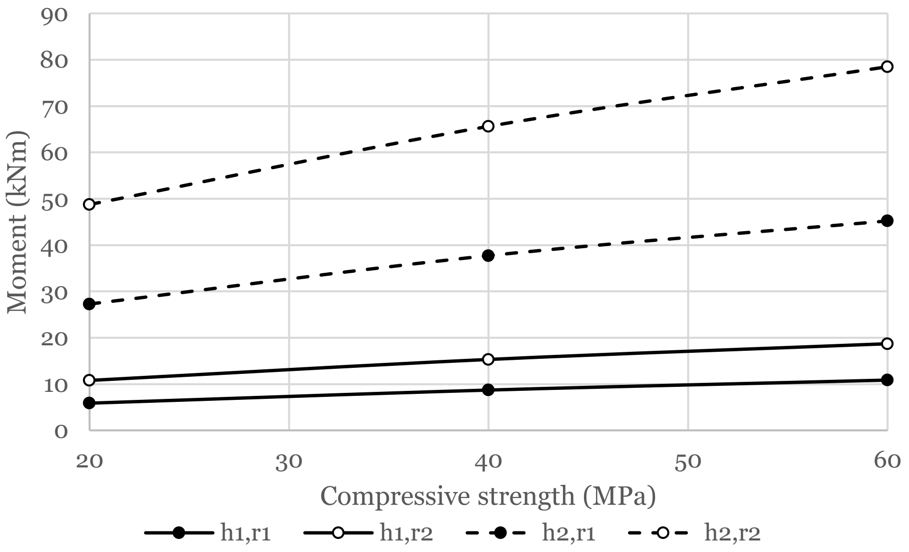

Figure 4.15: Effects of slab depth and baseplate radius on the compressive strength versus moment capacity for a centrally loaded slab; h_1 = 100 mm, h_2 = 200 mm, r_1 = 225 mm, r_2 = 387 mm

It can be seen that the concrete depth plays a significant role in the relationship between the compressive strength and the moment capacity. Changing from a thin slab (notated by a solid black line) to a thick slab (notated by a dashed black line) drastically increases both the initial starting capacity as well as the rate of change. Additionally, the effects of a larger baseplate (notated by white circles) are more pronounced at a thicker slab depth than at a thinner one.

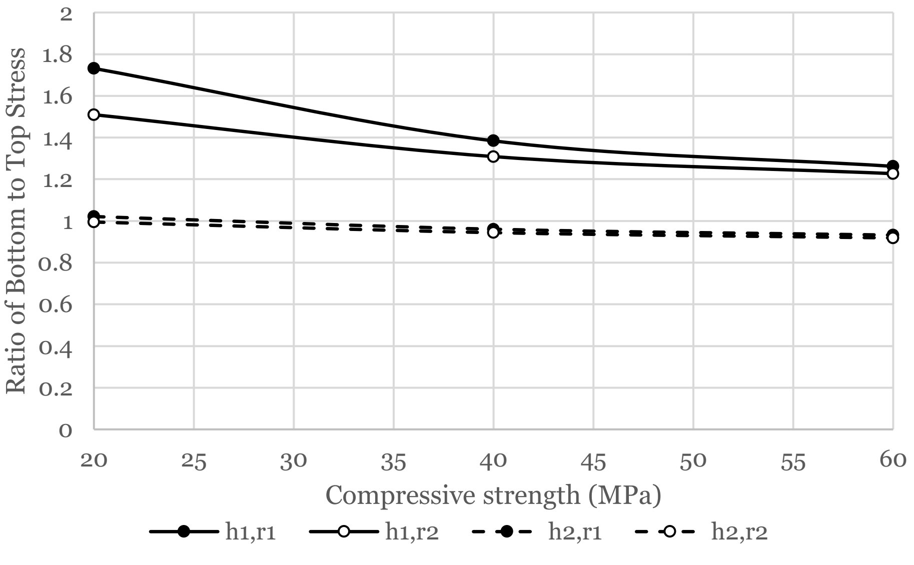

Figure 4.16: Effects of slab depth and baseplate radius on the compressive strength versus the ratio of bottom to top stress for a centrally loaded slab; h_1 = 100 mm, h_2 = 200 mm, r_1 = 225 mm, r_2 = 387 mm

As before, it is clear that the slab depth plays a larger role on the ratio of bottom to top stresses than the baseplate radius. For thin slabs (notated by a solid black line), increasing the baseplate radius decreases the ratio of bottom to top stress. Conversely, there is no noticeable effect on changing the baseplate radius at thicker slabs (notated by a dashed black line). For all combinations of *h* and *r*, increasing the compressive strength causes the ratio between the bottom and top stress to decrease until the slab becomes stress critical on the top surface.

4.2.3 Effects of *h* and *f'c* on *r* versus the moment capacity

The effects of various combinations of the slab depth and the compressive strength on the relationship between the baseplate radius and the moment capacity are summarized below. In each figure, *L* = 4,500 mm, *P* = 10 kN, and *k* = 180 psi/in.

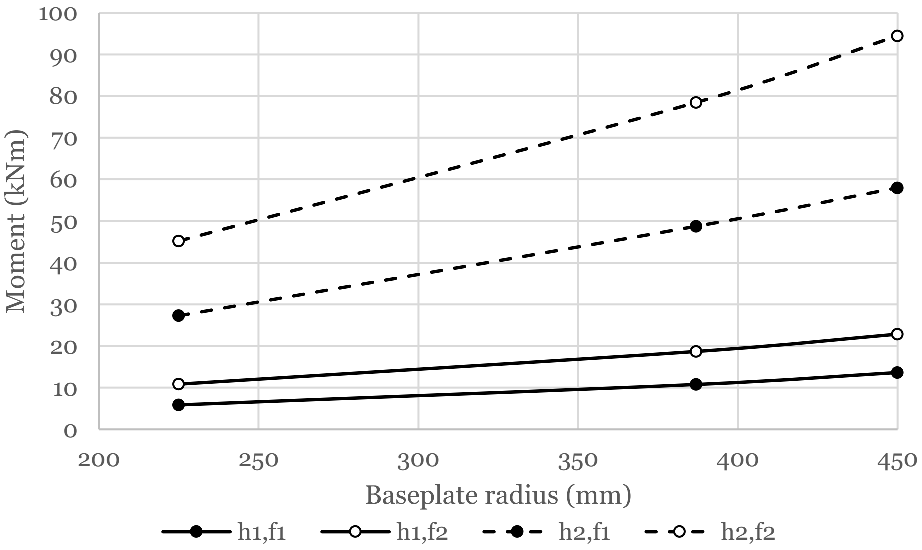

Figure 4.17: Effects of slab depth and compressive strength on the baseplate radius versus moment capacity for a centrally loaded slab; h_1 = 100 mm, h_2 = 200 mm, $f'_{c,1}$ = 20 MPa, $f'_{c,2}$ = 60 MPa

It can be seen that increasing the baseplate radius rapidly increases the moment capacity of the slab. The effects are more pronounced for thicker slabs (notated by a solid black line) than thinner slabs (notated by a dashed black line), regardless of the concrete compressive strength. Consequently, increasing the compressive strength from a low value (notated by black circles) to a high value (notated by white circles) produces significantly greater effects for thicker slabs.

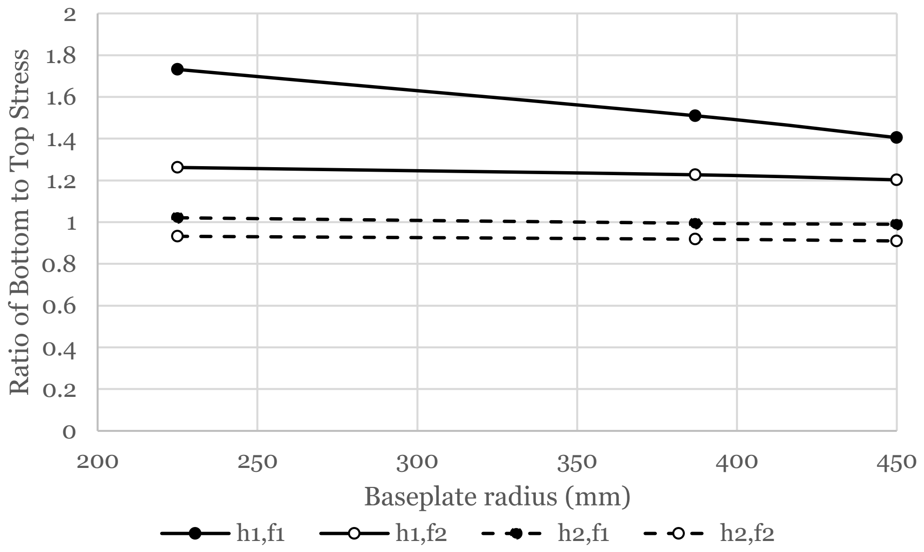

Figure 4.18: Effects of slab depth and compressive strength on the baseplate radius versus the ratio of bottom to top stress for a centrally loaded slab; h_1 = 100 mm, h_2 = 200 mm, $f'_{c,1}$ = 20 MPa, $f'_{c,2}$ = 60 MPa

Overall, increasing the baseplate radius reduces the ratio of bottom to top stress. However, it can be seen that there is little to no change in the ratio of bottom to top stress for most combinations of the compressive strength and slab depth. The exception is for very flexible slabs with a thin thickness (notated by a solid black line) and a low compressive strength (notated by black circles). Notably, very flexible slabs tend to be stress critical on the bottom surface and only shows signs of becoming critical on the top surface after large increases to the baseplate radius. Contrastingly, stiff slabs are stress critical on the top surface of the slab and remains critical on the top surface.

4.2.4 Effects of the *f'c, h,* and *r* on *P* versus the moment capacity

The effects of various combinations of the slab depth, compressive strength, and baseplate radius and on the compressive force versus the moment capacity are summarized below. In the following, L = 4,500 mm and k = 180 psi/in.

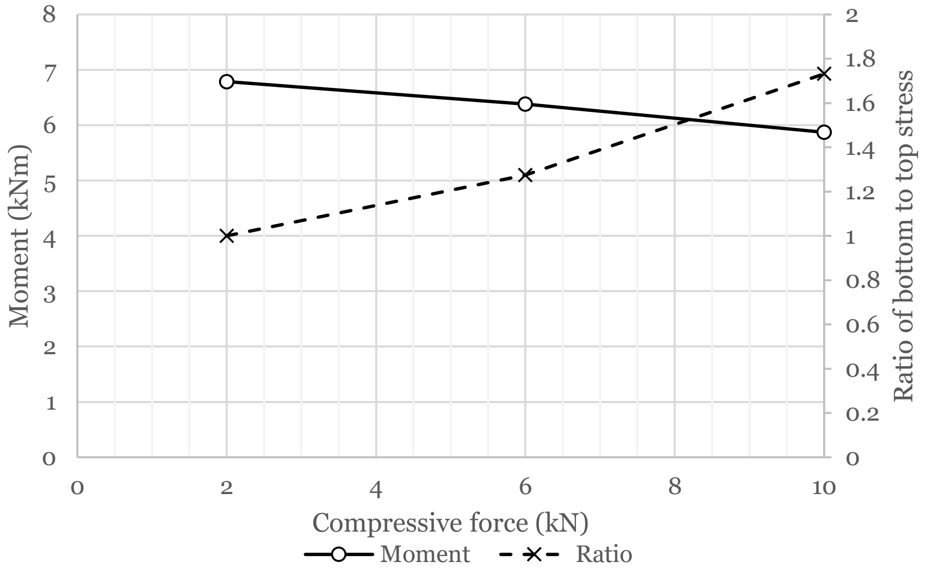

Figure 4.19: Compressive force versus the moment capacity and ratio of bottom to top stress for a centrally loaded slab; r = 225 mm, h = 100 mm, f'_c = 20 MPa

For a small baseplate and thin slab of low compressive strength, increasing the compressive force rapidly increases the ratio of bottom to top stress and decreases the moment capacity. Notably, these effects only occur beyond approximately P = 2 kN. As stated before, it is expected that once the ratio of bottom to top stress approaches unity from above, decreasing the compressive force will also decrease the moment capacity but also decrease the ratio of bottom to top stress.

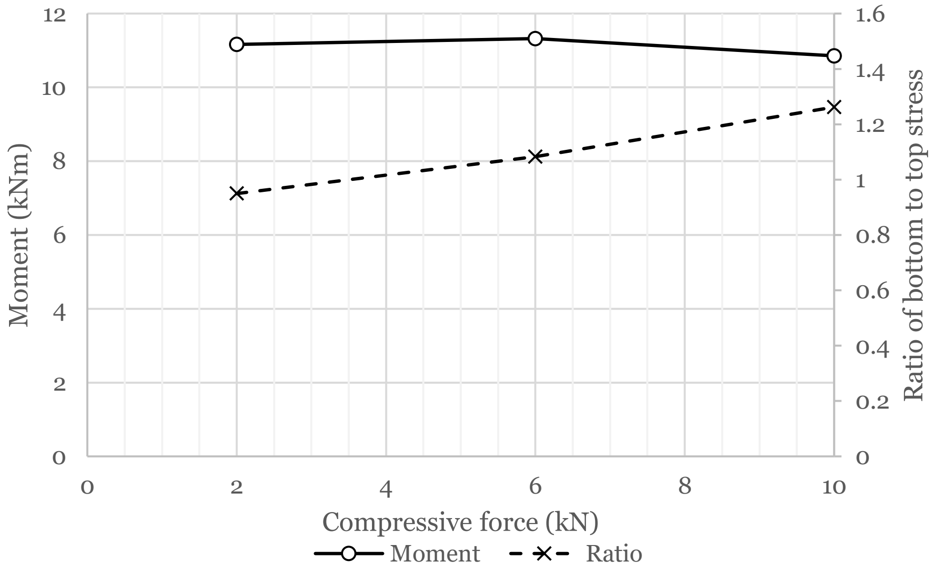

Figure 4.20: Compressive force versus the moment capacity and ratio of bottom to top stress for a centrally loaded slab; r = 225 mm, h = 100 mm, f'_c = 60 MPa

For a small baseplate and thin slab of high compressive strength, increasing or decreasing the compressive force beyond P = 6 kN decreases the moment capacity of the slab and increases or decreases the ratio of bottom to top stress, respectively. Again, it can be noted that the same theory is occurring, and the maximum moment capacity occurs when the ratio of bottom to top stress approaches unity.

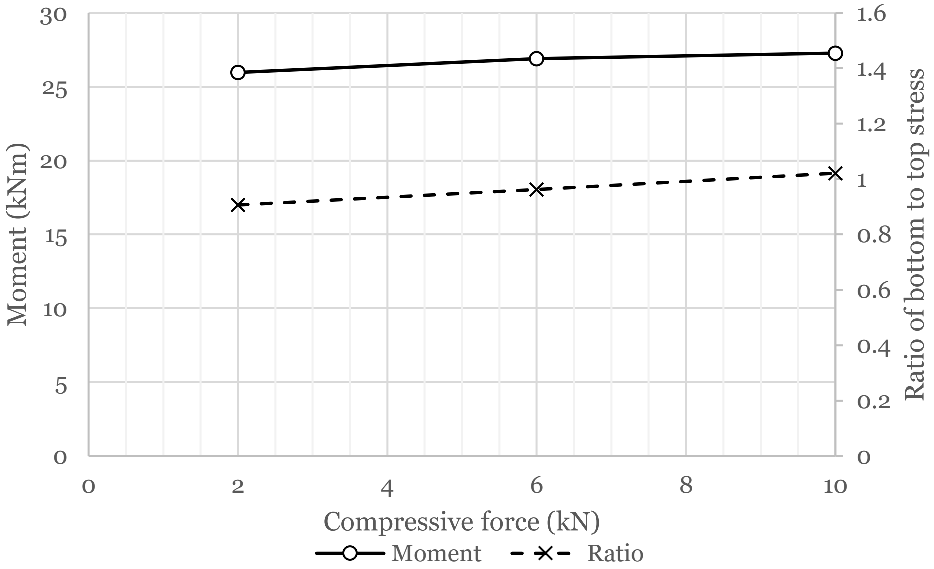

Figure 4.21: Compressive force versus the moment capacity and ratio of bottom to top stress for a centrally loaded slab; r = 225 mm, h = 200 mm, f'_c = 20 MPa

For a small baseplate on a thick slab of low compressive strength, increasing the compressive force increases the maximum moment as the ratio of bottom to top stress approaches unity from below. It is expected that at some point beyond P = 10 kN, subsequent increases to the compressive force will reduce the moment capacity instead as the ratio of bottom to top stress exceeds unity.

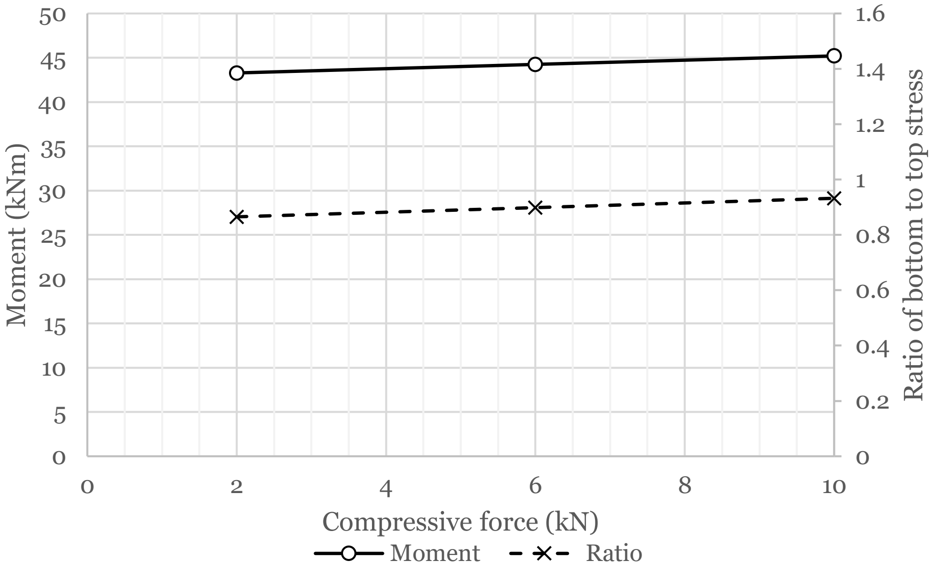

Figure 4.22: Compressive force versus the moment capacity and ratio of bottom to top stress for a centrally loaded slab; r = 225 mm, h = 200 mm, f'_c = 60 MPa

For a small baseplate on a thick slab of high compressive strength, increasing the compressive force increases the maximum moment as the ratio of bottom to top stress approaches unity from below. Like the figure before it, the maximum moment the slab can experience likely occurs at a point beyond P = 10 kN.

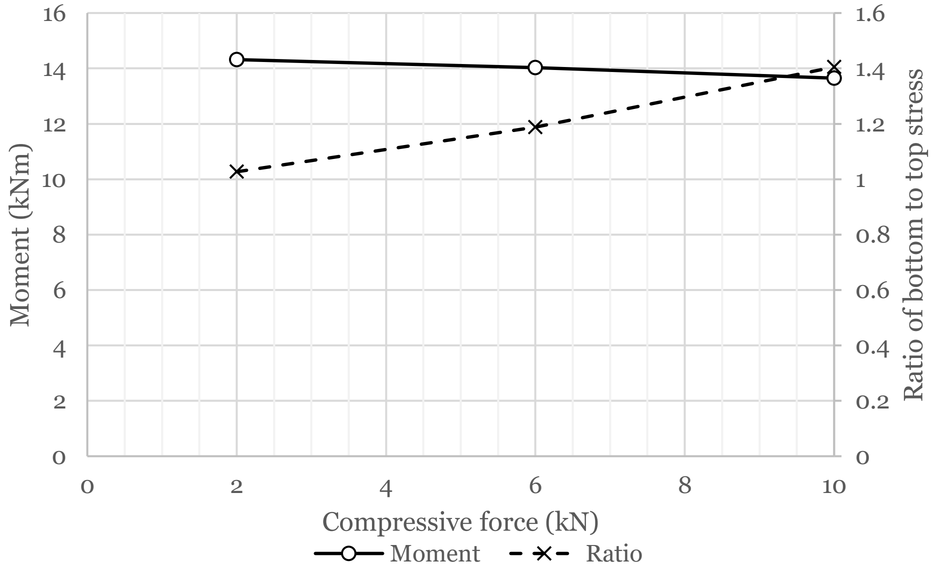

Figure 4.23: Compressive force versus the moment capacity and ratio of bottom to top stress for a centrally loaded slab; r = 450 mm, h = 100 mm, f'_c = 20 MPa

For a large baseplate on a thin slab of low compressive strength, increasing the compressive force decreases the moment capacity and increases the ratio of bottom to top stress. It can be expected that the maximum moment occurs somewhere prior to P = 2 kN, when the ratio of stresses reaches unity from above.

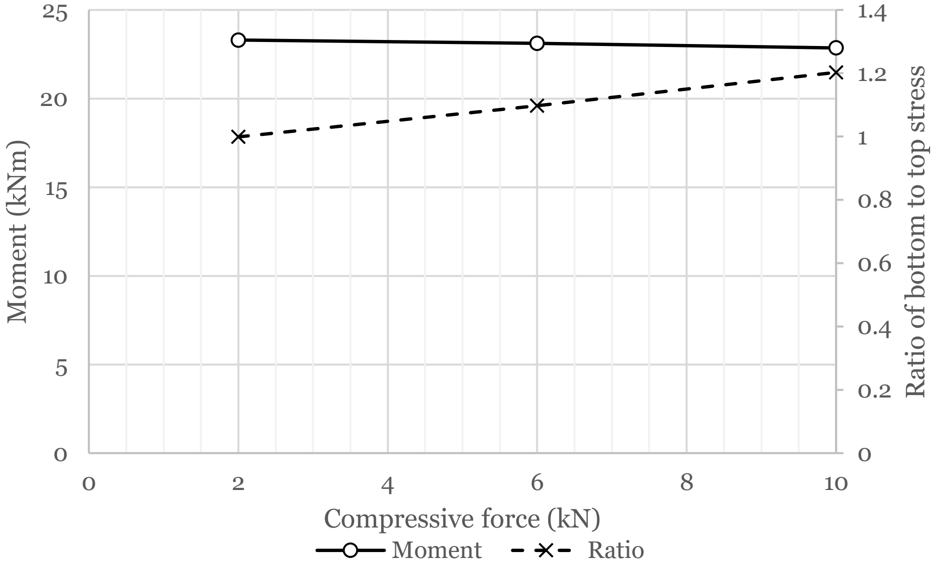

Figure 4.24: Compressive force versus the moment capacity and ratio of bottom to top stress for a centrally loaded slab; r = 450 mm, h = 100 mm, f'_c = 60 MPa

For a large baseplate on a thin slab of high compressive strength, increasing the compressive force decreases the moment capacity and increases the ratio of bottom to top stress. The projection of the ratio of bottom to top stress provides reasonable indication that the maximum moment capacity occurs at an uplifting tensile force acting on the slab (i.e., at some value P < 0 kN).

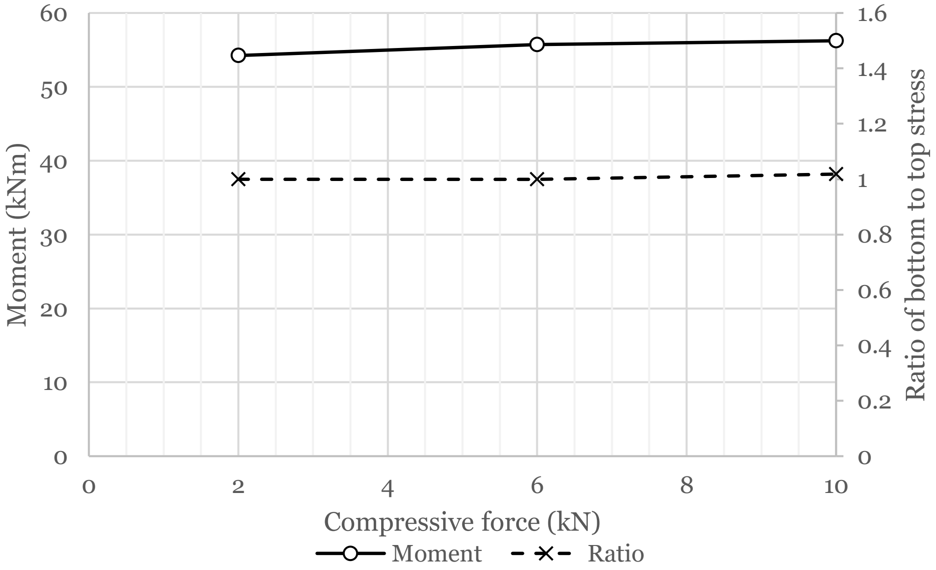

Figure 4.25: Compressive force versus the moment capacity and ratio of bottom to top stress for a centrally loaded slab; r = 450 mm, h = 200 mm, f'_c = 20 MPa

For a large baseplate on a thick slab of low compressive strength, increasing the compressive force increases the moment capacity and increases the ratio of bottom to top stress. The maximum moment occurs somewhere between P = 6 kN to 10 kN, and it can be expected that the moment capacity will slowly begin to decrease beyond P = 10 kN. It should be noted that for such a thick slab with a large area over which the load is distributed, changes to the compressive force have very little impact on the slab's moment capacity.

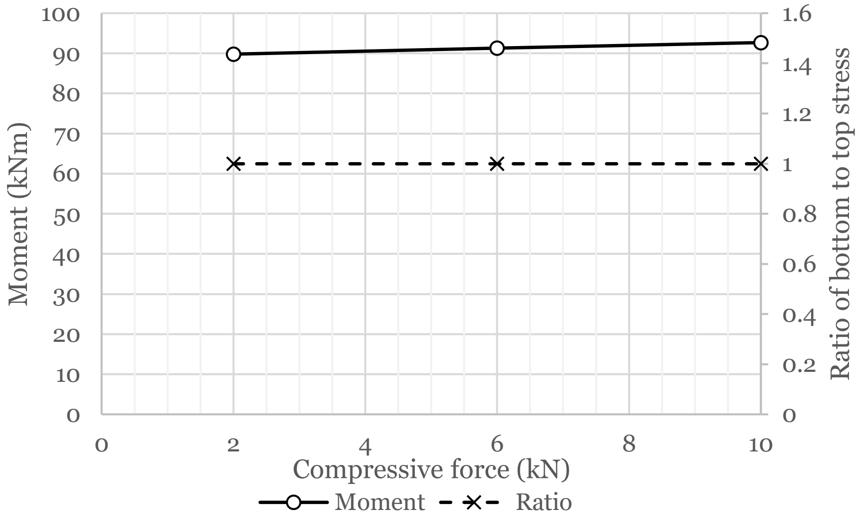

Figure 4.26: Compressive force versus the moment capacity and ratio of bottom to top stress for a centrally loaded slab; r = 450 mm, h = 200 mm, f'_c = 60 MPa

For a large baseplate on a thick slab of high compressive strength, increasing the compressive force increases the moment capacity and the ratio of bottom to top stress. Notably, the compressive force produces miniscule changes in the ratio of bottom to top stress, indicating that the maximum moment capacity is likely significantly beyond P = 10 kN.

The figures displayed in this section explains a lot of the behaviour that the compressive force has on the moment capacity of a slab-soil system. For any slab-soil system, there exists a particular compressive force that denotes the maximum moment capacity of the slab. This occurs when the ratio of bottom to top stress reaches unity. For flexible slabs that are largely dominated by critical stresses appearing on the bottom surface of the slab, subsequent increases to the compressive force merely increases the stresses at the critical location, therefore decreasing the moment capacity while increasing the ratio of bottom to top stress. Decreasing the compressive force contrastingly increases the moment capacity and decreases the ratio of bottom to top stress until unity, beyond which any subsequent decreases to the compressive force will decrease the moment capacity as the critical portion of the slab flips to the top surface of the slab. For stiffer slabs and for larger areas of distributed loads, larger changes in the compressive force are needed to establish the maximum moment capacity, as the rate of change in the moment capacity and ratio of bottom to top stress with respects to any subsequent change to the compressive force becomes very small. In general, if the ratio of bottom to top stress is less than unity, increases to the compressive force increases the moment capacity and ratio until unity. If the ratio of bottom to top stress is greater than unity, then the maximum moment capacity for the system has already been reached and subsequent increases to the compressive force decreases both the moment capacity and ratio of bottom to top stress.

For the range of compressive forces considered in this study (*P* = 2 to 10 kN), the compressive force plays a role in affecting the moment capacity of the slab for flexible slabs or for smaller baseplates resting on moderately stiff slabs. For all other combinations of baseplate, slab depth, and compressive strength, the compressive force had only minor impacts on the moment capacity of the slab.

4.2.5 Effects of the *f'c, h,* and *r* on *k* versus the moment capacity

The effects of various combinations of the slab depth, compressive strength, and baseplate radius and on the modulus of subgrade reaction versus the moment capacity are summarized below. In the following, *L* = 4,500 mm and *P* = 10 kN.

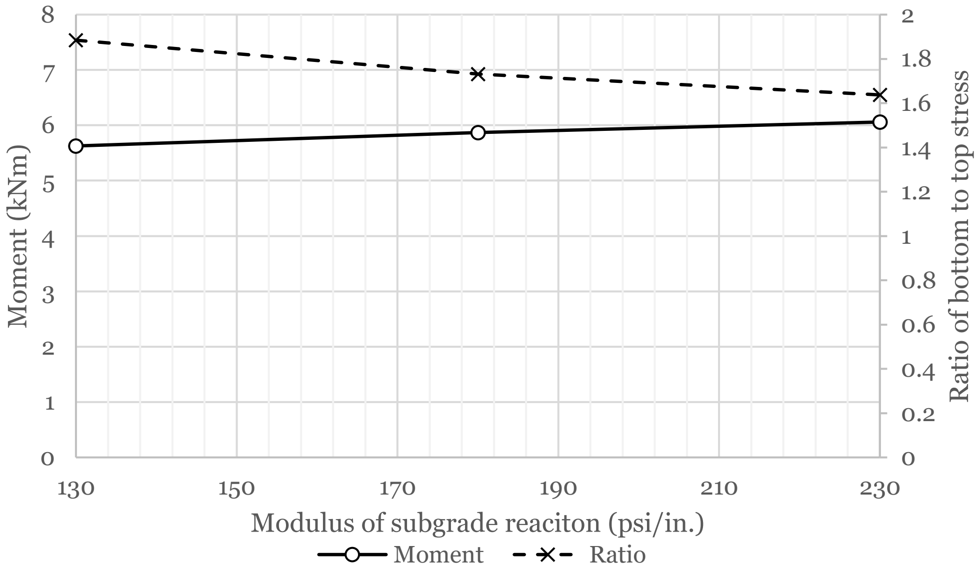

Figure 4.27: Modulus of subgrade reaction versus the moment capacity and ratio of bottom to top stress for a centrally loaded slab; r = 225 mm, h = 100 mm, f'_c = 20 MPa

For a small baseplate on a thin slab of low compressive strength, increasing the modulus of subgrade reaction increases the moment capacity and decreases the ratio of bottom to top stress. Increasing from the lower bound to the upper bound of the modulus of subgrade reaction here results in approximately 5% increased in the moment capacity. While this change is not negligible, it is largely insignificant.

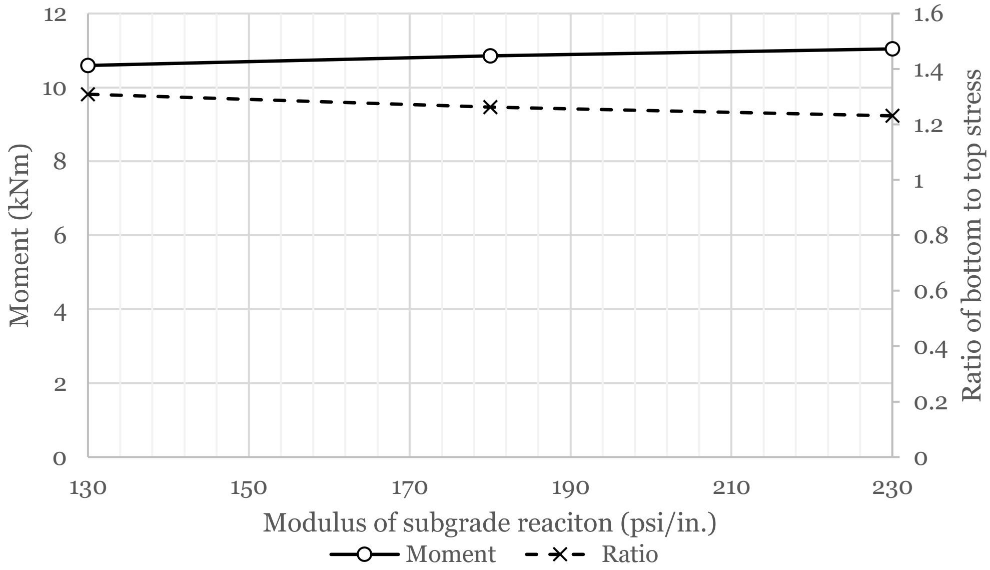

Figure 4.28: Modulus of subgrade reaction versus the moment capacity and ratio of bottom to top stress for a centrally loaded slab; r = 225 mm, h = 100 mm, f'_c = 60 MPa

For a small baseplate on a thin slab of high compressive strength, increasing the modulus of subgrade reaction increases the moment capacity and decreases the ratio of bottom to top stress.

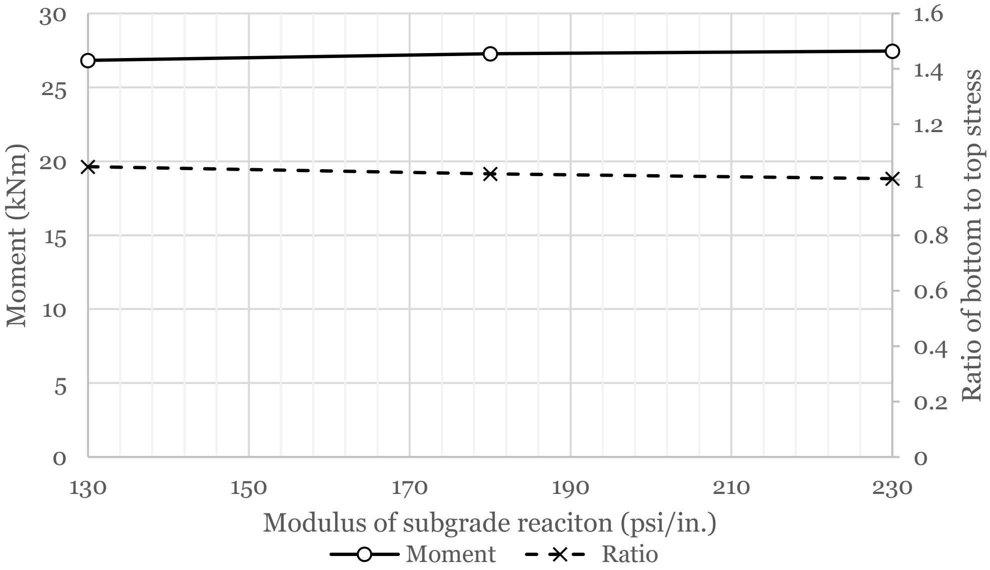

Figure 4.29: Modulus of subgrade reaction versus the moment capacity and ratio of bottom to top stress for a centrally loaded slab; r = 225 mm, h = 200 mm, f'_c = 20 MPa

For a small baseplate on a thick slab of low compressive strength, increasing the modulus of subgrade reaction increases the moment capacity and decreases the ratio of bottom to top stress.

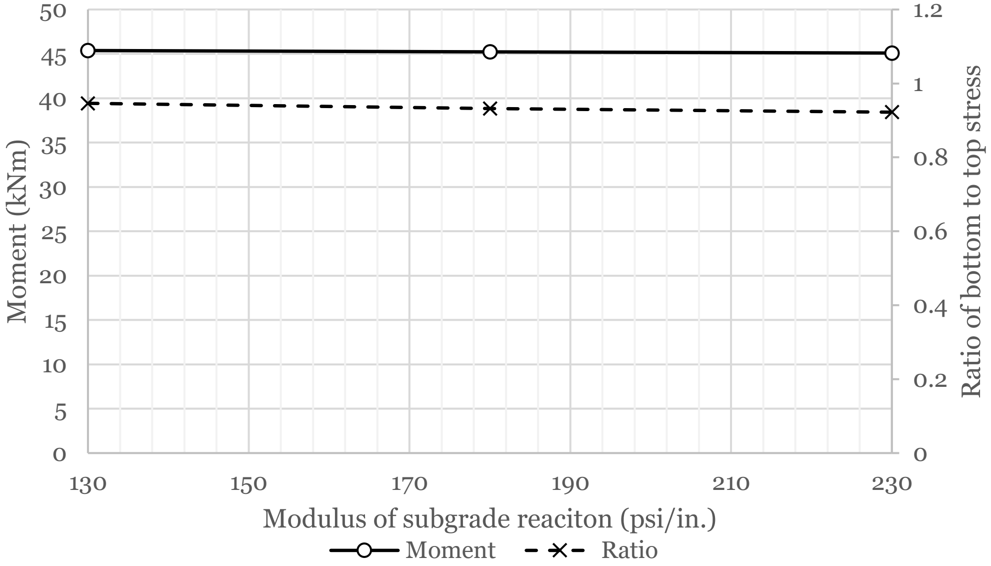

Figure 4.30: Modulus of subgrade reaction versus the moment capacity and ratio of bottom to top stress for a centrally loaded slab; r = 225 mm, h = 200 mm, f'_c = 60 MPa

For a small baseplate on a thick slab of high compressive strength, increasing the modulus of subgrade reaction decreases the moment capacity and decreases the ratio of bottom to top stress. This indicates a very similar effect to that of the compressive forces: increasing the modulus of subgrade reaction increases the moment capacity and the ratio of bottom to top stress from the bottom until unity, after which subsequent increases begins to decrease both the moment capacity and ratio of bottom to stress.

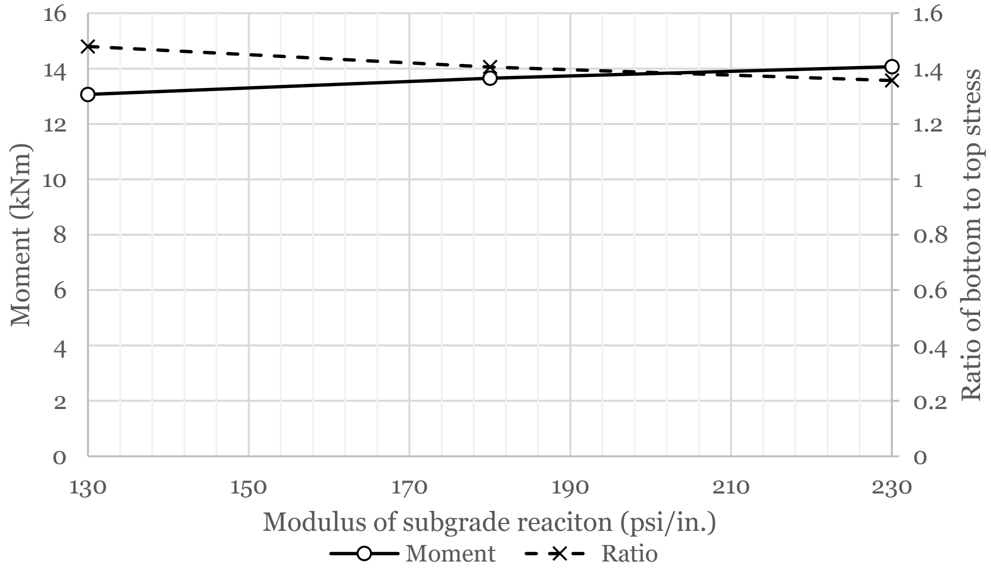

Figure 4.31: Modulus of subgrade reaction versus the moment capacity and ratio of bottom to top stress for a centrally loaded slab; r = 450 mm, h = 100 mm, f'_c = 20 MPa

For a large baseplate on a thin slab of low compressive strength, increasing the modulus of subgrade reaction increases the moment capacity and decreases the ratio of bottom to top stress. Notably, the increase and decrease of the moment capacity and ratio of bottom to top stress, respectively, is slower than when the baseplate is small.

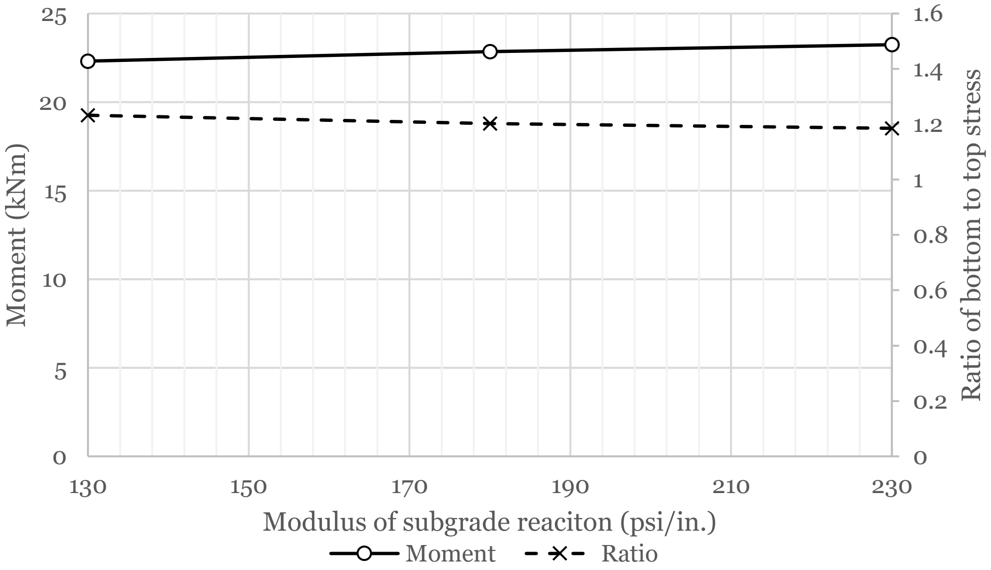

Figure 4.32: Modulus of subgrade reaction versus the moment capacity and ratio of bottom to top stress for a centrally loaded slab; r = 450 mm, h = 100 mm, f'_c = 60 MPa

For a large baseplate on a thin slab of high compressive strength, increasing the modulus of subgrade reaction increases the moment capacity and decreases the ratio of bottom to top stress.

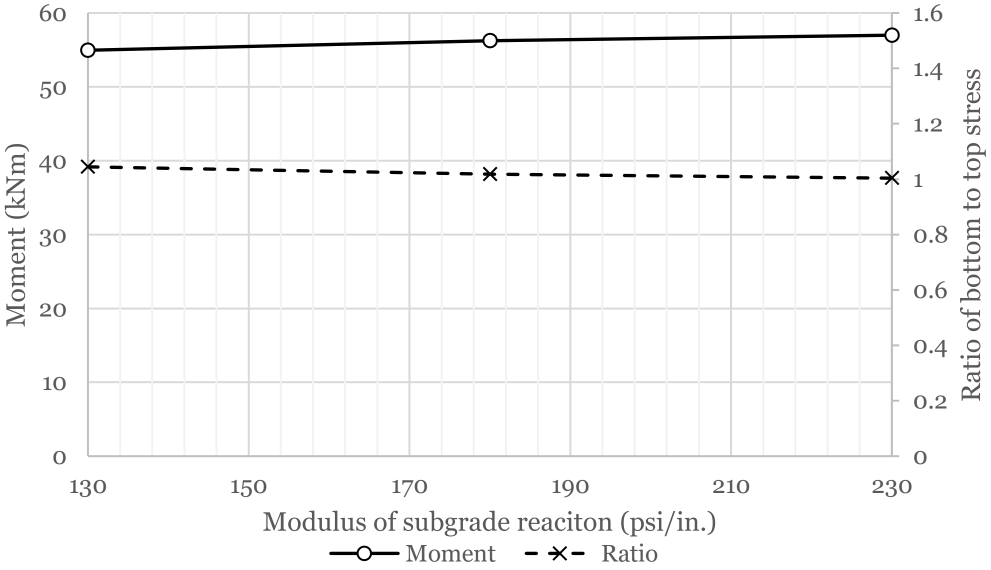

Figure 4.33: Modulus of subgrade reaction versus the moment capacity and ratio of bottom to top stress for a centrally loaded slab; r = 450 mm, h = 200 mm, f'_c = 20 MPa

For a large baseplate on a thick slab of low compressive strength, increasing the modulus of subgrade reaction increases the moment capacity and decreases the ratio of bottom to top stress.

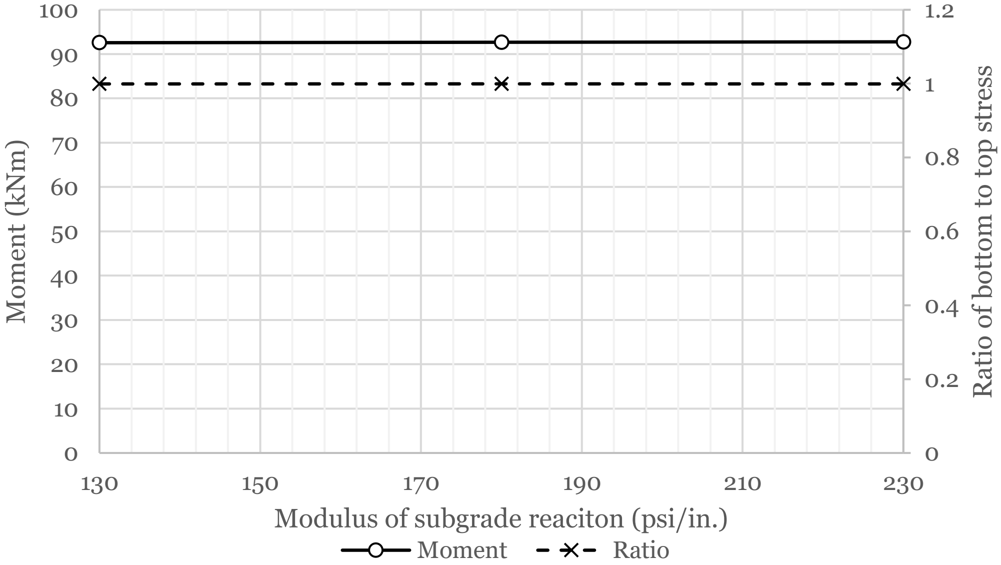

Figure 4.34: Modulus of subgrade reaction versus the moment capacity and ratio of bottom to top stress for a centrally loaded slab; r = 450 mm, h = 200 mm, f'_c = 60 MPa

For a large baseplate on a thick slab of high compressive strength, increasing the modulus of subgrade reaction increases the moment capacity and decreases the ratio of bottom to top stress. Both effects are miniscule and effectively zero. It is expected that the modulus of subgrade reaction must change dramatically to show any noticeable change in the moment capacity for this particular configuration.

The figures displayed in this section explains a lot of the behaviour that the modulus of subgrade reaction has on the moment capacity of a slab-soil system. There exists a specific modulus of subgrade reaction for every system that denotes the maximum moment capacity of the slab. This occurs when the ratio of bottom to top stress reaches unity. Like the compressive force, the effects of the modulus of subgrade reaction are most pronounced when considering flexible slabs of all baseplate sizes. For flexible slabs, increases to the modulus of subgrade reaction increase the moment capacity and decreases the ratio of bottom to top stress in the slab. For stiff slabs, changes in the modulus of subgrade reaction tend to have minimal impact on the moment capacity of the slab. In general, if the ratio of bottom to top stress is greater than unity, increasing the modulus of subgrade reaction increases the moment capacity and decreases the ratio until unity. If the ratio of bottom to top stress is less than unity, then the maximum moment capacity for the system has already been reached and subsequent increases to the modulus of subgrade reaction decreases both the moment capacity and ratio of bottom to top stress.

For the range of modulus of subgrade reaction values considered in this study (L = 130 to 230 psi/in.), the modulus of subgrade reaction plays only a minor role in affecting the moment capacity of the slab, specifically for flexible or moderately flexible slabs. For all other combinations of baseplate, slab depth, and compressive strength, the modulus of subgrade reaction had effectively no impact on the moment capacity of the slab.

4.2.6 Effects of the *f'c, h,* and *r* on *L* versus the moment capacity

The effects of various combinations of the slab depth, compressive strength, and baseplate radius and on the slab length versus the moment capacity are summarized below. In the following, k = 180 psi/in. and P = 10 kN.

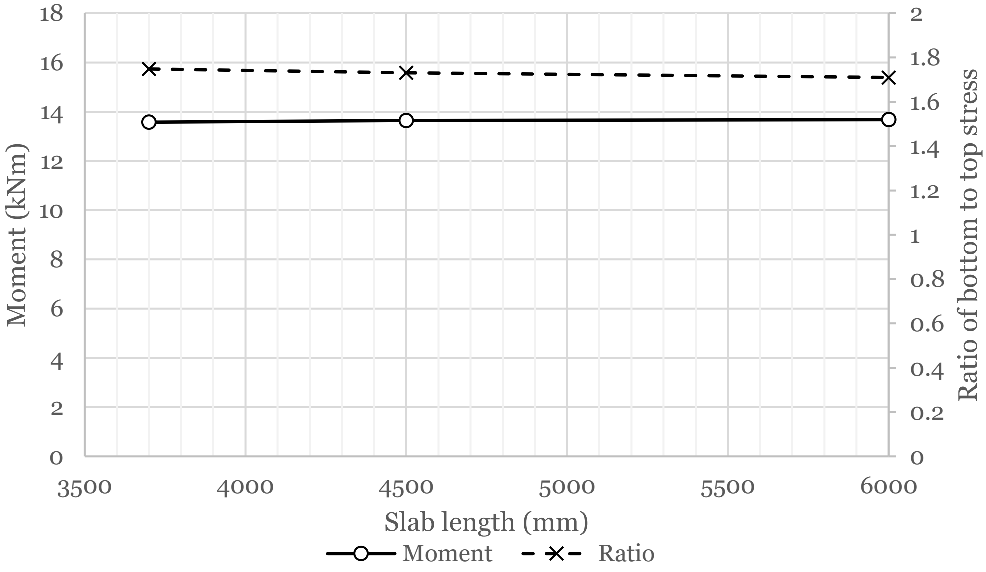

Figure 4.35: Slab length versus the moment capacity and ratio of bottom to top stress for a centrally loaded slab; r = 225 mm, h = 100 mm, f'_c = 20 MPa

For a small baseplate on a thin slab of low compressive strength, increasing the slab length increases the moment capacity and decreases the ratio of bottom to top stress. Changes to these values are miniscule, and the critical area is on the bottom surface of the slab.

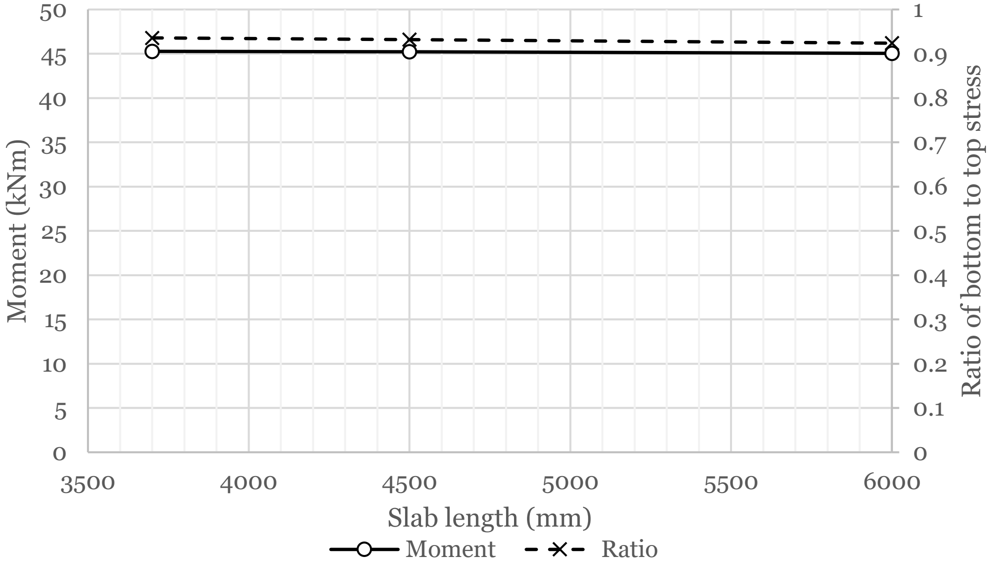

Figure 4.36: Slab length versus the moment capacity and ratio of bottom to top stress for a centrally loaded slab; r = 225 mm, h = 200 mm, f'_c = 60 MPa

For a small baseplate on a thick slab of high compressive strength, increasing the slab length decreases the moment capacity and decreases the ratio of bottom to top stress. The critical area is on the top surface of the slab.

Other combinations of the slab depth and compressive strength for a small baseplate have been omitted for conciseness, as the results obtained are very similar to the figures depicted above.

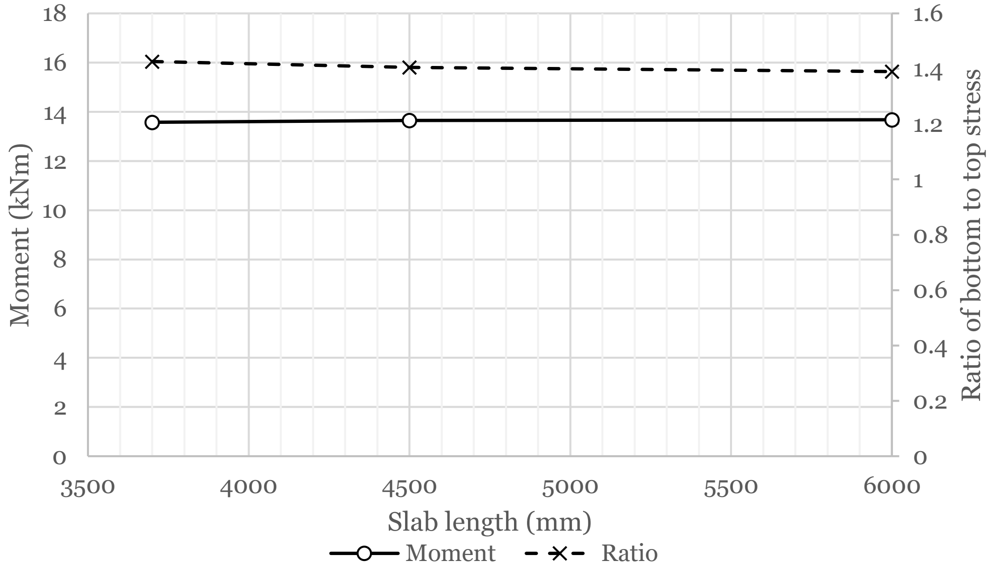

Figure 4.37: Slab length versus the moment capacity and ratio of bottom to top stress for a centrally loaded slab; r = 450 mm, h = 100 mm, f'_c = 20 MPa

For a large baseplate on a thin slab of low compressive strength, increasing the modulus of subgrade reaction increases the moment capacity and decreases the ratio of bottom to top stress. Changes to these values are, again, miniscule.

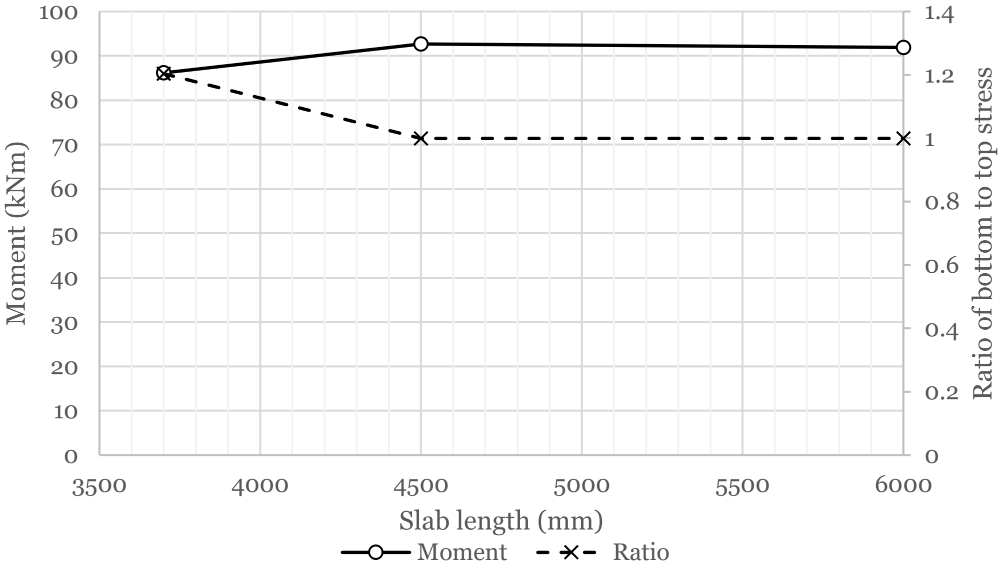

Figure 4.38: Slab length versus the moment capacity and ratio of bottom to top stress for a centrally loaded slab; r = 450 mm, h = 200 mm, f'_c = 60 MPa

For a large baseplate on a thick slab of high compressive strength, increasing the slab length until approximately L = 4500 mm rapidly increases the moment capacity and decreases the ratio of bottom to top stress until unity. Past unity, increases to the slab length only slighlty increases the moment capacity and decreases the ratio of bottom to top stress. The critical section remains on the bottom surface of the slab. Figure 4.38 appears to be an anomaly, or an outlier, given the previous plots. Figures 4.39 and 4.30 showcase additional effects of the slabs at other combinations of slab stiffness and baseplate radius:

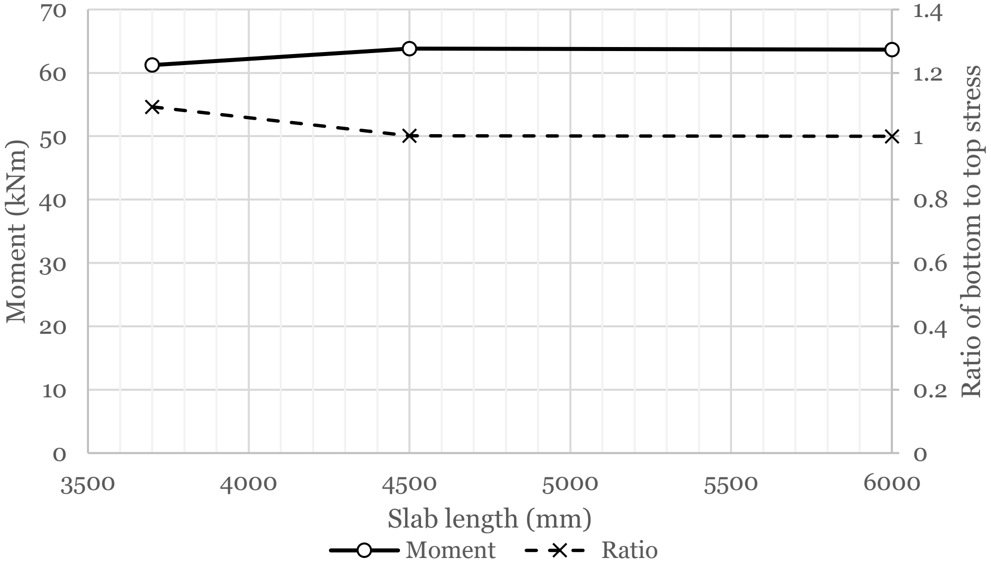

Figure 4.39: Slab length versus the moment capacity and ratio of bottom to top stress for a centrally loaded slab; *r* = 450 mm, *h* = 180 mm, *f'c* = 40 MPa

For a large baseplate on a moderately thick slab of moderate compressive strength, increasing the slab length until approximately *L* = 4500 mm increases the moment capacity and decreases the ratio of bottom to top stress until unity. Again, beyond unity, subsequent increases in the slab length results in miniscule decreases in the moment capacity and ratio of bottom to top stress. Notably, this increase and decrease are of lesser significance compared to the highly stiff slab shown in the previous figure.

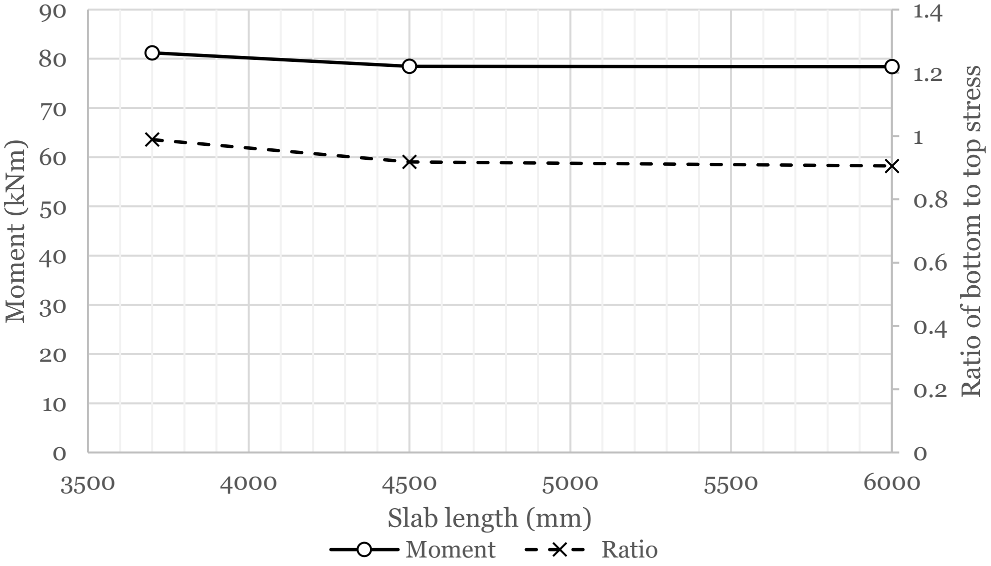

Figure 4.40: Slab length versus the moment capacity and ratio of bottom to top stress for a centrally loaded slab; *r* = 387 mm, *h* = 200 mm, *f'c* = 60 MPa

For a moderately sized baseplate on a thick slab of high compressive strength, increasing the slab length until approximately L = 4500 mm decreases the moment capacity and ratio of bottom to top stress. For this combination, the ratio of bottom to top stress is already under unity, and thus the critical section of the slab is on the top surface.

The figures displayed in this section explains a lot of the behaviour that the slab length has on the moment capacity of a slab-soil system. Like P and k, there exists a specific length for every system that denotes the maximum moment capacity of the slab. This occurs when the ratio of bottom to top stress reaches unity. For flexible slabs (i.e., combinations of thin slabs and low compressive strengths) of all baseplate sizes, the critical stress is overwhelmingly on the bottom surface of the slab, and subsequent increases to the slab length only marginally increases the moment capacity and decreases the ratio of bottom to top stress (i.e., the additional counterweight introduced by the additional area is negligible), For stiff slabs, the maximum moment capacity and stress unity is reached rapidly (i.e., L < 4500 mm), after which, subsequent increases to the slab length simply decreases the moment capacity and ratio of bottom to top stress at a very slow rate. In general, if the ratio of bottom to top stress is greater than unity, increasing the slab length increases the moment capacity and decreases the ratio until unity. If the ratio of bottom to top stress is less than unity, then the maximum moment capacity for the system has already been reached and subsequent increases to the slab length decreases both the moment capacity and ratio of bottom to top stress.

For the range of slab lengths considered in this study (L = 3700 to 6000 mm), the slab length plays a small role in affecting the moment capacity of the slab. In particular, the effects of the slab length are seen specifically for large baseplates resting on stiff slabs. For all other combinations of baseplate, slab depth, and compressive strength, the slab length had effectively no impact on the moment capacity of the slab.

4.2.7 Summary of Results

It is clear from the figures presented in this section that there were critical and less critical parameters out of the considered model parameters. In particular, the specific compressive strength of concrete, the thickness of the slab, and the radius of the baseplate were identified as the parameters with the most impact on the moment capacity of the slab. The modulus of subgrade reaction, the length of the slab, and the compressive force induced by self-weight of the crane were largely unimpactful in the scope of this study.

In general, increasing the effective stiffness of the slab (by increasing the value of any high-performance parameter) increased the total moment capacity of the slab and reduced the ratio of bottom to top stress. When a slab was very flexible, the critical area of the slab appeared on the bottom surface. As it became stiffer, the critical area eventually flipped to the top surface; when this occurred, the moment capacity continued to increase with subsequent increases to the stiffness.

In general, the behaviour of low-performance parameters could be evaluated by considering the ratio of bottom to top stress. Increasing the values of the modulus of subgrade reaction and slab length increased the moment capacity of the slab and decreased the ratio of bottom to top stress until unity, where the moment capacity reached maximum. Beyond unity, increases to the parameter values decreased both the moment capacity and ratio of bottom to top stress. For the compressive force, the reverse was true, and increasing the compressive force increased the moment capacity and ratio of bottom to top stress until unity, after which subsequent increases decreased the moment capacity but continued to increase the ratio of bottom to top stress.

4.3 Data Analysis

It is clear that at least some of the considered parameters have a non-linear relationship with the required moment for slab cracking. Therefore, a multivariate non-linear regression model will be required in order to develop a relationship between each of the parameters and the dependent variable. It should be noted that each of the independent variables considered are expected to be correlated with one another, rather than being true independent variables. This means that the rate of change in the dependent variable with respects to a change in any particular independent variable may be affected by any change in any other independent variable, as outlined in Section 4.2.

In non-linear regression, it is important to provide an initial functional form of the expected general equation. While many such non-linear forms exist (sinusoidal functions, power functions, exponential functions, etc.), a polynomial function was selected as the functional form of the regression model due to the correlated multivariate nature of the problem and the ease-of-use of creating polynomial forms. It is important when considering polynomial functions to not allow over-representation or over-fitting (i.e., fitting the equation perfectly to every data point); this is a common in higher order polynomial functions and occurs when the model begins to capture noise instead of trends in a particular dataset. In general, as the equation is to be used to predict values within a particular range of considered values rather than outside of the range, overfitting is not of significant concern.

As illustrated in the figures provided in Section 4.2, a polynomial form of order 2 appears sufficient to capture the underlying trends for each parameter without capturing any noise carried in-between. This is the case because the relationship between each parameter and the dependent variable exhibits a clear parabolic trend and/or at most a single vertex within the considered range of values. The assumption of a second-order polynomial form holds true so long as the equation is used with predictor values selected within the range of considered values used for fitting (i.e., the considered range of values for the slab length is between 3700 to 6000 mm; the fitted equation would not be appropriate for predicting the moment capacity of a slab of length 2000 or 9000 mm). Figure 4.41 and 4.42 showcases this idea:

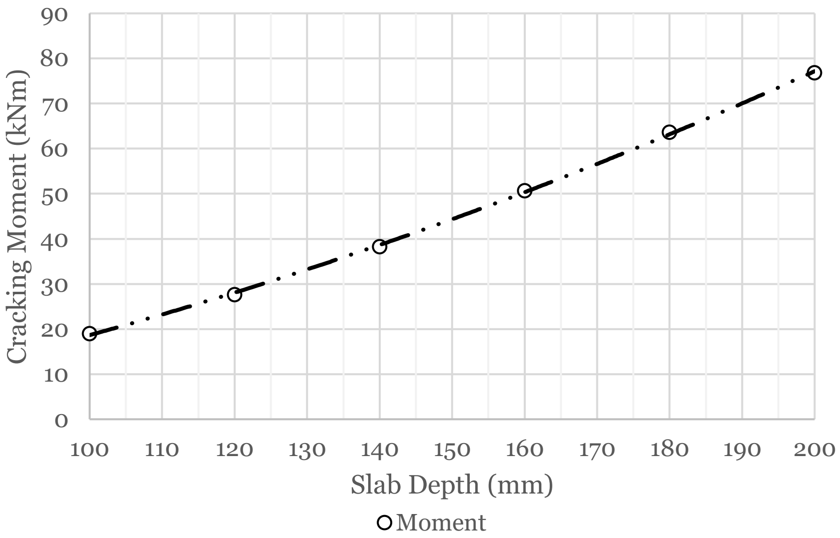

Figure 4.41: Quadratic trendline added to the relationship between slab depth and the moment capacity of a centrally loaded slab

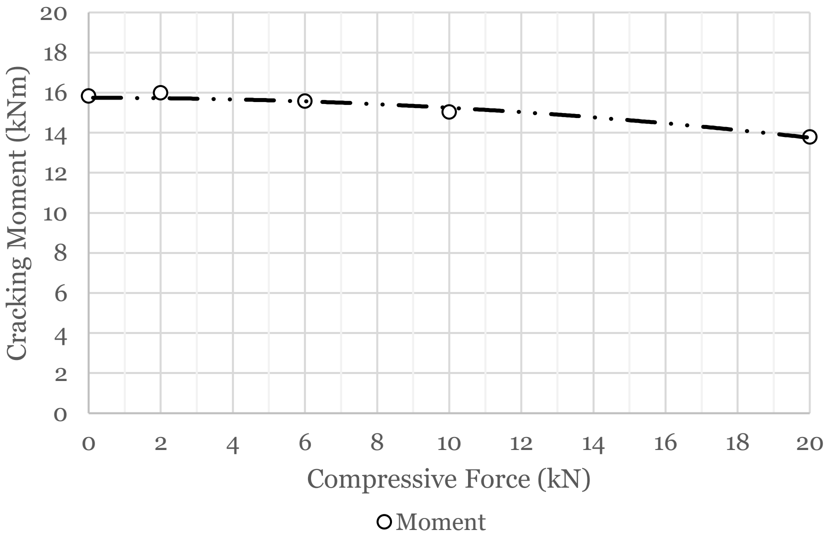

Figure 4.42: Quadratic trendline added to the relationship between the compressive force and the moment capacity of a centrally loaded slab

Equation 4.1 shows the basic form of the univariate quadratic polynomial:

$$y(x) = ax^2 + bx + c \tag{4.1}$$

in which *a, b,* and *c* are arbitrary constants to be determined via the regression model.

A multivariate quadratic polynomial with no correlation between independent variables may take the following form:

$$y(x_1, x_2) = a{x_1}^2 + b{x_2}^2 + cx_1 + dx_2 + e \tag{4.2}$$

Notably, when x_2 is taken as a static, constant value, the equation reduces to the form of the univariate quadratic polynomial presented in equation 4.1.

In the case of a correlated multivariate quadratic polynomial, additional correlation terms must be introduced between the independent variables. Consider the following:

$$y(x_1, x_2) = ax_1{}^2 + bx_2{}^2 + cx_1x_2 + dx_1 + ex_2 + f \tag{4.3}$$

The third term in the polynomial, cx_1x_2, is the correlation term that relates the two independent variables together. Again, when any independent variable is taken as a static, constant value, the equation reduces to the form of the univariate quadratic polynomial.

The general form of the correlated multivariate quadratic polynomial with n-number of independent variables used as the initial functional form of the regression model is as follows:

$$\begin{aligned} y(x_1, x_2, \dots, x_n) &= \sum_{i=1}^{n} (A_i x_i{}^2 + B_i x_i) + \sum_{i=1}^{n-1} \sum_{j=i+1}^{n} C_{ij} x_i x_j \\ &+ \sum_{i,j=1}^{n} (1 - \delta_{ij}) D_{ij} x_i{}^2 x_j + \sum_{i=1}^{n-2} \sum_{j=i+1}^{n-1} \sum_{k=j+1}^{n} E_{ijk} x_i x_j x_k \\ &+ F x_1 x_2 x_3 x_4 x_5 x_6 + G \end{aligned} \tag{4.4}$$

in which the *A, B, C, D, E, F,* and *G* are matrices of constants to be determined via the regression model. Included in this equation are the basic uncorrelated multivariate quadratic forms ($Ax_i^2 + Bx_i + G$) and also four types of correlation terms (Cx_ix_j, $Dx_i^2x_j$, $Ex_ix_jx_k$, and $Fx_1x_2x_3x_4x_5x_6$). In particular, it should be noted that this polynomial as a whole is not-quadratic; however, for any one particular independent variable, the highest power in any monomial is to the order of two, meaning that the equation is quadratic in each independent variable (i.e., the plots presented earlier in this section will retain a quadratic trendline rather than a higher-order trendline). When all but one of the independent variables are held as static, constant values, the above general equation reduces once again to the case of the general univariate quadratic polynomial.

For the purpose of data analysis, the considered range of values in this study were normalized to allow for a more accurate regression. All variables considered were normalized by rescaling the considered ranges to a unitless range of [0, 1], with the unitless value zero corresponding to the lower bound and one corresponding to the upper bound of the considered ranges.

The data analysis was completed by making use of Matlab's built-in *lsqcurvefit* function and by using a k-fold cross validation methodology. Matlab's *lsqcurvefit* determines the coefficients for a user-defined initial functional form that best fits the data set completed in a least-squares sense (MathWorks, 2012). The cross-validation method was used to reduce the likelihood of overfitting. The vast amount of data samples available makes a k-fold partition more attractive and easier to achieve good results with. The fit of the model was checked by considering the root mean squared error (RMSE), normalized root mean squared error (NRMSE), and by visual interpretation.

The procedure involved with repeated k-fold cross validation is as follows:

1. Arbitrarily and randomly distribute the sample set into k-partitions (folds) of equal size;
2. Arbitrarily and randomly assign 1 fold as the testing data set and the other folds as the training data sets;
3. Simulate the regression model on the training data set;
4. Use the fitted model to predict the testing data set;
5. Repeat steps 2 – 4, each time changing the fold used as the testing data.

For each iteration, the root mean squared error (in kNm) and the normalized root mean squared error was calculated and recorded. Table 4.1 summarizes the results obtained from the cross validation:

Table 4.1: Summary of 10-fold cross validation

	Training Data		Testing Data	
Fold	RMSE	NRMSE	RMSE	NRMSE
Iteration	kNm	--	kNm	--
1	0.57447	0.00659	0.70402	0.00852
2	0.58079	0.00666	0.66104	0.00781
3	0.58670	0.00673	0.59725	0.00766
4	0.58100	0.00667	0.64597	0.00749
5	0.58370	0.00670	0.62984	0.00763
6	0.58462	0.00671	0.61265	0.00703
7	0.60050	0.00689	0.45136	0.00526
8	0.58707	0.00674	0.59773	0.00700
9	0.57861	0.00664	0.67042	0.00771
10	0.58392	0.00670	0.62093	0.00737
Average	0.58414	0.00670	0.61912	0.00735

In general, the model obtained from any of the training folds was a good predictor for the test folds. The maximum RMSE and NRMSE observed in the testing folds were 0.7 kNm and 0.0085, respectively. The numerical results are summarized graphically in Figures 4.43 and 4.44:

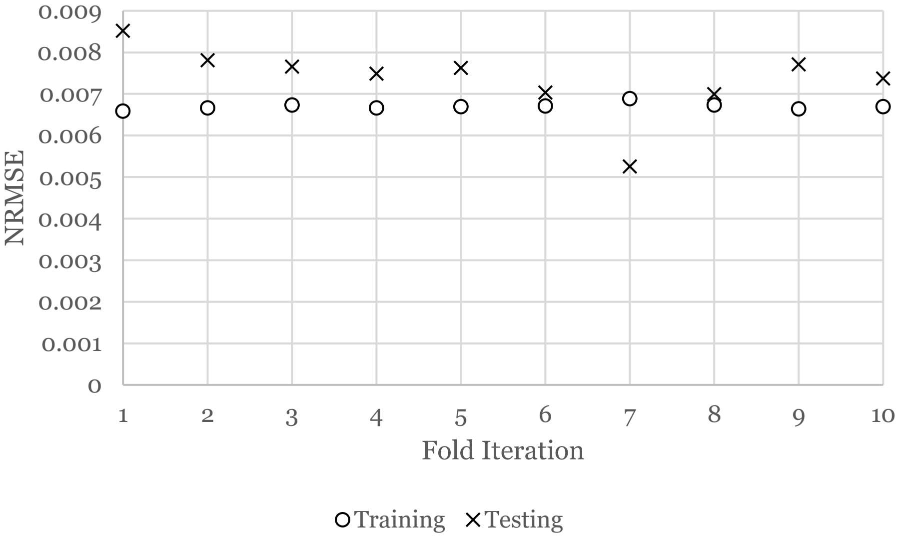

Figure 4.43: Normalized root mean squared errors for 10-fold cross validation

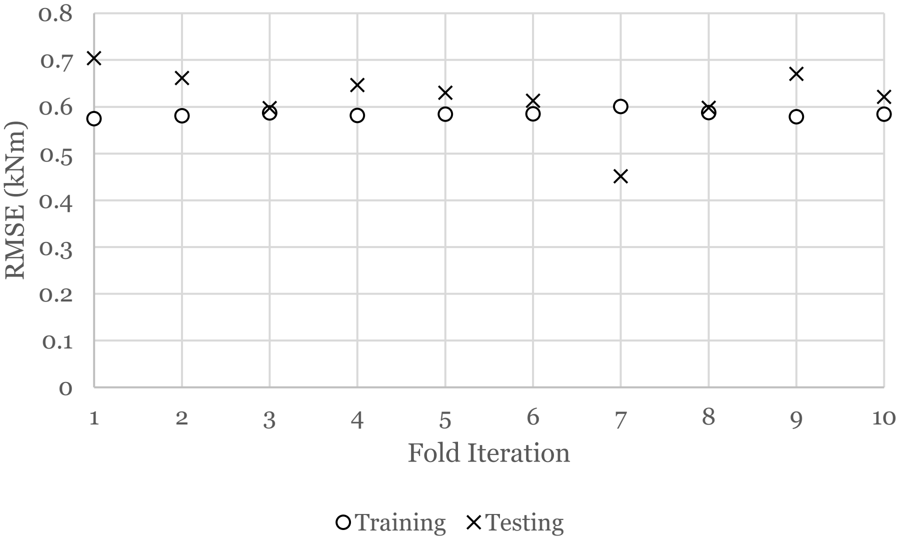

Figure 4.44: Root mean squared errors for 10-fold cross validation

Table 4.1 and Figures 4.43 and 4.44 indicate that the predictor model has good agreement with the actual expected results. The average root mean squared error observed was 0.58 kNm and 0.61 kNm for the training folds and testing folds, respectively. Since the actual range of expected moment was between approximately 6 – 90 kNm, this allowed for confidence in the model. Additionally, the average normalized root mean squared error observed was 0.067 and 0.007 for the training folds and testing folds, respectively. Again, because the normalized root mean squared errors were both very small (<< 1) and have little difference in-between the training and testing data, the predictor model was expected to be appropriate. Therefore, the coefficients for the general equation determined by fold iteration 4 was arbitrarily selected.

The general equation for a centrally loaded slab obtained from the multivariate nonlinear regression is presented:

$$\begin{aligned} M_{allow}&(x_1, x_2, x_3, x_4, x_5, x_6) \\ &= \sum_{i=1}^{6} (A_i x_i{}^2 + B_i x_i) + \sum_{i=1}^{5} \sum_{j=i+1}^{6} C_{ij} x_i x_j \\ &+ \sum_{i,j=1}^{6} (1 - \delta_{ij}) D_{ij} x_i{}^2\, x_j + \sum_{i=1}^{4} \sum_{j=i+1}^{5} \sum_{k=j+1}^{6} E_{ijk} x_i x_j x_k \\ &+ F x_1 x_2 x_3 x_4 x_5 x_6 + G \end{aligned} \tag{4.5}$$

in which M_{allow} is the unfactored maximum allowable moment for the slab-soil configuration and x_1, x_2, x_3, x_4, x_5, and x_6 are the model parameters corresponding respectively to *l,* the length of the slab, *P,* the vertical compressive force, *k,* the modulus of subgrade reaction, f'_c, the specific compressive strength of concrete, *h,* the depth of the slab, and *r,* the radius of the baseplate. Note that the order of the variables in equation 4.5 are important, as they correspond to a particular value in the matrices of coefficients. *A, B, C, D, E, F* and *G* are matrices of constants determined by the regression model and given by:

$$A = [\ 0.04168 \quad 0.02953 \quad -0.0215 \quad -0.00159 \quad 0.00754 \quad 0.07561]$$

$$B = [-0.03094 \quad 0.05616 \quad 0.00321 \quad -0.00127 \quad 0.04325 \quad 0.14564]$$

$$C = \begin{bmatrix} 0 & -0.02081 & 0.01689 & -0.00058 & 0.00751 & 0.0137 \\ 0 & 0 & 0.00229 & 0.00283 & 0.10572 & 0.11779 \\ 0 & 0 & 0 & 0.01009 & 0.0143 & 0.02387 \\ 0 & 0 & 0 & 0 & -0.0001 & 0.00912 \\ 0 & 0 & 0 & 0 & 0 & 0.19212 \\ 0 & 0 & 0 & 0 & 0 & 0 \end{bmatrix}$$

$$D = \begin{bmatrix} 0 & -0.03469 & -0.01556 & 0.00143 & -0.02744 & -0.02222 \\ 0.04249 & 0 & -0.01508 & 0.00508 & -0.02415 & 0.04417 \\ -0.00619 & 0.00389 & 0 & 0.00247 & 0.0085 & 0.00564 \\ 0.00133 & -0.00254 & -0.00262 & 0 & 0.00213 & 0.00195 \\ 0.00712 & -0.04488 & -0.01055 & 0.00227 & 0 & -0.0828 \\ -0.00875 & 0.10362 & -0.00634 & -0.00941 & 0.03886 & 0 \end{bmatrix}$$

$$E_{1,j,k} = \begin{bmatrix} 0 & 0 & 0 & 0 & 0 & 0 \\ 0 & 0 & 0.0114 & -0.00184 & 0.02205 & 0.01593 \\ 0 & 0 & 0 & -0.00114 & 0.00243 & 0.01591 \\ 0 & 0 & 0 & 0 & -0.00025 & -0.00442 \\ 0 & 0 & 0 & 0 & 0 & 0.00824 \\ 0 & 0 & 0 & 0 & 0 & 0 \end{bmatrix}$$

$$E_{2,j,k} = \begin{bmatrix} 0 & 0 & 0 & 0 & 0 & 0 \\ 0 & 0 & 0 & 0 & 0 & 0 \\ 0 & 0 & 0 & 0.00434 & 0.0019 & 0.00611 \\ 0 & 0 & 0 & 0 & -0.00258 & 0.00018 \\ 0 & 0 & 0 & 0 & 0 & 0.14974 \\ 0 & 0 & 0 & 0 & 0 & 0 \end{bmatrix}$$

$$E_{3,j,k} = \begin{bmatrix} 0 & 0 & 0 & 0 & 0 & 0 \\ 0 & 0 & 0 & 0 & 0 & 0 \\ 0 & 0 & 0 & 0 & 0 & 0 \\ 0 & 0 & 0 & 0 & -0.00632 & -0.0034 \\ 0 & 0 & 0 & 0 & 0 & 0.00268 \\ 0 & 0 & 0 & 0 & 0 & 0 \end{bmatrix}$$

$$E_{4,j,k} = \begin{bmatrix} 0 & 0 & 0 & 0 & 0 & 0 \\ 0 & 0 & 0 & 0 & 0 & 0 \\ 0 & 0 & 0 & 0 & 0 & 0 \\ 0 & 0 & 0 & 0 & 0 & 0 \\ 0 & 0 & 0 & 0 & 0 & -0.00684 \\ 0 & 0 & 0 & 0 & 0 & 0 \end{bmatrix}$$

$$F = 0.00254$$

$$G = 0.0156$$

Similar equations for the edge and corner loading cases may be found in Appendix A and B, respectively.

4.3.1 Visual comparison of model fit

While the RMSE and NRMSE presented in the previous section provides a good indicator of how the model performs, it is nonetheless worthwhile to compare predicted moment capacities versus the actual moment capacities visually. Figures 4.45 and 4.46 compares the predicted moment capacities to the actual values for various arbitrarily selected points:

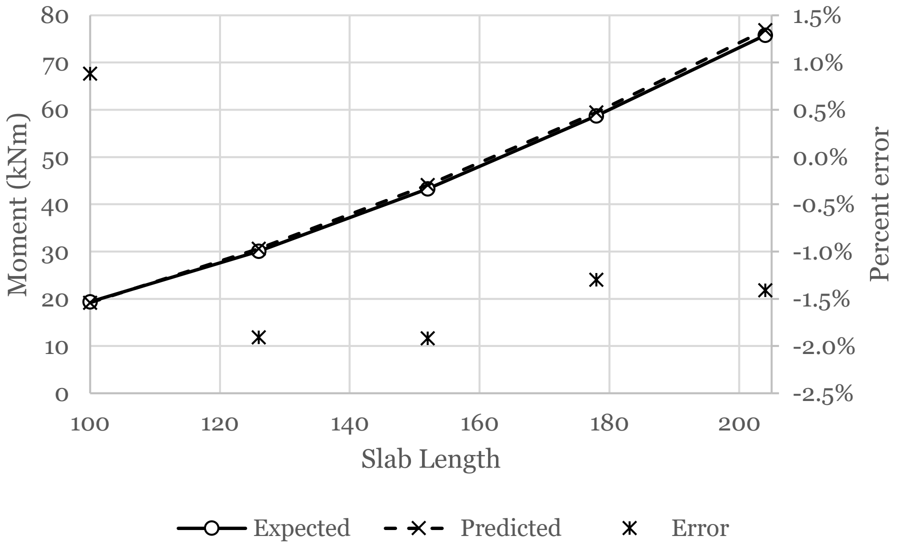

Figure 4.45: Slab depth versus moment capacity; *L* = 4,500 mm, *P* = 2 kN, *k* = 180 psi/in., *f'c* = 60 MPa, *r* = 387 mm

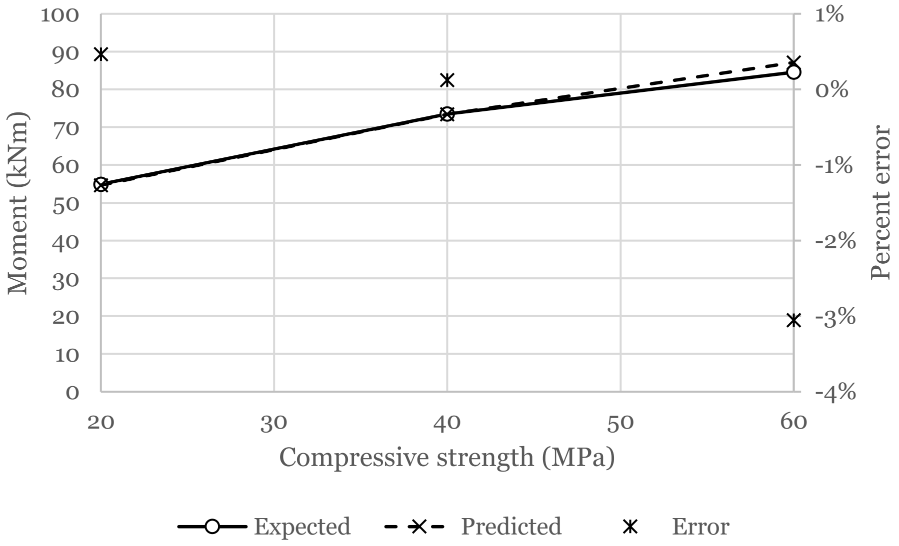

Figure 4.46: Concrete compressive strength versus moment capacity; L = 3,700 mm, P = 2 kN, k = 130 psi/in., r = 450 mm, h = 200 mm

As expected, the actual predicted values are in good agreement with the actual results. The percent errors are notated as individual data points because there is no correlation between the error and the considered independent variable. It can be seen that both flexible slab-soil systems and stiff slab-soil systems can experience a variance in the percent of error. From Figures 4.45 and 4.46, it can be seen that the error between the moment capacity predicted by the regression equation and the actual moment capacity can vary by up to 3%.

4.4 Example of Analysis Tool

The general equation has been packaged into a simple Microsoft Excel spreadsheet. The spreadsheet is composed of three portions: a user-defined input section where the input parameters are defined, an array of hidden cells containing the background calculations of the general equation, and finally an output section displaying the predicted moment capacity of the slab-on-grade. The use of the spreadsheet has been loosely summarized by considering the installation of a Gorbel WSJ360-250-12-12 workstation jib crane at the center of a warehouse slab-on-grade floor. Figure 4.47 and 4.48 showcases the dimensions and specifications for a Gorbel workstation jib crane:

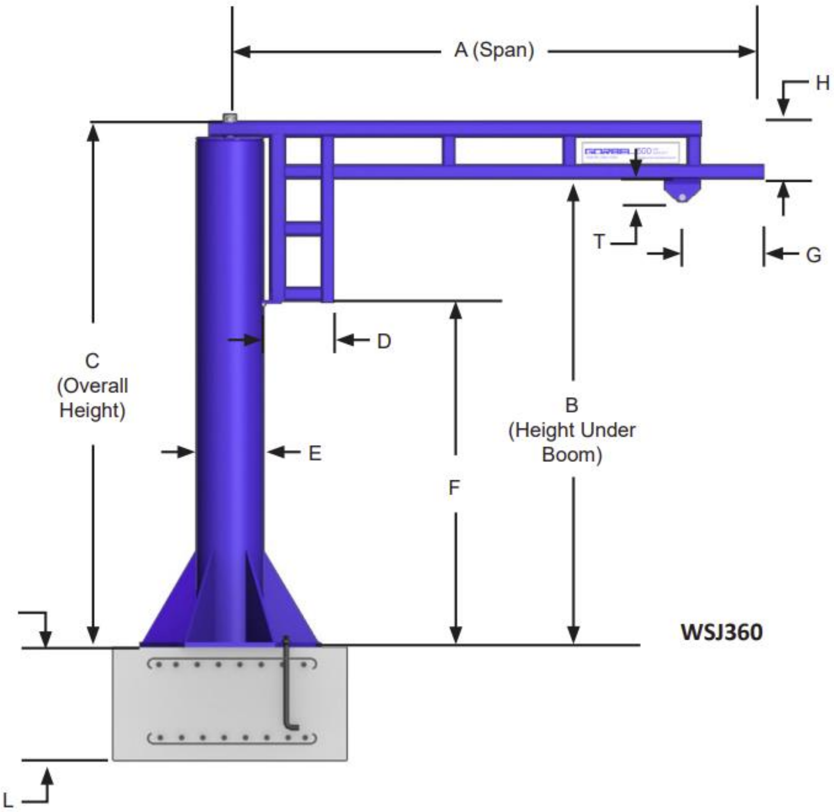

Figure 4.47: WSJ360 Free Standing Work Station Jib (Gorbel, 2012)

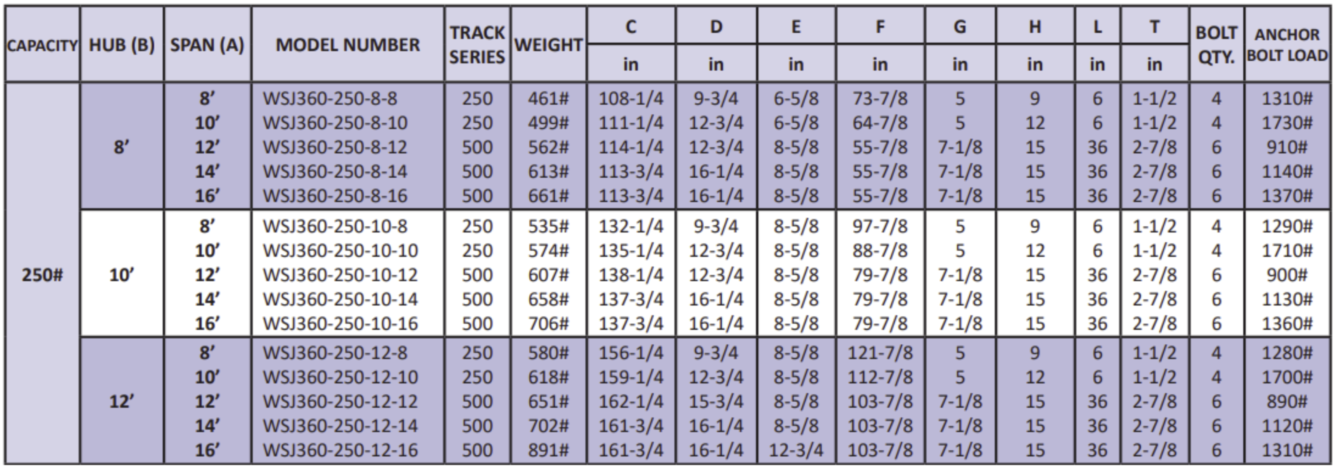

CAPACITY	HUB (B)	SPAN (A)	MODEL NUMBER	TRACK SERIES	WEIGHT	C in	D in	E in	F in	G in	H in	L in	T in	BOLT QTY.	ANCHOR BOLT LOAD
250#	8’	8’	WSJ360-250-8-8	250	461#	108-1/4	9-3/4	6-5/8	73-7/8	5	9	6	1-1/2	4	1310#
		10’	WSJ360-250-8-10	250	499#	111-1/4	12-3/4	6-5/8	64-7/8	5	12	6	1-1/2	4	1730#
		12’	WSJ360-250-8-12	500	562#	114-1/4	12-3/4	8-5/8	55-7/8	7-1/8	15	36	2-7/8	6	910#
		14’	WSJ360-250-8-14	500	613#	113-3/4	16-1/4	8-5/8	55-7/8	7-1/8	15	36	2-7/8	6	1140#
		16’	WSJ360-250-8-16	500	661#	113-3/4	16-1/4	8-5/8	55-7/8	7-1/8	15	36	2-7/8	6	1370#
	10’	8’	WSJ360-250-10-8	250	535#	132-1/4	9-3/4	8-5/8	97-7/8	5	9	6	1-1/2	4	1290#
		10’	WSJ360-250-10-10	250	574#	135-1/4	12-3/4	8-5/8	88-7/8	5	12	6	1-1/2	4	1710#
		12’	WSJ360-250-10-12	500	607#	138-1/4	12-3/4	8-5/8	79-7/8	7-1/8	15	36	2-7/8	6	900#
		14’	WSJ360-250-10-14	500	658#	137-3/4	16-1/4	8-5/8	79-7/8	7-1/8	15	36	2-7/8	6	1130#
		16’	WSJ360-250-10-16	500	706#	137-3/4	16-1/4	8-5/8	79-7/8	7-1/8	15	36	2-7/8	6	1360#
	12’	8’	WSJ360-250-12-8	250	580#	156-1/4	9-3/4	8-5/8	121-7/8	5	9	6	1-1/2	4	1280#
		10’	WSJ360-250-12-10	250	618#	159-1/4	12-3/4	8-5/8	112-7/8	5	12	6	1-1/2	4	1700#
		12’	WSJ360-250-12-12	500	651#	162-1/4	15-3/4	8-5/8	103-7/8	7-1/8	15	36	2-7/8	6	890#
		14’	WSJ360-250-12-14	500	702#	161-3/4	16-1/4	8-5/8	103-7/8	7-1/8	15	36	2-7/8	6	1120#
		16’	WSJ360-250-12-16	500	891#	161-3/4	16-1/4	12-3/4	103-7/8	7-1/8	15	36	2-7/8	6	1310#

Figure 4.48: Specifications for WSJ360 Free Standing Work Station Jib from Gorbel Brochure (Gorbel, 2012)

From Figure 4.48, a Gorbel WSJ360-250-12-12 workstation jib crane has a self-weight (excluding any loads) of 650 lbs and a maximum capacity of 250 lbs at a maximum lateral span of 12 ft. This corresponds to a total maximum self-weight of approximately 4.01 kN and an overturning moment of 4.07 kNm. The required baseplate radius for this crane is specified at approximately 387 mm. The slab and subgrade properties have been arbitrarily selected for this example as follows: the slab length, L = 5000 mm, the slab depth, h = 136 mm, the concrete strength, f'_c = 25 MPa, and the subgrade strength, k = 200 psi/in.

The established slab-soil properties and loading configuration are then inputted into the spreadsheet in the user-defined input section, as shown in Figure 4.49:

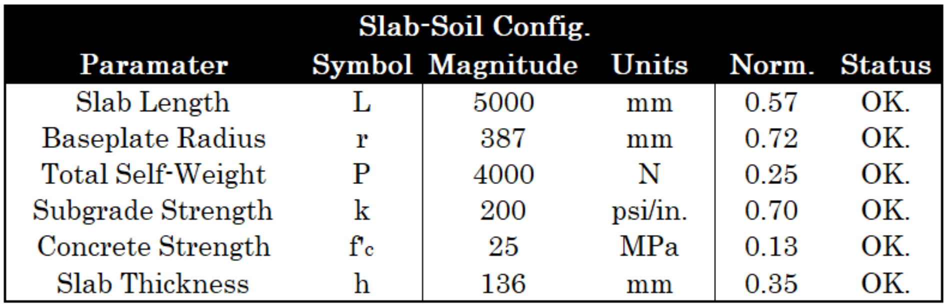

Slab-Soil Config.					
Paramater	Symbol	Magnitude	Units	Norm.	Status
Slab Length	L	5000	mm	0.57	OK.
Baseplate Radius	r	387	mm	0.72	OK.
Total Self-Weight	P	4000	N	0.25	OK.
Subgrade Strength	k	200	psi/in.	0.70	OK.
Concrete Strength	f'c	25	MPa	0.13	OK.
Slab Thickness	h	136	mm	0.35	OK.

Figure 4.49: User-defined input section of analysis tool

The initial parameters are inputted under the “Magnitude” column and are subsequently normalized under the “Norm.” column. If the normalized value of a particular parameter is less than zero or greater than one, a warning is issued under the column marked as “Status”. This indicates that the input value is outside of the range of values considered in the study, and therefore the spreadsheet would not be able to accurately predict the cracking moment. In this case, all of the inputted values are within the range of values considered, and therefore are all acceptable.

The spreadsheet handles all of the background calculations associated with equation 4.5 in a set of protected and hidden cells, as shown in Figure 4.50:

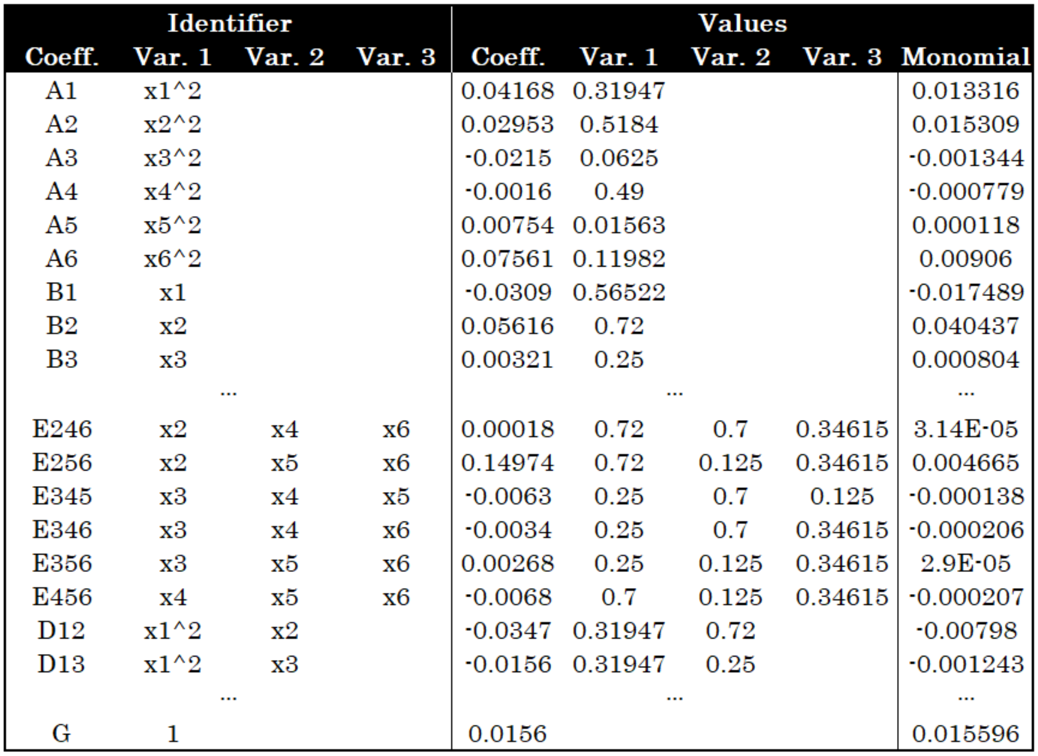

Identifier				Values				
Coeff.	Var. 1	Var. 2	Var. 3	Coeff.	Var. 1	Var. 2	Var. 3	Monomial
A1	x1^2			0.04168	0.31947			0.013316
A2	x2^2			0.02953	0.5184			0.015309
A3	x3^2			-0.0215	0.0625			-0.001344
A4	x4^2			-0.0016	0.49			-0.000779
A5	x5^2			0.00754	0.01563			0.000118
A6	x6^2			0.07561	0.11982			0.00906
B1	x1			-0.0309	0.56522			-0.017489
B2	x2			0.05616	0.72			0.040437
B3	x3			0.00321	0.25			0.000804
		...				...		...
E246	x2	x4	x6	0.00018	0.72	0.7	0.34615	3.14E-05
E256	x2	x5	x6	0.14974	0.72	0.125	0.34615	0.004665
E345	x3	x4	x5	-0.0063	0.25	0.7	0.125	-0.000138
E346	x3	x4	x6	-0.0034	0.25	0.7	0.34615	-0.000206
E356	x3	x5	x6	0.00268	0.25	0.125	0.34615	2.9E-05
E456	x4	x5	x6	-0.0068	0.7	0.125	0.34615	-0.000207
D12	x1^2	x2		-0.0347	0.31947	0.72		-0.00798
D13	x1^2	x3		-0.0156	0.31947	0.25		-0.001243
		...				...		...
G	1			0.0156				0.015596

Figure 4.50: Calculation cells of analysis tool

Figure 4.50 depicts a sample of the calculation cells. Finally, the spreadsheet sums all of the calculated monomials to establish a normalized cracking moment. De-normalizing consequently produces the moment capacity of the slab:

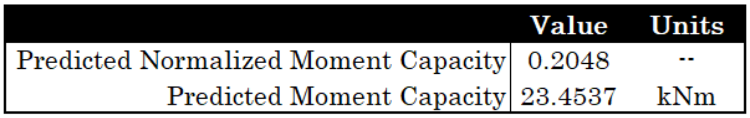

	Value	Units
Predicted Normalized Moment Capacity	0.2048	--
Predicted Moment Capacity	23.4537	kNm

Figure 4.51: Output section of analysis tool

For the example shown in this section, the moment capacity predicted by the analysis tool is 23.45 kNm, which is signifincalty greater than the actual moment induced on the slab by the eccentric loading of 4.07 kNm. This indicates that the configuration of the slab-on-grade is more than capable of safely handling the installation and operation of the WSJ360-250-12-12 workstation jib crane at the center of a slab-on-grade.

For completeness, the slab-soil properties and loading conditions were simulated in Abaqus. The actual moment that causes the maximum principal stress to exceed the modulus of rupture of the concrete for this configuration was found to be approximately 23.95 kNm, which is within 2% of the predicted moment capacity.

Readers are advised to contact the author to obtain the spreadsheet.

5.0 Conclusions

5.1 General Remarks

In this study, a general equation used to predict the moment capacity for plain, unreinforced concrete slabs subject to combined axial and overturning moments induced by foundationless jib cranes was developed via a nonlinear regression model and the mass simulation of finite element models in Abaqus. Three loading cases (central, near the edge, and near the corner) and six correlated parameters (radius of baseplate, slab thickness, specific compressive strength of concrete, modulus of subgrade reaction, compressive force, and slab length) were considered. The range of considered values for each parameter was selected based on the minimum requirements outlined by commercial crane manufacturing companies. The subgrade model was presented as a simplified elastic half-space based on an equivalent Winkler model and modulus of subgrade reaction.

The following conclusions were drawn from the results obtained in this study:

- In general, when the maximum principal stress is of primary concern, the use of an equivalent modulus of elasticity in place of the modulus of subgrade reaction determined by equating the analytical solutions for a long plate subject to a concentrated load resting on an elastic half-space or a Winkler model produces sufficiently equivalent results, especially under the loaded region. In particular, when calibrated for deflections, the maximum principal stress observed in the slab resting on an equivalent elastic half-space was only 10 – 15% less than that observed stress when resting on the actual Winkler model.
- The moment capacity of the slab was found to be, in general, significantly higher when loaded centrally compared to near the edge or corner. This is mostly due to the reduced volume of slab producing a counter-balancing effect on the applied moment, resulting in larger stresses developing in the bottom surface of the slab.
- For all loading cases, the area over which a load is distributed, the specific compressive strength of concrete, and the thickness of the slab were critical parameters in controlling the maximum moment capacity of the slab. Increasing the values of any of these parameters also directly increased the moment capacity. Within the range of considered values, these parameters can be considered the most critical.
- For all loading cases, the compressive force had a limited impact on the moment capacity of the slab for values within the considered range. In particular, flexible slabs were more prone to impactful changes in the moment capacity with respects to changes to the compressive force compared to stiffer slabs. In most cases, the compressive force would need to be significantly higher than the upper bound considered in this study to have a pronounced and significant affect.
- For all loading cases, the length of the slab had a limited impact on the moment capacity of the slab. In general, the minimum slab length used in the study of L = 3700 mm was

sufficiently long enough to produce insignificant changes with subsequent increases to the length. In particular, for slabs of high rigidity or for slabs loaded near the edge or the corner, the length of slab required to be sufficiently long increased to approximately L = 5000 mm. As long as the length of slab is sufficiently long, further increases to the length yield negligible impact on the moment capacity.

- For all loading cases, the modulus of subgrade reaction had a negligible impact on the moment capacity of the slab, especially within the range of considered values. The effects of the modulus of subgrade reaction were found to be slightly more pronounced for flexible slabs. An approximate value of the modulus of subgrade reaction is sufficient in capturing the critical moment capacity of a slab system. This falls in line with the conclusions developed by Westergaard (1926).
- The general, non-linear equation developed by the regression model predicts the moment capacity of a slab mounted with a jib crane with a mean squared error of 0.58 kNm; therefore, the general equation provides a good prediction when the values of the model parameter fall within the bounds of the range of considered values. The model is not developed with the intent to capture forecasting for values outside of the considered range.
- In regard to practical applications of crane installation, this study showed that the general rule of thumb of adopting an upper bound of 8 kip-ft (approximately 10.6 kNm) as the maximum allowable overturning moment is misguided. Crane manufacturers will often install cranes licensed at larger capacities (up to 21.6 kNm of overturning moment) or install cranes on slab-soil configurations with dimensions and/or properties lower than the specified requirements. The moment capacities of slabs in the latter category may be as low as 6.5 kNm. While the rule-of-thumb may often be ‘good enough’ for typical installations, the analytical tool produced from this study provides an additional layer of safety for checking cranes of larger capacity mounted to less-than-satisfactory slab-soil configurations.
- In regard to practical applications of crane installation, the analytical tool developed in this study is recommended to be used in conjunction with other slab-on-grade design checks, including one- and two-way shear, compressive bearing of concrete, compressive bearing of soil, allowable slab deflection, and anchor-associated failure, all of which are readily available and accessible.

5.2 Future Work

The scope of the work completed in this study specifically captures the maximum principal stresses observed in the top and bottom surface of the slab. It is recommended to additionally consider the effects of the outlined parameters on the maximum upwards and downwards deflections. For instance, it is expected that the deflections of the slab are more sensitive to changes in the modulus of subgrade reaction, as identified in earlier sections.

Furthermore, the work completed in this study was specifically concerned with slab failure defined by an observed maximum principal stress exceeding the modulus of rupture. Post-cracking behavior was considered outside the scope of this study. Therefore, it is also recommended to investigate the cracking patterns and post-linear elastic behavior of the slab.

The parametric study was completed with discrete loading cases (i.e., center, near the edge, near the corner). As a result, a general equation was produced for each case. It is recommended to simulate the finite element models further at several other locations between the center, edge, and corner cases. In this fashion, the distance between the center of the loaded region and the center of the slab may be considered as another model parameter, negating the need for additional, independent equations. Along this line of thought are the baseplate sizes considered in this study. It would be beneficial to the regression model to consider at least one additional baseplate size (r = 300 mm) to complement the considered radii values.

Lastly, the general equation was developed in the form of a multivariate correlated second order polynomial function. While the performance is sufficiently accurate for predictor values within the range of considered values, the functional form is inefficient and was originally selected due to ease of use. It is recommended that, if replicated, future equations be developed using spline analysis or Weibull survival regression modelling techniques.

References

Adebar et al. 2017. Concrete Design Handbook, 4 ed. Cement Association off Canada. ON, Canada.

Biot, M. A. 1935. Effect of Certain Discontinuities on the Pressure Distribution in a Loaded Soil. *Journal of Applied Physics,* 6: 367-375.

Biot, M. A. 1937. Bending of an Infinite Beam on an Elastic Foundation. *Journal of Applied Mechanics, ASME,* 4: 1-7.

Bowles, J. E. 2001. Foundation Analysis and Design, 5 ed. McGraw-Hill, NY, USA.

Boussinesq, J. 1885. Application des Potentiels a l'Etude de l'Equilibre et du Mouvement des Solides Elastique. Paris, France.

Cheung, Y.K. and Zienkiewicz, O.C. 1965. Plates and Tanks on Elastic Foundations – An Application of Finite Element Methods. *International Journal of Solid Structures*, 1: 451-461

Christopher, B. R. and Schwartz, C. 2006. Geotechnical Aspects of Pavements. Federal Highway Administration and U.S. Department of Transportation. USA.

Council of American Buildings Officials. 1995. CABO: One- and Two-Family Dwelling Code: Under the Nationally Recognized Model Codes. Council of American Building Officials, USA.

Daloglu A. T., Vallabhan C. V. 2000. Values of k for Slab on Winkler Foundation. *Journal of Geotechnical Geoenvironmental Engineering,* 126(5).

Davids, B. W. 2003. EverFE: Software for the 3D Finite Element Analysis of Jointed Plain Concrete Pavements. The University of Maine and Washington.

Filonenko-Borodich, M. M. 1945. A Very Simple Model of an Elastic Foundation Capable of Spreading the Load. Sb. Tr. Mosk. Elektro. Inst. Inzh. Trans. No: 53 Transzheldorizdat

Galin, L. A. 1943. On the Winkler-Zimmermann Hypothesis for Beams. *Journal of Applied Mathematics and Mechanics,* 7(4): 293-300.

Gorbel. 2012. Installation, Operation, & Maintenance Manual. NY, USA.

Gorbunov-Posadov, M. I. 1940. Analysis of Beams and Plates on an Elastic Half-Space. *Journal of Applied Mathematics and Mechanics,* 4(3): 60-80

Gorbunov-Posadov, M. I. 1959. Tables for Analysis of Thin Plates Resting on Elastic Foundations. Gosstroiizdat. Moscow, Russia.

Gorbunov-Posadov, M. I. and Serebrjanyi, R.V. 1961. Design of Structures on Elastic Foundations. *International Conference of Soil Mechanics*, 1: 643-648

Gurbuv, A., and Avci, B. 2018. Modulus of Subgrade Reaction that Varies with Magnitude of Displacement of Cohesionless Soil. *Arabian Journal of Geosciences*, 11(13)

Hertz, H. 1884. Miscellaneous Papers: On the Equilibrium of Floating Elastic Plates. *Wiedemann's Annalen der Physik und Chemie*, 22: 449 – 445.

Hetenyi, M. 1946. *Beams on Elastic Foundation,* Cushing-Malloy, Ann Arbor, MI, USA.

Hogg, A. H. A. 1938. Equilibrium of a thin Plate Symmetrically Loaded and Resting on an Elastic Foundation of Infinite Depth. *London Philosophical Magazine and Journal of Science,* 7(25): 576-582.

Horvath, J. S. 1983. Modulus of Subgrade Reaction: New Perspective. *Journal of Geotechnical Engineering, ASCE* 109(12): 1567-1587.

Hu, C. and Hartley, G. A. 1994. Elastic Analysis of Thin Plates with Beam Supports. *Engineering Analysis with Boundary Elements,* 13(3): 229-238.

Ioannides, A. M. 1984. Analysis of Slabs-on-grade for a Variety of Loading and Support Conditions. University of Illinois at Urbana-Champaign, IL, USA.

Ioannides, A. M., Thompson M. R., and Barenberg E. J. 1985. Westergaard Solutions Reconsidered. *Transportation Research Record.* 1043: 13-23.

Ioannides, A. M. 2005. Stress Prediction for Cracking of Jointed Plain Concrete Pavements. *Transportation Research Record.* 1919: 47-53.

Ioannides, A. M. 2006. Concrete Pavement Analysis: The First Eighty Years. *International Journal of Pavement Engineering,* 7(4): 233-249.

Ioannides, A. M., Peng J., and Swindler J.R. 2006. ABAQUS model for PCC slab cracking. *International Journal of Pavement Engineering,* 7(4): 311-321.

Kerr, A.D. 1964. Elastic and Viscoelastic Foundation Models. *Journal of Applied Mechanics, ASME,* 31(3): 491-498.

Kulhawy, F. H. and Mayne, P. W. 1990. Manual on Estimating Soil Properties for Foundation Design. Electric Power Research Institute. CA, USA.

Lenczner, D. 1962. Bending Moments and Pressure on Model Footings. *Concrete and Constructional Engineering,* 57: 181-187

Lukanen, E. 2002. Load Testing of Instrumented Pavement Sections. University of Minnesota. MN, USA.

Nielson, F.D. 1967. Modulus of Soil Reaction as Determined from the Triaxial Shear Test. *Highway Research Record,* 185: 80-90.

Nielson, F.D., Bhandhausavee, C., and Yeb, K. S. 1969. Determination of the Modulus of Soil Reaction from Standard Soil Tests. *Highway Research Record,* 285: 1-2

Mallela, J., Glover, L. T., Liang, R. Y., Chou, E. Y. 2009. Guidelines for Implementing NCHRP 1-37A Design Procedures. Federal Highway Administration and U.S. Department of Transportation. USA.

MathWorks. 2012. User Manual. The MathWorks Inc. MA, USA.

McKinney A. W. et al. 2006. *ACI 360R-06 Design of Slabs-on-Ground*. American Concrete Institute, USA.

Meyerhof, G. G. 1965. Shallow Foundations. *Journal of Soil Mechanics, ASCE,* 91(2): 21-31.

O'Donnel, M. 2016. Airport Pavement Design and Evaluation. Federal Aviation Administration and U.S. Department of Transportation. USA.

Packard R. G. 1996. *Slab Thickness Design for Industrial Concrete Floors on Grade*, Portland Cement Association, IL, USA.

Recordon, E. 1957. Determination of Soil Characteristics Necessary for Foundation Calculations of Elastic Soils. *International Conference of Soil Mechanics*, 1: 414-418

Reissner, E. 1955. On Transverse Vibrations of Thin, Shallow Elastic Shells. *Quarterly of Applied Mechanics, Brown University*, 13(2): 169-176.

Reti, A. A. 1967. Suggested Design Procedure for Combined Footings and Mats. American Concrete Institute. USA.

Ringo B. C. and Anderson R. B. 1996. *Designing Floor Slabs on Grade: Step-by-Step Procedures, Sample Solutions, and Commentary*. 2nd ed., The Aberdeen Group, IL, USA.

SCDOT. 2019. Geomechanics Design Manual. South Carolina Department of Transportation. South Carolina State library, USA.

Selvadurai, A.P.S. 1979. Elastic Analysis of Soil-Foundation Interactions. *Development in Geotechnical Engineering*. Elsevier Ltd. NY, USA.

Selvadurai, A.P.S. and Shi, L. 2015. Biot's problem for a Biot material. *International Journal of Engineering Science*, 97:133-147.

Silva, A.R.D., Silveria, R.A.M., Goncalves, P.B. 2001. Numerical Methods for Analysis off Plates on Tensionless Elastic Foundations. *International Journal of Solids and Structures*, 38(10): 2083-2100.

Smith, M. 2009. ABAQUS/Stander User's Manual. Dassault Systemes Simulia Corp. VV, France.

Snowden, W. L. 1981. Design of Slab-on-Ground Foundations. Wire Reinforcement Institute.

Spanco. 2018. 600-Series Foundationless Jib Crane Manual Addendum. PA, USA.

Spears, R. E. 1983. *Concrete Floors on Ground*. 2nd ed., Portland Cement Association, IL, USA.

Straughan, W. T. 1990. Analysis of Plates on Elastic Foundations. Texas Tech University.

Tanahashi, H. 2007. Pasternak Model Formulation of Elastic Displacements in the Case of a Rigid Circular Foundation, *Journal of Asian Architecture and Building Engineering,* **6**(1), 167-173.

Teng, W. C. 1962. Foundation Design. Prentice Hall Trade. NJ, USA.

Terzaghi, K. 1955. Evaluation of Coefficients of Subgrade Reaction. *Geotechnique*, 5(4): 41-50.

Thornton, W. A., et al. 2011. AISC Steel Construction Manual. American Institute of Steel Construction

U.S. Department of the Army and Airforce. 1987. Concrete Floors Slabs on Grade Subjected to Heavy Loads, Technical Manual No. 5-809-12. DC, USA.

Vallabhan, C. V., Straughan, W. T., Das, Y. C. 1991. Refifned Model for Analysis of Plates on Elastic Foundations. *Journal of Engineering Mechanics, ASCE,* 117(12): 2830-2843

Vesic A. S. 1961. Bending of Beams Resting on Isotropic Elastic Solid*, Journal of Soil Mechanics and Foundations Division, ASCE,* **87**(2): 35-53.

Vlasov V. Z. and Leontiev U. N. 1966. Beams, Plates and Shells on Elastic Foundations, *Isreal Program for Scientific Translations,* Jerusalem.

Weisman, G.F. and White, S.R. 1961. Small Angular Deflections of Rigid Foundations. *Geotechnique,* 11: 186-202.

Westergaard H. M. 1926. Stresses in Concrete Pavements Computed by Theoretical Analysis. *Public Roads,* 7(2): 25-35.

Westergaard H. M. 1939. Bearing Pressure and Cracks. *Journal of Applied Mechanics,* 6(2): 49-53.

Westergaard H. M. 1943. Stress Concentrations in Plates Loaded Over Small Areas, *Transactions of the American Society of Civil Engineers,* ASCE, 108(1): 831-886.

Westergaard H. M. 1948. New Formulas for Stresses in Concrete Pavement of Airfields. *Transactions of the American Society of Civil Engineers,* ASCE, 113(1): 425-439.

Winkler E. 1867. *Die Lehre von Elastizitat und Festigkeit (on Elasticity and Fixity).* Dominicus, Prague.

Worku, A. 2009. Winkler's Single Parameter Subgrade Model from the Perspective of an Improved Approach of Continuum-Based Subgrade Modeling, *Zede Journal,* 26(1).

Wong et al. 2015. Handbook of Steel Construction, 11 ed. *Canadian Institute of Steel Construction*. ON, Canada.

Wyman, M. 1950. Deflections of an Infinite Plate. *Canadian Journal of Engineering,* 28(3): 293-302.

Young, W. C., Budynas, R. G. 2001. Roark’s Formulas for Stress and Strain. McGraw Hill. NY, USA.

Appendices

Appendix A – Edge Loading Case

The relationships of the critical model parameters and the moment capacity of a slab with an edge loaded crane obtained from the parametric study have been summarized below. Additionally, figures showcasing the effects of any particular model parameter on the relationship between any other model parameter and the moment capacity of the slab are provided.

Table A.1: Coefficients for general equation, edge loaded case

x_{ijk}	Value
A1	0.03565
A2	-0.1176
A3	-0.0366
A4	-0.0006
A5	-0.0042
A6	0.06856
B1	-0.017
B2	0.20156
B3	0.00901
B4	-0.0052
B5	0.0755
B6	0.21126
C12	-0.2844
C13	0.01254
C14	0.00288
C15	0.02331
C16	0.06488
C23	0.00529
C24	0.00775
C25	0.02652
C26	0.0456
C34	0.01626
C35	0.0109
C36	0.00545
C45	0.00339
C46	0.00704
C56	0.16294
E123	-0.0219
E124	0.00299
E125	0.06179
E126	0.12046
E134	-0.0051
E135	-0.0094
E136	-0.0208
E145	-0.0017
E146	-0.0008
E156	0.0088
E234	-0.0024
E235	0.00913
E236	-0.0105
E245	-0.0079
E246	-0.0052
E256	0.09747
E345	-0.0064
E346	-0.0048
E356	-0.0088
E456	-0.0073
D12	-0.019
D13	0.00285
D14	-0.0025
D15	-0.0557
D16	-0.1227
D21	0.28364
D23	0.01894
D24	-0.0009
D25	-0.008
D26	0.02547
D31	0.00678
D32	0.00872
D34	0.00041
D35	0.01214
D36	0.0267
D41	0.00015
D42	-0.0007
D43	-0.0023
D45	0.0014
D46	6.6E-05
D51	0.00028
D52	-0.0278
D53	-0.0099
D54	0.0023
D56	-0.067
D61	0.00236
D62	0.11191
D63	-0.0059
D64	-0.0002
D65	0.08994
F	0.02014
G	0.00755

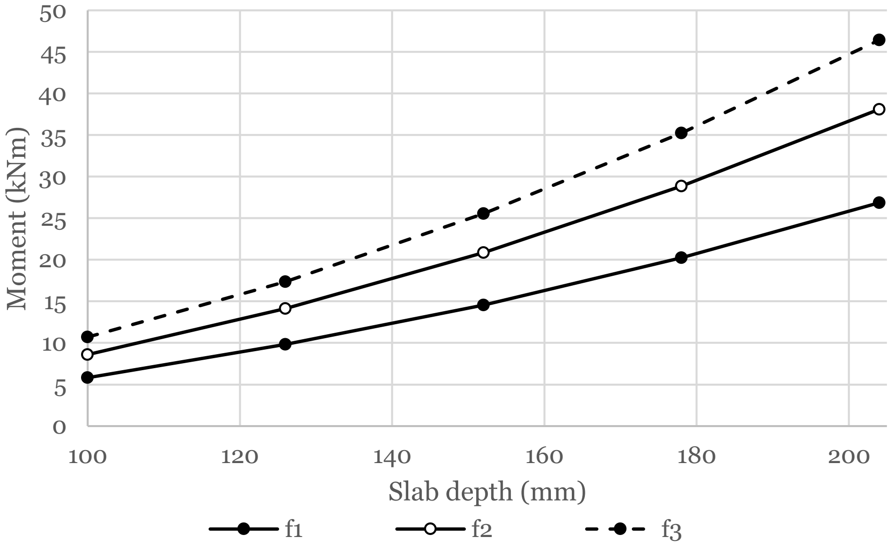

Figure A.1: Effects of compressive strength and baseplate radius on the slab depth versus the moment capacity for an edge loaded slab; $f'_{c,1}$ = 20 MPa, $f'_{c,2}$ = 40 MPa, $f'_{c,3}$ = 60 MPa, r = 225 mm, P = *10* kN, L = 4500 mm, and k = 180 psi/in.

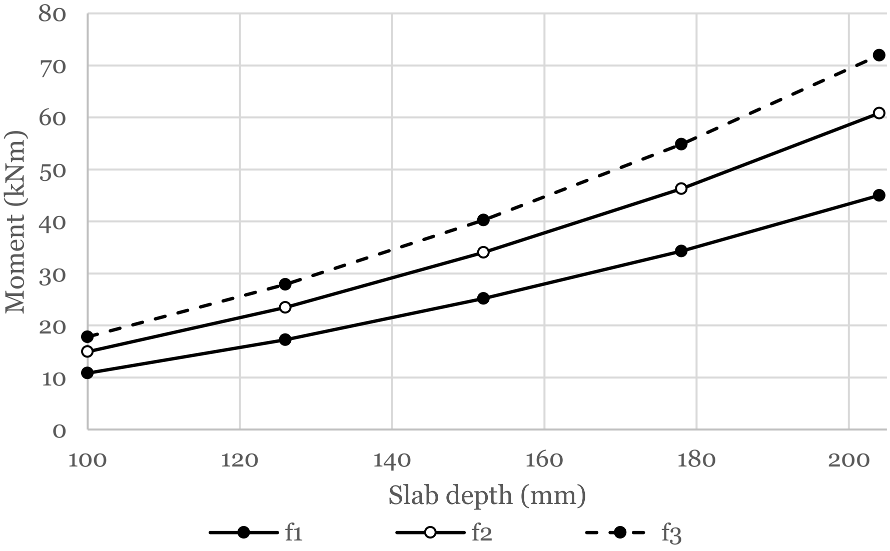

Figure A.2: Effects of compressive strength and baseplate radius on the slab depth versus the moment capacity for an edge loaded slab; $f'_{c,1}$ = 20 MPa, $f'_{c,2}$ = 40 MPa, $f'_{c,3}$ = 60 MPa, r = 225 mm, P = *10* kN, L = 4500 mm, and k = 180 psi/in.

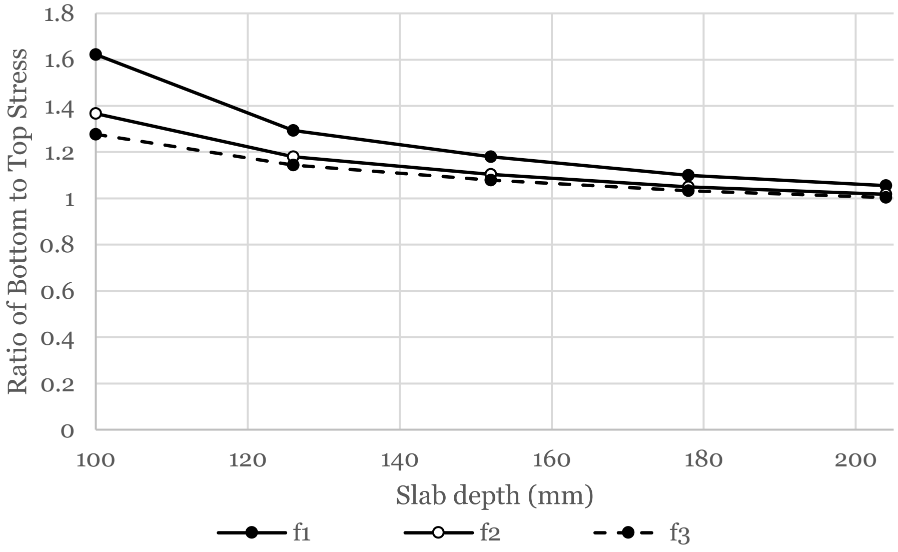

Figure A.3: Effects of compressive strength and baseplate radius on the slab depth versus the ratio of bottom to top stress for an edge loaded slab; $f'_{c,1}$ = 20 MPa, $f'_{c,2}$ = 40 MPa, $f'_{c,3}$ = 60 MPa, r = 225 mm, P = *10* kN, L = 4500 mm, and k = 180 psi/in.

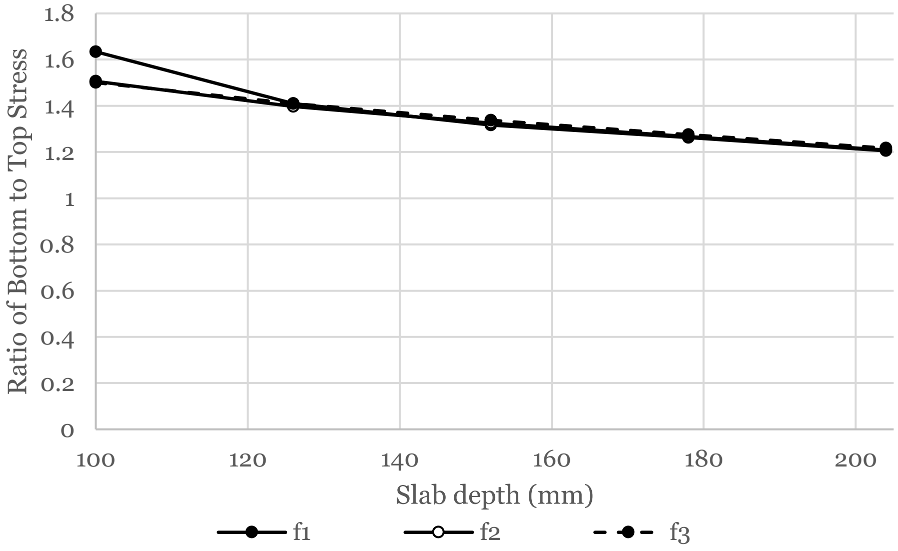

Figure A.4: Effects of compressive strength and baseplate radius on the slab depth versus the ratio of bottom to top stress for an edge loaded slab; $f'_{c,1}$ = 20 MPa, $f'_{c,2}$ = 40 MPa, $f'_{c,3}$ = 60 MPa, r = 387 mm, P = *10* kN, L = 4500 mm, and k = 180 psi/in.

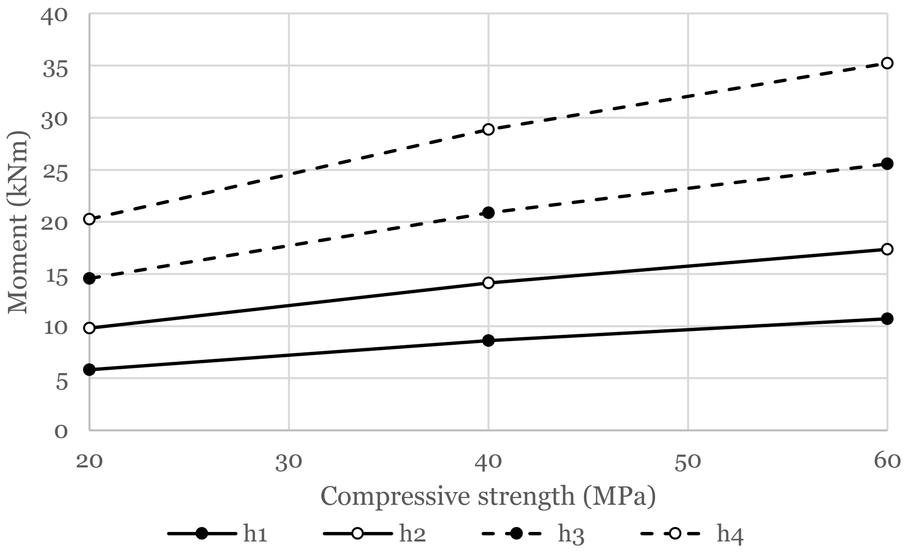

Figure A.5: Effects of slab depth and baseplate radius on the compressive strength versus moment capacity for an edge loaded slab; h_1 = 100 mm, h_2 = 125 mm, h_3 = 150 mm, h_4 = 175 mm r = 225 mm, P = *10* kN, L = 4500 mm, and k = 180 psi/in.

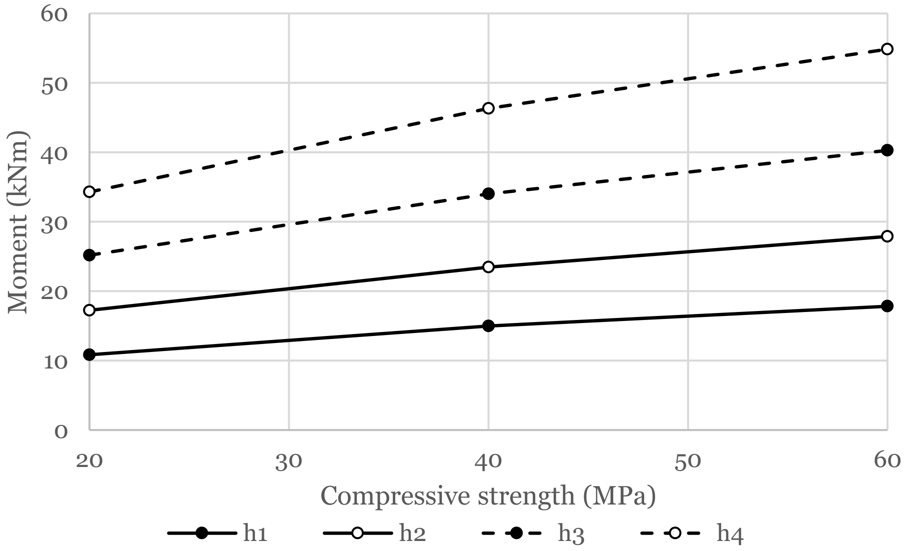

Figure A.6: Effects of slab depth and baseplate radius on the compressive strength versus moment capacity for an edge loaded slab; h_1 = 100 mm, h_2 = 125 mm, h_3 = 150 mm, h_4 = 175 mm r = 387 mm, P = *10* kN, L = 4500 mm, and k = 180 psi/in.

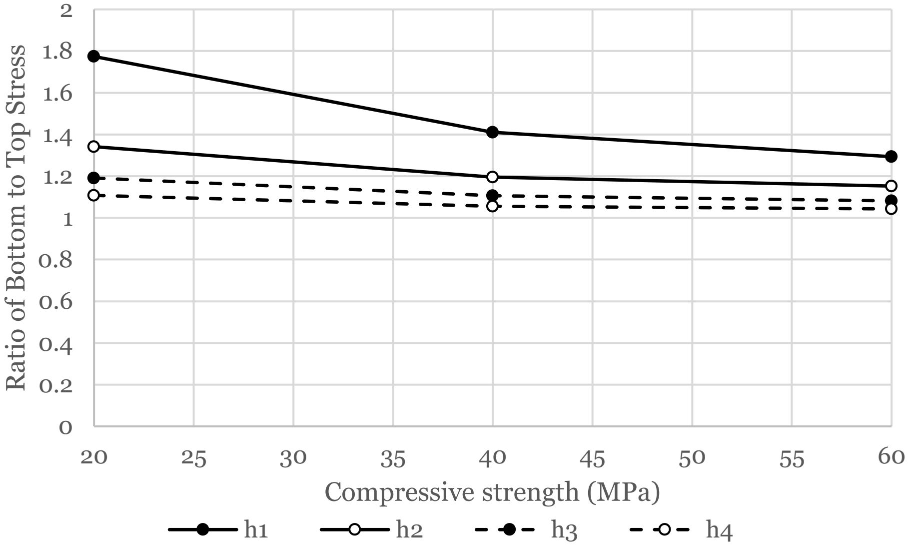

Figure A.7: Effects of slab depth and baseplate radius on the compressive strength versus ratio of bottom to top stress for an edge loaded slab; h_1 = 100 mm, h_2 = 125 mm, h_3 = 150 mm, h_4 = 175 mm r = 225 mm, P = *10* kN, L = 4500 mm, and k = 180 psi/in.

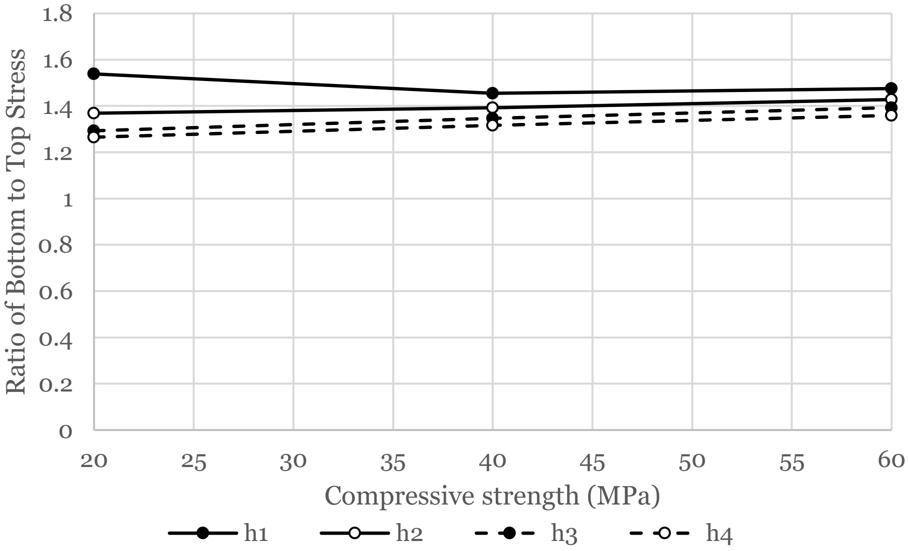

Figure A.8: Effects of slab depth and baseplate radius on the compressive strength versus ratio of bottom to top stress for an edge loaded slab; h_1 = 100 mm, h_2 = 125 mm, h_3 = 150 mm, h_4 = 175 mm r = 387 mm, P = *10* kN, L = 4500 mm, and k = 180 psi/in.

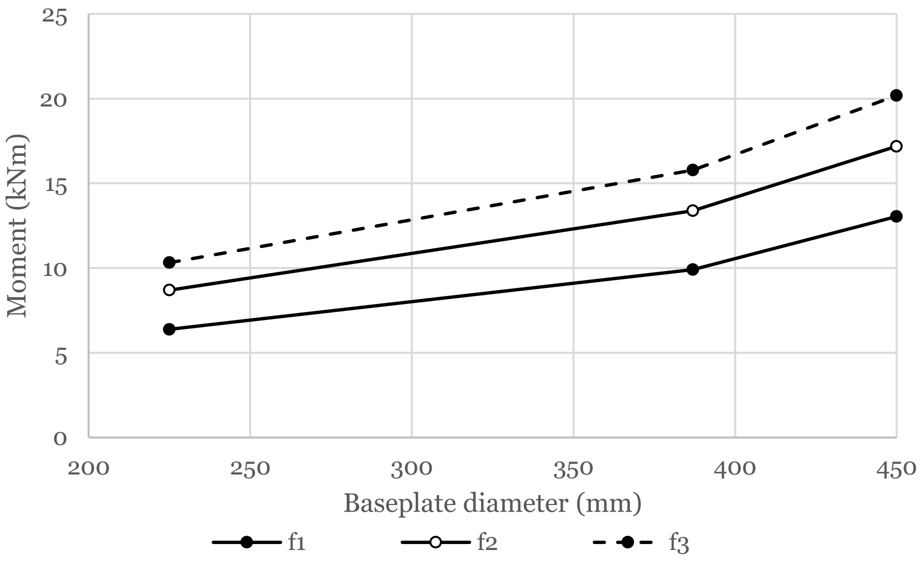

Figure A.9: Effects of slab depth and compressive strength on the baseplate radius versus moment capacity for an edge loaded slab; *h* = 100 mm, $f'_{c,1}$ = 20 MPa, $f'_{c,2}$ = 40 MPa, $f'_{c,3}$ = 60 MPa, *P = 10* kN, *L* = 4500 mm, and *k* = 180 psi/in.

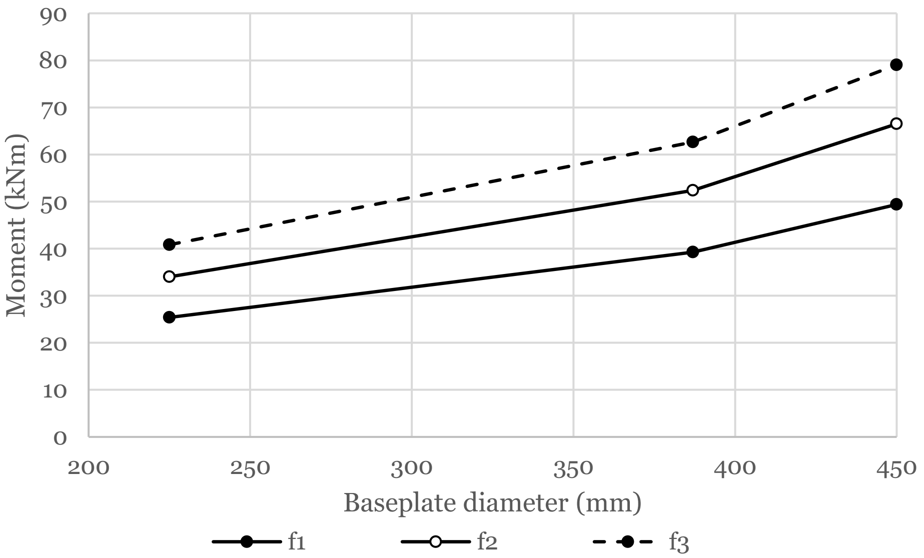

Figure A.10: Effects of slab depth and compressive strength on the baseplate radius versus moment capacity for an edge loaded slab; *h* = 200 mm, $f'_{c,1}$ = 20 MPa, $f'_{c,2}$ = 40 MPa, $f'_{c,3}$ = 60 MPa, *P = 10* kN, *L* = 4500 mm, and *k* = 180 psi/in.

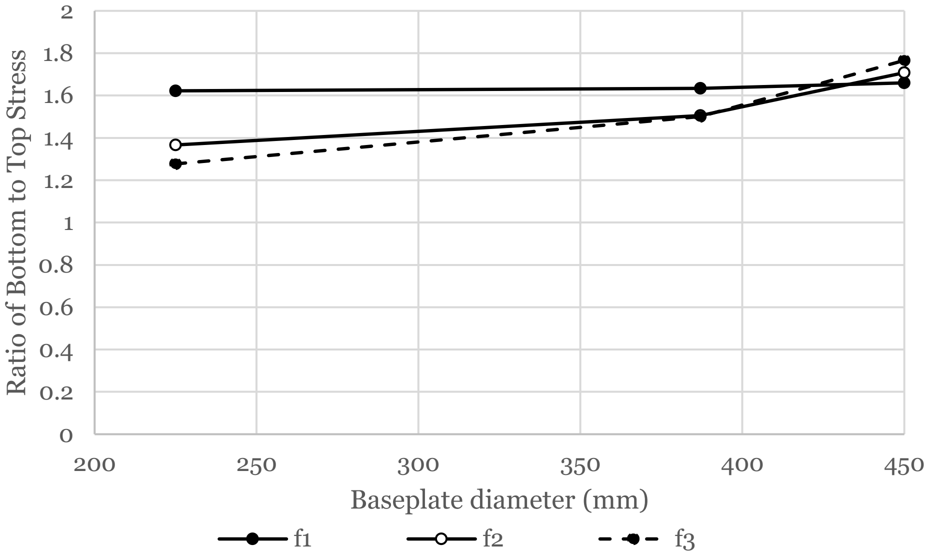

Figure A.11: Effects of slab depth and compressive strength on the baseplate radius versus ratio of bottom to top stress for an edge loaded slab; h = 100 mm, $f'_{c,1}$ = 20 MPa, $f'_{c,2}$ = 40 MPa, $f'_{c,3}$ = 60 MPa, P = *10* kN, L = 4500 mm, and k = 180 psi/in.

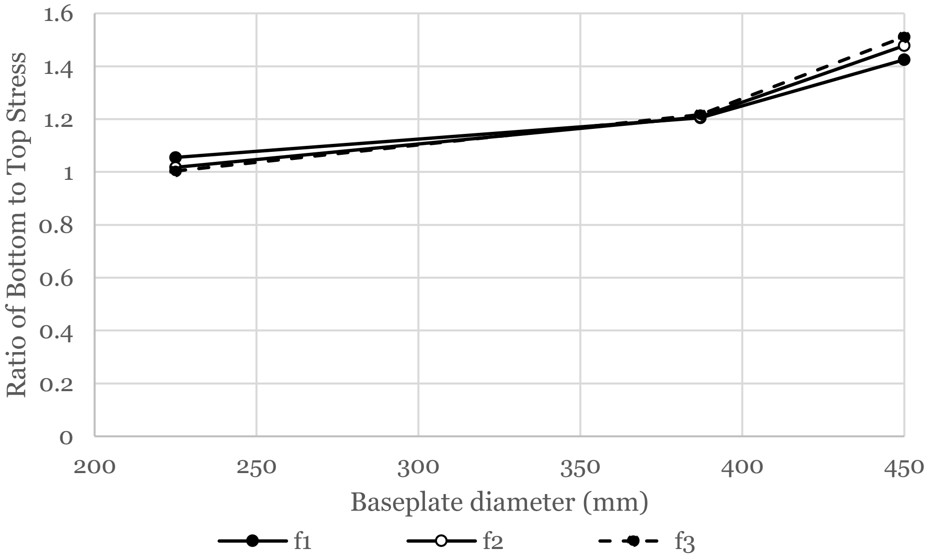

Figure A.12: Effects of slab depth and compressive strength on the baseplate radius versus ratio of bottom to top stress for an edge loaded slab; h = 200 mm, $f'_{c,1}$ = 20 MPa, $f'_{c,2}$ = 40 MPa, $f'_{c,3}$ = 60 MPa, P = *10* kN, L = 4500 mm, and k = 180 psi/in.

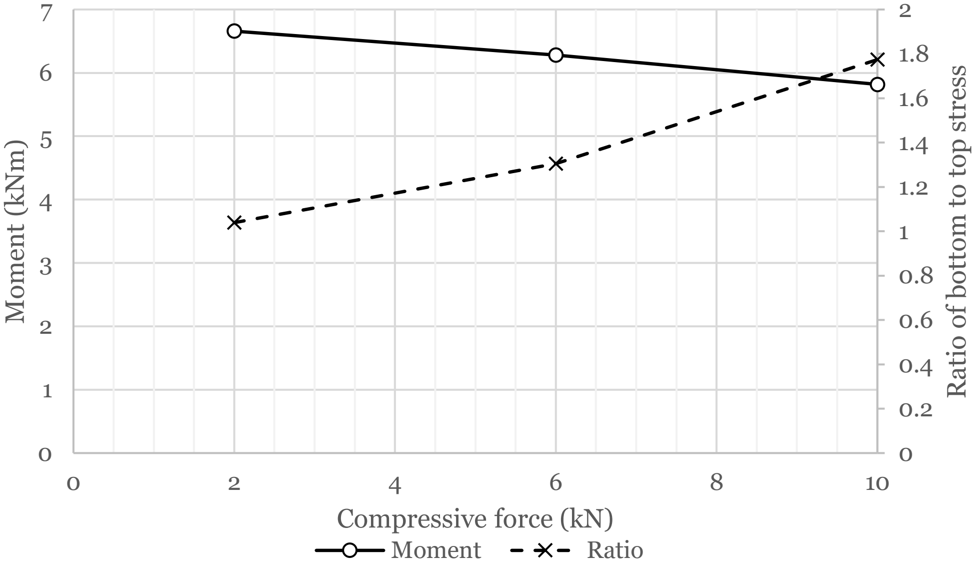

Figure A.13: Compressive force versus the moment capacity for an edge loaded slab; r = 225 mm, h = 100 mm, f'_c = 20 MPa, L = 4500 mm, and k = 180 psi/in.

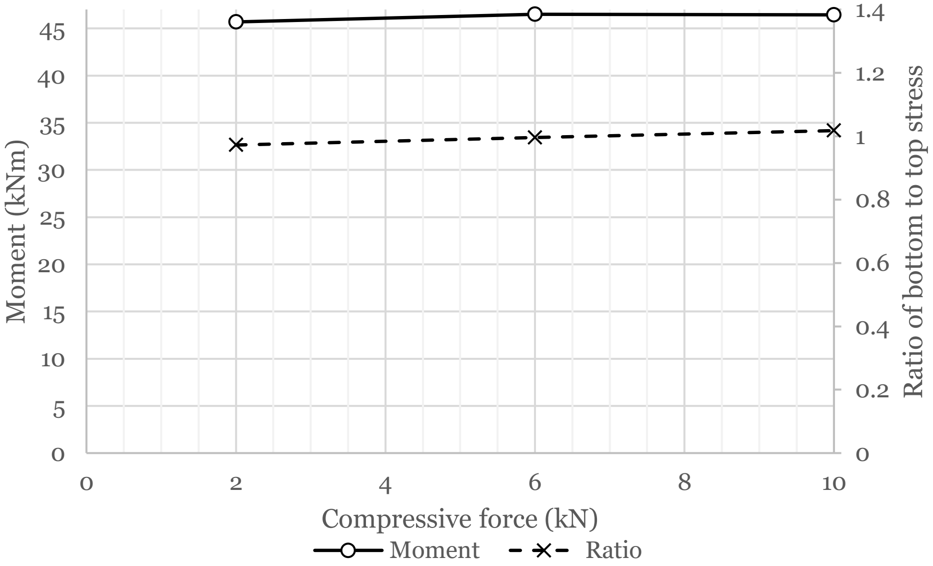

Figure A.14: Compressive force versus the moment capacity for an edge loaded slab; r = 225 mm, h = 200 mm, f'_c = 60 MPa, L = 4500 mm, and k = 180 psi/in.

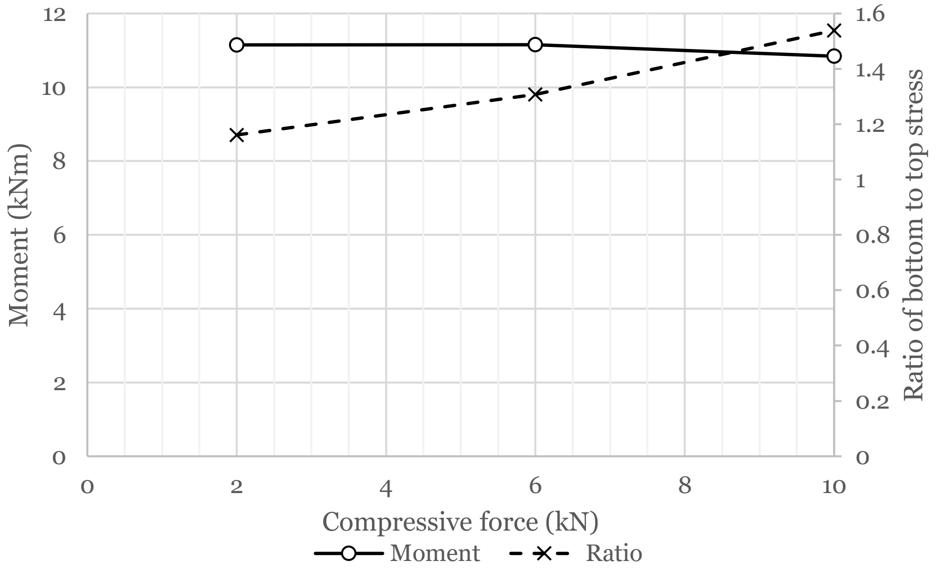

Figure A.15: Compressive force versus the moment capacity for an edge loaded slab; *r* = 450 mm, *h* = 100 mm, *f'c* = 20 MPa, *L* = 4500 mm, and *k* = 180 psi/in.

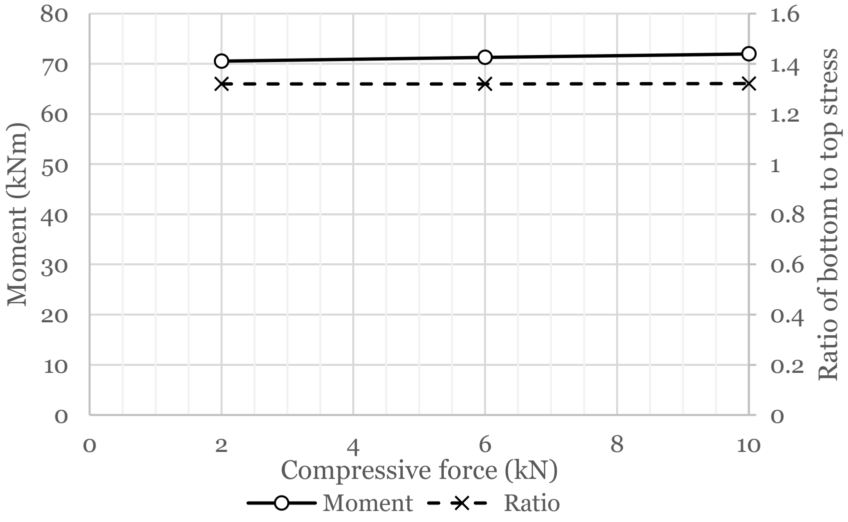

Figure A.16: Compressive force versus the moment capacity for an edge loaded slab; *r* = 450 mm, *h* = 200 mm, *f'c* = 60 MPa, *L* = 4500 mm, and *k* = 180 psi/in.

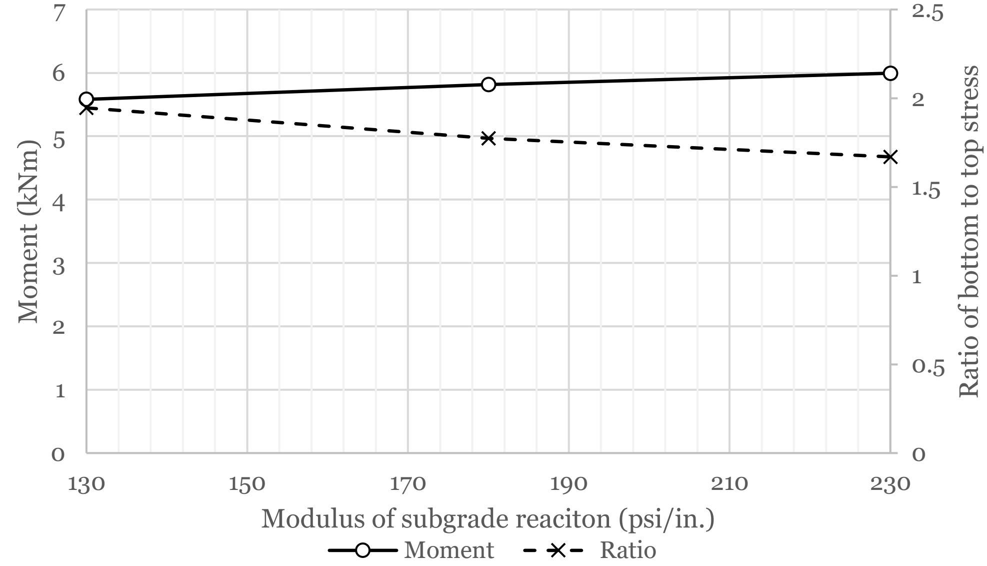

Figure A.17: Modulus of subgrade reaction versus the moment for an edge loaded slab; *r* = 225 mm, *h* = 100 mm, f'_c = 20 MPa, *L* = 4500 mm, and *P = 10 kN*

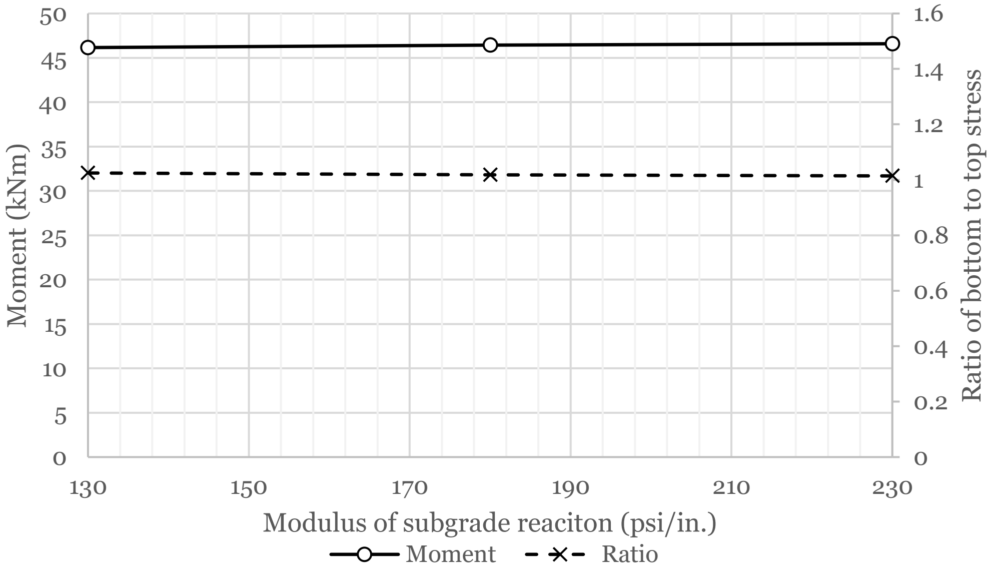

Figure A.18: Modulus of subgrade reaction versus the moment for an edge loaded slab; *r* = 225 mm, *h* = 200 mm, f'_c = 60 MPa, *L* = 4500 mm, and *P = 10 kN*

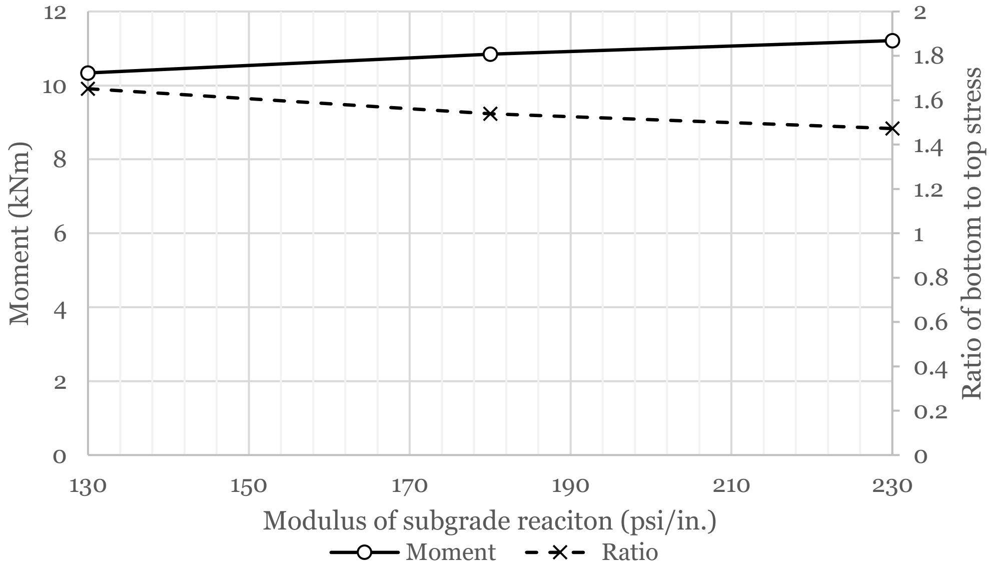

Figure A.19: Modulus of subgrade reaction versus the moment capacity for an edge loaded slab; r = 450 mm, h = 100 mm, f'_c = 20 MPa, L = 4500 mm, and P = *10 kN*

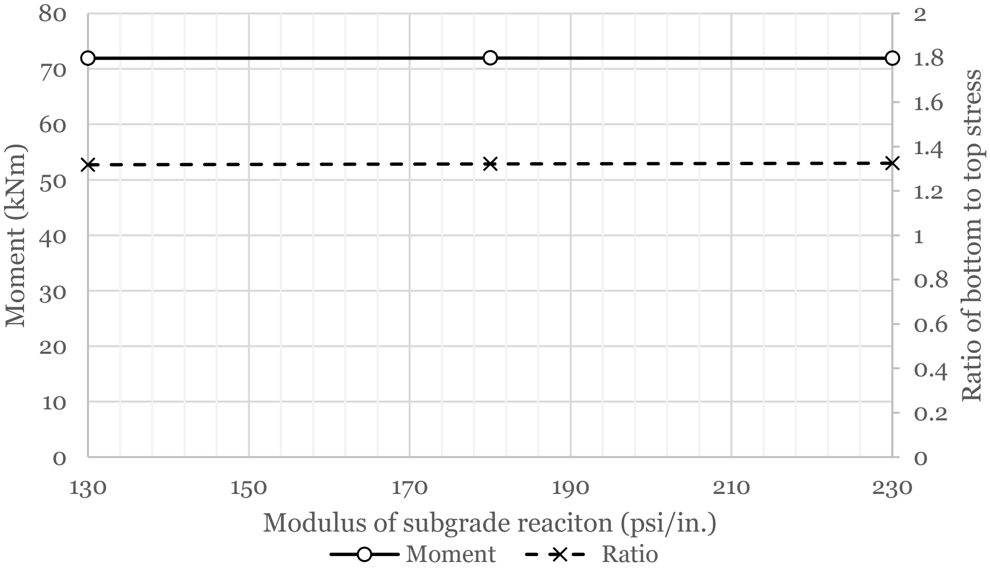

Figure A.20: Modulus of subgrade reaction versus the moment capacity for an edge loaded slab; r = 450 mm, h = 200 mm, f'_c = 60 MPa, L = 4500 mm, and P = *10 kN*

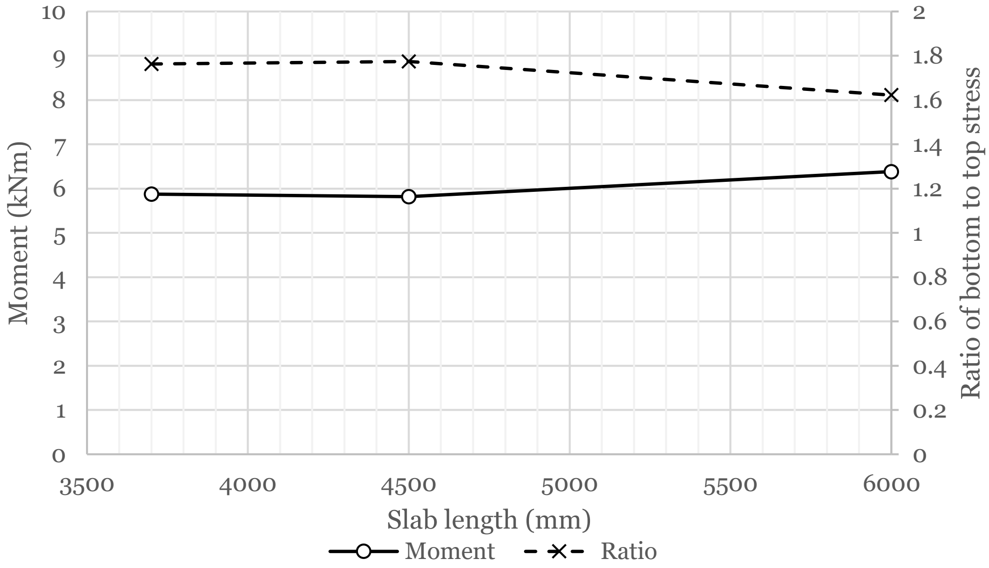

Figure A.21: Length versus the moment capacity for an edge loaded slab; *r* = 225 mm, *h* = 100 mm, f'_c = 20 MPa, *P = 10 kN*, and *k* = 180 psi/in.

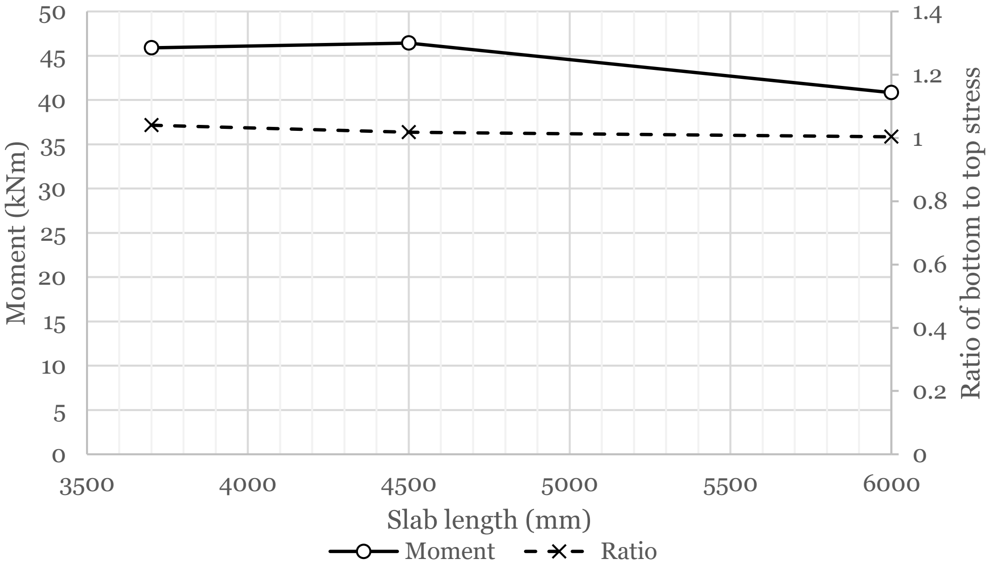

Figure A.22: Length versus the moment capacity for an edge loaded slab; *r* = 225 mm, *h* = 200 mm, f'_c = 60 MPa, *P = 10 kN*, and *k* = 180 psi/in.

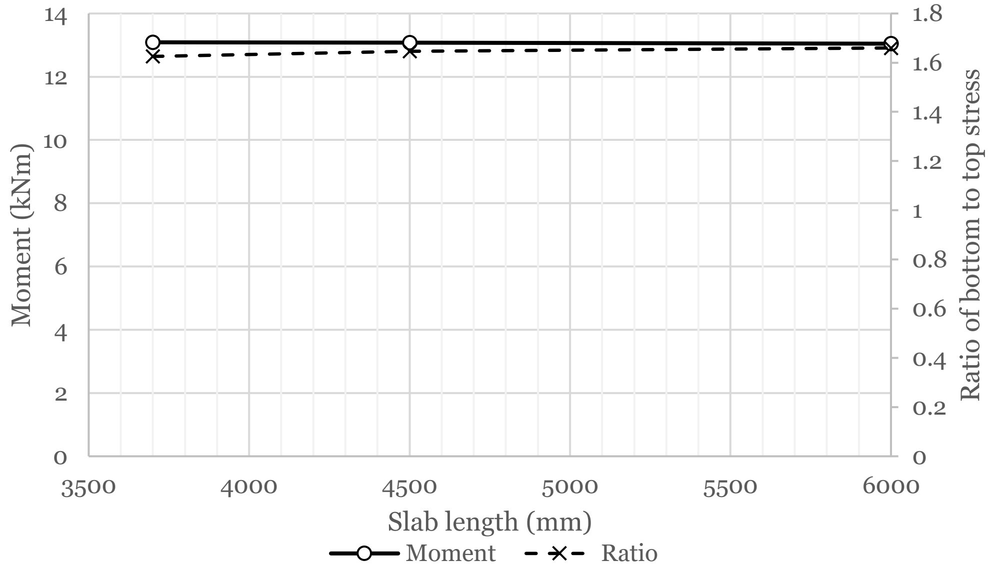

Figure A.23: Length versus the moment capacity for an edge loaded slab; r = 450 mm, h = 100 mm, f'_c = 20 MPa, P = *10 kN*, and k = 180 psi/in.

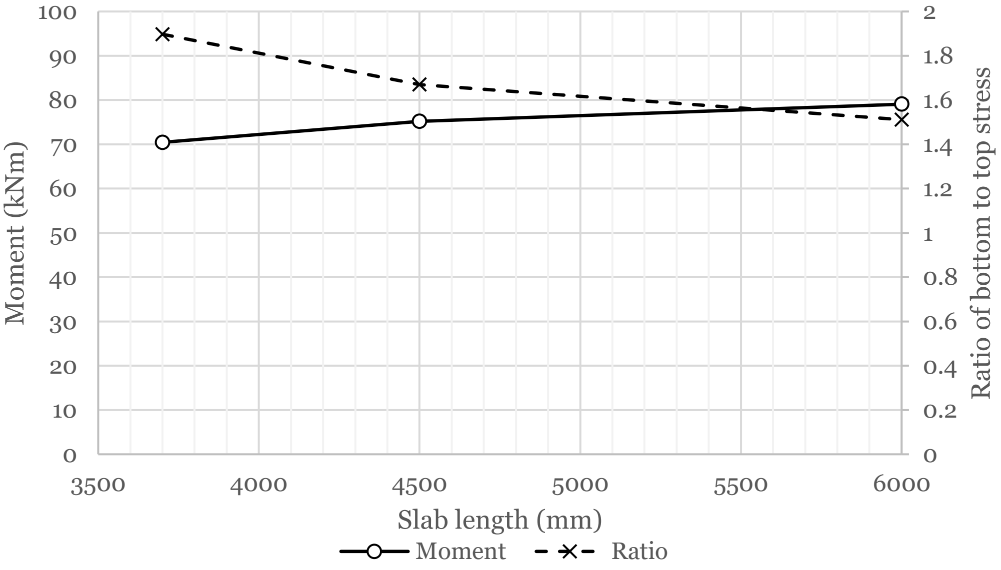

Figure A.24: Length versus the moment capacity for an edge loaded slab; r = 450 mm, h = 200 mm, f'_c = 60 MPa, P = *10 kN*, and k = 180 psi/in.

Appendix B – Corner Loading Case

The relationships of the critical model parameters and the moment capacity of a slab with a corner loaded crane obtained from the parametric study have been summarized below. Additionally, figures showcasing the effects of any particular model parameter on the relationship between any other model parameter and the moment capacity of the slab are provided.

Table B.1: Coefficients for general equation, corner loaded case

n_{ijk}	Value	n_{ijk}	Value	x_{ijk}	Value
A1	0.0063	C56	0.1263	D21	0.00458
A2	-0.0048	E123	-0.0015	D23	-0.0405
A3	-0.0121	E124	0.00062	D24	0.00121
A4	-0.0021	E125	0.00258	D25	-0.0151
A5	-0.0291	E126	0.00257	D26	-0.0446
A6	0.09131	E134	0.00102	D31	-0.0124
B1	-0.0077	E135	-0.0017	D32	-0.0063
B2	0.0784	E136	-0.0041	D34	0.00301
B3	-0.023	E145	2.6E-05	D35	0.00899
B4	0.00285	E146	-0.0008	D36	0.01718
B5	0.10378	E156	0.00287	D41	0.00012
B6	0.24306	E234	-0.0014	D42	0.001
C12	-0.0016	E235	-0.0095	D43	-0.0021
C13	0.01665	E236	-0.0141	D45	0.00188
C14	-0.0013	E245	1E-05	D46	0.00166
C15	0.00227	E246	-0.0043	D51	0.00167
C16	0.00687	E256	0.13556	D52	0.00529
C23	0.10416	E345	-0.0061	D53	-0.0127
C24	-0.0027	E346	-0.008	D54	0.00275
C25	0.00244	E356	-0.0224	D56	-0.0592
C26	0.09411	E456	-0.0008	D61	0.00473
C34	0.01147	D12	-0.0027	D62	0.12197
C35	0.03416	D13	0.00213	D63	-0.0111
C36	0.02096	D14	0.00058	D64	0.00297
C45	-0.0053	D15	-0.0062	D65	0.13586
C46	-0.0012	D16	-0.0111	F	-0.0029
				G	0.02211

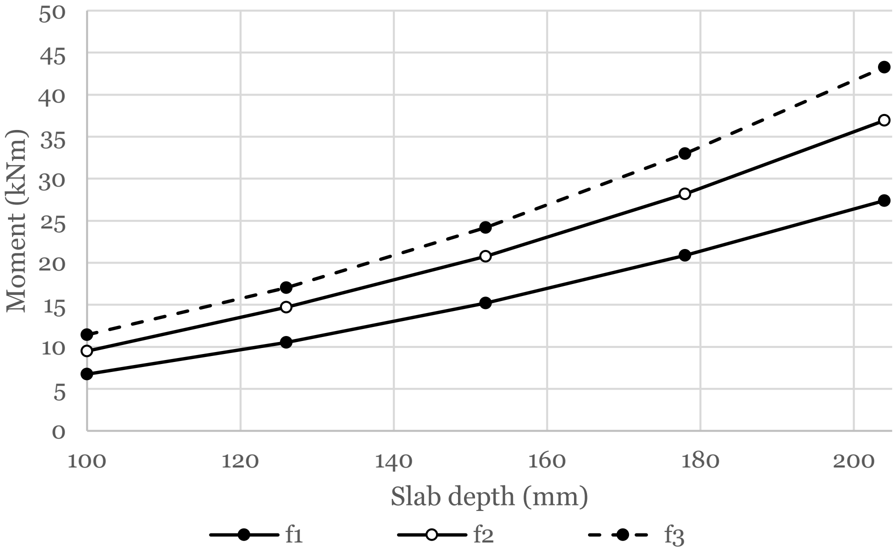

Figure B.1: Effects of compressive strength and baseplate radius on the slab depth versus the moment capacity for a corner loaded slab; $f'_{c,1}$ = 20 MPa, $f'_{c,2}$ = 40 MPa, $f'_{c,3}$ = 60 MPa, r = 225 mm, P = 10 kN, L = 4500 mm, and k = 180 psi/in.

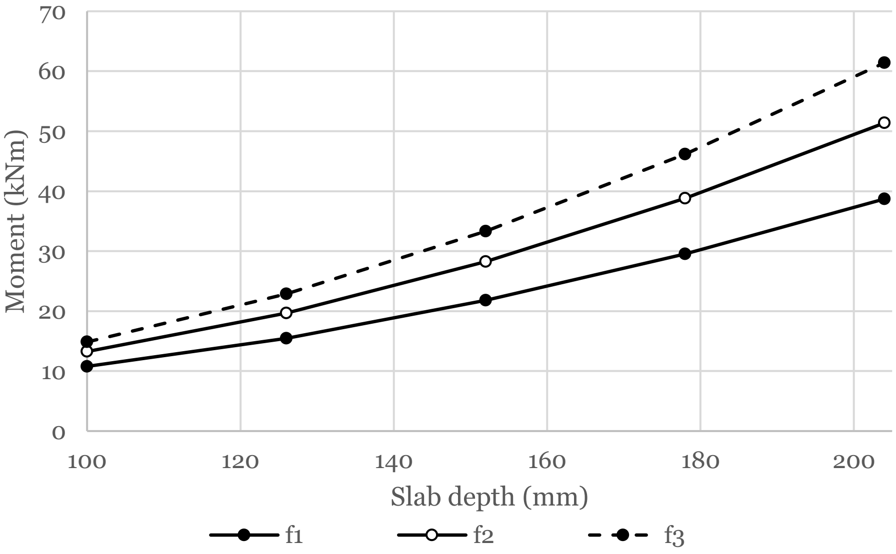

Figure B.2: Effects of compressive strength and baseplate radius on the slab depth versus the moment capacity for a corner loaded slab; $f'_{c,1}$ = 20 MPa, $f'_{c,2}$ = 40 MPa, $f'_{c,3}$ = 60 MPa, r = 387 mm, P = 10 kN, L = 4500 mm, and k = 180 psi/in.

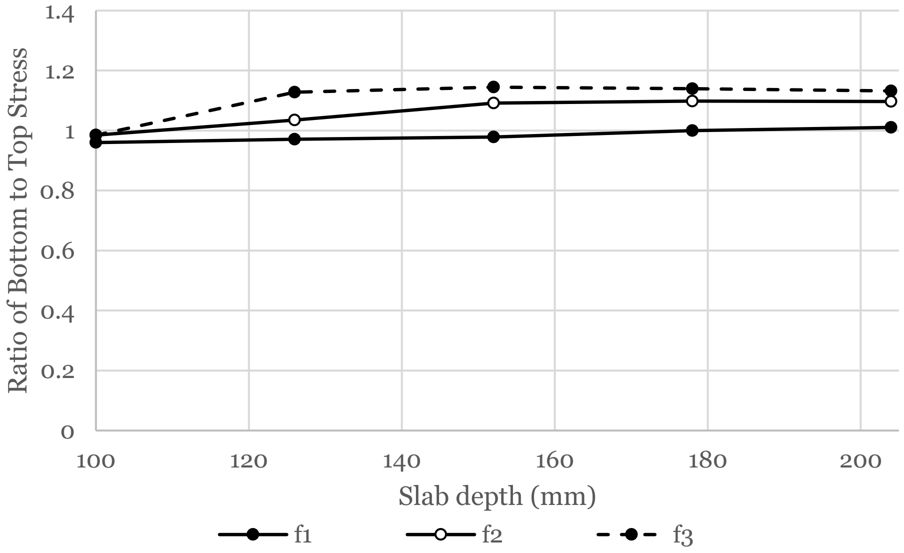

Figure B.3: Effects of compressive strength and baseplate radius on the slab depth versus the ratio of bottom to top stress for a corner loaded slab; $f'_{c,1}$ = 20 MPa, $f'_{c,2}$ = 40 MPa, $f'_{c,3}$ = 60 MPa, r = 225 mm, P = 10 kN, L = 4500 mm, and k = 180 psi/in.

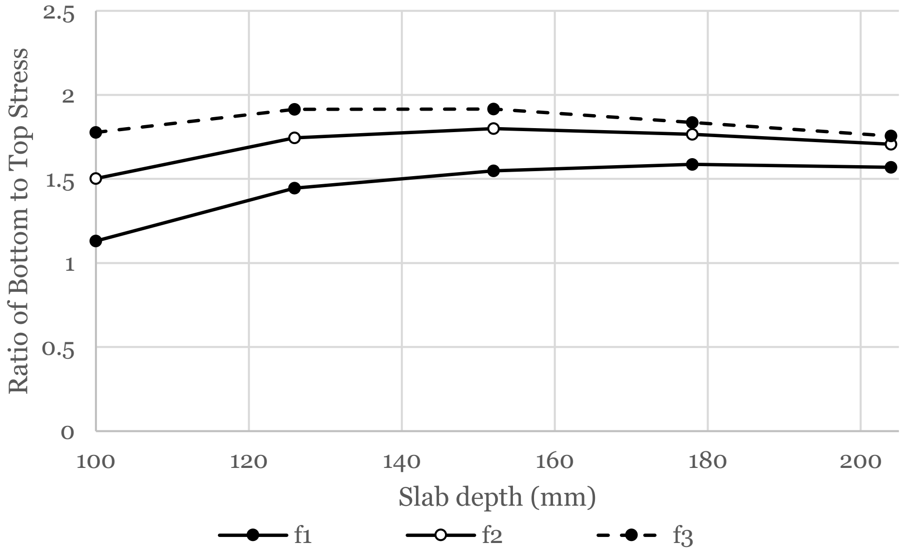

Figure B.4: Effects of compressive strength and baseplate radius on the slab depth versus the ratio of bottom to top stress for a corner loaded slab; $f'_{c,1}$ = 20 MPa, $f'_{c,2}$ = 40 MPa, $f'_{c,3}$ = 60 MPa, r = 387 mm, P = 10 kN, L = 4500 mm, and k = 180 psi/in.

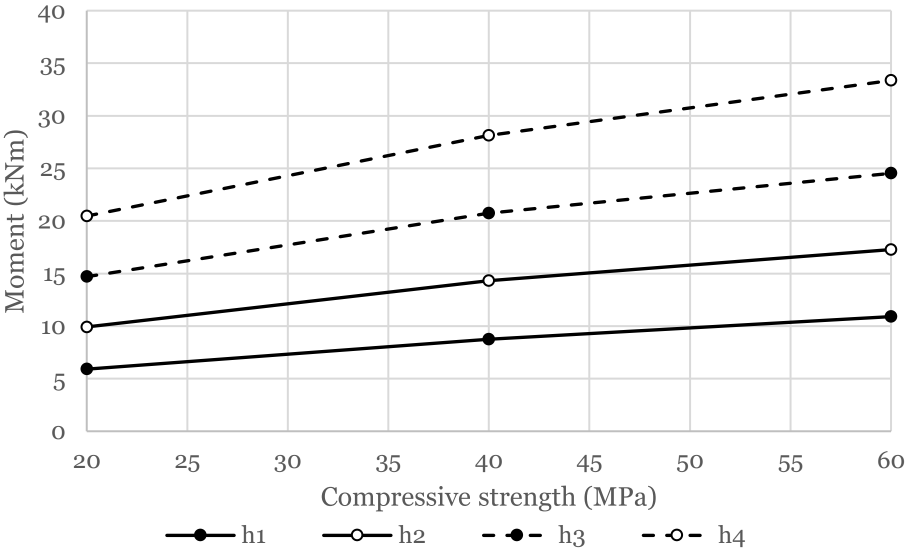

Figure B.5: Effects of slab depth and baseplate radius on the compressive strength versus moment capacity for a corner loaded slab; h_1 = 100 mm, h_2 = 125 mm, h_3 = 150 mm, h_4 = 175 mm r = 225 mm, P = *10* kN, L = 4500 mm, and k = 180 psi/in.

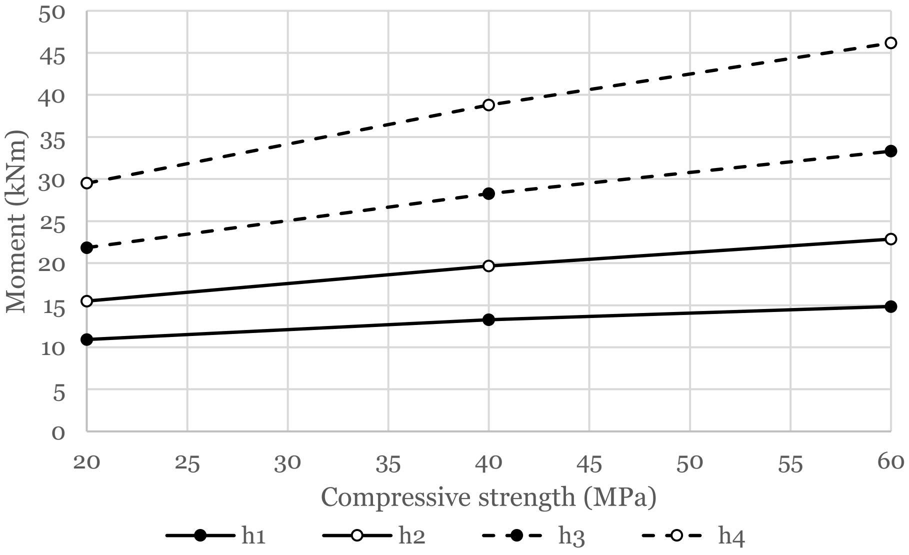

Figure B.6: Effects of slab depth and baseplate radius on the compressive strength versus moment capacity for a corner loaded slab; h_1 = 100 mm, h_2 = 125 mm, h_3 = 150 mm, h_4 = 175 mm r = 387 mm, P = *2* kN, L = 4500 mm, and k = 180 psi/in.

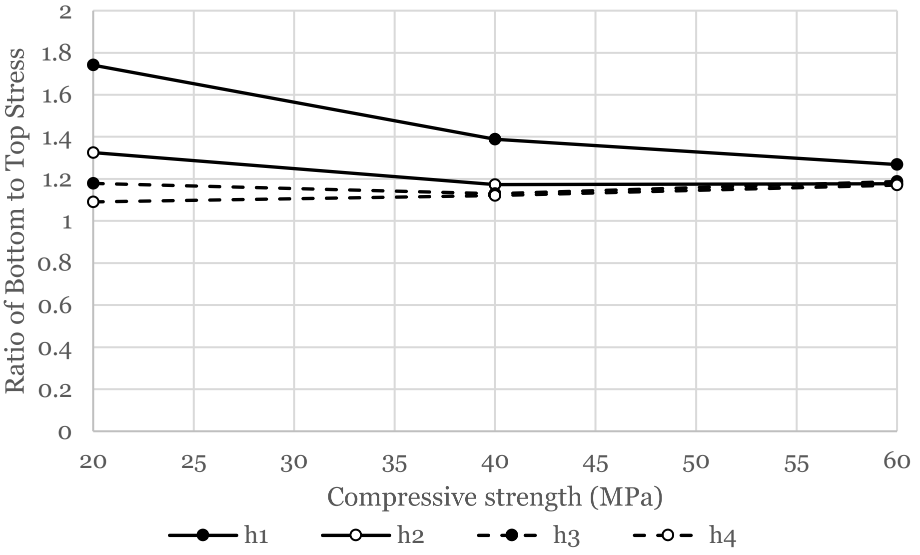

Figure B.7: Effects of slab depth and baseplate radius on the compressive strength versus ratio of bottom to top stress for a corner loaded slab; h_1 = 100 mm, h_2 = 125 mm, h_3 = 150 mm, h_4 = 175 mm r = 225 mm, P = *10* kN, L = 4500 mm, and k = 180 psi/in.

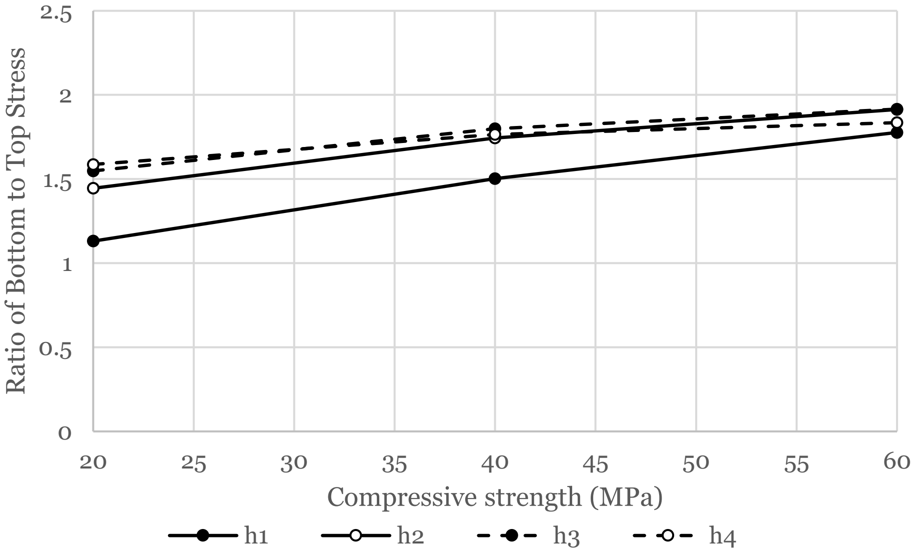

Figure B.8: Effects of slab depth and baseplate radius on the compressive strength versus ratio of bottom to top stress for a corner loaded slab; h_1 = 100 mm, h_2 = 125 mm, h_3 = 150 mm, h_4 = 175 mm r = 387 mm, P = *2* kN, L = 4500 mm, and k = 180 psi/in.

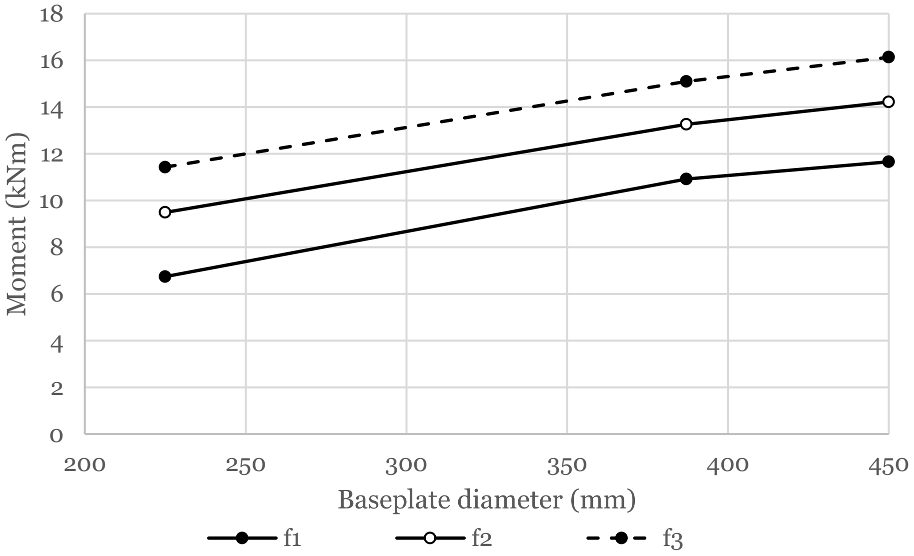

Figure B.9: Effects of slab depth and compressive strength on the baseplate radius versus moment capacity for a corner slab; *h* = 100 mm, $f'_{c,1}$ = 20 MPa, $f'_{c,2}$ = 40 MPa, $f'_{c,3}$ = 60 MPa, *P* = 2 kN, *L* = 4500 mm, and *k* = 180 psi/in.

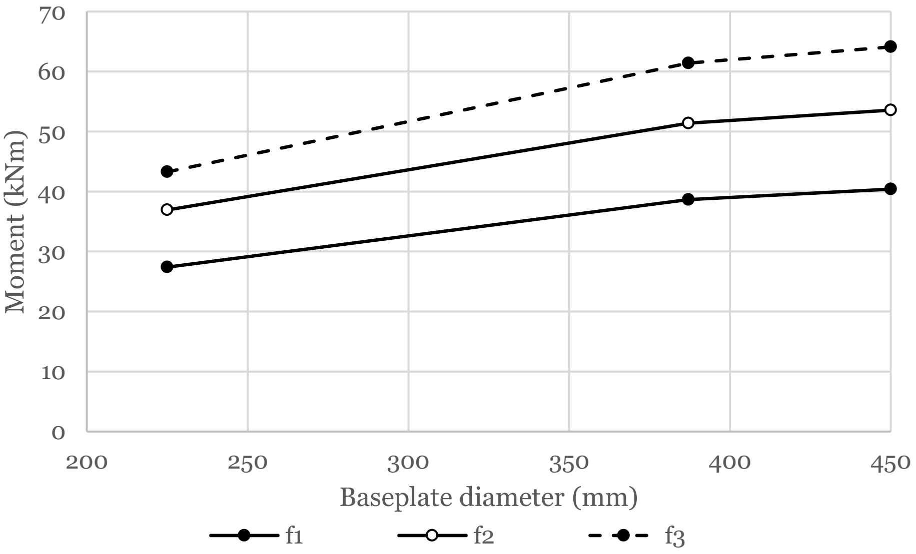

Figure B.10: Effects of slab depth and compressive strength on the baseplate radius versus moment capacity for a corner loaded slab; *h* = 200 mm, $f'_{c,1}$ = 20 MPa, $f'_{c,2}$ = 40 MPa, $f'_{c,3}$ = 60 MPa, *P* = 2 kN, *L* = 4500 mm, and *k* = 180 psi/in.

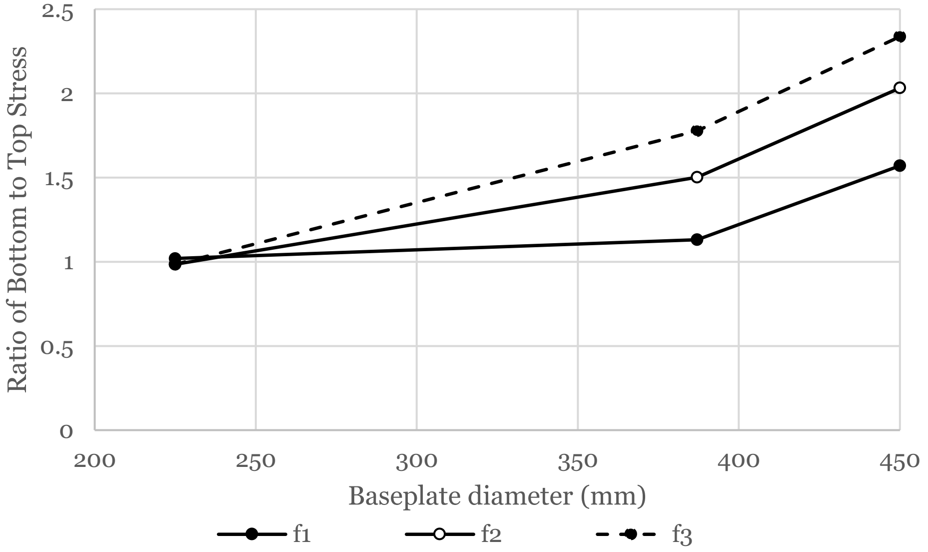

Figure B.11: Effects of slab depth and compressive strength on the baseplate radius versus ratio of bottom to top stress for a corner loaded slab; h = 100 mm, $f'_{c,1}$ = 20 MPa, $f'_{c,2}$ = 40 MPa, $f'_{c,3}$ = 60 MPa, P = 2 kN, L = 4500 mm, and k = 180 psi/in.

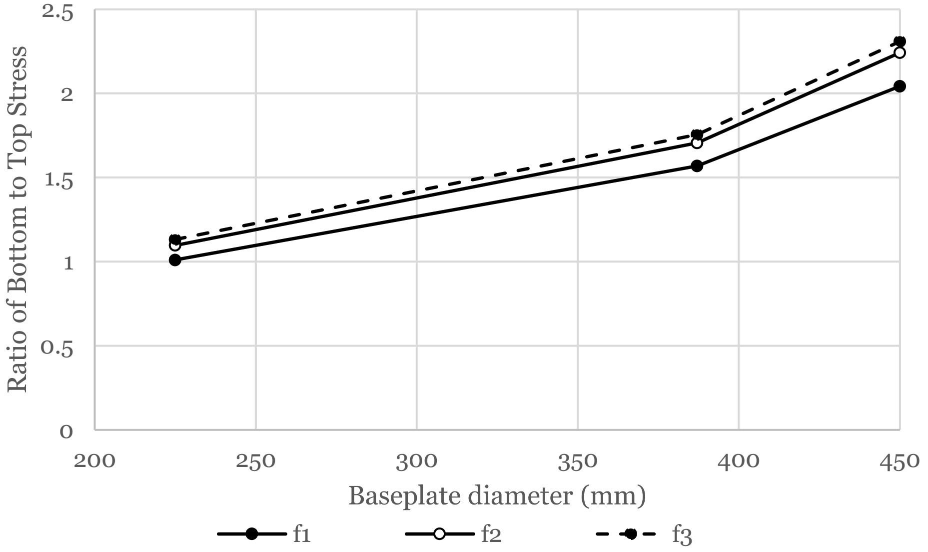

Figure B.12: Effects of slab depth and compressive strength on the baseplate radius versus ratio of bottom to top stress for a corner loaded slab; h = 200 mm, $f'_{c,1}$ = 20 MPa, $f'_{c,2}$ = 40 MPa, $f'_{c,3}$ = 60 MPa, P = 2 kN, L = 4500 mm, and k = 180 psi/in.

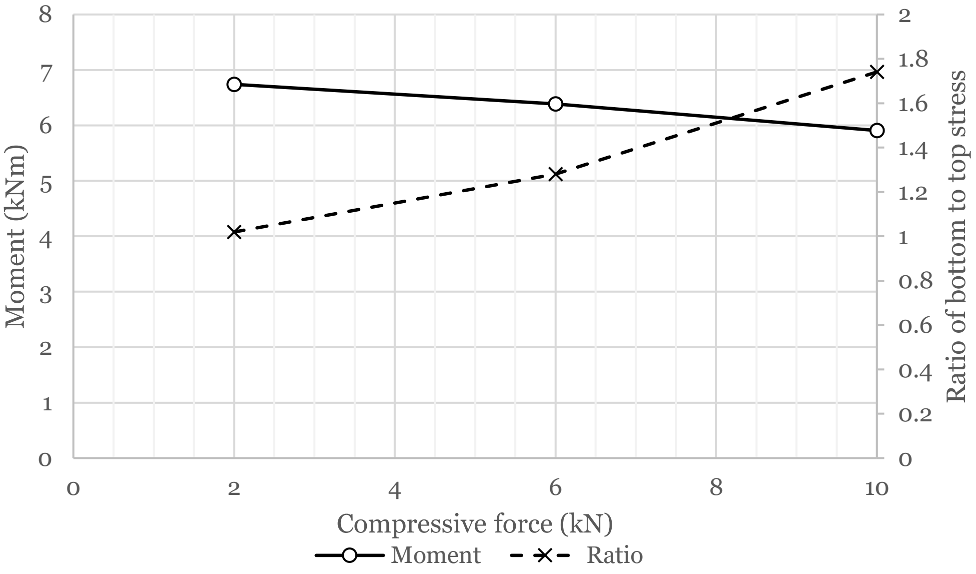

Figure B.13: Compressive force versus the moment capacity for a corner loaded slab; r = 225 mm, h = 100 mm, f'_c = 20 MPa, L = 4500 mm, and k = 180 psi/in.

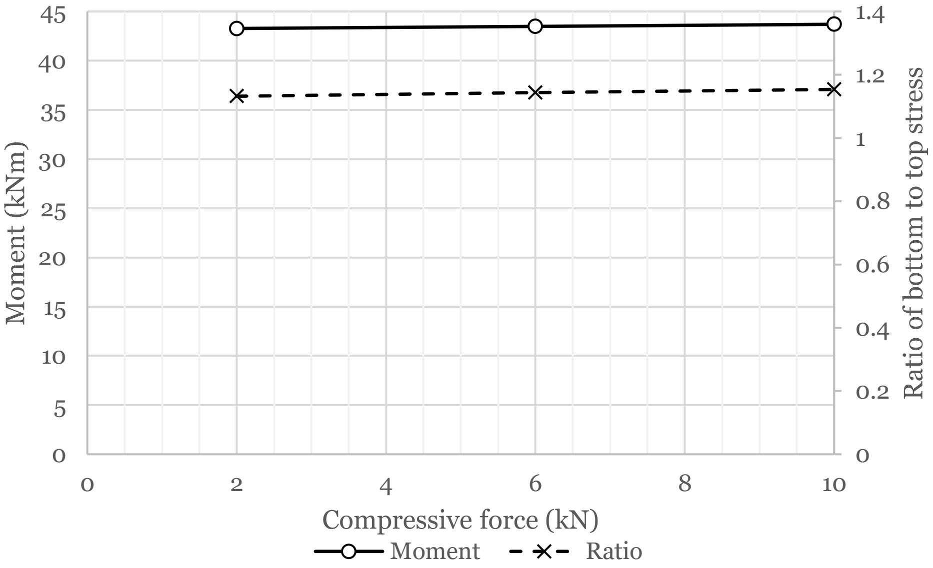

Figure B.14: Compressive force versus the moment capacity for a corner loaded slab; r = 225 mm, h = 200 mm, f'_c = 60 MPa, L = 4500 mm, and k = 180 psi/in.

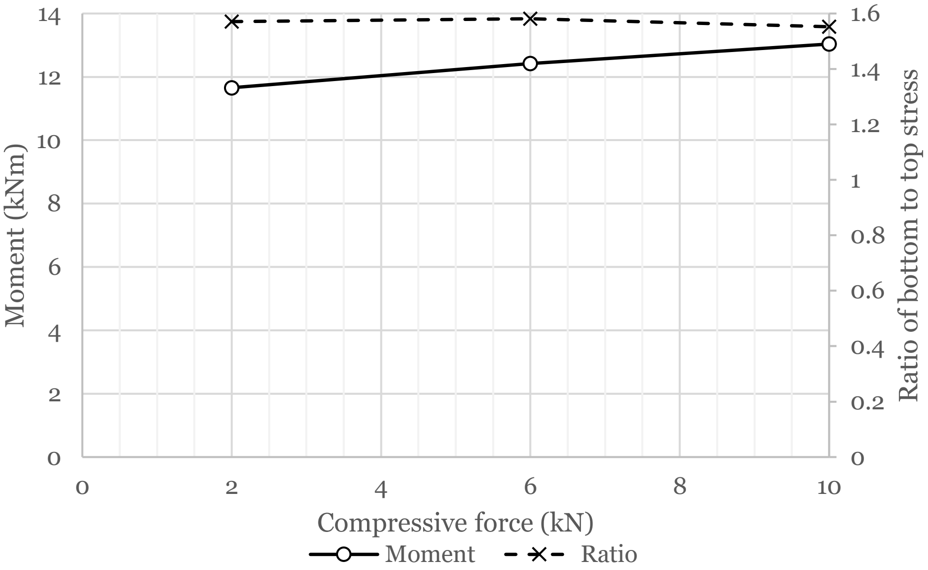

Figure B.15: Compressive force versus the moment capacity for a corner loaded slab; *r* = 450 mm, *h* = 100 mm, *f'c* = 20 MPa, *L* = 4500 mm, and *k* = 180 psi/in.

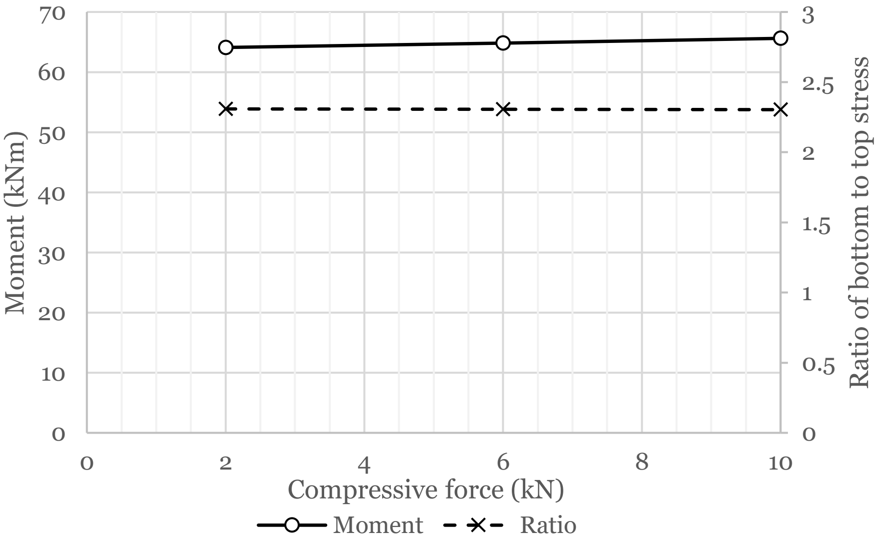

Figure B.16: Compressive force versus the moment capacity for a corner loaded slab; *r* = 450 mm, *h* = 200 mm, *f'c* = 60 MPa, *L* = 4500 mm, and *k* = 180 psi/in.

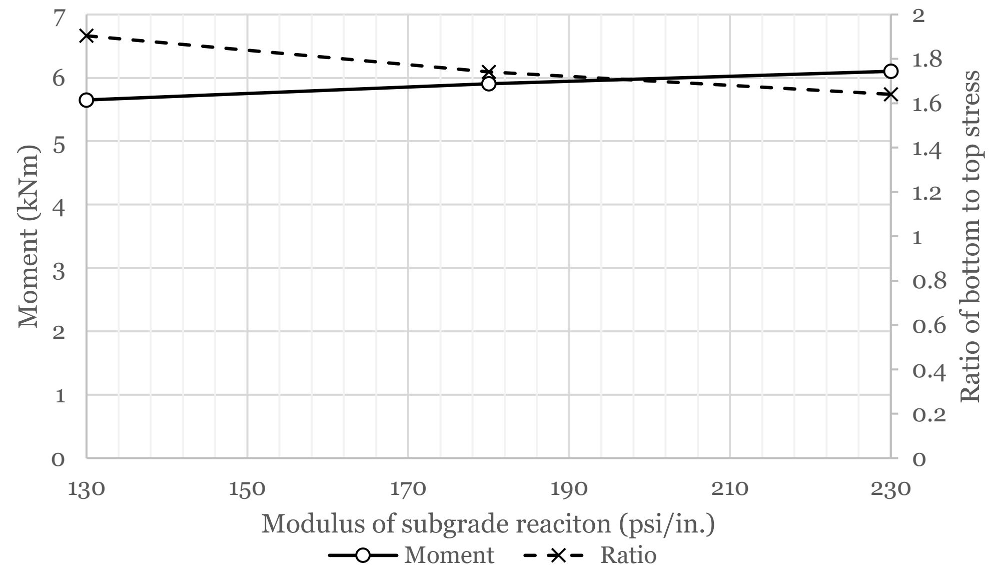

Figure B.17: Modulus of subgrade reaction versus the moment for a corner loaded slab; r = 225 mm, h = 100 mm, f'_c = 20 MPa, L = 4500 mm, and P = *10 kN*

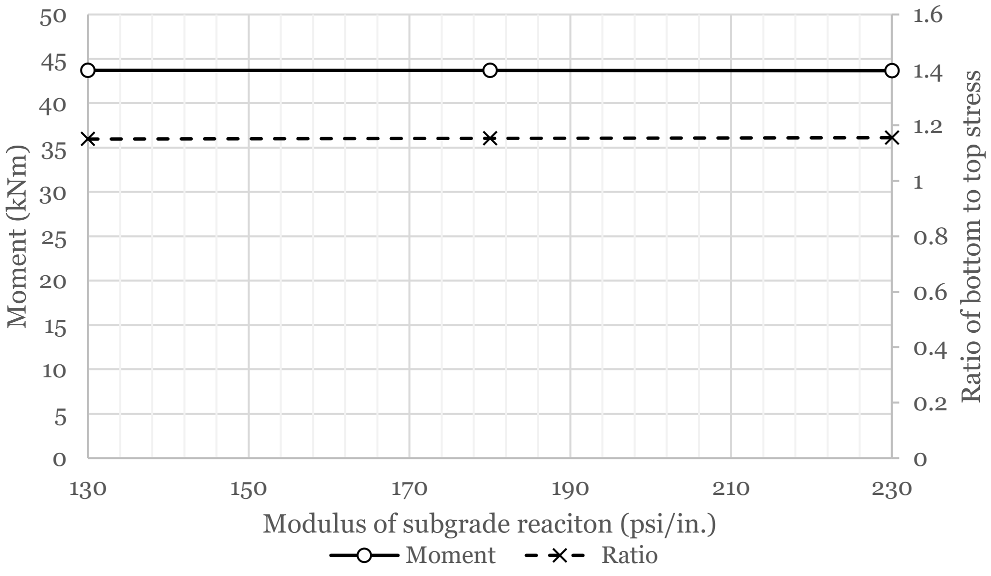

Figure B.18: Modulus of subgrade reaction versus the moment for a corner loaded slab; r = 225 mm, h = 200 mm, f'_c = 60 MPa, L = 4500 mm, and P = *10 kN*

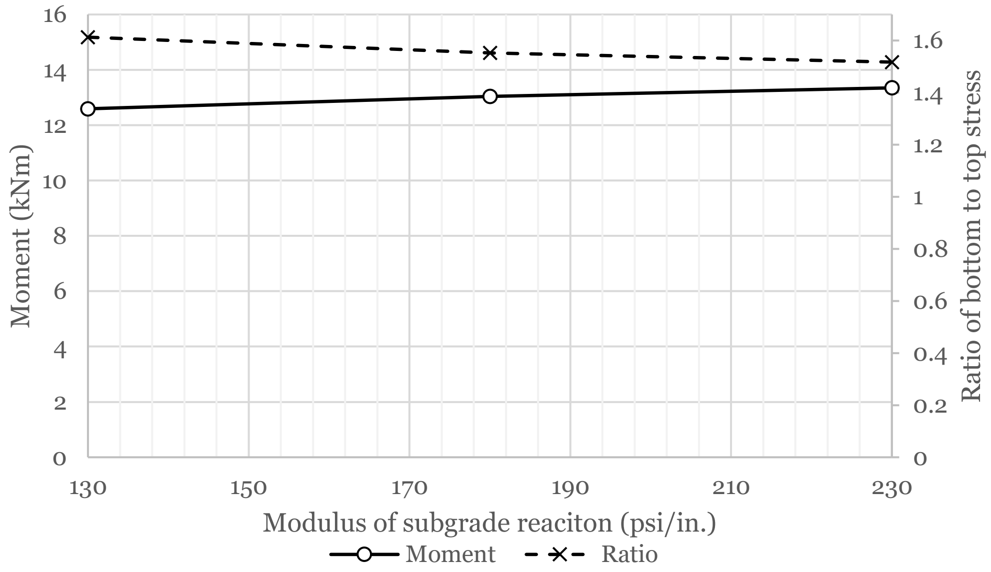

Figure B.19: Modulus of subgrade reaction versus the moment capacity for a corner loaded slab; *r* = 450 mm, *h* = 100 mm, f'_c = 20 MPa, *L* = 4500 mm, and *P = 10 kN*

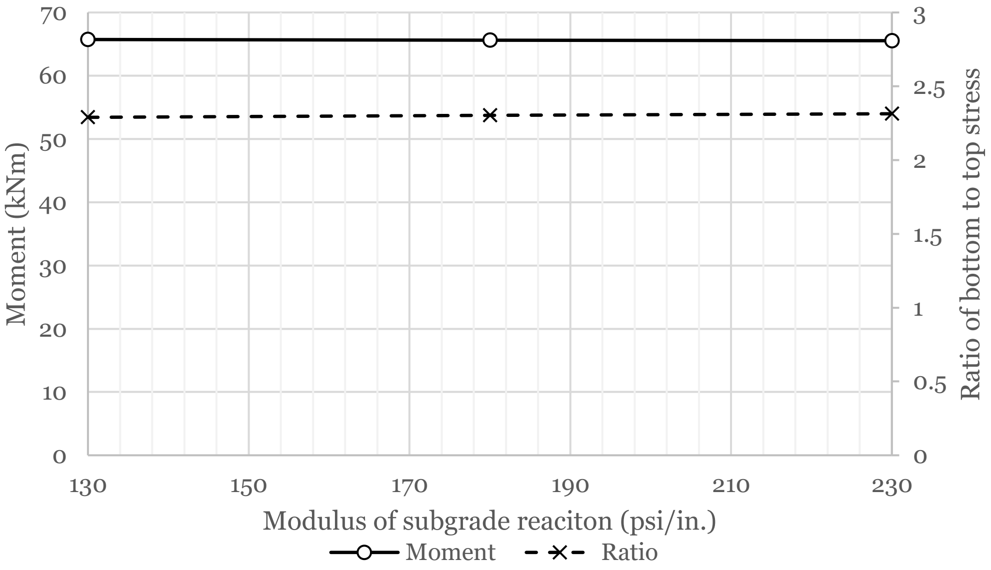

Figure B.20: Modulus of subgrade reaction versus the moment capacity for a corner loaded slab; *r* = 450 mm, *h* = 200 mm, f'_c = 60 MPa, *L* = 4500 mm, and *P = 10 kN*

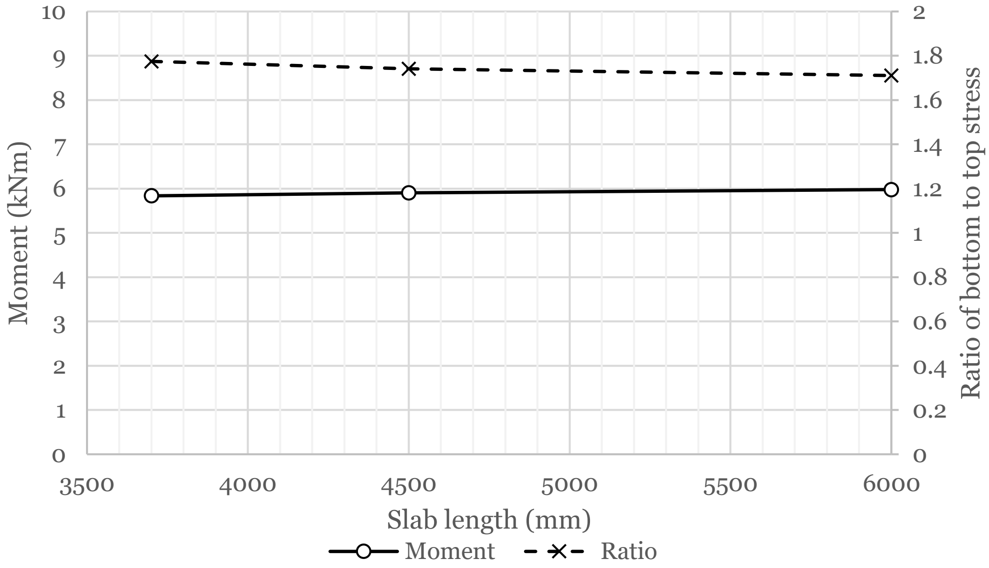

Figure B.21: Length versus the moment capacity for a corner loaded slab; *r* = 225 mm, *h* = 100 mm, *f'*$_c$ = 20 MPa, *P* = *10 kN*, and *k* = 180 psi/in.

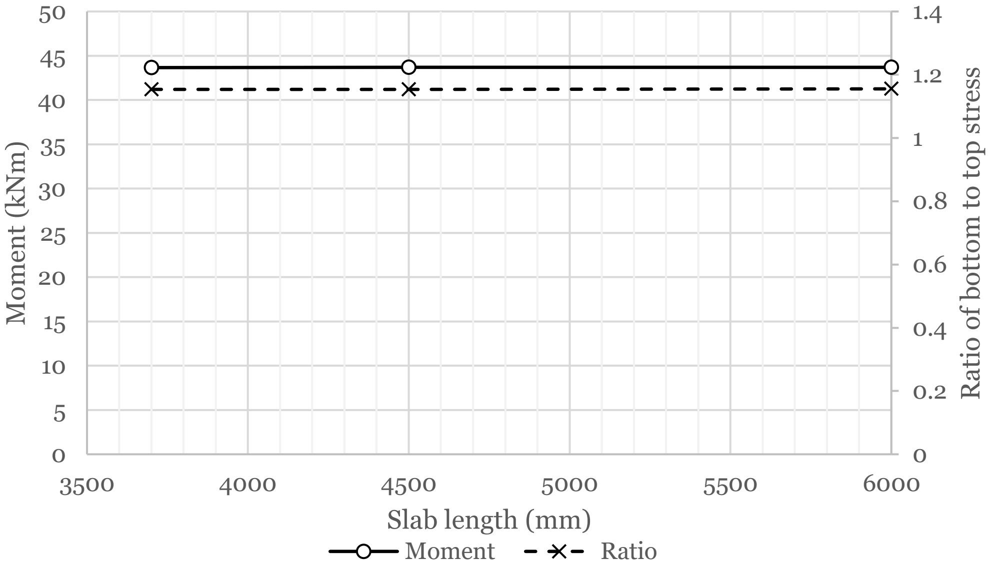

Figure B.22: Length versus the moment capacity for a corner loaded slab; *r* = 225 mm, *h* = 200 mm, *f'*$_c$ = 60 MPa, *P* = *10 kN*, and *k* = 180 psi/in.

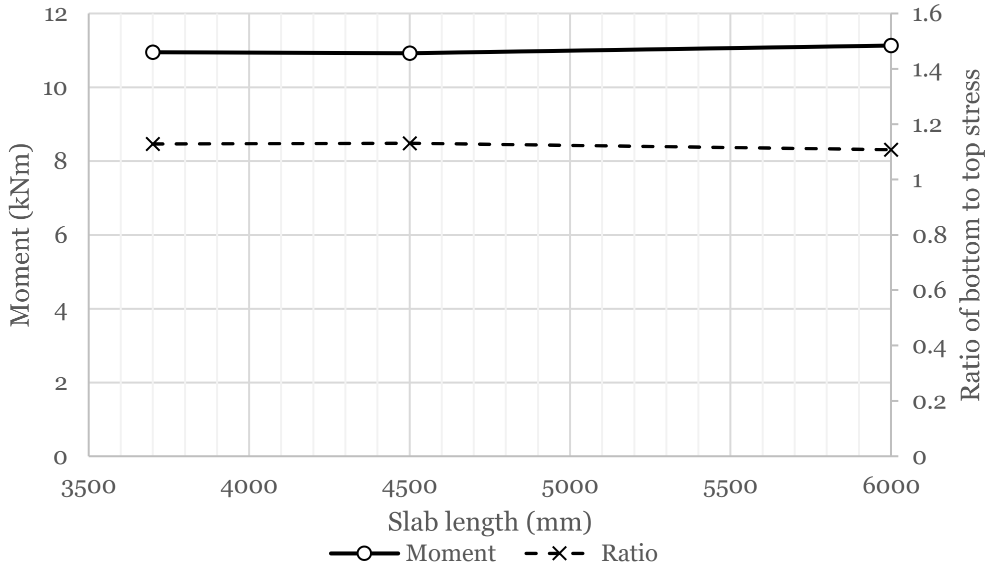

Figure B.23: Length versus the moment capacity for a corner loaded slab; *r* = 387 mm, *h* = 100 mm, *f'c* = 20 MPa, *P = 10 kN*, and *k* = 180 psi/in.

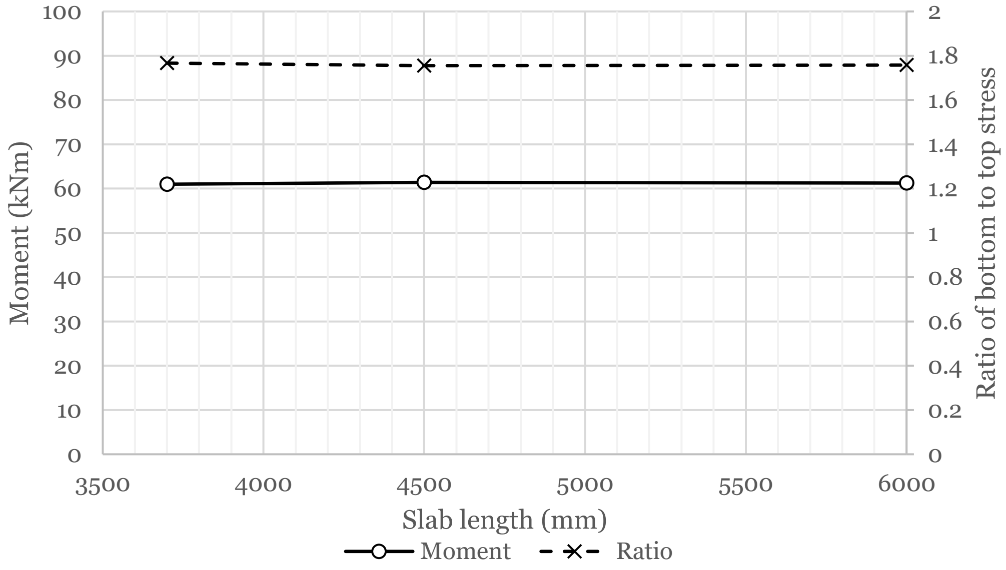

Figure B.24: Length versus the moment capacity for a corner loaded slab; *r* = 387 mm, *h* = 200 mm, *f'c* = 60 MPa, *P* = 10 kN, and *k* = 180 psi/in.